Mechanical Engineering Advances

https://ojs.acad-pub.com/index.php/MEA

ACADEMIC
ACADEMIC PUBLISHING PTE LTD

2023 VOLUME 1 ISSUE 1
ISSN: 3029-1232

1

Volume 1 Issue 1 • 2023

Mechanical Engineering Advances

Editor-in-Chief

Prof. Nidal Helmi Abu-Hamdeh

King Abdulaziz University, Saudi Arabia

ACADEMIC
ACADEMIC PUBLISHING PTE LTD

2023 | Volume 1 | Issue 1

Mechanical Engineering Advances

https://ojs.acad-pub.com/index.php/MEA/index

Contents

Mechanical Engineering Advances 2023; 1(1): 66.
Original Research Article

Theoretical analysis using thermal efficiency concept in straight micro channel printed circuit heat exchanger

Élcio Nogueira[1,*], Humberto Araújo Machado[1,2]

[1] *Faculdade de Tecnologia–FAT/UERJ, Resende 27537-000, Brazil*

[2] *Instituto de Aeronáutica e Espaço–IAE, São José dos Campos 12228-904, Brazil*

*** Corresponding author:** Élcio Nogueira, elcionogueira@hotmail.com

ARTICLE INFO

Received: 13 June 2023
Accepted: 14 July 2023
Available online: 21 August 2023

doi: 10.59400/mea.v1i1.66

ABSTRACT: The objective is to analyze the thermal and hydraulic performance in a Micro Channel Straight Printed Circuit Heat Exchanger. Counterflow and parallel flow configurations were analyzed for water cooling using ethylene glycol-based fluid and platelet-shaped non-spherical Boehmite alumina nanoparticles. The work presents results from applying a dimensionless theory that uses the concepts of thermal efficiency of heat exchangers and quantities associated with the second law of thermodynamics. Thermal efficiency, thermal effectiveness, thermal and viscous irreversibilities, thermodynamic Bejan number, and outlet water temperatures are presented in graph form. The data obtained allow us to conclude that the heat exchanger can work in a range of water and refrigerant flow rates below the design parameters. With the inclusion of nanoparticles with a volume fraction equal to 5.0%, the flow rates of the refrigerant fluid can be significantly reduced. The analysis performed shows that the use of nanoparticles improves the operational cost-benefit of the heat exchanger with a significant reduction in the hot water outlet temperature.

KEYWORDS: printed circuit heat exchanger (PCHE); microchannels; thermal efficiency; second law of thermodynamics; dimensionless theoretical analysis; non-spherical nanoparticles

1. Introduction

The work presents results from applying a dimensionless theory that uses the concepts of thermal efficiency of heat exchangers and quantities associated with the second law of thermodynamics. The influence of the refrigerant flow rate and the effect of the inclusion of non-spherical Alumina Boehmite nanoparticles on the thermohydraulic performance of a microchannel printed circuit heat exchanger is analyzed. The volume fraction of nanoparticles in the form of platelets corresponds to 5.0% of the volume of the refrigerant fluid, composed of 50% ethylene glycol. The fluid to be cooled is water at an initial temperature of 98 °C. The analysis method is dimensionless, and it applies the definition of thermal efficiency in heat exchangers and the second law of thermodynamics. Counter-flow and parallel-flow configurations were included in the analyses. A version of this article was presented at the 19th Brazilian Congress of Thermal Sciences and Engineering[1].

Seo et al.[2] performed performance tests on a micro-channel printed circuit heat exchanger (PCHE) in a single-phase regime. In counterflow and parallel flow configurations, Reynolds numbers ranged from 100 to 850. They developed empirical correlations for heat transfer coefficient and pressure drop as functions of the Reynolds number.

Rosa et al.[3] state inconsistencies between results published in recent decades for single-phase microscale heat transfer and that there is still no consensual model. They review experimental and numerical models available in the open literature. They clarify that scale effects, often insignificant in macro channels, can significantly influence the results and must be carefully considered. They call attention to measurement uncertainties due to their reduced characteristic dimensions. They analyze mathematical models for fluid dynamics and believe these should gain more interest because dimensional analyses migrate from microscale to nanoscale. They claim that correlations available for macro channels can be trusted at the microscale if all scale effects are negligible. However, simulations may be the only alternative for evaluating heat transfer rates when scale effects cannot be neglected.

Steinke and Kandlikar[4] clarify that the development of microchannels for heat exchangers and microfluidic devices depends on understanding the processes in these systems. In this sense, they compare experimental data to identify discrepancies between published works. They analyzed more than 150 works addressing flow and heat transfer aspects in microchannels, but approximately 40 were effectively valuable. The survey did not consider flow inlet and outlet regions, errors in channel geometry measurements, and experimental uncertainties. They concluded the need for more studies on heat transfer correlations for micro-channel heat exchangers. Despite this, the available data generally agree with the macro-scale theories. Therefore, they conclude that the classical theory applies to micro-channel and mini-channel flows.

Katz et al.[5] present a multilayer printed circuit heat exchanger prototype with 17 transparent plates photochemically bonded by diffusion. They measure pressure losses and heat transfer in zigzag flow geometry and orientation of glued shims. Results are available in a dimensionless form to facilitate comparisons with thermo-hydraulic correlations. Two fluids with drastically different properties provide a unique method of exploring the effect of the working fluid on PCHE performance. Friction factor and Nusselt number were determined for laminar, transition, and turbulent regimes spanning Reynolds number between 500 and 18,000. The friction factor shows an agreement of 10% and the heat transfer results of 15%, within the range of the tests performed. They end with an analysis of the thermo-hydraulic performance to establish a standard of comparison with other projects.

Baik et al.[6] developed a PCB exchanger design and analysis code to predict thermohydraulic performance. The range of Reynolds numbers considered corresponds to 2000–58,000. A prototype was manufactured to test the accuracy of the developed code. The experimental results demonstrated acceptable thermal performance and small pressure losses. The experimental results showed effectiveness above 90% in a small core of 200 mm. The code reproduced a similar performance. Regarding the pressure drop, they observe differences between experimental data and results obtained through the code, but they justify the difference by not including the losses located in the code.

Chai and Tassou[7] review and establish a comprehensive understanding of printed circuit heat exchangers (PCHEs). The study covered existing heat exchangers on the market and projects under development. They conclude that more work is needed to increase the range of applications for printed circuit heat exchangers. The work to be carried out must aim to optimize and develop new correlations that can reliably predict the performance of heat exchangers.

Zhao et al.[8] study a promising plate-type heat exchanger, the printed circuit (PCHE), of high compactness, suitable for high-pressure conditions. They investigate the thermohydraulic performance numerically of the heat exchanger using the SST k-ω turbulence model. They evaluate heat transfer and pressure loss and loss using Nusselt and Euler numbers. To define better-operating conditions, they propose the Nu/Eu ratio for a comprehensive evaluation of the heat exchanger, considering thermal and hydrodynamic aspects. They conclude that thermal performance is better with a higher mass flow and lower operating pressures.

Bhosale and Acharya[9] state that microchannels can be explored as turbine blades, rocket engines, hybrid vehicles, refrigeration cooling, thermal control in microgravity, and microgravity heat sinks channels may be the solution to 21st-century cooling problems. They establish that the microchannel heat exchanger is more effective than the cross fin and tube heat exchanger. It helps to reduce the amount of refrigerant in residential air conditioning systems. They advise those wishing to design a microchannel heat exchanger that the pressure loss and heat transfer characteristics must be accurately established. They state that the theoretical basis is not mature and that there is no uniform industry standard in manufacturing. They believe, however, that existing problems in manufacturing and applications will be resolved, and the microchannel heat exchanger will be widely used in industry.

Tang et al.[10] numerically analyze the effect of axial heat conduction on thermal performance in a zigzag channel printed circuit heat exchanger (PCHE). The analysis includes Reynolds number, operating pressure, cold side inlet temperatures, and wall thermal conductivity. The results obtained indicate that axial heat conduction can significantly affect the thermal performance of PCHE at low Reynolds numbers but decreases at high Reynolds numbers for different working conditions. Furthermore, reducing the thermal conductivity of the wall can improve the thermal performance of the PCHE due to the influence of axial heat conduction on the partition wall.

Timofeeva et al.[11] experimentally investigate various alumina nanoparticles' thermal conductivity and viscosity in a fluid consisting of an equal amount of water and ethylene glycol. They develop a theoretical model for the analysis of experimental data. They claim that the presence of small fractions of nanoparticles significantly increases the viscosity of the suspension due to structural constraints. However, they demonstrate that the viscosity of alumina can be reduced by adjusting the pH of the nanofluid. They conclude that the use of alumina nanoparticles is of no benefit unless the viscosity of the nanofluid is diminished.

Monfared et al.[12] studied nanoparticle shape's effects on entropy generation in Boehmite alumina nanofluid flow in a double tube heat exchanger. Non-spherical nanoparticles are of the brick, sheet, platelet, and cylindrical type, suspended in a water and ethylene glycol mixture. Water flows from the annular side of the heat exchanger. The influence of the Reynolds number on the thermal and total entropy generation rates through the Bejan number was investigated numerically. The results obtained indicate that non-spherical nanoparticles in the form of platelets produce a lower rate of frictional entropy and that this increases with the increasing concentration of nanoparticles. The opposite occurs for the thermal entropy generation rate. They conclude that non-spherical nanoparticles in platelets have the best performance, and non-spherical nanoparticles have the worst performance.

To determine the thermal performance of different shapes of Boehmite Alumina compared to Al_2O_3 aluminum oxide, Nogueira[13] applied the second law of thermodynamics in a Straight Microchannel Printed Circuit heat exchanger. He concluded that the nanoparticles' shapes create greater thermal irreversibility and affect the interaction between the fluid base and the nanoparticles.

2. Methodology

Experimental data and specifications of the used heat exchanger were obtained from theoretical and experimental work prepared by Seo et al.[1]. The author performed thermal and dynamic performance tests for a PCHE. The tests were carried out for configuration in counterflow, for Reynolds numbers in the range of 100–850, with inlet temperatures equal to 50° and 20°. Developed empirical correlations for the heat transfer coefficient as a function of the Reynolds number for both fluids, Equations (17) and (18).

Table 1 presents the properties of hot and cold fluids and Boehmite Alumina Platelet Nanoparticles.

Table 1. Fluid and nanoparticle properties, hot (Water), cold (Ethylene Glycol 50%), Boehmite Alumina platelets (Timofeeva et al.[11] and Monfared et al.[12]).

	ρ kg/m³	k W/ (m K)	Cp J/(kg K)	μ kg/(m s)	ν m/s²	α m/s²	Pr
Quente	994	0.623	4178	0.72×10^{-3}	7.24×10^{-7}	1.5×10^{-7}	4.83
Frio	1067.5	0.3799	3300	3.39×10^{-3}	2.4045×10^{-5}	1.08×10^{-7}	0.02
B Alumina	3050	30	618.3	-	-	-	-

2.1. Procedure for thermal analysis

$$\phi = 0.05\ fixed \tag{1}$$

$$Th_i = 98.0ºC\ fixed \tag{2}$$

$$Tc_i = 25.0ºC\ fixed \tag{3}$$

$$Re_h = 200\ fixed \tag{4}$$

$$Re_c = Re^{*}Re_h \tag{5}$$

ϕ is the volume fraction of the nanoparticles. Th_i and Tc_i are the inlet temperatures for hot and cold fluids, respectively. is the Reynolds number associated with the hot fluid and Re^* is the ratio of the Reynolds number of the cold fluid to the Reynolds number of the hot fluid.

$$Dh_C = \frac{4Ac_C Lf_C}{As_C} \tag{6}$$

Dh_C is the hydraulic diameter, $Ac_C = 42.2 \times 10^{-6}$ m² $Lf_C = 137 \times 10^{-3}$ m, $Lf_C = 137 \times 10^{-3}\ m$ is the channel length, $Asc = 34.716 \times 10^{-3}\ m^2$ is the heat transfer area for the cold fluid.

$$Dh_h = Dh_C \tag{7}$$

$$Lf_h = \frac{Dh_h As_h}{4Ac_h} \tag{8}$$

Lf_h is the channel length, $As_h = 26.037 \times 10^{-3}$ m² is the heat transfer area for the hot fluid.

The properties of the nanofluid are obtained by:

$$\rho_{nano} = \rho_{Particle}\phi + (1-\phi)\rho_C \tag{9}$$

$$\mu_{nano} = \frac{\mu_C}{(1-\phi)^{2.5}} \tag{10}$$

$$Cp_{nano} = \frac{Cp_{Particle}\rho_{Particle}\phi + (1-\phi)Cp_C\rho_C}{\rho_{nano}} \tag{11}$$

$$k_{nano} = \frac{[k_{Particle} + 2k_C + 2(k_{Particle} - k_C)(1-0.1)^3\phi]}{[k_{Particle} + 2k_C + 2(k_{Particle} - k_C)(1-0.1)^2\phi)}]K_c \tag{12}$$

$$\nu_{nano} = \frac{\mu_{nano}}{\rho_{nano}} \tag{13}$$

$$\alpha_{nano} = \frac{k_{nano}}{\rho_{nano}Cp_{nano}} \tag{14}$$

$$Pr_{nano} = \frac{\mu_{nano}}{\alpha_{nano}} \tag{15}$$

$$\mu_W = \frac{\mu_{nnao} + \mu_h}{2} \tag{16}$$

μ_W is the assumed value for the fluid's viscosity at the channel wall.

$$h_{nano} = 0.1706\ 6^{0.44}\ Re_{nano}{}^{0.324}\ Pr_{nano}{}^{\frac{1}{3}} \left(\frac{\mu_{nano}}{\mu_W}\right)^{0.14} \left(\frac{k_{nano}}{Dh_C}\right) \tag{17}$$

$$h_h = 0.1729\ 5^{0.44}\ Re_h{}^{0.324}\ Pr_h{}^{1/3} \left(\frac{\mu_h}{\mu_W}\right)^{0.14} \left(\frac{k_h}{Dh_h}\right) \tag{18}$$

The heat transfer coefficients of both fluids, cold (h_{nano}) and hot (h_h), were obtained by regression fit[4].

$$A_{Med} = \frac{As_h + As_C}{2} \tag{19}$$

The overall heat transfer coefficient is obtained by:

$$UoA = \frac{1}{\frac{1}{h_h\ As_h} + \frac{1}{h_{nano}\ As_C} + \frac{L}{k_{Metal}\ A_{Med}}} \tag{20}$$

$k_{Metal} = 16.2\ W/(m\ K)$ is the thermal conductivity of the heat transfer plate and $L = 0.4 \times 10^{-3}\ m$ is the thickness between the cold and hot channels.

$$\dot{m}_h = \frac{Re_h\ \mu_h\ Ac_h}{Dh_h} \tag{21}$$

$$\dot{m}_{nano} = \frac{Re_{nano}\ \mu_{nano}\ Ac_C}{Dh_C} \tag{22}$$

$$\dot{m}^* = \frac{\dot{m}_{nano}}{\dot{m}_h} \tag{23}$$

$\dot{m}_h$ and $\dot{m}_{nano}$ are the mass flow rates of the hot and cold fluid, respectively.

$$C_h = \dot{m}_h\ Cp_h \tag{24}$$

$$C_{nano} = \dot{m}_{nano}\ Cp_{nano} \tag{25}$$

C_h and C_{nano} are the heat capacities of the hot and cold fluids, respectively.

$$C^* = \frac{C_{min}}{C_{max}} \tag{26}$$

where C_{min} is the minimum value between C_h and C_{nano}.

$$NTU = \frac{UoA}{C_{min}} \tag{27}$$

NTU is the number of thermal units associated with the heat exchanger.

$$Fa = \frac{NTU(1 - C^*)}{2} counter\ flow \tag{28}$$

$$Fa = \frac{NTU(1 + C^*)}{2} parallel\ flow \tag{29}$$

Fa is the fin analogy for heat exchanger[13,14].

$$\eta_T = \frac{tanh(Fa)}{Fa} \tag{29}$$

η_T is the thermal efficiency.

$$\varepsilon_T = \frac{1}{\frac{1}{\eta_T\ NTU} + \frac{1 + C^*}{2}} \tag{30}$$

ε_T is the thermal effectiveness.

$$\dot{Q}_{Max} = (Th_i - Tc_i)\ C_{min} \tag{31}$$

$\dot{Q}_{Max}$ is the maximum heat transfer rate for the situation under analysis.

$$\dot{Q} = \frac{(Th_i - Tc_i)\ C_{min}}{\frac{1}{\eta_T\ NTU} + \frac{1 + C^*}{2}} \tag{32}$$

$\dot{Q}$ is the actual rate of heat transfer.

The outlet temperatures for both fluids, Th_O and Tc_O, are obtained by:

$$Th_O = Th_i - \frac{\dot{Q}}{\dot{m}\ Cp_h} \tag{33}$$

$$Tc_O = Tc_i - \frac{\dot{Q}}{\dot{m}\ Cp_{nano}} \tag{34}$$

$$\sigma_T = \left(\frac{C_h}{C_{min}}\right) ln \left(\frac{Th_o}{Tc_i}\right) + \left(\frac{C_{nano}}{C_{min}}\right) ln \left(\frac{Tc_o}{Tc_i}\right) \tag{35}$$

σ_T is the thermal irreversibility of the heat exchanger.

2.2. Procedure for hydrodynamic analysis

$$D_P = 0.6 \times 10^{-3}\ m\ fixed \tag{36}$$

D_P is the diameter of the entrance port.

$$Gc = \frac{\dot{m}_c}{Ac_c} \tag{37}$$

$$Gh = \frac{\dot{m}_h}{Ac_h} \tag{38}$$

$$Gp_c = \frac{4\dot{m}_c}{\pi {D_P}^2} \tag{39}$$

$$Gp_h = \frac{4\dot{m}_h}{\pi {D_P}^2} \tag{40}$$

Gc and Gh are the mass fluxes of the cold and hot fluids, respectively. Gp_c and Gp_h are the mass flows through the portals.

$$fc_c = \frac{0.316}{Re_{nano}^{0.25}} \tag{41}$$

$$fc_h = \frac{0.316}{Re_h^{0.25}} \tag{41}$$

$$fc_{Exp} = \frac{1.3383}{Re_{nano}^{0.5003}} \tag{42}$$

$$fh_{Exp} = \frac{1.3383}{Re_h^{0.5003}} \tag{43}$$

fc_c and fc_h are the theoretical friction factors associated with hot and cold fluids; fc_{Exp} and fh_{Exp} are the experimental coefficients of friction[3].

$$\Delta P_c = \frac{4fc_c Lf_c Gc^2}{2Dh_c \rho_{nano}} \tag{44}$$

$$\Delta P_h = \frac{4fc_h Lf_h Gh^2}{2Dh_h \rho_h} \tag{45}$$

$$\Delta P_{Pc} = \frac{1.5{Gp_c}^2}{2\rho_{nano}} \tag{46}$$

$$\Delta P_{Ph} = \frac{1.5{Gp_h}^2}{2\rho_h} \tag{47}$$

ΔP_c and ΔP_h are the pressure drops along the channels; ΔP_{Pc} and ΔP_{Ph} are the pressure drops in the portals.

$$P_{2c} = Patm\ assumed \tag{48}$$

$$P_{2h} = Patm\ assumed \tag{49}$$

$$P_{1c} = \Delta P_c + \Delta P_{Pc} + P_{2c} \tag{50}$$

$$P_{1h} = \Delta P_h + \Delta P_{Ph} + P_{2h} \tag{51}$$

$$\sigma_f = -\left(\frac{C_h}{C_{min}}\right) Rln\left(\frac{P_{2h}}{P_{1h}}\right) - \left(\frac{C_{nano}}{C_{min}}\right) Rln\left(\frac{P_{2c}}{P_{1c}}\right) \tag{52}$$

$$R = \frac{Th_i - Th_o}{Tc_o - Tc_i} \tag{53}$$

then:

$$\dot{S}_{genf} = \sigma_f C_{min} \tag{54}$$

σ_f and $\dot{S}_{genf}$ are the viscous irreversibility and the entropy generation rate[12].
finally:

$$Be = \frac{\dot{S}_{genT}}{\dot{S}_{genT+\dot{S}_{genf}}} \tag{55}$$

Be is the thermodynamic Bejan number[14–16].

3. Results and discussion

Figure 1 shows the relationships between the mass flows of fluids within the working range between them. The hot fluid flow corresponds to a fixed Reynolds number equal to 200, and the coolant flow corresponds to a variation for the Reynolds number between 50 and 1000. When you have ethylene glycol flowing, with zero nanofluid mass fraction, the change in mass of the cold fluid is not significantly more significant when compared to the flow rate of the hot fluid. For Re_c= 1000, that is, $Re^* = 5$, the ratio between the masses of the cold fluid by the hot fluid is approximately equal to 20. However, when fractions of nanoparticles are included, the mass flow increases significantly with the increase in the number of nanoparticles. Reynolds is associated with soda. When $Re_{nano} = 200$, i.e., $Re^* = 1$, the nanofluid mass flow rate approximately corresponds to the ethylene glycol mass flow rate for $Re^* = 5$. This increase in mass flow significantly affects all parameters that will be analyzed in the context of this work.

Figure 2 shows the variation in the number of thermal units associated with the heat exchanger for the two situations under analysis: a flow of 50% pure ethylene glycol and a flow of 50% ethylene glycol plus 0.05 volume fraction Alumina Boehmite nanoparticles. For low flow rates of the refrigerant fluid, a significant increase in the number of thermal units of the nanofluid can be observed compared to the number of thermal units of the 50% pure ethylene glycol. However, the initial difference becomes less pronounced for high flow rates of the refrigerant fluid, tending to a limit value when $Re^* = 5$. The same occurs with the relationship between the thermal capacities of both fluids, **Figure 3**, with a significant difference for low flows and a slight difference for higher flows. These two parameters, NTU and C*, are primarily responsible for determining the thermal efficiency of the heat exchanger, as defined in this work.

The thermal efficiency of the heat exchanger is shown in **Figure 4**. In this context, the thermal efficiency represents the potential for heat exchange between the fluids. When the efficiency approaches 1, there is the maximum potential for heat exchange. After that, the heat exchange between the fluids tends to a minimum value, and this potential tends to zero. For example, there is a high heat exchange potential for 50% ethylene glycol at low refrigerant flow rates and an approximate 10% drop for nanofluid at a volume fraction equal to 0.05. It can be anticipated, in this case, that the potential presented by ethylene glycol was better used when introducing nanoparticles.

When comparing the relationship between the heat transfer rates, represented by the thermal effectiveness, **Figure 5**, shows that the heat transfer rate associated with the nanofluid is higher than that of ethylene glycol by 50%. In this case, it is observed again that the greatest difference occurs for lower refrigerant flows. For the lowest flow rate of the refrigerant, there is an approximate increase of 27% in the heat transfer rate when adding the nanofluid, and this value drops to approximately 6% for high flow rates. Regarding the two heat exchanger configurations under analysis, counterflow and parallel flow, it is evident that there is greater heat exchange for the counterflow type exchanger.

The thermal effectiveness of the heat exchanger is very similar to what is observed for the thermal irreversibility, **Figure 6**, making it evident that these are equivalent quantities when comparing the thermal performance of the heat exchanger.

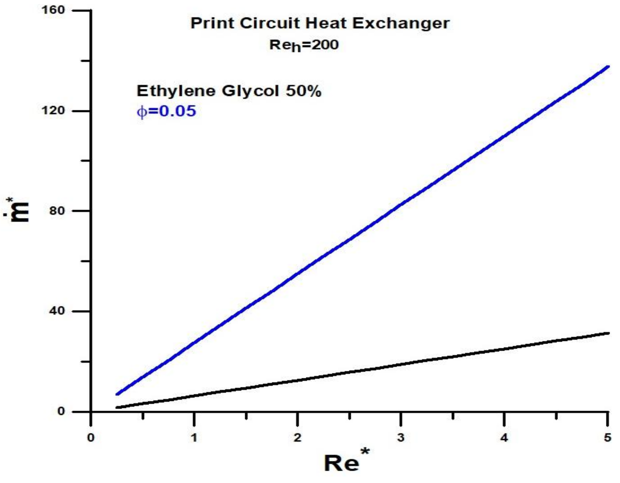

Figure 1. Ratio of mass flow rates of the cold fluid to the hot fluid.

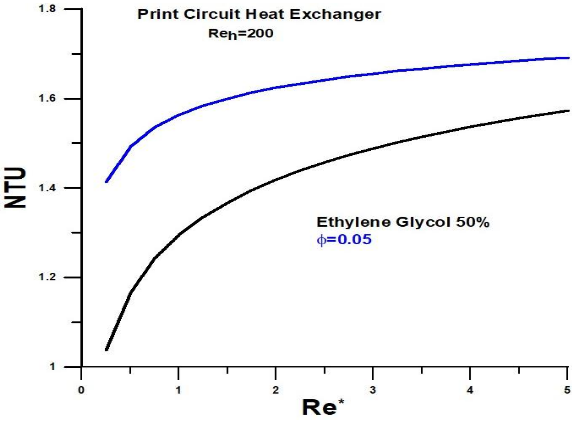

Figure 2. Number of thermal units (NTU) versus the ratio of Reynolds numbers.

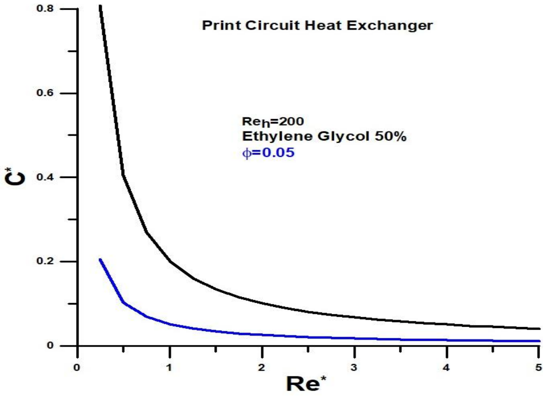

Figure 3. Ratio of heat capacities versus the ratio of Reynolds numbers.

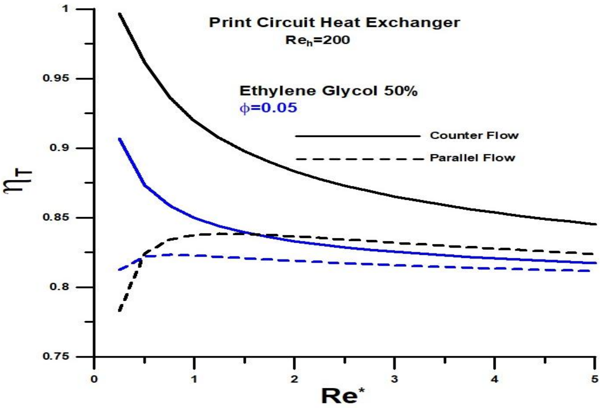

Figure 4. Thermal efficiency of the heat exchanger versus the ratio of Reynolds numbers.

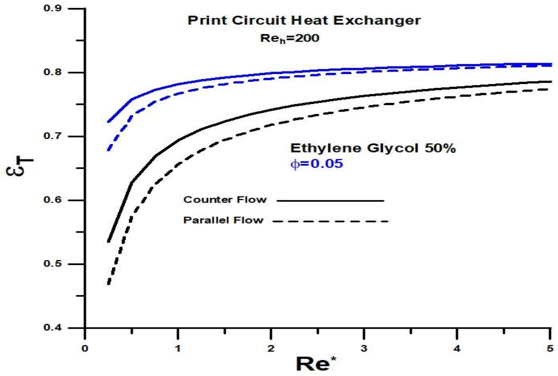

Figure 5. Thermal effectiveness of the heat exchanger versus the ratio of Reynolds numbers.

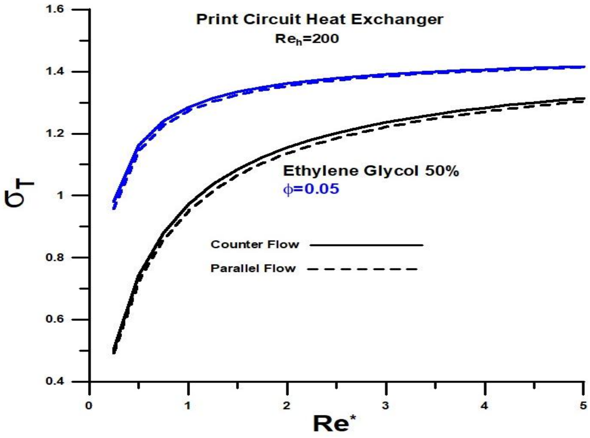

Figure 6. Thermal irreversibility versus the ratio of Reynolds numbers.

Regarding the last two analyzed quantities, thermal effectiveness and thermal irreversibility, it should be noted that none of them makes it possible to determine the absolute value of the heat transfer rate that occurs during the exchange process between fluids. Instead, they only indicate how close or far away the heat transfer rate is concerning the maximum possible heat transfer rate.

For a systemic analysis of the heat exchanger, considering quantities related to heat exchange and viscous dissipation, it becomes relevant to determine quantities associated with hydrodynamic aspects. The most pertinent parameter related to the flow is the friction factor. Just as the Nusselt number modulates the heat transfer, it effectively determines the pressure drop in the flow. **Figure 7** presents theoretical and empirical results for the friction factor for comparison purposes. The empirical correlation was obtained through experimental results determined by Rosa et al.[3] and the theoretical expression presented by Zhao et al.[8]. In this work, we chose to use empirical correlation to determine the magnitudes dependent on the friction factor since the results obtained experimentally are within the Reynolds numbers of the designed device.

The viscous irreversibility is represented in **Figure 8**, as a function of the refrigerant fluid flow, with and without the inclusion of nanoparticles fraction. As already observed, when fractions of nanoparticles are included in the flow, the mass flow increases, significantly affecting the viscous irreversibility. In this particular case, the addition is exceptionally high for higher flows, preliminarily indicating the impossibility of working at the upper limit of flows for the refrigerant. At lower flow rates, however, the viscous dissipation added by the nanoparticles is of the same order of magnitude as the viscous dissipation caused by 50% pure ethylene glycol. Therefore, it is expected that nanoparticles can be used for lower refrigerant flow rates.

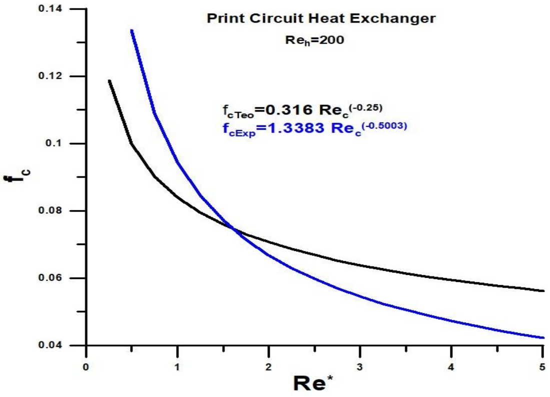

Figure 7. Theoretical and empirical friction factor versus the ratio of Reynolds numbers.

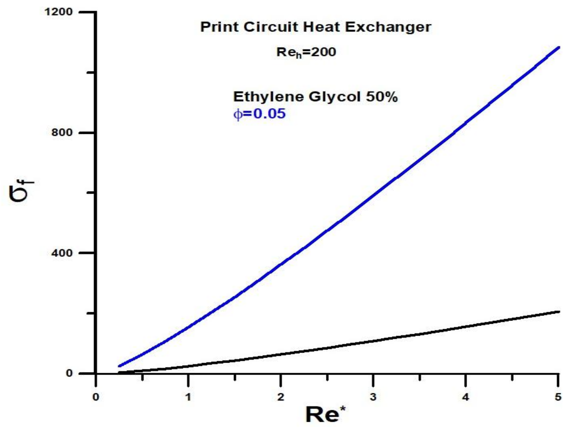

Figure 8. Viscous irreversibility versus the ratio of Reynolds numbers.

The ratio between thermal irreversibility and total irreversibility is represented in **Figure 9** through the Bejan thermodynamic number for a counterflow heat exchanger. At lower flow rates for the refrigerant, the thermal irreversibility is of the order of magnitude of the total irreversibility, which indicates a non-prevalence of viscous irreversibility. However, with the increase in the flow rate for the refrigerant, the Bejan number presents shallow values. It tends to a minimum value at medium and high flows, with significant relevance for the nanofluid concerning 50% pure ethylene glycol.

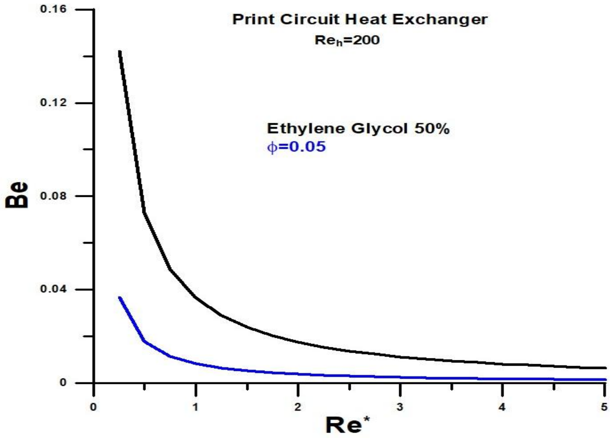

Figure 9. Bejan thermodynamic number versus the ratio of Reynolds numbers.

The data show that the heat exchanger should not work in the upper flow rate range for the refrigerant for a favorable cost-benefit ratio. However, the reasonable flow limit for 50% pure ethylene glycol is higher than the practical flow limit for the nanofluid. Preliminarily, based on the Bejan number, the threshold value for the Reynolds number in ethylene glycol is approximately equal to Re* = 3, and for the nanofluid, Re* = 1 is a probable indicator.

Figure 10 shows the relationship between the hot fluid outlet temperatures between nanofluid and 50% ethylene glycol. For lower flow rates, the outlet temperature for nanofluid is between 0.76 to 0.86 of the outlet temperature for 50% ethylene glycol for both counterflow and parallel flow configurations. For high flow rates, the ratio tends to be one, and, in this situation, there is no advantage in using nanoparticles. However, **Figure 10** does not indicate the absolute values of the outlet temperatures for the hot fluid.

The absolute values for the hot fluid outlet temperatures, when Reh = 200, are represented in **Figure 11**. The results obtained corroborate the previous conclusions and allow a decision of the flow ranges where a cost-benefit ratio is advantageous. For low flows, the temperature drop is significant. Still, from a given value, the decrease in temperature is negligible and does not justify the effort and energy consumption in the form of viscous dissipation. Therefore, we indicate again that the justifiable threshold flow for nanofluid corresponds to approximately Re* = 1, and for 50% pure ethylene glycol, Re* = 3 is a reasonable threshold value.

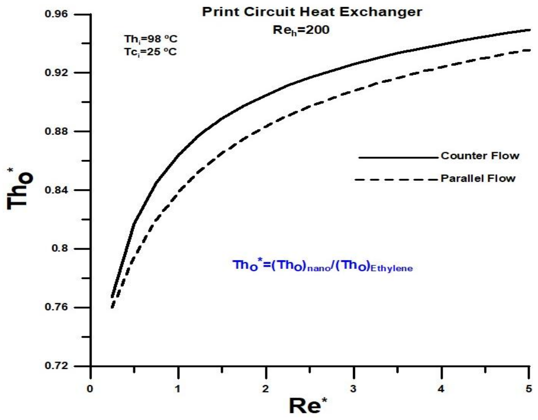

Figure 10. Hot fluid outlet temperatures ratio versus the ratio of Reynolds numbers.

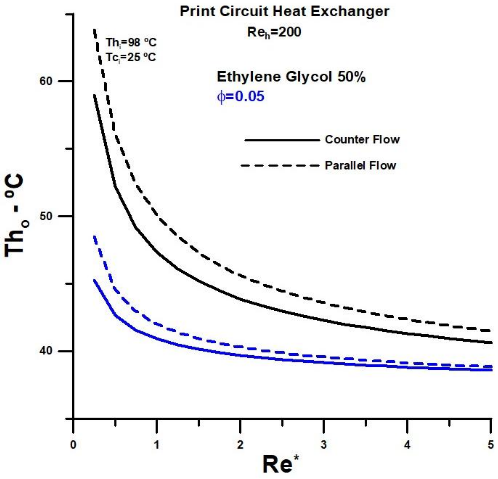

Figure 11. Hot fluid outlet temperatures for Reh = 200 versus the ratio of Reynolds numbers.

4. Conclusion

The work presents results from applying a dimensionless theory that uses the concepts of thermal efficiency in heat exchangers and quantities associated with the second law of thermodynamics. Thermohydraulic performance analysis was performed on a straight microchannel printed circuit heat exchanger. Counter-flow and parallel-flow configurations were analyzed for water cooling using 50% ethylene glycol base fluid and platelet-shaped non-spherical Boehmite Alumina nanoparticles.

The heat exchanger was designed to work in a range of Reynolds numbers between 200 and 850. However, high values for the Reynolds number increase viscous dissipation and lead to a degradation of the thermal potential, which is amplified with the inclusion of nanoparticles.

It is concluded that the heat exchanger under analysis must operate at low flow rates for the refrigerant fluid, where the potential for heat exchange remains high and reasonably above a minimum threshold. For lower refrigerant flows, viscous irreversibilities are relatively low concerning thermal irreversibilities, allowing a viable cost-benefit for the heat exchanger, even with nanoparticles at a volume fraction equal to 5.0%.

It is proven that what should act to improve the thermal performance of the heat exchanger works in the sense of increasing viscous dissipations.

It is shown that the dimensionless analysis of heat exchangers, in the form presented, is a valuable tool for thermo-hydraulic optimization of heat exchangers.

5. List of symbols

Asc—the heat transfer area for the cold fluid, $[m^2]$

As_h—the eat transfer area for the hot fluid, $[m^2]$

A_{cc}—channel cross-sectional free flow area, $[m^2]$

Cp_c—specific heat of the cold fluid, $[\frac{J}{kg\ K}]$

$Cp_{\hbar}$—specific heat of the hot fluid, $[\frac{J}{kg\ K}]$

Cp_{nano}—thermal capacity of the nanofluid, $[\frac{W}{K}]$

C_{min}—minimum thermal capacity between the hot and cold fluids, $[\frac{W}{K}]$

$$C^* = \frac{C_{min}}{C_{max}}$$

D_h—hydraulic diameter, $[m]$

D_P—port diameter, $[m]$

Fa—fin analogy for heat exchanger

Gc and Gh are the mass fluxes of the cold and hot fluids, respectively. Gp_c and Gp_h are the mass flows through the portals.

Gc—mass velocity of the cold fluid, $[\frac{kg}{m^2 s}]$

Gh—mass velocity of the hot fluid, $[\frac{kg}{m^2 s}]$

Gp_c—cold mass flows through the portal, $[\frac{kg}{m^2 s}]$

Gp_h—hot mass flows through the portal, $[\frac{kg}{m^2 s}]$

h_h—coefficient of heat convection for hot fluid, $[\frac{W}{m^2 K}]$

h_c—coefficient of heat convection for cold fluid, $[\frac{W}{m^2 K}]$

h_{nano}—coefficient of heat convection for nanofluid, $[\frac{W}{m^2 K}]$

$k_{\hbar}$—thermal conductivity of the hot fluid, $[\frac{W}{m\ K}]$

k_c—thermal conductivity of the cold fluid, $[\frac{W}{m\ K}]$

k_{nano}—thermal conductivity of the nanofluid, $[\frac{W}{m\ K}]$

$\dot{m}_c$—total mass flow rate of the cold fluid, $[\frac{kg}{s}]$

$\dot{m}_h$—total mass flow rate of the hot fluid, $[\frac{kg}{s}]$

Pr_{nano}—is the Prandtl number of the nanofluid

$\dot{Q}$—actual heat transfer rate, $[W]$

$\dot{Q}_{max}$—maximum heat transfer rate, $[W]$

Re_c—Reynolds number for cold fluid

Re_h—Reynolds number for hot fluid

Tc_i—inlet temperatures of water, $[^{\circ}C]$

Th_i—inlet temperatures of vegetable oil, $[^{\circ}C]$

Tc_o—outlet temperatures for cold fluid, $[^{\circ}C]$

Th_o—outlet temperatures for hot fluid, $[^{\circ}C]$

Uo—global heat transfer coefficient, $[\frac{W}{m^2\ K}]$

UoA—overall heat transfer coefficient

Greek symbols

α_{nano}—thermal diffusivity of the nanofluid, $[\frac{m^2}{s}]$

ρ_{nano}—density of the nanofluid, $[\frac{kg}{m^3}]$

μ_{nano}—dynamic viscosity of nanofluid, $[\frac{kg}{m^3}]$

υ_{nano}—is the kinematic viscosity of the cold fluid, $[\frac{kg}{m^3}]$

ε_T—thermal effectiveness

η_T—thermal efficiency

Acronyms

NTU—number of thermal units

Author contributions

Conceptualization, EN; methodology, EN; software, EN; validation, EN; formal analysis, EN; investigation, EN; resources, EN; data curation, EN; writing—original draft preparation, EN; writing—review & editing, EN and HAM; visualization, HAM; supervision, HAM.

Conflict of interest

The authors declare no conflict of interest.

Reference

1. Nogueira É, Machado HA. Thermal efficiency and second law of thermodynamics applied in a straight microchannel printed circuit heat exchanger. In: Proceedings of the 19th Brazilian Congress of Thermal Sciences and Engineering (ENCIT 2022); 6–10 November 2022; Bento Gonçalves-RS, Brazil.
2. Seo JW, Kim YH, Kim D, et al. Heat transfer and pressure drop characteristics in straight microchannel of printed circuit heat exchangers. *Entropy* 2015; 17: 3438–3457. doi: 10.3390/e17053438
3. Rosa P, Karayiannis TG, Collins MW. Single-phase heat transfer in microchannels: The importance of scaling effects. *Applied Thermal Engineering* 2009; 29(17–18): 3447–3468. doi: 10.1016/j.applthermaleng.2009.05.015
4. Steinke ME, Kandlikar SG. Single-phase liquid heat transfer in microchannels. In: Proceedings of ICMM2005 3rd International Conference on Microchannels and Mini channel; 13–15 June 2005; Toronto, Canada. pp. 667–678.
5. Katz A, Aakre SR, Anderson MH, Ranjan D. Experimental investigation of pressure drop and heat transfer in high-temperature supercritical CO_2 and helium in a printed-circuit heat exchanger. *International Journal of Heat and Mass Transfer* 2021; 171: 121089. doi: 10.1016/j.ijheatmasstransfer.2021.121089
6. Baik SJ, Kim SG, Son SM, Lee JI. Printed circuit heat exchanger design, analysis and experiment. In: Proceedings of the 16th International Topical Meeting on Nuclear Reactor Thermal Hydraulics (NURETH-16); 30 August–4 September 2015; Chicago, United States.
7. Chai L, Tassou SA. A review of printed circuit heat exchangers for helium and supercritical CO_2 Brayton cycles. *Thermal Science and Engineering Progress* 2020; 18: 100543. doi: 10.1016/j.tsep.2020.100543
8. Zhao Z, Zhou Y, Ma X, et al. Numerical study on thermal hydraulic performance of supercritical LNG in zigzag-type channel PCHEs. *Energies* 2019; 12(3): 548. doi: 10.3390/en12030548
9. Bhosale SS, Acharya AR. Review on applications of micro-channel heat exchanger. *International Research Journal of Engineering and Technology* 2020; 7(3).
10. Tang LH, Yang BH, Pan J, Sundén B. Thermal performance analysis in a zigzag channel printed circuit heat exchanger under different conditions. *Heat Transfer Engineering* 2022; 43(7): 567–583. doi: 10.1080/01457632.2021.1896832
11. Timofeeva EV, Routbort JL, Singh D. Particle shape effects on thermophysical properties of alumina nanofluids. *Journal of Applied Physics* 2009; 106(1): 014304. doi: 10.1063/1.3155999
12. Monfared M, Shahsavar A, Bahrebar MR. Second law analysis of turbulent convection flow of Boehmite alumina nanofluid inside a double-pipe heat exchanger considering various shapes for nanoparticle. *Journal of Thermal Analysis and Calorimetry* 2019; 135(2): 1521–1532. doi: 10.1007/s10973-018-7708-7
13. Nogueira É. Influence of nanoparticles shapes of Boehmite alumina on the thermal performance of a straight microchannel printed circuit heat exchanger. *Journal of Metallic Material Research* 2022; 5(1): 8–24. doi: 10.30564/jmmr.v5i1.4364
14. Bejan A. The thermodynamic design of heat and mass transfer processes and devices. *International Journal of Heat and Fluid Flow* 1987; 8(4): 258–276. doi: 10.1016/0142-727X(87)90062-2
15. Fakheri A. Heat exchanger efficiency. *Journal of Heat Transfer* 2007; 129(9): 1268–1276. doi: 10.1115/1.2739620
16. Nogueira E. Thermal performance in heat exchangers by the irreversibility, effectiveness, and efficiency concepts using nanofluids. *Journal of Engineering Sciences* 2020; 7(2): F1–F7. doi: 10.21272/jes.2020.7(2).f1

Mechanical Engineering Advances 2023; 1(1): 67.
Original Research Article

Analysis of spiral plate heat exchanger used to cool vegetable oil with nanofluid consisting of water and non-spherical boehmite alumina nanoparticles

Élcio Nogueira

Universidade do Estado do Rio de Janeiro—UERJ/FAT/DME, Resende, RJ 27537-000, Brazil; elcionogueira@hotmail.com

ARTICLE INFO

Received: 13 June 2023
Accepted: 19 July 2023
Available online: 6 September 2023

doi: 10.59400/mea.v1i1.67

ABSTRACT: The objective is to use dimensionless analysis through the thermal efficiency method to determine the thermohydraulic performance of a spiral plate heat exchanger (SPHE) used to cool sunflower oil. The coolant consists of water as a base fluid and non-spherical Boehmite Alumina nanoparticles with a defined volume fraction. The concept of thermal efficiency for heat exchangers is used to determine the main quantities used in the analysis. Graphical results are presented for the number of thermal units (NTU), thermal efficiency, thermal effectiveness, hot fluid outlet temperature, thermal and viscous irreversibilities, and Bejan number. The analyzed heat exchanger provides excellent thermal performance for refrigerants consisting of water and non-spherical nanoparticles in platelets or cylindrical, with a volume fraction equal to 12%. Viscous dissipation significantly increases concerning the dissipation associated with pure water, but the cost-benefit is within reason for the proposed objective, within the flow rate under analysis.

KEYWORDS: Spiral Plate Heat Exchanger (SPHE); thermal efficiency method; vegetable oil; nanofluid; non-spherical shaped nanoparticles

1. Introduction

The second law of thermodynamics is applied in spiral plate heat exchangers (SPHE), emphasizing the thermal efficiency of heat exchangers. It is an analytical solution for cooling vegetable oil using non-spherical alumina nanoparticles in the shape of platelets and cylindrical. The results for heat transfer coefficients, number of thermal units (NUT), thermal efficiency, thermal effectiveness, thermal and viscous irreversibilities, hot fluid outlet temperature, and Bejan number are obtained and presented graphically through thermo-hydrodynamic performance analysis.

Shirazi et al.[1] present an exegetical analysis of spiral plate heat exchangers (SPHEs) using an algorithm that makes it possible to obtain a more compact and efficient SPHE Mathematical Modeling numbers based on dimensionless energy, in addition to thermal efficiency and temperature difference number and modified. These dimensionless numbers allow the evaluation of exergy in channels. Furthermore, the temperature distribution was validated with a computer simulation of fluid dynamics. The results show the most significant increase in the relative heat transfer rate by volume of SPHE, up to 54%, compared to other projects.

Khorshidi and Heidari[2] analyze the performance of a spiral plate heat exchanger. Using Fluent software, they design and build prototypes of galvanized iron sheets for analysis and comparison with the theoretical model. They claim that the spiral heat exchanger is an excellent alternative to other heat exchangers, especially for highly viscous fluids. In addition, the low fouling rate reduces the need for frequent cleaning.

Kolasiński and Rogala[3] state that spiral plate heat exchangers are often used in domestic heating because of less material used and lower installation expense. What makes the spiral plate heat exchanger competitive is the relatively high heat transfer rate achieved. The complex mathematical analysis results show that the SPHE is effectively an interesting alternative to other types of heat exchangers due to the reduction in installation size and expenses.

Kumar et al.[4] state that researchers are becoming more aware of using spiral heat exchangers for heat transfer. They describe the heat exchanger as formed by a sheet arrangement with two channels wound around each other, and the distance between the sheets is kept constant to keep the cross-sectional area along the flow path. They analyze the performance of SPHE in a counterflow type configuration. The results obtained make it possible to determine how to optimize the flow of fluids to increase the efficiency of the heat exchanger.

Núñez et al.[5] present an alternative design approach for dimensioning single-phase counter-current spiral plate heat exchangers. The method used results in a design methodology that maximizes the pressure drop and results in the design of the most diminutive dimensions. In the counter-current arrangement, both fluids have the same flow length. The degree of freedom used in the design is the spacing of the plates which can be changed so that both flows maximize their allowable pressure drop. The results obtained by the adopted approach are compared with the results of projects presented in the open literature and show that the method is reliable and easy to implement.

Monfared et al.[6] state that one way to increase the thermal heat performance in a spiral plate heat exchanger is to employ nanofluid. In this sense, they present a numerical analysis of the effects of nanofluids and validate them through experimental results in a counterflow heat exchanger. The nanoparticles used were titanium dioxide (TiO_2) and silicon dioxide (SiO_2) with water as the base fluid. The results obtained show a 20% to 25% increase in heat transfer at a volume concentration equal to 3%.

2. Methodology

The SPHE is used to cool sunflower vegetable oil with an inlet temperature equal to 110 °C. The nanofluid, made up of water and nanoparticles in the form of platelets or cylinders, is the coolant. The inlet temperature of the refrigerant fluid is equal to 30 °C. The heat exchanger has a height of 1.2 m, and the spiral has a length of 2485 m, with turns equal to 10. The inner diameter is equal to 0.1 m, and the outer diameter is equal to 0.225 m. The total heat exchange area is 6 m^2. The channel width is equal to 0.005 m. The average temperature of the hot fluid is 55 °C.

Figure 1 represents a spiral plate heat exchanger and its basic dimensions. **Figure 2** schematically illustrates a counter-current heat exchanger of length L.

Table 1 presents the values of the basic properties of hot and cold fluids and Boehmite Alumina nanoparticles. **Table 2** shows coefficients that characterize the non-spherical nanoparticles in the shape of platelets and cylindrical.

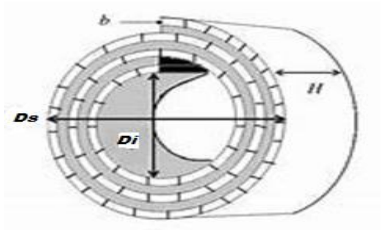

Figure 1. Spiral Plate Heat Exchanger (SPHE)[4].

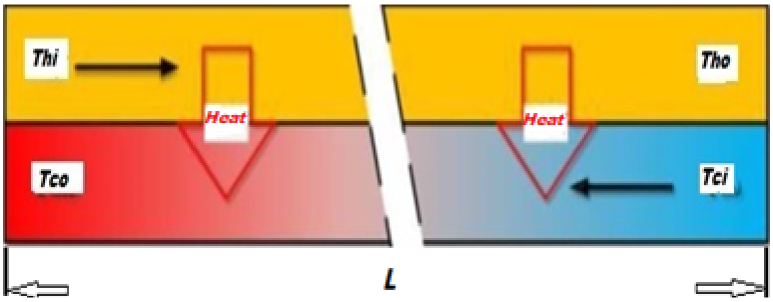

Figure 2. Schematic representation of Counter-Flow Heat Exchanger[5].

Table 1. Properties of cold fluid (water) and Boehmite Alumina nanoparticles[6].

	ρ kg/m³	**k W/(m.K)**	**Cp J/(Kg.K)**	**μ kg/(m.s)**
Frio	994.5	0.605	4182.5	0.875×10^{-3}
Alumina	3050	30	618.3	-

Table 2. Coefficients that characterize the non-spherical shape of nanoparticles in dynamic viscosity and thermal conductivity[6].

Type	C_k	A_1	A_2
Platelet	2.61	37.1	612.6
Cylindrical	3.95	13.5	904.4

$$L = 2.485\ m \tag{1}$$

$$b_c = 0.005\ m \tag{2}$$

$$b_h = 0.005\ m \tag{3}$$

$$b = \frac{b_c + b_n}{2} \tag{4}$$

$$H = 1.2\ m \tag{5}$$

The properties of the cold fluid are obtained from the quantities represented in **Table 1**.

$$v_c = \frac{\mu_c}{\rho_c} \tag{6}$$

$$a_c = \frac{k_c}{\rho_c C p_c} \tag{7}$$

$$Pr_c = \frac{v_c}{\alpha_c} \tag{8}$$

$$Th_{Med} = 55.0 \tag{9}$$

The properties of the hot fluid are obtained through polynomial interpolation of the data given in the study of Rojas et al.[7]:

$$\rho_h = 920.8893939 - 0.09046037296 Th_{Med} - 0.0003712121212 Th_{Med}^2 + 2.33100233110^{-6} Th_{Med}^3 \tag{10}$$

$$\mu_h = 0.1446810076 - 0.00571479528 Th_{Med} + 9.8117277110^{-5} Th_{Med}^2 - 7.88058566410^{-7} Th_{Med}^3 + 2.40260780910^{-9} Th_{Med}^4 \tag{11}$$

$$k_h = 0.1595212121 + 7.62626262610^{-5} Th_{Med} - 5.30303030310^{-7} Th_{Med}^2 + 2.52525252510^{-9} Th_{Med}^3 \tag{12}$$

$$Cp_h = 2046.651515 + 3.511130536 Th_{Med} + 0.005606060606 Th_{Med}^2 + 9.90675990710^{-6} Th_{Med}^3 \tag{13}$$

$$\nu_h = \frac{\mu_h}{\rho_h} \tag{14}$$

$$\alpha_h = \frac{k_h}{\rho_h Cp_h} \tag{15}$$

$$Pr_h = \frac{\nu_h}{\alpha_c} \tag{16}$$

The properties of nanofluids are given by Nogueira[8] and Hemanth et al.[9]:

$$\rho_{nano} = \rho_{Particle}\,\phi + (1-\phi)\,\rho_C \tag{17}$$

$$\mu_{nano} = \frac{\mu_C}{(1-\phi)^{2.5}} \tag{18}$$

$$\mu_{nano} = \mu_C\,(1 + A_1\,\phi + A_2\phi^2)\; forma\ não\ esférica \tag{19}$$

$$Cp_{nano} = \frac{Cp_{Particle}\,\rho_{Particle}\,\phi + (1-\phi)\,Cp_C\,\rho_C}{\rho_{nano}} \tag{20}$$

$$k_{nano} = \left[\frac{[k_{Particle} + 2\,k_C + 2\,(k_{Particle} - k_C)\,(1-0.1)^3\,\phi]}{[k_{Particle} + 2\,k_C + 2\,(k_{Particle} - k_C)\,(1-0.1)^2\,\phi)]}\right] K_c \tag{21}$$

$$k_{nano} = k_C\,(1 + C_k\,\phi)\; forma\ não\ esférica \tag{22}$$

$$\nu_{nano} = \frac{\mu_{nano}}{\rho_{nano}} \tag{23}$$

$$\alpha_{nano} = \frac{k_{nano}}{\rho_{nano}\,Cp_{nano}} \tag{24}$$

$$Pr_{nano} = \frac{\mu_{nano}}{\alpha_{nano}} \tag{25}$$

ϕ is the volume fraction of the nanoparticles.

$$\gamma_{nano} = \rho_{nano} G \tag{26}$$

$$\gamma_h = \rho_h G \tag{27}$$

$$S_{nano} = \frac{\rho_{nano}}{\rho_c} \tag{28}$$

$$S_h = \frac{\rho_h}{\rho_c} \tag{29}$$

$$k_p = 44.5\ W/(mK) \tag{30}$$

$$t_p = 0.001\ m \tag{31}$$

$$D_i = 0.1\ m \tag{32}$$

k_p is the thermal conductivity of the surface that separates the fluids. t_p is the thickness of the surface. D_i is the inner diameter of the spiral[1].

$$N = \frac{-D_i + (b_h - b_c)/2 + \sqrt{(D_i + (b_h - b_c))^2 + (4L/\pi)(b_h + b_c + 2t_p)}}{b_h + b_c + 2t_p} \tag{33}$$

N is the number of turns of the spiral.

$$A_{troca} = 2LH\ m^2 \tag{34}$$

$$A_{cc} = b_c H\ m^2 \tag{35}$$

$$A_{hc} = b_h H\ m^2 \tag{36}$$

A_{troca} is the heat transfer area of the heat exchanger. A_{cc} and A_{hc} are the cross-sectional areas for the cold and hot fluids, respectively.

$$D_S = D_i + (b_h + t_p) + N(b_h + b_c + 2t_p) \tag{37}$$

$$D_h = \frac{4Hb}{2(H + b)} \tag{38}$$

D_S is the outer diameter of the spiral. D_h is the hydraulic diameter of the heat exchanger.

$$\varepsilon = \frac{D_h}{D_s} \tag{39}$$

ε is a dimensionless parameter characteristic of the heat exchanger.

$$Re_h = 30000\ by\ definition \tag{40}$$

Re_h is the maximum allowable Reynolds number for hot and cold fluids.

$$Re_{crit} = 20000\varepsilon^{0.32} \tag{41}$$

Re_{crit} is the Reynolds number of transitions from laminar to the turbulent regime.

$$Re^* = \frac{Re_{nano}}{Re_h} \tag{42}$$

Re_{nano} is the Reynolds number associated with the nanofluid by Shirazi et al.[1] and Núñez et al.[5].

$$h_h = \left[\frac{0.04\, Re_h^{0.74}\, Pr_h^{0.4}\, k_h}{D_h}\right](1 + 1.77\varepsilon)\ 400 \le Re_h \le 30000 \tag{43}$$

$$h_{nano} = \left[\frac{0.04\, Re_{nano}^{0.74}\, Pr_{nano}^{0.4}\, k_{nano}}{D_h}\right](1 + 1.77\varepsilon)\ 400 \le Re_{nano} \le 30000 \tag{44}$$

$$h^* = \frac{h_{nano}}{h_h} \tag{45}$$

h_h and h_{nano} are the heat transfer coefficients of the hot and cold fluids, respectively. $(1 + 1.77\varepsilon)$ is the factor that considers the curvature of the spiral.

$$\dot{m}_h = \frac{\pi D_h \mu_h Re_h}{4} \tag{46}$$

$$\dot{m}_{nano} = \frac{\pi D_h \mu_{nano} Re_{nano}}{4} \tag{47}$$

$$\dot{m}^* = \frac{\dot{m}_{nano}}{\dot{m}_h} \tag{48}$$

$\dot{m}_h$ and $\dot{m}_{nano}$ are the mass flow rates of the hot and cold fluids, respectively.

$$C_h = Cp_h \dot{m}_h \tag{49}$$

$$C_{nano} = Cp_{nano} \dot{m}_{nano} \tag{50}$$

C_h and C_{nano} are the heat capacities of the hot and cold fluids, respectively.

$$C^* = \frac{C_{min}}{C_{max}} \tag{51}$$

C_{min} is the smallest of the fluid heat capacities.

$$Uo = \frac{1}{\frac{1}{h_h} + \frac{t_p}{k_p} + \frac{1}{h_{nano}}} \tag{52}$$

Uo is the overall heat transfer coefficient.

$$NTU = \frac{UoA_{troca}}{C_{min}} \tag{53}$$

NTU is the number of thermal units associated with the heat exchanger.

$$Fa = \frac{NTU(1 - C^*)}{2} \tag{54}$$

Fa is the dimensionless number called the fin analogy.

$$\eta_T = \frac{Tanh(Fa)}{Fa} \tag{55}$$

$$\varepsilon_T = \frac{1}{\frac{1}{\eta_T NTU} + \frac{(1 + c\,*)}{2}} \tag{56}$$

η_T and ε_T are thermal efficiency and thermal effectiveness, respectively by Bejan[10] and Fakheri[11].

$$\dot{Q} = \varepsilon_T C_{min}(Th_i - Tc_i) \tag{57}$$

$$\dot{Q}_{max} = C_{min}(Th_i - Tc_i) \tag{58}$$

$\dot{Q}$ is the heat transfer rate. Th_i and Tc_i are the inlet temperatures of the hot and cold fluids, respectively.

$$Tc_o = Tc_i + \frac{\dot{Q}}{C_{nano}} \tag{59}$$

$$Th_o = Th_i - \frac{\dot{Q}}{C_h} \tag{60}$$

$$T^* = \frac{Th_o - Tc_i}{Th_i - Tc_i} \tag{61}$$

$$\sigma_T = \frac{c_h}{c_{min}} ln\left(\frac{Th_o}{Th_i}\right) + \frac{C_{nano}}{C_{min}} ln\left(\frac{Tc_o}{Tc_i}\right) \tag{62}$$

$$\Delta P_c = \left(0.001\left(\frac{L}{S_{nano}}\right)\left(\frac{\dot{m}_{nano}}{D_s H}\right)\left[\frac{1.035\mu_{nano}^{1/2}}{D_s + 0.125}\left(\frac{H}{\dot{m}_{nano}}\right)^{1/2} + 1.5 + \frac{16}{L}\right]\right)10^4 \quad Re_{nano} < Re_{Crit} \tag{63}$$

$$\Delta P_{nano} = \left(0.001\left(\frac{L}{S_{nano}}\right)\left(\frac{\dot{m}_{nano}}{D_s H}\right)^2\left[\frac{1.035\mu_{nano}^{1/3}}{D_s + 0.125}\left(\frac{H}{\dot{m}_{nano}}\right)^{1/3} + 1.5 + \frac{16}{L}\right]\right)10^4 \quad Re_{nano} > Re_{Crit} \tag{64}$$

$$\Delta P_h = \left(0.001 (\frac{L}{S_h})(\frac{\dot{m}_h}{D_s H})^2 \left[\frac{1.035 \mu_h^{1/3}}{D_s + 0.125} (\frac{H}{\dot{m}_h})^{1/3} + 1.5 + \frac{16}{L} \right] \right) 10^4 \tag{65}$$

$$P_{nano2} = P_{atm} \tag{66}$$

ΔP_{nano} and ΔP_h are the pressure drops in the cold and hot fluids in the Pascal, respectively Shirazi et al.[1] and Núñez et al.[5].

$$P_{h2} = P_{atm} \tag{67}$$

$$P_{nano1} = \Delta P_{nano} + P_{nano2} \tag{68}$$

$$P_{h1} = \Delta P_h + P_{h2} \tag{69}$$

$$R = \frac{Th_i - Th_{o)}}{Tc_o - Tc_i} \tag{70}$$

$$\sigma_f = -\frac{C_h}{C_{min}} R ln\left(\frac{P_{h2}}{P_{h1}}\right) - \frac{C_{nano}}{C_{min}} R ln\left(\frac{P_{c2}}{P_{C1}}\right) \tag{71}$$

$$\sigma_T = -\frac{C_h}{C_{min}} ln\left(\frac{Th_o}{Th_i}\right) + \frac{C_{nano}}{C_{min}} ln\left(\frac{Tc_o}{Tc_i}\right) \tag{72}$$

σ_T and σ_f are the thermal and viscous irreversibilities, respectively.

$$\dot{S}_{genT} = \sigma_T C_{min} \tag{73}$$

$$\dot{S}_{genf} = \sigma_f C_{min} \tag{74}$$

$\dot{S}_{genT}$ and $\dot{S}_{genf}$ are the thermal and viscous entropy generation rates, respectively.

Finally,

$$Be = \frac{\dot{S}_{genT}}{\dot{S}_{genT} + \dot{S}_{genf}} \tag{75}$$

Be is the Bejan[10] number, referenced by Fakheri[11] and Ashrafizadeh[12].

3. Results and discussions

Figure 3 presents results for the mass flow of refrigerant compared to the flow of hot fluid. The volume fraction of the nanoparticles ranges from 3% to 12%. The mass flow rate increases significantly when nanoparticles are added compared to the mass flow rate of pure water. There is no significant difference between the value obtained for the non-spherical nanoparticles analyzed. It can be predicted that the increase in mass should result in greater viscous dissipation, requiring greater power for the flow of nanofluid.

The two main quantities for determining the thermal efficiency of the heat exchanger are the ratio of the thermal capacities of the fluids (c*) and the number of thermal units (NTU). **Figure 4** presents values for the relationship between the thermal capacities with volume fraction variation for the nanoparticles. The relationship between the thermal capacities grows with the increase in the refrigerant fluid flow, with a significant increase when the nanoparticles are added addition that will affect the thermal performance of the heat exchanger. A relevant fact is that, with the rise in the mass flow rate of the nanofluid, there is an exchange between the values of C_{min} and C_{max}; that is, the thermal capacity of the nanofluid exceeds the value of the thermal capacity of the hot fluid, when the volume fraction is equal to 12%.

The heat transfer coefficients associated with hot and cold fluids affect thermal performance and reflect variations in the number of thermal units (NTU). **Figure 5** shows that the heat transfer coefficient of the cold fluid exceeds the transfer coefficient of the hot fluid when the flow rate of the cold fluid increases. This increase is greater when nanoparticles are added, being on the order of three times greater for a volume fraction equal to 12%. For lower flow rates, the heat transfer coefficients associated with nanoparticles in the form of platelets are higher than the heat transfer coefficients for nanoparticles in the cylindrical shape. However, this trend is reversed for more significant fractions in volume.

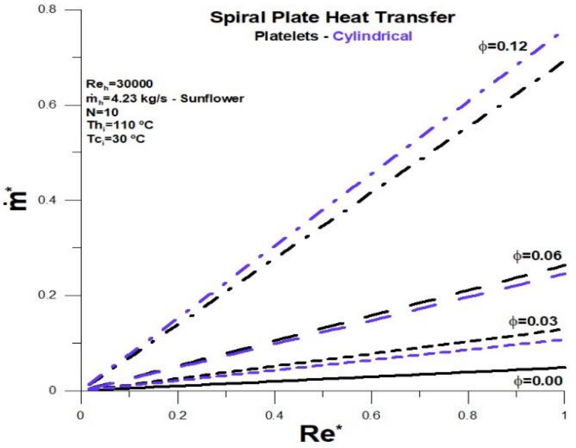

Figure 3. Dimensionless mass flow rate versus Reynolds number.

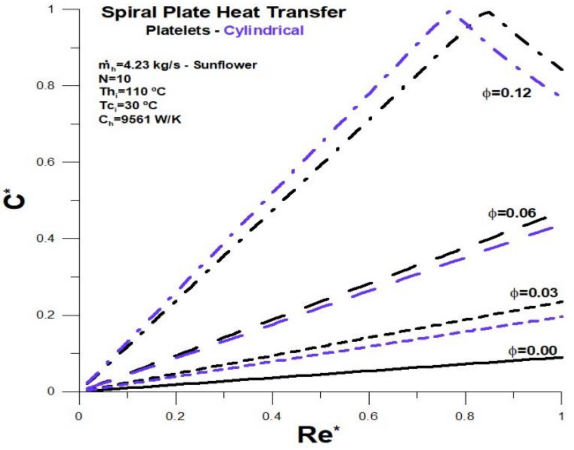

Figure 4. Relationship between heat capacities versus Reynolds number.

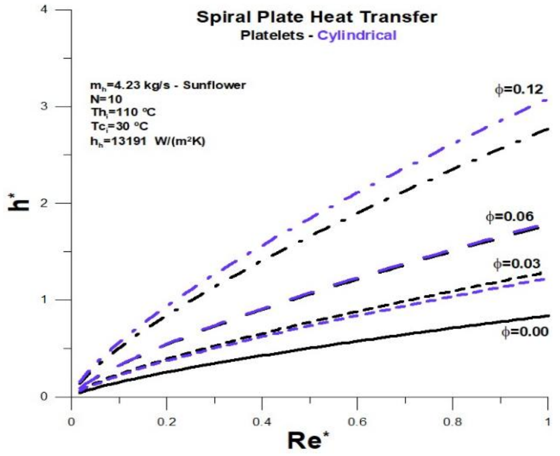

Figure 5. Relationship between heat transfer coefficients versus Reynolds number.

Figure 6 presents the number of thermal units associated with the current heat exchanger configuration. The number of thermal units decreases with increasing refrigerant flow rate. The decrease is greater when nanoparticles are added. For smaller volume fractions, the decline associated with nanoparticles in platelets is greater than that associated with nanoparticles in the cylindrical form. The situation is reversed with the increase in the volume fraction, reflecting what has already been observed for the heat transfer coefficients.

The thermal efficiency associated with the heat exchanger plays an essential role in the analysis, as the thermal effectiveness and the thermal irreversibility are defined. **Figure 7** presents results for thermal efficiency as a function of refrigerant flow. Efficiency grows with the increased inflow, and the increase is more significant with the rise in the volume fraction of the nanoparticles. In qualitative terms, the variation of the thermal efficiency is very similar to the variation of the ratio between the thermal capacities. From a maximum value, thermal efficiency equal to 1, there is a decrease with the increase in flow when the volume fraction is equal to 12%. The lower the efficiency value, the more effective the heat exchange between the fluids, indicating that the heat transfer rate is close to the maximum possible. In this case, the heat exchange potential has already been exhausted, and the difference between the fluid temperatures reached the lowest possible value in the situation under analysis. In contrast, a higher value for efficiency means that there is potential for heat exchange between fluids.

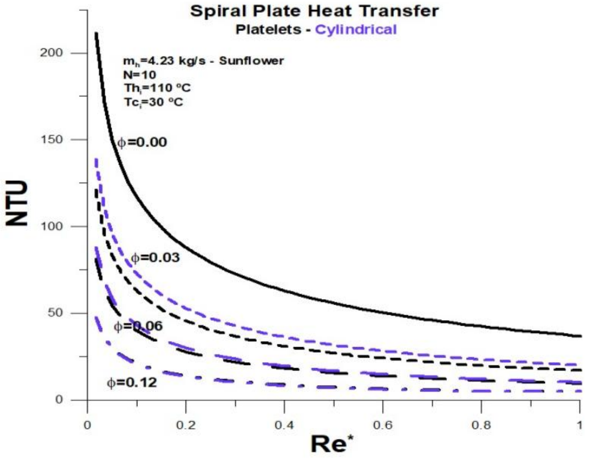

Figure 6. Number of thermal units (NTU) versus Reynolds number.

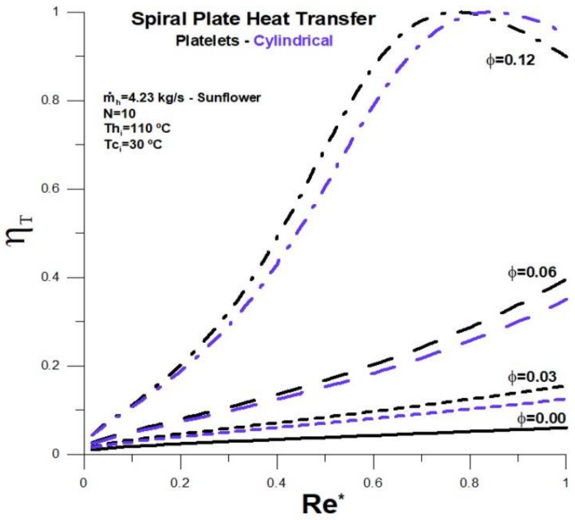

Figure 7. Thermal efficiency versus Reynolds number.

The thermal effectiveness, which measures the heat transfer rate concerning the maximum theoretically possible, is represented in **Figure 8**. The result shows that for refrigerant fluid with a nanoparticle volume fraction lower than 12%, the heat exchange between the fluids reached its maximum value for the entire flow range under analysis.

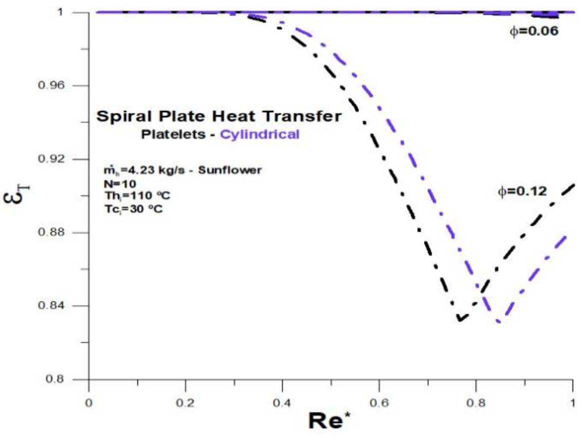

Figure 8. Thermal effectiveness versus Reynolds number.

For a volume fraction equal to 12%, it is shown that the heat transfer rate between the fluids is below the maximum possible and that a closer approximation occurs when there is an exchange of thermal capacity in determining the relationship between the thermal capacities.

Thermal irreversibility, **Figure 9** shows a similar trend to thermal effectiveness and in the opposite direction to thermal efficiency. However, the sensitivity to the effects of flow and volume fraction is greater than thermal effectiveness and very similar to thermal efficiency in qualitative terms, and vice versa. The greater the thermal irreversibility, the greater the probability that the heat exchange between the fluids has reached its maximum value and vice versa.

The viscous irreversibility, **Figure 10**, measures the influence of viscous dissipation with the variation of the flow rate of the refrigerant fluid. The effect of viscous dissipation, when compared to the viscous dissipation of pure water, is relatively low for volume fractions less than 12%. However, when the volume fraction equals 12%, the viscous dissipation reaches relatively high values for Re* > 0.6. This effect significantly weighs the cost-benefit ratio for the heat exchanger in the configuration under analysis. In addition, the power required for the flow to occur can be high.

The relationship between thermal irreversibility and total irreversibilities, the sum of irreversibilities, is associated with the Bejan number, **Figure 11**. Viscous dissipation, represented by viscous irreversibility, is not significant for pure water, and thermal irreversibility is a predominant factor. When nanoparticles are added, viscous dissipation has a greater relative weight, around 40% for volume fractions below and equal to 6%. For a volume fraction equal to 12%, it can be observed that the relative weight of viscous dissipation can reach the level of 80% when the flow of the refrigerant fluid approaches the flow of the hot fluid.

The most important results related to the heat exchange are represented in **Figure 12** through the outlet temperature of the sunflower oil. Pure water has very little influence on the drop in temperature of the hot fluid in the entire flow range analyzed. However, with the increase in the volume fraction, the temperature drop has accentuated values for both forms of nanoparticles. There is a more significant temperature drop for nanoparticles in the form of platelets, with a volume fraction below and equal to

6%. For volume fraction equal to 12%, the situation is reversed, but the temperature difference between both forms of nanoparticles is not significant. In the limiting condition under analysis, the lowest temperature of the hot fluid is approximately equal to 35 °C.

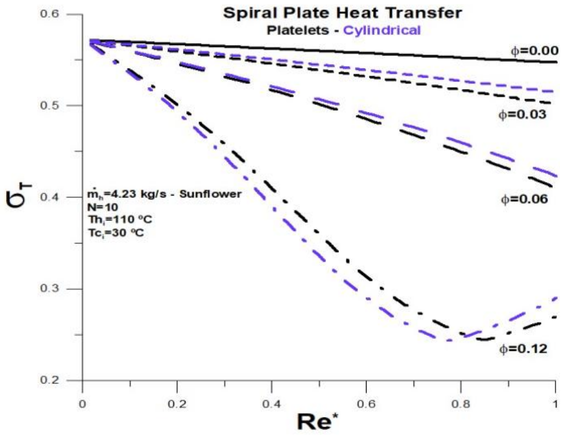

Figure 9. Thermal irreversibility versus Reynolds number.

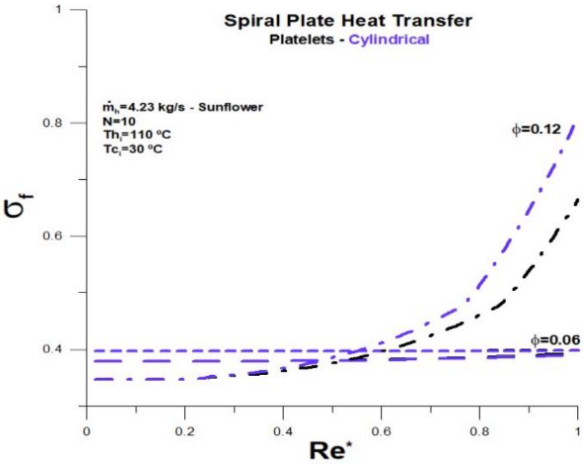

Figure 10. Viscous irreversibility versus Reynolds number.

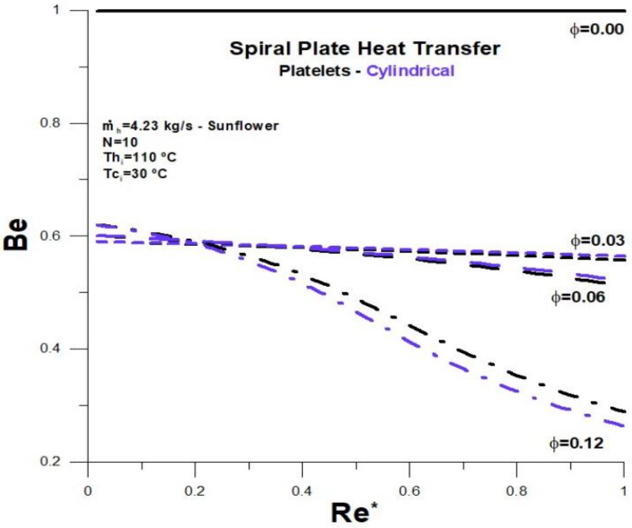

Figure 11. Bejan number versus Reynolds number.

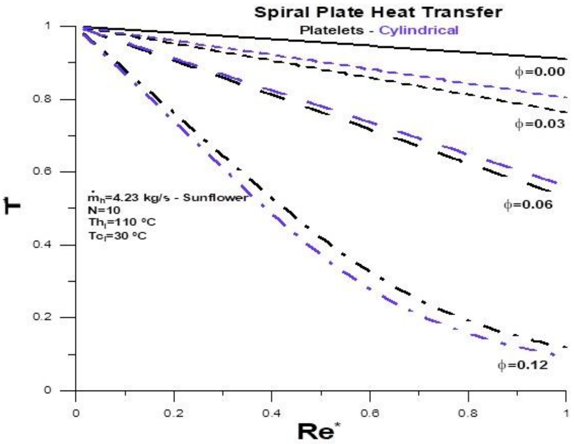

Figure 12. Hot fluid outlet temperature versus Reynolds number.

4. Conclusion

The influence of non-spherical Boehmite Alumina nanoparticles on the hydraulic and thermal performance of a spiral plate heat exchanger (SPHE) was analyzed. The formats of the analyzed nanoparticles are platelet and cylindrical. The fluid to be cooled is sunflower vegetable oil, and the base fluid is water, with an inlet temperature equal to 110 °C.

The thermal performance of the heat exchanger when using only pure water is poor, with a tiny drop in the temperature of the hot fluid. However, with the introduction of nanoparticles, added to the increase in the flow rate of the nanofluid, the temperature drop increases significantly. It achieves a better result for maximum flow within the flow rate under analysis. In this situation, with a volume fraction equal to 12%, the hot fluid outlet temperature reaches 35 °C.

It is concluded that the use of non-spherical nanoparticles provides excellent thermal performance, reflected in a lower outlet temperature of the hot fluid. By analyzing the Bejan number, it is possible to see that it is possible to increase the flow rate of the nanofluid in values slightly above what was studied or an increase in the volume fraction, which will reflect in a lower outlet temperature for the hot fluid. However, there will be an increase in viscous dissipation, compromising the cost-benefit ratio.

Conflict of interest

The author declares no conflict of interest.

References

1. Shirazi AHS, Behnia M, Ghodrat M. Energy and exergy analysis of spiral turns in optimum design spiral plate heat exchangers. *Heat Transfer* 2022; 51(1): 701–732. doi: 10.1002/htj.22326
2. Khorshidi J, Heidari S. Design and construction of a spiral heat exchanger. *Advances in Chemical Engineering and Science* 2016; 6(2): 201–208. doi: 10.4236/aces.2016.62021
3. Kolasiński P, Rogala Z. The use of spiral heat exchangers in the orc domestic systems. *Scientific Letters of Rzeszow University of Technology—Mechanics* 2015; 87(1/15): 23–35. doi: 10.7862/rm.2015.3
4. Kumar KPM, Vijayan V, Kumar BS, et al. Computational analysis and optimization of spiral plate heat exchanger. *Journal of Applied Fluid Mechanics* 2018; 11: 121–128. doi: 10.36884/jafm.11.si.29428
5. Núñez MP, Canizalez-Dávalos L, Morales-Fuentes A. Alternative design approach for spiral plate heat exchangers. *Chemical Engineering Transactions* 2007; 12: 183–188.
6. Monfared M, Shahsavar A, Bahrebar MR. Second law analysis of turbulent convection flow of boehmite alumina nanofluid inside a double-pipe heat exchanger considering various shapes for nanoparticle. *Journal of Thermal Analysis and Calorimetry* 2019; 135: 1521–1532. doi: 10.1007/s10973-018-7708

7. Rojas EEG, Coimbra JSR, Telis-Romero J. Thermophysical properties of cotton, canola, sunflower, and soybean oils as a function of temperature. *International Journal of Food Properties* 2013; 16(7): 1620–1629. doi: 10.1080/10942912.2011.604889
8. Nogueira E. Thermal performance in heat exchangers by the irreversibility, effectiveness, and efficiency concepts using nanofluids. *Journal of Engineering Sciences* 2020; 7(2): F1–F7. doi: 10.21272/jes.2020.7(2).f1
9. Hemanth B, Rao KP, Rao SV. Heat transfer enhancement in spiral plate heat exchanger using nanofluids. *International Journal of Creative Research Thoughts (IJCRT)* 2022; 10(1): 10–15.
10. Bejan A. The thermodynamic design of heat and mass transfer processes and devices. *Heat and Fluid Flow* 1987; 8(4): 258–276. doi: 10.1016/0142-727X(87)90062-2
11. Fakheri A. Heat exchanger efficiency. *ASME Journal of Heat and Mass Transfer* 2007; 129(9): 1268–1276. doi: 10.1115/1.2739620
12. Ashrafizadeh SA. Application of second law analysis in heat exchanger systems. *Entropy* 2019; 21(6): 606. doi:10.3390/e21060606

Mechanical Engineering Advances 2023; 1(1): 106.
Original Research Article

Analysing entropy generation of MHD (50:50) slip flow over an inclined needle

Selvaraj Priya[1], Gundada Raju Rajamani[1], Bhose Ganga[2], Abdul Kaffoor Abdul Hakeem[1,*], Pachiyappan Ragupathi[1,*]

[1] *Department of Mathematics, Sri Ramakrishna Mission Vidyalaya College of Arts and Science, Coimbatore 641020, India*

[2] *Department of Mathematics, Providence College for Women, Coonoor 643104, India*

*** Corresponding author:** Abdul Kaffoor Abdul Hakeem, drabdulmaths@gmail.com; Pachiyappa Ragupathi, ragupathiprs@gmail.com

ARTICLE INFO

Received: 3 July 2023
Accepted: 16 August 2023
Available online: 19 September 2023

doi: 10.59400/mea.v1i1.106

ABSTRACT: The primary objective of this study is to quantify the rate of entropy generation within the Magnetohydrodynamic (MHD) slip flow system over the inclined needle. Entropy generation is a measure of the irreversibility and inefficiency in the flow process. The slip flow condition at the fluid interface can significantly impact the flow characteristics and heat transfer rates. In the hybrid nanofluid flow, which consists of non-magnetic and magnetic (Al_2O_3 and Fe_3O_4) are nanoparticles, $H_2O + C_2H_6O_2$ (50: 50) are considered as the base fluid. Furthermore, the effects of inclined magnetic fields are taken into interpretation. The PDE's governing equations are converted into ODE's using similarity transformations and solved by a numerical technique based on BVP4C. The results illustrate that crucial parameter such as the magnetic parameter, mixed convection parameter, nanoparticles of solid volume fractions, and Prandtl numbers are pointedly impacted by momentum and thermal profiles. The entropy and Bejan number also consider being various relationship combined parameters. These analyses protest that raising the magnetic parameter estates an increase in the hybrid nanofluid thermal profile under slip circumstances. Examined magnetic field impact on flow and entropy generation in MHD flows, revealing significant changes in entropy generation due to interaction between magnetic field and nanoparticles. This analysis understands the impact of MHD and slip effects on entropy generation, particularly in the context of the newly emerging 50:50 fluid mixture. Hybrid nanofluids have been shown to have improved thermal conductivity compared to traditional fluids, which can enhance the cooling or heating capabilities of the inclined needle.

KEYWORDS: inclined needle; heat transfer; hybrid nanofluid; entropy generation; Bejan number

1. Introduction

Hybrid nanofluids can significantly enhance heat transfer properties compared to traditional heat transfer fluids. The combination of nanoparticles with distinct thermal conductivities can lead to improved cooling efficiency in various systems, such as heat exchangers, electronic devices, and power plants. This research analysis an inclined surface, the gravitational force acts as an additional driving force, influencing the flow behavior. If the gravitational force component parallel to the inclined surface exceeds the yield stress of the material, the material will start to flow downhill[1]. This research analyzes the understanding of these dynamics is crucial for various engineering and environmental applications and requires careful consideration of factors such as viscosity, particle characteristics, and channel inclination[2]. Vertical thin needle in porous medium offers mathematical framework for analyzing heat and mass transfer rates, enabling researchers and engineers to optimize designs and make informed decisions[3]. Nanofluids are colloidal suspensions with nanoparticles dispersed in base fluids like water, oil, or ethylene glycol. These unique properties significantly improve thermal conductivity of the base fluid. Enhancing the thermal conductivity of fluids using nanoparticles is a process known as nanofluid technology. This research improved thermal properties make them promising candidates for enhancing heat transfer efficiency and improving the overall performance of thermal systems[4]. This research analysis identifies the most influential parameters and their impact on the system's behavior. This can help optimize the system design or suggest areas for further research[5,6]. This review analyzes numerical simulations on lid-driven cavity flow with nanofluids, providing valuable insights for researchers and engineers seeking to understand the complexities and potential applications of nanofluid flows in lid-driven cavities[7]. The study examines magnetic separation and filtration processes in industries like wastewater treatment and mining, utilizing nanoparticle magnetization for efficient fluid flow manipulation and control[8]. This study explores magnetic field-electrically conductive fluid interactions, affecting heat and mass transfer in magnetic drug targeting and hyperthermia cancer treatment applications[9]. This study examines non-Fourier heat flux, ferromagnetic properties, and autocatalytic chemical reactions for understanding thermal and dynamical behavior in complex systems, including magnetic fluids[10]. This research analyzes bioconvection, the collective movement of living microorganisms in fluids, particularly nanofluids. Bioconvection can enhance heat transfer and improve the thermal performance of nanofluids, such as bacteria and algae[11]. Investigated in this study nanoparticle materials like metal oxides, carbon-based materials, and ferromagnetic nanoparticles for optimizing viscous dissipation in cooling systems and microfluidic devices[12]. Recent research in the field of hybrid nanofluids is ongoing, and new applications continue to emerge as scientists explore their unique properties and potential in various fields. This research analyzes Lorentz force and viscous dissipation to predict propylene glycol-water mixture behavior, optimizing system design, controlling fluid flow, and enhancing heat transfer and transport efficiency[13]. This study investigates the effects of natural convection, micropolar hybrid nanofluid, needle orientation, and boundary heating conditions on heat transfer, fluid flow patterns, and temperature distribution in a thin needle[14]. This research investigated stratification in nanoliquids, examining the impact on fluid dynamics and microorganism behavior, potentially affecting bioconvection patterns and gyrotactic microorganism behavior[15,16]. The research examined stretching parameters' impact on fluid flow and heat transfer characteristics, focusing on non-linear profiles in parabolic shapes for realistic scenarios and practical applications[17]. MHD refers to the study of the behavior of electrically conducting fluids in the presence of magnetic fields. The utilization of hybrid nanofluids in MHD systems aims to improve their performance, efficiency, and control. Some of the recent research in this area has focused on investigating the effects of different factors, such as nanoparticle concentration, fluid flow rate, and geometrical shapes, on the overall performance of MHD systems. In recent years, researchers have been investigating the application of hybrid nanofluids in MHD systems with different geometrical shapes. Some of the research areas are following, wedges[18], curve[19], vertical plate[20], sphere[21], flexible walls[22], sinusoidal walls[23]. This research investigates slip effects refer to the motion of the fluid near the surface, where the fluid molecules slip along the solid boundary instead of adhering to it. The findings of such studies can provide valuable insights into the design and optimization of various engineering systems and processes involving heat and mass transfer[24]. Investigated the behavior of nanoparticles in the nanofluid near the wavy cylinder and understanding their potential aggregation or settling tendencies due to the presence of the magnetic field[25]. This study investigates the exact and specific results that would depend on the assumptions, boundary conditions, and modelling approaches used in the study. Therefore, the findings may vary across different research works and experimental setups[26]. Researchers have investigated this study is the use of reversible chemical reactions to store and release heat, which is crucial for renewable energy integration and grid stabilization[27]. Investigated this analysis how the combination of thermal radiation and shear-thinning behavior impacts the overall heat transfer rate in the system[28]. This study examines activation energy, a crucial parameter in nanofluids, which influences chemical reactions and thermal behavior, focusing on energy barriers and their impact on chemical reactions[29]. Studies have investigated the dynamics of the melting front in nanofluids, analyzing how nanoparticles affect the solid-liquid interface and the overall melting process[30]. Recent research may have focused on investigating the impact of different types of nanoparticles, their concentrations, and fluid compositions on entropy generation. Studies may have explored the behavior of hybrid nanofluids in specific applications, such as heat exchangers, refrigeration systems, or power generation. Some studies have shown that the use of hybrid nanofluids can lead to reduced entropy generation compared to traditional fluids. The enhanced thermal conductivity of nanofluids allows for improved heat transmission, reducing the temperature gradients and associated entropy generation. Some of the following recent researches are based on entropy generation[31–37].

The main aim of this paper, using slip flow conditions at the inclined needle and the impact of the inclined magnetic field needs to be considered. To calculate analytical results can be used scattering shooting techniques and obtain solutions for velocity, temperature, and other relevant variables. In MHD slip flow, the slip boundary conditions are applied at the fluid interface, for the presence of nanoparticles need to considered. These models may include the Brownian motion and Thermophoresis effects on nanoparticles. Thermal convection refers to the process of heat transmission in fluids due to the combined effect of buoyancy and fluid motion. The application of a Lorentz force can influence fluid stream and heat transmission processes through Magnetohydrodynamics (MHD). The outcomes of this research can provide insights into the thermodynamic efficiency of the system, the impression of slip flow and nanofluid on entropy creation, and the influence of the magnetic field. This information can be useful for optimizing the design and operation of MHD systems utilizing hybrid nanofluids in slip flow conditions with horizontal needle geometries. Entropy generation and the Bejan number are essential concepts in thermodynamics and fluid mechanics. Hybrid nanofluids can potentially progress the performance and efficiency of the needle. Another potential application is in enhancing the heat transmission properties of the needle.

2. Mathematical formulation

- For the research, stable, an incompressible 2D axisymmetric dissipative hybrid fluid flow was applied to a moving object with an inclined magnetic field.
- The fluid was composed of $\mathrm{H_2O + C_2H_6O_2(50-50) + Al_2O_3 + Fe_3O_4}$.
- The magnetic field intensity applied normally towards the needle is decided by $B = B(x) = \frac{B_0}{\sqrt{x}}$, T_∞ *and* T_w were chosen to represent ambient, surface temperatures.
- The needle passages in the similar or conflicting way as the constant velocity U_w normal with free continual velocity U_∞ and the flow pattern is shown in **Figure 1**. **Table 1** determines the status of

magnetic and nonmagnetic nanoparticle thermophysical properties, as well as hybrid nanofluid thermal properties.

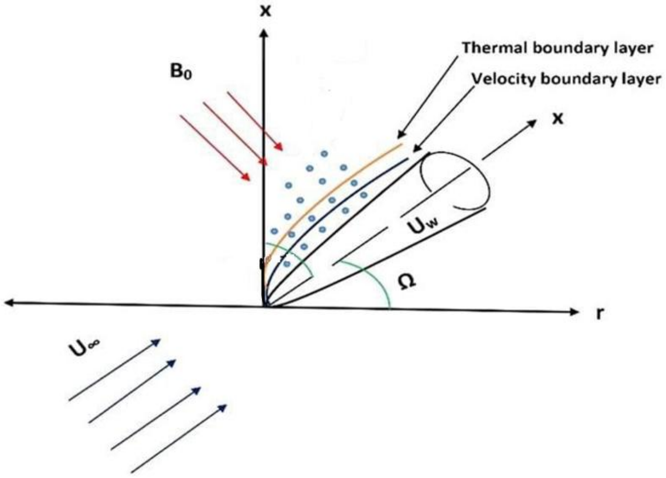

Figure 1. Stream outline of contemporary problem.

These conventions allow for the specification of flow controlling equations as[13]

Continuity equation:

$$r(u)_x + r(v)_r = 0 \tag{1}$$

Momentum equation:

$$uu_x + vu_r = \frac{\mu_{hnf}}{\rho_{hnf}}\left(\frac{1}{r}\right)(ru_r)_r - u\frac{\sigma B^2}{\rho_{hnf}}\sin^2\alpha + \frac{g(\rho\beta)_{hnf}(T - T_\infty)}{\rho_{hnf}}\sin\Omega \tag{2}$$

Energy equation:

$$(\rho C_p)_{hnf}(uT_x + vT_r) = k_{hnf}\left(\frac{1}{r}\right)(rT_r)_r \tag{3}$$

With the boundary conditions[6],

$$\left.\begin{array}{c} u = U_w + \Gamma_1\left(\frac{\mu_{hnf}}{\rho_{hnf}}\right)\frac{\partial u}{\partial r}, v = 0, T = T_w + \Gamma_2\frac{\partial T}{\partial r} at r = R(x) \\ u \to u_\infty, T \to T_\infty \; as \; r \to \infty \end{array}\right\} \tag{4}$$

Table 1. Thermophysical characteristics attributes of solid volume fractions of nanoparticles and base fluid[5,6].

Attributes	$\mathbf{Al_2O_3}$	$\mathbf{Fe_3O_4}$	$\mathbf{H_2O + C_2H_6O_2\ (50:50)}$
Density (kg/m^3)	3970	5180	1067.5
Specific heat (j/kg/k)	765	670	3300
Thermal conductivity (w m k)	9.7	40	0.3799
Dynamic viscosity (kg/ms)	-	-	0.00339
Thermal expansion $\beta/10^{-5}$(1/k)	0.85	1.3	58

The hybrid nanofluid is strategized different volumetric solid fractions (ϕ_1, ϕ_2) such as $Al_2O_3 -$ (0.5%) and $Fe_3O_4 -$ (1.5%).

The hybrid nanofluid properties are considered by Sajja et al.[13].

$$\rho_{hnf} = \{(1-\phi_2)[(1-\phi_1)\rho_f + \phi_1\rho_{s_1}]\} + \phi_2\rho_{s_2} \tag{5}$$

$$\mu_{hnf} = \frac{\mu_f}{(1-\phi_1)^{2.5}(1-\phi_2)^{2.5}} \tag{6}$$

$$k_{hnf} = \frac{k_{s_2} + 2k_{nf} - 2\phi_2\left(k_{nf} - k_{s_2}\right)}{k_{s_2} + 2k_{nf} + \phi_2\left(k_{nf} - k_{s_2}\right)} \times k_{nf} \tag{7}$$

$$k_{nf} = \frac{k_{s_1} + 2k_f - 2\phi_1\left(k_f - k_{s_1}\right)}{k_{s_1} + 2k_f + \phi_1\left(k_f - k_{s_1}\right)} \times k_f \tag{8}$$

$$\left(\rho C_p\right)_{hnf} = \left\{(1-\phi_2)\left[(1-\phi_1)(\rho C_p)_f + \phi_1(\rho C_p)_{s_1}\right]\right\} + \phi_2(\rho C_p)_{s_2} \tag{9}$$

$$(\rho\beta)_{hnf} = \left\{(1-\phi_2)\left[(1-\phi_1)(\rho\beta)_f + \phi_1(\rho\beta)_{s_1}\right]\right\} + \phi_2(\rho\beta)_{s_2} \tag{10}$$

Along with variables such as[13],

$$\left.\begin{array}{c} \varepsilon = \frac{Ur^2}{\nu x}, \psi = \nu x f(\varepsilon), u = \frac{1}{r}\left(\frac{\partial\psi}{\partial r}\right) \\ v = -\frac{1}{r}\left(\frac{\partial\psi}{\partial x}\right), T = T_\infty + (T_w - T_\infty)\theta(d) \end{array}\right\} \tag{11}$$

we can get $R(x) = \left(\frac{\nu d x}{U}\right)^{\frac{1}{2}}$ where $U = U_w + U_\infty \neq 0$ is the governing equations is satisfied by reinforced acceleration. and transforms (Equations (2) and (3)) as:

$$\frac{2}{E_1E_2}(\varepsilon F''' + F'') - \frac{1}{2E_2}MF'sin^2\alpha + \lambda E_5(sin\Omega)\theta = 0 \tag{12}$$

$$\frac{2E_3E_{31}}{E_4}\frac{1}{Pr}(\varepsilon\theta'' + \theta') + F\theta' = 0 \tag{13}$$

and changes the circumstances in Equation (4) as,

$$\left.\begin{array}{c} F'(d) = \frac{\delta}{2} + \frac{2\gamma_1\sqrt{d}}{E_1E_2}, F(d) = d\left(\frac{\delta}{2} + \frac{2\gamma_1\sqrt{d}}{E_1E_2}\right), \theta(d) = 1 + \gamma_2\theta'(\varepsilon) \\ F'(\infty) \to \frac{1-\delta}{2}, \theta(\infty) \to 0 \end{array}\right\} \tag{14}$$

The hybrid nanofluid properties are considered by Sajja et al.[13].

$$E_1 = (1-\phi_1)^{2.5}(1-\phi_2)^{2.5} \tag{15}$$

$$E_2 = \left\{(1-\phi_2)\left[(1-\phi_1) + \phi_1\frac{\rho_{s1}}{\rho_f}\right]\right\} + \phi_2\frac{\rho_{s2}}{\rho_f} \tag{16}$$

$$E_{31} = \frac{k_{s1} + 2k_f - 2\phi_1\left(k_f - k_{s1}\right)}{k_{s1} + 2k_f + \phi_1\left(k_f - k_{s1}\right)} \tag{17}$$

$$E_3 = \frac{k_{s2} + 2E_{31}k_f - 2\phi_2\left(E_{31}k_f - k_{s2}\right)}{k_{s2} + 2E_{31}k_f + \phi_2\left(E_{31}k_f - k_{s2}\right)} \tag{18}$$

$$E_4 = (1-\phi_2)\left[(1-\phi_1) + \phi_1\frac{(\rho C_p)_{s1}}{(\rho C_p)_f}\right] + \phi_2\frac{(\rho C_p)_{s1}}{(\rho C_p)_f} \tag{19}$$

$$E_5 = (1-\phi_2)\left[(1-\phi_1) + \phi_1\frac{(\rho\beta)_{s1}}{(\rho\beta)_f}\right] + \phi_2\frac{(\rho\beta)_{s2}}{(\rho\beta)_f} \tag{20}$$

$$Gr_x = \frac{g\beta_f(T_w - T_\infty)L^3}{\nu^2}, Re_x = \frac{UL}{\nu}, M = \frac{\sigma B_0^2}{\rho U}, \delta = \frac{U_w}{U} = \frac{constant\ velocity}{composite\ velocity} \tag{21}$$

$$\lambda = \frac{Gr_x}{Re_x^2} = \frac{g\beta_f(T_w - T_\infty)L^3}{U^2}, Pr = \frac{\mu c_p}{k} \tag{22}$$

Nusselt number and skin friction

Another important external of the contemporary examination is the Nusselt number, Skin friction which is prearranged by,

$$N_{ux} = \frac{xq_w}{k_f\left((T_w - T_\infty)\right)}\bigg|_{r=R(x)} \tag{23}$$

$$C_{fx} = \frac{\tau_w}{\frac{1}{2}\rho U^2}\bigg|_{r=R(x)} \tag{24}$$

where $q_w = -k_{hnf}\frac{\partial T}{\partial r}(wall\ heat\ flux),\ \tau_w = \mu_{hnf}\frac{\partial u}{\partial r}\ (wall\ shear\ stress)$.

The following terms from Equations (19) and (20) are described in non-dimensional form

$$(Re_x)^{-\frac{1}{2}}N_{ux} = -E_3E_{31}2\sqrt{d}\theta'(d) \tag{25}$$

$$(Re_x)^{-\frac{1}{2}}C_{fx} = \frac{8F''(\varepsilon)\sqrt{d}}{E_1} \tag{26}$$

where $Re_x = \frac{UL}{\nu}(Reynolds\ number)$.

3. Entropy analysis

The countenance for the entropy analysis is specified below[35]

$$S_{gen}''' = \frac{k}{T_\infty^2}((T_r)^2) + \frac{\mu}{T_\infty}((u_r)^2) + \frac{\sigma B_0^2}{T_\infty}u^2 \tag{27}$$

where the primary term displays the entropy analysis proportion due to heat transmission S_h''' the next term confirmations the entropy analysis proportion due to fluid resistance S_f''', the third tenure illustrations the entropy analysis proportion owing to the magnetic field S_m'''.

$$S_{gen}''' = S_h''' + S_f''' + S_m''' \tag{28}$$

The proportion of total entropy analysis that can remain engraved in a dimensionless process is

$$N_s = \frac{S_{gen}'''}{\left(\frac{4k_f}{x^2}\right)\Omega_T} = \varepsilon Re_x\Omega_T\theta'^2 + 4\varepsilon Re_xBrF''^2 + MRe_xBrF'^2 \tag{29}$$

where $Br = \frac{\mu U^2}{k_f(T_w - T_\infty)}$ represents the Brinkman number.

Bejan analysis

Regarding the entropy analysis examination of convective heat transmission issues, Bejan stated the irreversibility distribution proportion as follows:

$$\Phi = \frac{S_{prod,frc}'''}{S_{prod,\Delta T}'''} \tag{30}$$

It is imperative to note that the fluid resistance (N_{sf}) irreversibility plays a major role when $\Phi > 1$. Therefore, the heat transmission irreversibility (N_{sh}) is fundamental. When $\Phi = 1$, the perfections related to heat transference (N_{sh}) and fluid resistance (N_{sf}) are the equivalent.

Equation Φ could very well establish.

$$\Phi = \frac{4BrF''^2 + \frac{Br}{\Omega T\eta} MF'^2}{\theta'^2} \tag{31}$$

The impermissibility ratio, or Bejan multitude, is

$$Be = \frac{S'''_{prod\ ,\Delta T}}{S'''_{prod}} = \frac{\frac{k}{T_\infty^2}((T_r)^2)}{\frac{k}{T_\infty^2}((T_r)^2) + \frac{\mu}{T_\infty}((u_r)^2)} \tag{32}$$

As a direct consequence of the method developed, it begins to develop in and out of

$$Be = \frac{\theta'^2}{\theta'^2 + 4BrF''^2 + \frac{Br}{\Omega T\eta} MF'^2} \tag{33}$$

$Be = 1$ symbolizes the boundary at which irreversibility is entirely owed to heat transmission,
$Be = 0$ is the boundary at which the irreversibility is due to fluid resistance only.
$Be >> 1/2$ when irreversibility outstanding to heat transmission takes antecedence.
$Be << 1/2$ demonstrates that irreversibility due to fluid resistance is foremost.

4. Physical explanation

Analyzing this research needs to resolve the governing equivalences for mass, velocity, and thermal conservation. These equations are typically solved using numerical techniques such as BVP4C. The governing equations for this problem can be expressed in non-dimensional form using suitable dimensionless variables such as Reynolds variable, Prandtl quantity, inclined magnetic. **Figures 2–16** depict the appearances and structures of various pertinent variables appearing in the problematic on the profiles of hybrid nanofluid momentum, thermal, entropy and Bejan profile. **Table 1** demonstrates the importance of magnetic and nonmagnetic nanoparticle thermophysical properties, as well as hybrid nanofluid thermal properties. **Table 2** displays heat transfer rate and surface drag force values. **Table 3** and **Figures 17** and **18** are compares our results to available outcomes in order to validate our problem with other research and discover its remarkable similarity. The transmuted nonlinear differential Equations (1)–(3), moreover the boundary restriction (Equations (13) and (14)), are numerically resolved using the BVP4C solver. The values that appear in the problem through computation are fixed as $\phi_1 = 0.005,\ \phi_2 = 0.015,\ d = 0.5,\ Pr = 29.45,\ M = 3,\ \delta = 1, v_1 = t_1 = 1.5$. The detailed numerical solution is below,

$$y_1 = f \ and \ y_4 = \theta$$

$$y_1' = y_2$$

$$y_2' = y_3$$

$$y_3' = -\frac{1}{\varepsilon}\left[y_3 + \frac{E_1E_2}{2}\left(y_1y_3 - \frac{1}{2E_2} \times y_2 \times X + \lambda E_5(\sin\Omega)y_4\right)\right]$$

$$y_4' = y_5$$

$$y_5' = \frac{1}{\varepsilon}\left[-y_5 - \frac{E_4}{2E_3E_{31}} \times Pr \times y_1y_5\right]$$

$$y_2(a) = \frac{\delta}{2} + \frac{\nu_{1\sqrt{d}}}{2} \times \frac{1}{E_1E_2}$$

$$y_1(a) = d * \left[\frac{\delta}{2} + \frac{\nu_{1\sqrt{d}}}{2} * \frac{1}{E_1 E_2}\right]$$

$$y_4(a) = 1 + t_1 * y_5$$

$$y_2(b) = \frac{1-\delta}{2}$$

$$y_4(b) = 0$$

5. Review and discussion of the results

Figure 1 depicts the items are placed of the conundrum. In regard to physical behaviour and attitude are explanations in the figures. **Figures 2–16** have been drawn for EG-Water (50:50) + Al_2O_3 + Fe_3O_4, to demonstrate the impression of numerous parameters on acceleration, entropy generation, and Bejan number.

5.1. Velocity and thermal profile

Figure 2 explains, the increase in the magnetic parameter ($M = 1, 2, 3$) strengthens the opposing magnetic force, while the increase in the inclination angle ($\Omega = 0^o, 45^o, 90^o$) magnifies the gravitational force component acting parallel to the surface. Both of these factors contribute to a decline in the velocity profile of the inclined needle.

Velocity profile:

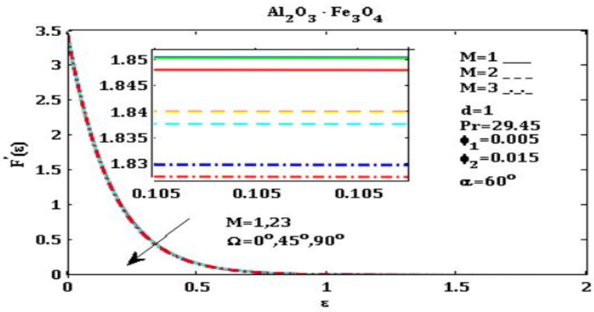

Figure 2. The impacts of $M = 1, 2, 3$ on $F'(\varepsilon)$.

When both the needle size ($d = 0.5, 1, 1.5$) and angle ($\Omega = 0^o, 45^o, 90^o$) increase simultaneously, their combined effect enhances the fluid flow even more. The larger needle diameter allows for a greater fluid volume, while the steeper angle generates a higher pressure drop. This combination results in a more pronounced upsurge in the velocity profile as explained in **Figure 3**.

Velocity profile:

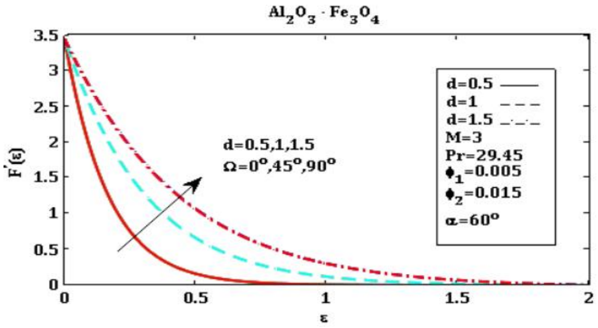

Figure 3. The impacts of $d = 0.5, 1, 1.5$ on $F'(\varepsilon)$.

Figure 4 explains, when the velocity, temperature slip parameter ($v_1 = t_1 = 1.5, 2.5, 3.5$), and angle ($\Omega = 0^o, 45^o, 90^o$) of an inclined needle are increased, the velocity profile tends to become more uniform and less parabolic. The increased velocity promotes turbulence, the higher temperature slip parameter introduces thermal effects, and the steeper angle amplifies the influence of gravity. These factors combine to produce a higher velocity profile along the surface of the needle.

Velocity profile:

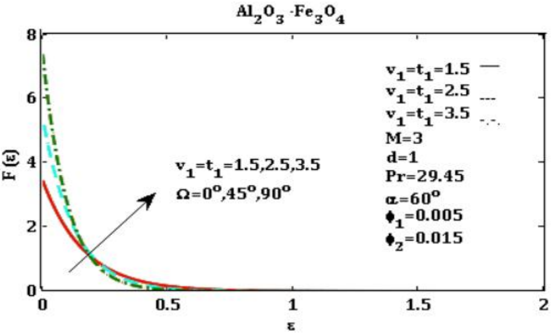

Figure 4. The impacts of $v_1 = t_1 = 1.5, 2.5, 3.5$ on $F'(\epsilon)$.

Figure 5 as shown, when both the velocity ratio parameter ($\delta = 1, 2, 3$) and the angle ($\Omega = 0^o, 45^o, 90^o$) increase, the fluid experiences an increased velocity due to a combination of factors. The higher velocity ratio parameter indicates a faster flow rate, while the increased angle leads to a more pronounced directional component of the fluid velocity. As a result, the overall momentum profile of the fluid in the inclined needle increases.

Velocity profile:

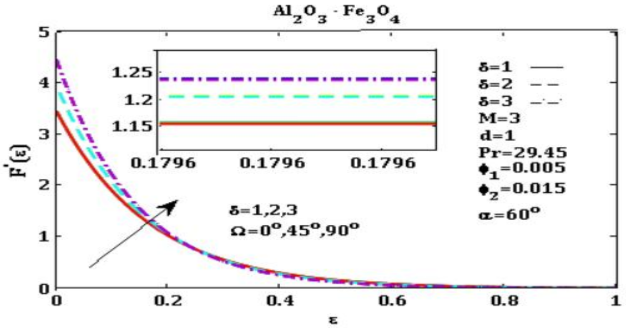

Figure 5. The impacts of $\delta = 1, 2, 3$ on $F'(\varepsilon)$.

A mixed convection parameter is a dimensionless number that characterizes a system's relative importance of forced and natural convection. When both the mixed convection parameter ($\lambda = 0.5, 1.5, 2.5$) and the angle of inclination ($\Omega = 0^o, 45^o, 90^o$) increase simultaneously, the mutual consequence of enhanced forced convection and increased natural convection results in an even greater velocity profile in the inclined needle. The fluid is influenced by both the external source (forced convection) and the buoyancy forces (natural convection), leading to an intensified flow pattern with higher velocities, as appeared in **Figure 6**.

Velocity profile:

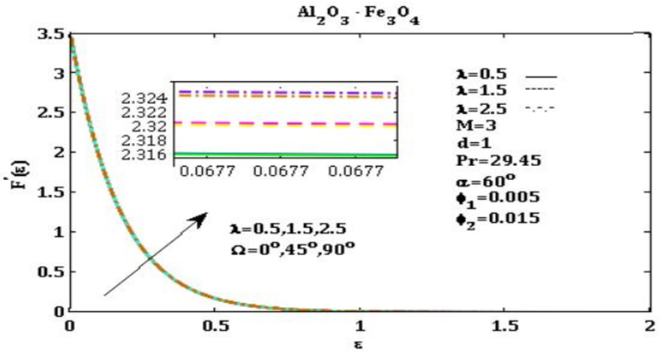

Figure 6. The impacts of $\alpha = 0^o, 45^o, 90^o$ on $F'(\varepsilon)$.

Figure 7 explains, when both the magnetic parameter ($M = 1, 2, 3$) and the inclination angle ($\Omega = 0^o, 45^o, 90^o$) increase simultaneously, their combined effects result in a more pronounced enhancement of heat transfer. The stronger magnetic field induces more vigorous fluid motion, while the larger inclination angle modifies the buoyancy-driven flow patterns. These changes collectively lead to increased heat transfer from the needle, resulting in an increase in the temperature profile.

Thermal profile:

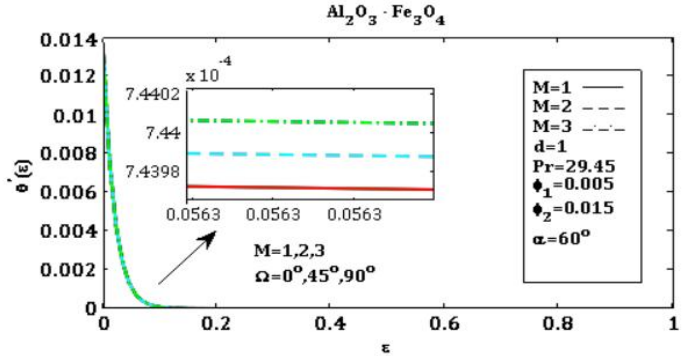

Figure 7. The impact of $M = 1, 2, 3$ on $\theta'(\varepsilon)$.

When both the needle size ($d = 0.5, 1, 1.5$) and angle ($\Omega = 0^o, 45^o, 90^o$) increase, the combined effect of increased surface area (due to larger needle size) and enhanced convection (due to higher needle angle) can outweigh the reduction in the surface area caused by the inclination. This results in an overall intensification in the temperature profile of the inclined needle as exposed in **Figure 8**.

Thermal profile:

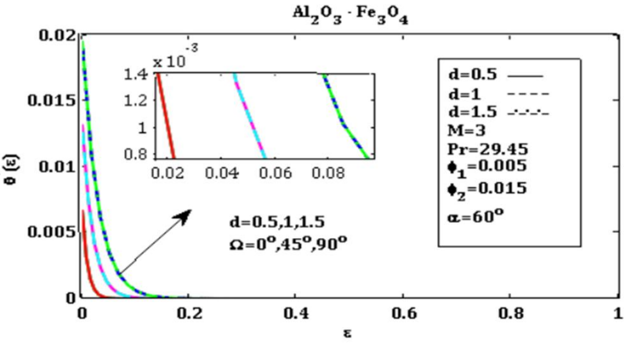

Figure 8. The impact of $d = 0.5, 1, 1.5$ on $\theta'(\varepsilon)$.

Figure 9 explains, when the velocity, temperature slip parameter ($v_1 = t_1 = 1.5, 2.5, 3.5$), and angle ($\Omega = 0^o, 45^o, 90^o$) increase in an inclined needle, the temperature profile tends to decrease. This is primarily due to enhanced convective heat transfer resulting from higher fluid velocity, larger temperature difference at the interface (temperature slip parameter), and increased fluid turbulence caused by the inclination angle.

Thermal profile:

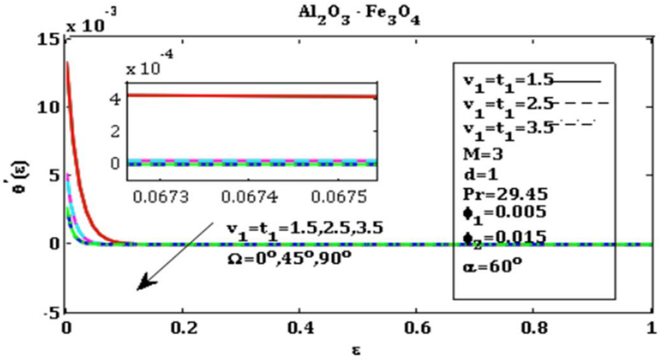

Figure 9. The impact of $v_1 = t_1 = 1.5, 2.5, 3.5$ on $\theta'(\varepsilon)$.

When both the velocity ratio ($\delta = 1, 2, 3$) parameter and the angle ($\Omega = 0^o, 45^o, 90^o$) of inclination increase, the combined effect is a significant enhancement in fluid mixing and heat transfer. The increased velocity ratio increases turbulence and shear stresses, promoting better mixing. The increased angle of inclination strengthens the gravity-driven flow, further enhancing the mixing. The enhanced mixing and heat transfer result in a more efficient transmission of thermal energy from the fluid to the needle walls. Consequently, the temperature profile of the fluid decreases explained in **Figure 10**.

Thermal profile:

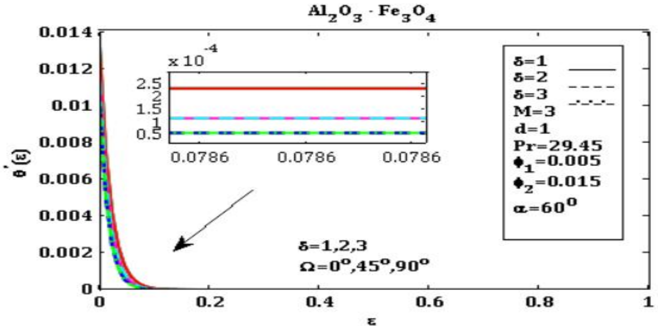

Figure 10. The impacts of $\delta = 1, 2, 3$ on $\theta'(\varepsilon)$.

5.2. Entropy and Bejan profile

The relationship between aluminium oxide and magnetic parameters would largely depend on the introduction of magnetic impurities or the formation of composite materials. If aluminium oxide is doped with magnetic elements or combined with magnetic materials, then its magnetic properties can be influenced in an inclined needle. As the magnetic parameter (field strength or magnetic moment) increases, the alignment of the needle with the field may become more pronounced. This alignment can affect the entropy distribution along the needle, as shown in **Figure 11**.

Entropy and Bejan profile:

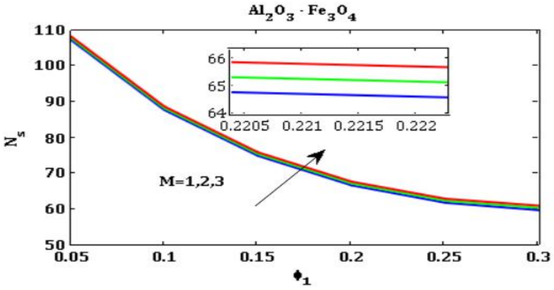

Figure 11. Relationship between M and ϕ_1 on entropy profile.

The relationship between the (*Br*) and (*Re*) determines the behavior of the fluid flow. As the Brinkman number increases, the flow becomes more influenced by viscous forces, leading to an increase in the entropy profile. This is because higher viscous forces result in more energy dissipation and heat generation within the flow. Consequently, entropy which is a measure of the disorder or randomness of a system tends to increase as shown in **Figure 12**.

Entropy and Bejan profile:

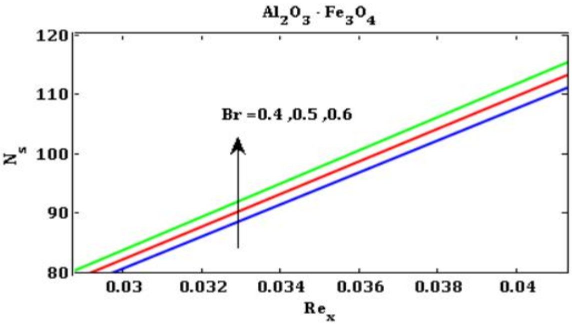

Figure 12. Relationship between Br and Re_x on entropy profile.

Figure 13 explained, the relationship between the (*Br*) and (*M*) determines the behavior of the fluid flow. The Brinkman number represents the proportion of viscous forces to inertial forces. This implies that the fluid flow is more influenced by the viscosity of the fluid. When the magnetic parameter increases, it signifies a stronger influence of the magnetic field on the fluid flow. In the presence of a magnetic field, the fluid may experience additional forces and interactions, such as magnetic induction and Lorentz forces. These forces can alter the flow behaviour and have an impact on the entropy profile.

Entropy and Bejan profile:

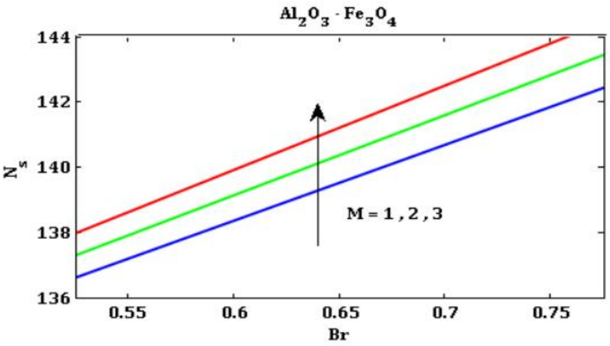

Figure 13. Relationship between Br and M on entropy profile.

The relationship between a magnetic field and a nanoparticle of Al_2O_3, specifically in the context of a horizontal needle, as the magnetic field $M = (1, 2, 3)$, increases, the Bejan number decreases in the case of a horizontal needle with a nanoparticle of Al_2O_3. Since the Bejan number is inversely proportional to the convective heat transfer, an intensification in convective heat transfer caused by the altered flow pattern will result in a decrease in the Bejan number, as shown in **Figure 14**.

Entropy and Bejan profile:

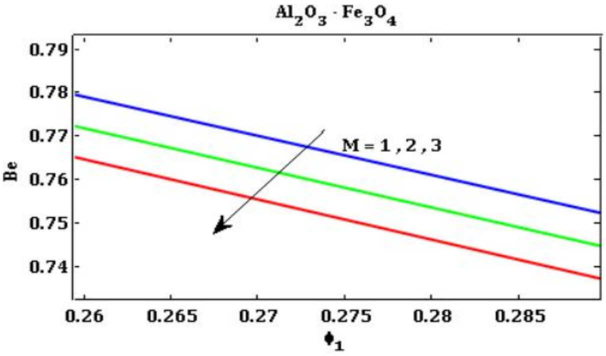

Figure 14. Relationship between M and ϕ_1 on bejan profile.

Figure 15 explained, the relationship between the Brinkman number and the Reynolds number in the context of flow around a horizontal needle, as the Brinkman number ($Br = 0.1, 0.2, 0.3$) increases, the viscous dissipation becomes more significant, leading to a decrease in convective heat transfer and a decrease in the Bejan number.

Entropy and Bejan profile:

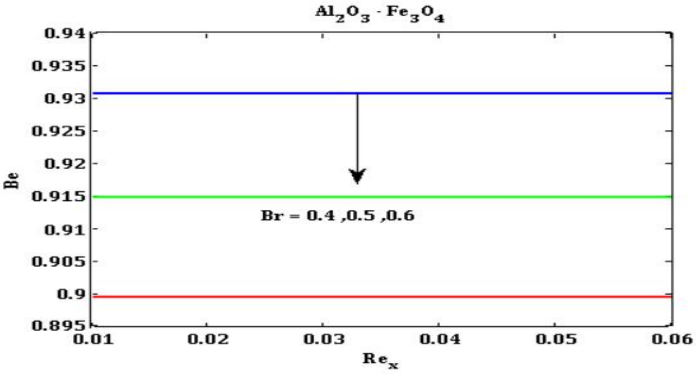

Figure 15. Relationship between Br and Re_x on bejan profile.

The relationship between the Brinkman number and the magnetic field, when the magnetic field $M = (1, 2, 3)$, increases, the convective heat transfer tends to decrease, while the conductive heat transfer may remain relatively unchanged. Consequently, the ratio of heat conduction to convective heat transfer, represented by the Bejan number decreases as explained in **Figure 16**.

Entropy and Bejan profile:

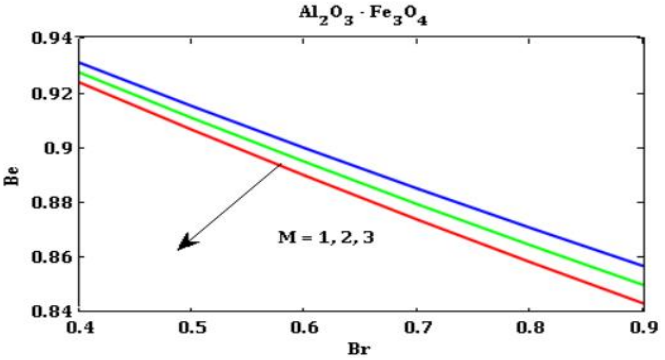

Figure 16. Relationship between Br and M on bejan profile.

Table 2 examined the heat transfer rate and surface drag force for various parameters. The values that appear in the problem through computation are fixed as $\phi_1 = 0.005$, $\phi_2 = 0.015$, $d = 1$, $Pr = 29.45$, $M = 3$, $\delta = 1$, $v_1 = t_1 = 1.5$, $\alpha = 45^o$, $\lambda = 0.5$, $\Omega = 45^o$. Assessment of $f''(\varepsilon)$ and $-\theta'(\varepsilon)$ with the study of Sajja et al.[13] when $\phi_1 = \phi_2 = \delta = 0$ are revealed in **Table 3**, and also it's explained in graphically **Figures 17** and **18**.

Table 2. Disparity of $d, M, \phi_1, \phi_2, Pr, \alpha, \lambda$ on Nu_x and Cf_x.

Nu_x and Cf_x								
d	M	ϕ_1	ϕ_2	Pr	α	λ	Nu_x	Cf_x
1	3	0.005	0.015	29.45	45^0	0.5	1.3892	−92.2282
2							1.3717	−51.7194
3							1.3551	−38.5092
1	1	0.005	0.015	29.45	45^0	0.5	1.3892	−89.5042
	2						1.3892	−90.8821
	3						1.3892	−92.2282
1	3	0.005	0.015	29.45	45^0	0.5	1.3892	−92.2282
		0.010					1.4091	−93.3588
		0.015					1.4292	−94.5255
1	3	0.005	0.015	29.45	45^0	0.5	1.3892	−92.2282
			0.020				1.4073	−92.9950
			0.025				1.4255	−93.8023
1	3	0.005	0.015	1	45^0	0.5	1.1444	−92.1319
				2			1.2317	−92.1868
				3			1.2747	−92.2051
1	3	0.005	0.015	29.45	0^0	0.5	1.3892	−88.0924
					45^0		1.3892	−92.2282
					90^0		1.3892	−92.6414
1	3	0.005	0.015	29.45	45^0	0.5	1.3892	−92.2282
						1.5	1.3892	−92.2273
						2.5	1.3892	−92.2264

Table 3. Assertion of present rankings when volumetric solid fractions (ϕ_1, ϕ_2) and the velocity ratio parameter δ are zero.

	Reference 13 (Sajja)		**Present outcomes**	
ε	$F''(\varepsilon)$	$-\theta'(\varepsilon)$	$F''(\varepsilon)$	$-\theta'(\varepsilon)$
0.1	1.289074	2.441675	1.287564	2.438536
0.01	8.492173	16.306544	8.490543	16.282928
0.001	62.161171	120.55034	62.148128	120.254769

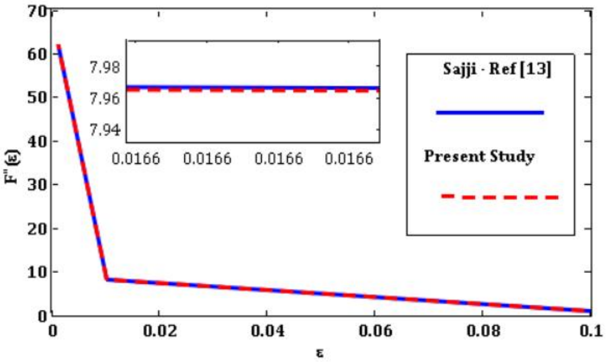

Figure 17. Comparison of $F''(\varepsilon)$[13].

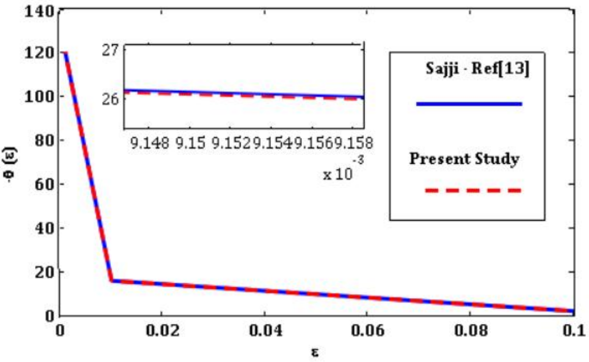

Figure 18. Comparison of $-\theta'(\varepsilon)$[13].

6. Conclusion

Analyzed to this paper, the main things entropy generation in a Magnetohydrodynamic (MHD) slip flow with a hybrid nanofluid over an inclined needle involves investigating the effects of fluid flow, magnetic field, and nanoparticle additives on the thermodynamic performance of the system. This analysis can provide valuable insights into the efficiency and energy losses in the flow, and it is essential for optimizing the design and operation of such systems. The effects of an inclined Lorentz force and entropy generation on the flow of ferrous and aluminium oxide nanoparticles in a hybrid nano liquid with water and ethylene glycol (50:50) as base fluids have been analysed numerically.

- The presence of nanoparticles in the base fluid can significantly enhance heat transfer characteristics, leading to improved thermal performance compared to conventional fluids. The heat transfer rate can be influenced by various factors such as nanoparticle volume fraction, size, shape, and type.
- Effects of magnetic field: the presence of a magnetic field can alter the flow and heat transfer behavior in MHD slip flow. Magnetic fields can induce fluid motion, alter nanoparticle distribution, and affect the heat transfer rate.

- The angle of inclination can influence the flow pattern, boundary layer formation, and consequently, the overall heat transfer and entropy generation.
- The entropy generation rate is given by the product of the local irreversibility and the volume element. The irreversibility term can be calculated based on the flow variables and their gradients.
- The velocity ratio has a higher bearing the thermal profile has been decreased.
- Entropy generation analysis helps quantify the irreversibilities within the system. It provides insights into the energy losses and efficiency of the process.
- The entropy rate increases with increasing the values of Brinkman, Reynolds, and magnetic field criteria.

Understanding MHD and slip flow phenomena is crucial for engineering applications like aerospace, energy, and biomedical fields. Entropy generation analysis optimizes systems for efficiency, reduced energy losses, and cost savings, while energy-related research contributes to sustainable practices and reduced environmental impact. Researchers can optimize MHD systems by considering practical constraints like material properties, manufacturing limitations, and cost, leading to viable engineering solutions. This approach could be applied in nanofluids, advanced materials, and biomedical devices.

Author contributions

Conceptualization, AKAH and SP; methodology, AKAH; software, BG; validation, AKAH, BG and PR; formal analysis, AKAH; investigation, AKAH; resources, GRR; data curation, GRR; writing—original draft preparation, SP; writing—review and editing, SP; visualization, BG; supervision, AKAH; project administration, AKAH; funding acquisition, BG. All authors have read and agreed to the published version of the manuscript.

Conflict of interest

The authors declare no conflict of interest.

Nomenclature

B	Magnetic field intensity, kgs^{-2}a^{-1}
C_f	Skin friction coefficient
C_p	Specific heat, jkg^{-1}k^{-1}
K	Thermal conductivity, wm^{-1}k^{-1}
M	Magnetic parameter
Nu_x	Local Nusselt number
Pr	Prandtl number
q_w	Surface heat flux, wm^{-2}
Re	Local reynolds number
Gr_x	Grashof number
$R(x)$	Equivalence of the surface of a thin needle
F	Dimensionless fluid velocity
T	Temperature of fluid
T_w	Ambient thermal
T_∞	Surface thermal

U	Reference velocity, ms^{-1}
U_w	Constant velocity
U_∞	Free stream momentum
u	Momentum factor in the x way
x, r	Cylindrical directs
Greek letters	
α	Angle
β	Thermal expansion coefficient
ε	The magnitude of the needle (ε = d)
ϕ_1, ϕ_2	Nanoparticles of volume fraction
μ	Dynamic viscosity, kgm^{-1}s^{-1}
υ	Kinematic viscosity, m^{2}s^{-1}
σ	Electrical conductivity, sm^{-1}
ρ	Density, kgm^{-3}
θ	Dimensionless fluid temperature
λ	Mixed convection parameter
δ	Velocity ratio parameter
ψ	Dimensionless stream function
τ_w	Wall shear stress, nm^{-2}
Γ_1	Velocity slip factor
Γ_2	Thermal slip factor
γ_1	Velocity slip coefficient
γ_2	Thermal slip coefficient
Subscripts	
Hnf	Hybrid nanofluid
Nf	Nanofluid
F	Fluid
S	Solid

References

1. Balmforth NJ, Craster RV, Rust AC, Sassi R. Viscoplastic flow over an inclined surface. *Journal of Non-Newtonian Fluid Mechanics* 2007; 142(1–3): 219–243. doi: 10.1016/j.jnnfm.2006.07.013
2. Wong J, Lindstrom M, Bertozzi AL. Fast equilibration dynamics of viscous particle-laden flow in an inclined channel. *Journal of Fluid Mechanics* 2019; 879: 28–53. doi: 10.1017/jfm.2019.685
3. Bano N, Singh BB. An integral treatment for coupled heat and mass transfer by natural convection from a radiating vertical thin needle in a porous medium. *International Communications in Heat and Mass Transfer* 2017; 84: 41–48. doi: 10.1016/j.icheatmasstransfer.2017.03.007
4. Choi SUS, Eastman JA. Enhancing thermal conductivity of fluids with nanoparticles. In: Proceedings of 1995 International Mechanical Engineering Congress and Exhibition; 12–17 November 1995; San Francisco, US.
5. Iqbal Z, Yashodha S, Abdul Hakeem AK, et al. Energy transport analysis in natural convective flow of water: Ethylene glycol (50:50)-based nanofluid around a spinning down-pointing vertical cone. *Frontiers in Materials* 2022; 9: 1037201. doi: 10.3389/fmats.2022.1037201
6. Ganesh NV, Al-Mdallal QM, Reena K, Aman S. Blasius and Sakiadis slip flow of $H_2O–C_2H_6O_2$ (50:50) based nanoliquid with different geometry of boehmite alumina nanoparticles. *Case Studies in Thermal Engineering* 2019; 16: 100546. doi: 10.1016/j.csite.2019.100546

7. Chamkha AJ, Rashad AM, Mansour MA, et al. Effects of heat sink and source and entropy generation on MHD mixed convection of a Cu-water nanofluid in a lid-driven square porous enclosure with partial slip. *Physics of Fluids* 2017; 29(5): 052001. doi: 10.1063/1.4981911
8. Khan WA. Significance of magnetized Williamson nanofluid flow for ferromagnetic nanoparticles. *Waves in Random and Complex Media* 2023. doi: 10.1080/17455030.2023.2207390
9. Khan WA. Impact of time-dependent heat and mass transfer phenomenon for magnetized Sutterby nanofluid flow. *Waves in Random and Complex Media* 2022. doi: 10.1080/17455030.2022.2140857
10. Irfan M, Khan WA, Pasha AA, et al. Significance of non-Fourier heat flux on ferromagnetic Powell-Eyring fluid subject to cubic autocatalysis kind of chemical reaction. *International Communications in Heat and Mass Transfer* 2022; 138: 106374. doi: 10.1016/j.icheatmasstransfer.2022.106374
11. Anjum N, Khan WA, Hobiny A, et al. Numerical analysis for thermal performance of modified Eyring Powell nanofluid flow subject to activation energy and bioconvection dynamic. *Case Studies in Thermal Engineering* 2022; 39: 102427. doi: 10.1016/j.csite.2022.102427
12. Tabrez M, Khan WA. Exploring physical aspects of viscous dissipation and magnetic dipole for ferromagnetic polymer nanofluid flow. *Waves in Random and Complex Media* 2022. doi: 10.1080/17455030.2022.2135794
13. Sajja VS, Gadamsetty R, Muthu P, et al. Significance of Lorentz force and viscous dissipation on the dynamics of propylene glycol: Water subject to Joule heating conveying paraffin wax and sand nanoparticles over an object with a variable thickness. *Arabian Journal for Science and Engineering* 2022; 47: 15505–15518. doi: 10.1007/s13369-022-06658-z
14. Sen SSS, Das M, Nayak MK, Makinde OD. Natural convection and heat transfer of micropolar hybrid nanofluid over horizontal, inclined and vertical thin needle with power-law varying boundary heating conditions. *Physica Scripta* 2023; 98: 015206. doi: 10.1088/1402-4896/aca3d7
15. Waqas M, Khan WA, Ali Pasha A, et al. Dynamics of bioconvective Casson nanoliquid from a moving surface capturing gyrotactic microorganisms, magnetohydrodynamics and stratifications. *Thermal Science and Engineering Progress* 2022; 36: 101492. doi: 10.1016/j.tsep.2022.101492
16. Hussian Z, Khan WA. Impact of thermal-solutal stratifications and activation energy aspects on time-dependent polymer nanoliquid. *Waves in Random and Complex Media* 2022. doi: 10.1080/17455030.2022.2128229
17. Salahuddin T, Akram A, Awais M, Khan M. A hybrid nanofluid analysis near a parabolic stretched surface. *Journal of the Indian Chemical Society* 2022; 99(8): 100558. doi: 10.1016/j.jics.2022.100558
18. Indhumathi N, Ganga B, Charles S, Abdul Hakeem AK. Magnetohydrodynamics boundary layer flow past a wedge of Casson CuO-TiO_2/EG embedded in non-Darcian porous media: Viscous dissipation effects. *Journal of Nanofluids* 2022; 11(6): 906–914. doi: 10.1166/jon.2022.1888
19. Salahuddin T, Akram A, Khan M, Altanji M. A curvilinear approach for solving the hybrid nanofluid model. *International Communications in Heat and Mass Transfer* 2022; 137: 106179. doi: 10.1016/j.icheatmasstransfer.2022.106179
20. Mahdy A, El-Zahar ER, Rashad AM, et al. The magneto-natural convection flow of a micropolar hybrid nanofluid over a vertical plate saturated in a porous medium. *Fluids* 2021; 6(6): 202. doi: 10.3390/fluids6060202
21. El-Zahar ER, Mahdy AEN, Rashad AM, et al. Unsteady MHD mixed convection flow of non-Newtonian Casson hybrid nanofluid in the stagnation zone of sphere spinning impulsively. *Fluids* 2021; 6(6): 197. doi: 10.3390/fluids6060197
22. Chamkha AJ, Armaghani T, Mansour MA, et al. MHD convection of an Al_2O_3–Cu/water hybrid nanofluid in an inclined porous cavity with internal heat generation/absorption. *Iranian Journal of Chemistry and Chemical Engineering* 2022; 41(3): 936–956. doi: 10.30492/IJCCE.2021.136201.4328
23. Salahuddin T, Bashir AM, Khan M, et al. Hybrid nanofluid analysis for a class of alumina particles. *Chinese Journal of Physics* 2022; 77: 2550–2560. doi: 10.1016/j.cjph.2021.11.012
24. Reddy PS, Sreedevi P, Chamkha AJ. Hybrid nanofluid heat and mass transfer characteristics over a stretching/shrinking sheet with slip effects. *Journal of Nanofluids* 2023; 12: 251–260. doi: 10.1166/jon.2023.1996
25. Salahuddin T, Siddique N, Khan M, Chu YM. A hybrid nanofluid flow near a highly magnetized heated wavy cylinder. *Alexandria Engineering Journal* 2022; 61(2): 1297–1308. doi: 10.1016/j.aej.2021.06.014
26. Rashad AM, Chamkha AJ, Ismael MA, Salah T. Magnetohydrodynamics natural convection in a triangular cavity filled with a Cu–Al_2O_3/water hybrid nanofluid with localized heating from below and internal heat generation. *Journal of Heat Mass Transfer* 2018; 140(7): 072502. doi: 10.1115/1.4039213
27. Khan WA, Sun H, Shahzad M, et al. Importance of heat generation in chemically reactive flow subjected to convectively heated surface. *Indian Journal of Physics* 2021; 95: 89–97. doi: 10.1007/s12648-19-01678-2

28. Khan WA, Waqas M, Chammam W, et al. Evaluating the characteristics of magnetic dipole for shear-thinning Williamson nanofluid with thermal radiation. *Computer Methods and Programs in Biomedicine* 2020; 191: 105396. doi: 10.1016/j.cmpb.2020.105396
29. Khan WA, Ali M, Shahzad M, et al. A note on activation energy and magnetic dipole aspects for cross nanofluid subjected to cylindrical surface. *Applied Nanoscience* 2020; 10: 3235–3244. doi: 10.1007/s13204-019-01220-0
30. Khan WA, Ali M, Irfan M, et al. A rheological analysis of nanofluid subjected to melting heat transport characteristics. *Applied Nanoscience* 2020; 10: 3161–3170. doi: 10.1007/s13204-019-01067-5
31. Bejan A. A study of entropy generation in fundamental convective heat transfer. *Journal of Heat and Mass Transfer* 1979; 101(4): 718–725. doi: 10.1115/1.3451063
32. Mansour MA, Siddiqa S, Reddy Gorla RS, Rashad AM. Effects of heat source and sink on entropy generation and MHD natural convection of a Al_2O_3–Cu/water hybrid nanofluid filled with square porous cavity. *Thermal Science and Engineering Progress* 2018; 6: 57–71. doi: 10.1016/j.tsep.2017.10.014
33. Barman T, Roy S, Chamkha AJ. Entropy generation analysis of MHD hybrid nanofluid flow due to radiation with non-erratic slot-wise mass transfer over a rotating sphere. *Alexandria Engineering Journal* 2023; 67: 271–286. doi: 10.1016/j.aej.2022.12.051
34. Khan I, Khan WA, Qasim M, et al. Thermodynamic analysis of entropy generation minimization in thermally dissipating flow over a thin needle moving in a parallel free stream of two Newtonian fluids. *Entropy* 2019; 21(1): 74. doi: 10.3390/e21010074
35. Khan S, Ali F, Khan WA, et al. Quasilinearization numerical technique for dual slip MHD Newtonian fluid flow with entropy generation in thermally dissipating flow above a thin needle. *Scientific Reports* 2021; 11: 15130. doi: 10.1038/s41598-021-94312-3
36. Chamkha AJ, Rashad AM, Armaghani T, Mansour MA. Effects of partial slip on entropy generation and MHD combined convection in a lid-driven porous enclosure saturated with a Cu-water nanofluid. *Journal of Thermal Analysis and Calorimetry* 2018; 132(2): 1291–1306. doi: 10.1007/s10973-017-6918-8
37. Khan WA, Waqas M, Kadry S, et al. On the evaluation of stratification based entropy optimized hydromagnetic flow featuring dissipation aspect and Robin conditions. *Computer Methods and Programs in Biomedicine* 2020; 190: 105347. doi: 10.1016/j.cmpb.2020.105347

Mechanical Engineering Advances 2023; 1(1): 131.
Original Research Article

Theoretical thermal performance of cross-flow finned heat pipe heat exchanger used for air conditioning in surgery rooms

Élcio Nogueira

Department of Mechanic and Energy, State University of Rio de Janeiro, Resende RJ 27537-000, Brazil; elcionogueira@hotmail.com

ARTICLE INFO

Received: 18 July 2023
Accepted: 29 August 2023
Available online: 17 October 2023

doi: 10.59400/mea.v1i1.131

ABSTRACT: The thermal efficiency of heat exchangers was applied for theoretical analysis of the thermal performance of a finned heat pipe heat exchanger (FHPHE) used as an auxiliary device to control the temperature and quality of the air conditioning in operating rooms. The theoretical analysis performed is punctual and distributed. It is divided into three aspects: analysis of the evaporator section, analysis of the condenser section, and analysis of the heat exchanger in terms of overall performance. The distributed procedure contrasts with the theoretical-experimental study, which uses the concept of thermal effectiveness (ε-NTU) for global heat exchanger analysis. The developed approach considers the number of heat pipes, the number of fins, and the flow rate variation at the inlet of the heat exchanger as fundamental parameters for determining the thermophysical quantities of interest. Theoretical values were determined for the average velocities, Nusselt numbers, thermal effectiveness, heat transfer rates, and exit temperatures. The localized theoretical-experimental comparisons are consistent, and the absolute relative error for the global heat transfer rate ranges from 0.5% to 35%.

KEYWORDS: finned heat pipe; heat exchanger; air conditioning; surgery rooms; thermal efficiency

1. Introduction

This work aims to apply the thermal efficiency method to heat exchangers to theoretically analyze temperature control systems in the surgery rooms. The developed procedure is original, punctual, and distributed, contrasting with the design that applies the effectiveness method (ε-NTU) for global heat exchanger analysis. The analysis subdivides the heat exchanger into three regions: the evaporator region (precooling), the condenser region (energy recovery), and the entire system's overall effect for determining the heat exchanger's theoretical air outlet temperature.

Sukarno et al.[1] developed an experimental heating, ventilation, and air conditioning system for the operating room for energy efficiency analysis and heat recovery using a finned heat tube heat exchanger (FHPHE). The heat pipe system, arranged in a staggered configuration, consists of three, six, and nine rows of four pipes. The fresh air inlet temperature varies from 30 °C to 45 °C. In addition to experimental analysis, the authors performed a global theoretical analysis of the heat exchanger using the thermal effectiveness method (ε-NTU). They obtained maximum effectiveness of 62.7% for an inlet temperature equal to 45 °C and a heat exchanger with nine rows, that is, 36 heat pipes. They state that the global ε-NTU method can be used to compare and analyze energy recovery in air conditioning systems and that using heat pipes improves efficiency and reduces emissions.

Hakim et al.[2] investigated the HVAC system using a U-shaped finned heat exchanger to analyze the processes of heating and cooling the air. They present efficiency, coefficient of performance, and dehumidification capacity results in one and two-row heat pipe configurations, with eight pipes per row. They note that the two-line configuration significantly affects precooling and reheating processes more than the one-line configuration. They conclude that the U-shaped heat pipe is a solution for HVAC systems that require air cooling and subsequent heating.

Putra et al.[3] conducted an experimental study with finned heat pipes to investigate heat recovery performance from the exhaust air in an ambient room. The system consists of heat pipes staggered in six lines, with external diameters equal to 13 mm and a length of 700 mm, and water as the working fluid. They analyze the inlet temperature effects, the influence of the number of heat pipelines, and the air inlet velocity. They found that the higher the air temperature at the inlet, the greater the performance of the HPHE, that is, the greater the cooling capacity of the system. Furthermore, economic analysis of system performance showed that energy consumption decreases by 0.6–4.1 GJ/year for eight h/day and 365 days/year of operation.

Barrak[4] reports that energy consumption in tropical countries should increase at a higher rate than in other countries and that energy recovery is one of the alternatives to improve thermal performance. He claims that air conditioning units and the electrical cost to run them account for half the value of energy bills and that energy recovery systems can lower this high cost. He states that heat pipes working as heat exchangers are an excellent alternative for energy recovery and that, in addition, their use can improve the quality of fresh air by decreasing the relative humidity of the air by 10%. It describes heat pipes as very efficient passive elements for heat transfer with minimal temperature differences and no need for pumping. He classifies heat pipes partially filled by the working fluid into traditional (HP), thermosyphon, and oscillating (OHP). However, he reports that the heat and mass transfer mechanisms in oscillating heat pipes (OHP) operation are partially misunderstood.

Stewart et al.[5] developed a refrigeration system emphasizing the details of the finned tube condenser using an optimization algorithm focused on efficiency. The research found that the optimization process makes it possible to determine an ideal condenser with the same performance as a traditional system, which has a cost of 23% higher. Furthermore, the optimized capacitor is demonstrated to satisfy the minimum entropy generation condition.

Nogueira[6] develops a theoretical model for determining the thermal and hydraulic performance of externally finned shell and tube heat exchangers (SFTHE) used in machine oil cooling, including non-spherical nanoparticles in the form of a cylinder. The main parameter used in the optimization process is the number of finned tubes, and the second most important is the number of heat exchanger units connected through clamps. Six finned tubes have cost-effective thermal and hydrodynamic performance despite the high viscous dissipation caused by oil in the annular region. In addition, it was demonstrated that including nanoparticles improves thermal performance, with a slight decrease in the thermodynamic Bejan number.

Górecki et al.[7] present a theoretical-experimental study of a finned heat pipe heat exchanger for small air conditioning systems. The heat exchanger uses R4044 as it is the best working fluid. The staggered arrangement of heat pipes in 20 rows has an effectiveness of 60%. The optimization process determined the configuration to minimize pressure loss. The theoretical-experimental comparison showed a level of agreement of 10%. They conclude that heat pipes with individual fins are an alternative to the heat exchanger of conventional heat pipes. Heat pipes with individual fins withstand more significant pressure differential and are less susceptible to deformation than solid fins; they allow substitution and make cleaning easier.

Jouhara et al.[8] present a comprehensive review of heat pipes: potential applications, construction materials, and available heat pipes' performance. It subdivides the analysis directed to heat pipes into three topics: low-temperature applications, high-temperature applications, and modeling applied to heat pipes. The applications discussed in the article focus on solar, nanoparticles, thermoelectric modules, and other relevant applications. The modeling analysis includes non-Newtonian fluids, nanofluids, and automotive and nuclear systems. Finally, they discuss the limitations of heat pipes and the future perspectives related to their application.

Jouhara et al.[9] conducted theoretical-experimental work to analyze the thermal performance of a multi-pass heat pipe heat exchanger. The objective is to heat water through hot gas (air). They explore the effect of the Reynolds number changing the number of passes by incorporating deflectors and variations in the water flow rate. Experimentally, they found a significant influence of the Reynolds number on the performance of the heat exchanger. They predict the global implementation of the heat exchanger through two basic theoretical models: Log Mean Temperature Difference (LMTD) and Effectiveness Method (ε-NTU). Finally, they report the importance of heat exchangers in recovering residual energy.

2. Methodology

The system under analysis has three sets of heat pipes with 12 pipes each. Each group consists of three rows with four tubes in each row, as shown in **Figure 1a,c**, reported in reference[1]. The heated fresh air enters the pipes where the evaporation section of the heat pipes, called precooling, and a conventional heat exchanger used to keep the operating room air at a temperature between 20 °C and 25 °C are located. The air is sucked from the room through a duct system where the condenser is located, called energy recovery, as shown in **Figure 1b**. Fresh air entering the operating room must not be contaminated with any toxic elements and must be changed at a frequency of 20 to 25 times per hour. The fresh air inlet temperature varies between 30 °C and 45 °C, with a flow rate running between 0.050 kg/s to 0.095 kg/s. The saturation temperature of the working fluid is not specified. Even so, the experimental values presented by the work used as a reference must be lower than 28 °C and higher than 26 °C. For numerical simulation, we used the value of 27 °C. The number of fins used in the evaporator and condenser sections was also not explained. However, the spacing between fins is experimentally defined as 2.0 mm, leading to excessive fins in the evaporator and condenser. The number of fins on the evaporator corresponds to 77 fins, and on the condenser, 96 fins. The theoretical numerical results obtained for these numbers of fins demonstrate an over-dimensioning of the heat exchanger. Despite the increase in thermal performance, it is essential to emphasize that many fins significantly affect viscous dissipation, making the heat exchanger design unfeasible in terms of cost-effectiveness. The thermophysical properties of the air and the working fluid (water) are determined through Equations (2)–(24). The physical quantities relevant to obtaining numerical results are described through Equations (25)–(32).

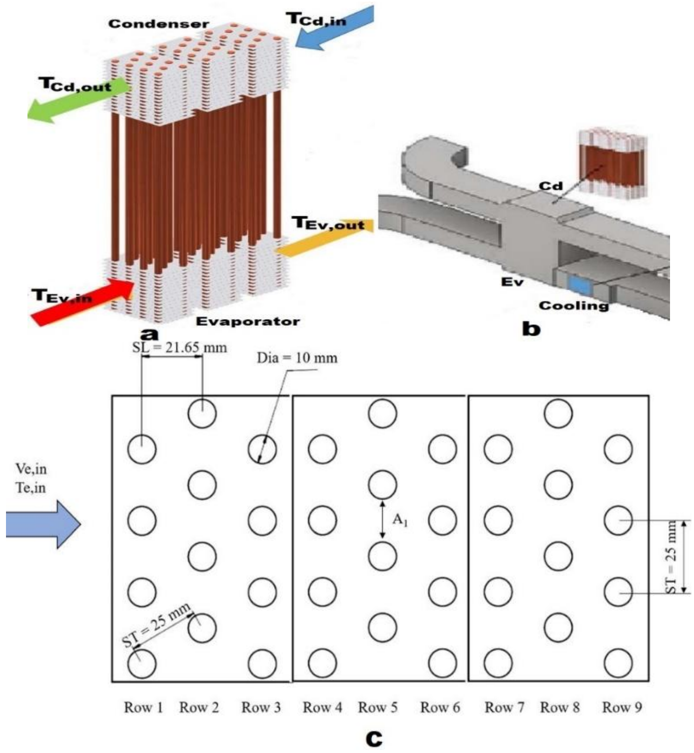

Figure 1. **(a)** represents the set of finned heat pipes[1]; **(b)** represents the evaporator (precooling), conventional cooling, condenser (energy recovery), and air circulation pipes[1]; **(c)** schematically represents the set of finned heat pipes arranged in the heat exchanger shell[1].

$$T_{sat} = 27.0\ ℃\ fixed \tag{1}$$

Equation (1) represents the saturation temperature of the working fluid (water) in the heat pipe.

The properties of the air, dependent on the inlet temperature $Tair_{in}$, can be obtained by the following Equations (1)–(5):

$$k_{air} = 6.91744186\ 10^{-5} Tair_{in} + 0.02462173663 \tag{2}$$

$$\mu_{air} = 1.95483621\ 10^{-5} + 2.735058039\ 10^{-9} Tair_{in} + 2.309587479\ 10^{-10} Tair_{in}^2 - 4.505882353\ 10^{-13} Tair_{in}^3 \tag{3}$$

$$Cp_{air} = 1003.728948 + 0.06727399886 * Tair_{in} + 3.565918367\ 10^{-6} Tair_{in}^2 + 8.222222222\ 10^{-7} Tair_{in}^3 \tag{4}$$

$$\rho_{air} = 1.219135515 - 0.002152770329 Tair_{in} - 3.64047479\ 10^{-7} Tair_{in}^2 + 1.705882353\ 10^{-9} Tair_{in}^3 \tag{5}$$

Equation (2) is represented by thermal conductivity. The dynamic, absolute viscosity of air characterizes Equation (3). The specific heat of air represents Equation (4). The density of air represents Equation (5).

$$\nu_{air} = \frac{\mu_{air}}{\rho_{air}} \tag{6}$$

$$\alpha_{air} = \frac{k_{air}}{\rho_{air} Cp_{air}} \tag{7}$$

$$Pr_{air} = \frac{\nu_{air}}{\alpha_{air}} \tag{8}$$

Equation (8) is represented by the Prandtl number associated with air.

The properties of the working fluid (water) can be obtained by Equations (9)–(15):

$$k_W = 0.5521904762 + 0.002561507937T_W - 1.87202381\ 10^{-5}T_W^2 + 5.902777778\ 10^{-8}T_W^3 \tag{9}$$

$$\begin{gathered} Cp_W = 4217.8 - 3.412833333T_W + 0.109375T_W^2 - 0.0016890625T_W^3 \\ +1.34375\ 10^{-5}T_W^4 - 4.088541667\ 10^{-8}T_W^5 \end{gathered} \tag{10}$$

$$\rho_W = 1002.676071 - 0.06559821429T_W - 0.003582589286T_W^2 \tag{11}$$

$$\begin{gathered} \nu_W = 1.787666667\ 10^{-6} - 5.532222222\ 10^{-8}T_W + 9.827083333\ 10^{-10}T_W^2 \\ -8.965277778\ 10^{-12}T_W^3 + 3.177083333\ 10^{-14}T_W^4 \end{gathered} \tag{12}$$

$$\mu_W = \rho_W \nu_W \tag{13}$$

$$\alpha_W = \frac{k_W}{\rho_W Cp_W} \tag{14}$$

$$Pr_W = \frac{\nu_W}{\alpha_W} \tag{15}$$

The saturation pressure of the working fluid (water) can be obtained through Equation (16):

$$P_{sat} = 216.7691429 - 5.927342857T_{sat} + 0.04774285714T_{sat}^2 \tag{16}$$

The properties of saturated steam are obtained through the Equations (17)–(23):

$$\begin{gathered} \nu_l = 0.001585485714 - 1.831904762\ 10^{-5}T_{sat} + 1.957142857\ 10^{-7} \\ T_{sat}^2 - 6.666666667\ 10^{-10}T_{sat}^3 \end{gathered} \tag{17}$$

$$\rho_l = \frac{1}{\nu_l} \tag{18}$$

$$\nu_V = 21.45466571 - 0.3398517143T_{SAT} + 0.001419714286T_{sat}^2 \tag{19}$$

$$\rho_v = \frac{1}{\nu_v} \tag{20}$$

$$h_l = 2.184 + 4.2124T_{sat} \tag{21}$$

$$h_v = 1.540666667T_{sat} + 2521.596667 \tag{22}$$

$$h_{lv} = h_v - h_l \tag{23}$$

h_{lv} is the latent heat of vaporization.

Equation (24), represented by σ_{Water} and reported by Putra et al.[3], is the surface tension for water:

$$\sigma_{Water} = 0.07275d0\big(1 - 0.002d0(K - 291)\big) \tag{24}$$

where K is saturation temperature in Kelvin.

$$C_{sf} = 0.006 \tag{25}$$

The assumed constant for the surface-fluid combination represents Equation (25). The value 0.006 originally presented by Rhosenow, valid for the copper-water pair, is reported by Jouhara et al.[9].

$$NHP = 12\ default;\ 12 \le NHP \le 36 \tag{26}$$

$$N_{Fin} = 22\ default;\quad 0 \le N_{Fin} \le 30 \tag{27}$$

$$NHP_{byrows} = 4 \tag{28}$$

$$Nrows = \frac{NHP}{NHP_{byrows}},\quad 3 \le Nrows \le 9 \tag{29}$$

The total number of heat pipes in the heat exchanger represents Equation (26). The number of fins $NFin$ considered in the evaporator or condenser is defined by Equation (27). The number of heat pipes per row NHP_{byrows} is defined by Equation (28).

$$Vair_{inlet} = 1.5\ m/s\ default; \quad 1.5 \le\ Vair_{inlet} \le 2.5 \tag{30}$$

$$0.050 \le \dot{m}_{air} \le 0.095 \tag{31}$$

The experimental value of the air velocity at the inlet of the heat exchanger $Vair_{inlet}$ is defined by Equation (30). The mass flow rate of air at the inlet of the heat exchanger $\dot{m}_{air}$ is defined by Equation (31).

The distributed analytical approach is subdivided into the Evaporator, the Condenser, and the global FHPHE.

2.1. The evaporator section of the heat pipe

In the specific case under analysis, the evaporator region is called precooling of the heated fresh air, which enters the pipe before passing through a conventional cooling system. The inlet temperature of heated fresh air varies between 30 °C and 45 °C. The cooled air enters the operating room at a temperature that varies from 20 °C minimum to 25 °C maximum. The air inside the room is changed with a frequency of 20 to 25 times per hour. For this to happen, it passes through the exhaust pipe where the energy recovery system is located, that is, the condensation region of the working fluid of the heat pipe. The inlet flow rate of fresh heated air in the evaporator region varies between 0.050 kg/s to 0.095 kg/s.

$$\dot{m}_{air} = 0.050\ kg/s\ defaut \tag{32}$$

The formulation used to simulate the heat exchange process in the evaporator is established through Equations (33)–(72).

$$TEv_{in} = 30.0\ ℃\ default; \quad 30.0℃ \le TE_{in} \le 45.0℃ \tag{33}$$

The fresh air inlet temperature in the evaporator region, defined by Equation (33), is represented by TEv_{in} .

$$h_{boil} = \mu_l h_{lv} \left(\frac{g(\rho_l - \rho_v)}{\sigma_{water}}\right)^{1/2} \left(\frac{Cp_l}{C_{sf} h_{lv} Pr_l}\right)^3 \Delta T_{sat}^2 \tag{34}$$

The estimated heat transfer coefficient for the boiling process, initially presented by Rohsenow[10] and related by Jouhara et al.[9], is given by Equation (34), represented by h_{boil}.

$$\Delta T_{Evsat} = TEv_{in} - T_{sat} \tag{35}$$

$$D_{ext} = 10.3\ 10^{-3}\ m \tag{36}$$

$$D_{\text{int}} = 10.0\,10^{-3}\ m \tag{37}$$

The outside and inside diameters of the heat pipe are represented by D_{ext} and D_{int} are given by Equations (36) and (37).

$$kW = 380.0 \tag{38}$$

The thermal conductivity of the heat pipe material (Copper), represented by Equation (38), is given by kW.

$$LEv = 160.010^{-3} \tag{39}$$

$$LEv_H = N_{Rows} \frac{LEv}{9.0} \tag{40}$$

LEv Equation (39) illustrates the length of the heat pipe evaporation section and LEv_H, represented by Equation (40), is the shell's width in the evaporator region. Note that it depends on the number of heat pipes and, by hypothesis, is equal to the height of the evaporator section under analysis for nine rows of tubes.

$$t_{Fin} = 0.10510^{-3} \tag{41}$$

$$k_{Fin} = 180.0 \tag{42}$$

The thermal conductivity of the fin material (Aluminium), represented by Equation (42), is given by k_{Fin}.

$$Sp_{Fin} = 7.4\ 10^{-3}\ by\ definition;\ N_{Fin} = \frac{Lev + Sp_{Fin}}{Sp_{Fin} + t_{Fin}} \tag{43}$$

Equation (43) defines the space between fins used in the theoretical model, through which the number of fins for the evaporator can be obtained.

$$C1 = 0.36;\ C2 = 0.84\ for\ NHP = 12; C2 = 0.94\ for\ NHP = 24; C2 = 0.96\ for\ NHP = 36 \tag{44}$$

The thickness of a fin, represented by Equation (41), is given by t_{Fin}. The space between fins, defined through Equation (43), is provided by Sp_{Fin}. $C1$ and $C2$ are adjustment constants to experimental results[1].

$$Dh_{EV} = \frac{4LEv_H LEv}{2(LEv_H + LEv)} \tag{45}$$

$$Re_{Ev} = \frac{4\dot{m}_{air}}{\pi Dh_{Ev}\mu_{air}} \tag{46}$$

The hydraulic diameter of the heat exchanger in the evaporator region is given by Dh_{Ev} Equation (45). The Reynolds number associated with air, represented by Equation (46), is provided by Re_{Ev}.

$$A\,sec_{Ev} = \frac{\dot{m}_{air} Dh_{Ev}}{Re_{air}\,\mu_{air}} \tag{47}$$

Equation (41), represented by $A\sec_{Ev}$, is the effective area occupied by the air in the evaporator.

$$V_{Ev} = \frac{\dot{m}_{air}}{A\,sec_{Ev}\,\rho_{air}} \tag{48}$$

The air velocity in the evaporator, V_{Ev}, is represented by Equation (48).

$$ST = 25.010^{-3} \tag{49}$$

$$SL = 21.6510^{-3} \tag{50}$$

The geometric parameters ST and SL of the heat exchanger (**Figure 1**) are defined through Equations (49) and (50).

$$Vair_{\max} = \frac{ST}{SL - Dext} Vair_{inlet} \tag{51}$$

The maximum experimental speed associated with the heat exchanger, $Vair_{max}$, is represented by Equation (51).

$$Atr_{EvFin} = NFinLEv_H LEv \tag{52}$$

$$Atr_{EvHP} = NHP\pi D_{ext}(LEv - NFinSp_{Fin}) \tag{53}$$

$$A_{EvTotal} = Atr_{EvFin} + Atr_{EvHP} \tag{54}$$

The effective heat transfer area in the evaporator $AEvtr_{HP}$, associated with heat pipes, is established by Equation (53). The effective heat transfer area associated with the fin system, Atr_{EvFin}, and the total heat transfer area, $A_{EvTotal}$, are represented by Equations (52) and (54).

$$Nu_{Ev} = C1C2\,0.71\,\mathrm{Re}_{Ev}^{0.5}\,\mathrm{Pr}_{Ev}^{0.36}\left(\frac{\mathrm{Pr}_{Evair}}{\mathrm{Pr}_{EvSurf}}\right)^{0.25} \tag{55}$$

The Nusselt number for the air, as reported by Jouhara et al.[9], Nu_{Ev} is represented by Equation (55). Pr_{EvSurf} it is the Prandtl number on the surface of the heat pipe.

$$h_{Ev} = \frac{Nu_{Ev} k_{air}}{Dh_{EV}} \tag{56}$$

The convection heat transfer coefficient associated with air in the evaporator, Equation (56), is given by h_{Ev}.

$$mL_{EvFin} = \sqrt{\frac{2h_{Ev}}{k_{Fin} t_{Fin}}} LEv_{H} \tag{57}$$

$$\eta_{EvFin} = \frac{\mathrm{Tanh}(mL_{EvFin})}{mL_{EvFin}} \tag{58}$$

The fin efficiency for the evaporator section is defined through Equation (58) by η_{EvFin}[6].

$$\beta_{Ev} = \frac{Atr_{EvFin}}{A_{Total}} \tag{59}$$

$$\eta'_{EvFin} = \beta_{Ev} \eta_{EvFin} + (1 - \beta_{Ev}) \tag{60}$$

The efficiency associated with the set of fins in the evaporator, weighted by the area of change of the fins η'_{EvFin}, is represented through Equation (60).

$$Uo_{Ev} = \frac{1}{\frac{1}{h_{boil}} + \frac{D_{ext} - D_{int}}{kW} + \frac{1}{\eta'_{EvFin} h_{Evair}}} \tag{61}$$

The global heat transfer coefficient associated with air in the evaporator, Uo_{air}, is given by Equation (61).

$$C_{Air} = \dot{m}_{air} Cp_{air} \tag{62}$$

The heat capacity of the air in the evaporator, C_{Air}, is given by Equation (62).

$$C_{Ev} = C_{air} \tag{63}$$

$$NTU_{Ev} = \frac{Uo_{Ev} A_{EvTotal}}{CEv} \tag{64}$$

The number of thermal units associated with air in the evaporator, NTU_{Ev}, is given by Equation (64).

$$Fa = \frac{NTU\sqrt{1 + C^{*2}}}{2} \quad for\ cross - flow \tag{65}$$

The dimensionless number, called "fin analogy", Fa is represented by Equation (65) as defined by Fakheri[11] and reported by Nogueira and other researchers[6,11,12].

$$\eta_{T} = \frac{tanh(Fa)}{Fa} \tag{66}$$

The thermal efficiency associated with the heat exchanger is η_T[11].

$$\varepsilon_T = \frac{1}{\frac{1}{\eta NTU} + \frac{1 + C^*}{2}} \tag{67}$$

The thermal effectiveness associated with the heat exchanger is ε_T[11].

The heat exchanger's thermal efficiency depends on two fundamental parameters: NTU e $C^* = \frac{C_{min}}{C_{max}}$. For the physical conditions under analysis $C^* = 0.0$. Then[11],

$$Fa_{Ev} = \frac{NTU_{Ev}}{2} \tag{68}$$

$$\eta_{TEv} = \frac{tanh(Fa_{Ev})}{Fa_{Ev}} \tag{69}$$

$$\varepsilon_{TEv} = \frac{1}{\frac{1}{\eta_{TEv} NTU_{Ev}} + \frac{1}{2}} \tag{70}$$

$$\dot{Q}_{Ev} = \frac{C_{Ev} \Delta T_{Evsat}}{\frac{1}{\eta_{TEv} NTU_{Ev}} + \frac{1}{2}} \tag{71}$$

The heat transfer rate between the air and the heat pipe in the evaporating region $\dot{Q}_{Ev}$ is given by the Equation (71).

$$TEv_{out} = TEv_{in} - \frac{\dot{Q}_{Ev}}{C_{Ev}} \tag{72}$$

After passing through the evaporator (precooling), the outlet air temperature is represented through Equation (72).

2.2. The condenser section of the heat pipe

The operating room air conditioning is sucked through the exhaust pipes and passes through the heat pipe condenser region. The saturation temperature of the working fluid is higher than the temperature of the air conditioning, which varies between 20 °C and 25 °C. The heated air leaving the heat exchanger's energy recovery region is directed out of the operating room. The air conditioner's temperature that passes through the exhaust pipe and enters the condenser section is not uniform and has an average value of 22.5 °C. The air conditioning inlet flow in the condenser region varies between 0.050 kg/s to 0.095 kg/s.

The formulation used to simulate the heat exchange process in the condenser is established through Equations (73)–(102).

$$TCd_{in} = 20.0\ ℃\ default;\quad 20.0℃ \le TCd_{in} \le 25.0℃ \tag{73}$$

The air temperature at the condenser inlet, TCd_{in}, is represented by Equation (73).

$$\Delta T_{Cdsat} = T_{sat} - TCd_{in} \tag{74}$$

Equation (74) represents the temperature difference between the condenser's air and the working fluid.

$$LCd = 190.0\ 10^{-3}\ m \tag{75}$$

The length of the condenser section, LCd, is represented through Equation (75).

$$LCd_H = LEv_H \tag{76}$$

The width of the shell LCd_H where the heat pipes are installed is represented by Equation (76).

$$Sp_{Fin} = 7.4\ 10^{-3}\ by\ definition;\ N_{Fin} = \frac{LCd + Sp_{Fin}}{Sp_{Fin} + t_{Fin}} \tag{77}$$

Equation (77) defines the space between fins used in the theoretical model, through which the number of fins for the condenser can be obtained.

$$Dh_{Cd} = \frac{4LCd_H LCd}{2(LCd_H + LCd)} \tag{78}$$

The hydraulic diameter in the region of the capacitor, Dh_{Cd}, is represented by Equation (78).

$$Re_{Cd} = \frac{4\dot{m}_{air}}{\pi Dh_{Cd}\mu_{air}} \tag{79}$$

The Reynolds number of air in the condenser region, Re_{Cd}, is represented through Equation (79).

$$A\,sec_{Cd} = \frac{\dot{m}_{air}Dh_{Cd}}{Re_{Cd}\,\mu_{air}} \tag{80}$$

The airflow area in the condenser, $A\sec_{Cd}$, is given by Equation (80).

$$Atr_{CdFin} = NFinLCd_{H}LCd \tag{81}$$

The heat exchange area associated with the fins in the condenser, Atr_{CdFin}, is established through Equation (81).

$$Atr_{CdHP} = NHP\,\pi D_{ext}(LCd - NFin\,Sp_{Fin}) \tag{82}$$

The heat exchange area of the air with the heat pipes in the condenser, Atr_{CdHP}, is given by Equation (82).

$$A_{CdTotal} = Atr_{CdFin} + Atr_{CdHP} \tag{83}$$

$$h_{Cond} = 0.943[\frac{[\rho_l(\rho_l - \rho_v)h_{lv}gk_W^3]}{(\mu_W LCd\Delta T_{sat})}]^{1/4} \tag{84}$$

The condensation transfer coefficient in the heat pipe, h_{Cond}, is given by Equation (84), as reported in the study of Jouhara et al.[9].

$$Nu_{Cd} = C1C2\,0.71\mathrm{Re}_{Cd}^{0.5}\,\mathrm{Pr}_{Cd}^{0.36}(\frac{\mathrm{Pr}_{Cd}}{\mathrm{Pr}_{CdSurf}})^{0.25} \tag{85}$$

Equation (85) represents the Nusselt number in the condenser Nu_{Cd}, as reported in the study of Jouhara et al.[9].

$$h_{Cd} = \frac{Nu_{Cd}k_{air}}{Dh_{Cd}} \tag{86}$$

Equation (86) represents the convection heat exchange coefficient, h_{Cd}, between the air and the surface of the heat pipe.

$$mL_{CdFin} = \sqrt{\frac{2h_{Cd}}{k_{Fin}t_{Fin}}}LCd_H \tag{87}$$

$$\eta_{CdFin} = \frac{\mathrm{Tanh}(mL_{CdFin})}{mL_{CdFin}} \tag{88}$$

The fin efficiency, η_{CdFin}, is determined through Equation (88)[6,11,12].

$$\beta_{Cd} = \frac{Atr_{CdFin}}{A_{CdTotal}} \tag{89}$$

$$\eta'_{CdFin} = \beta_{Cd}\eta_{CdFin} + (1 - \beta_{Cd}) \tag{90}$$

The efficiency associated with the fin system, weighted by the heat exchange area, is represented by Equation (90).

$$Uo_{Cd} = \frac{1}{\frac{1}{h_{Cond}} + \frac{D_{ext} - D_{int}}{kW} + \frac{1}{\eta'_{CdFin}h_{Cd}}} \tag{91}$$

Equation (91) represents the global heat transfer coefficient.

$$C_{Air} = \dot{m}_{air}Cp_{air} \tag{92}$$

$$C_{Cd} = C_{air} \tag{93}$$

The heat capacity of the air in the region of the condenser, C_{Cd}, is represented by Equation (93).

$$NTU_{Cd} = \frac{Uo_{Cd}A_{CdTotal}}{C_{Cd}} \tag{94}$$

Equation (94) represents the number of thermal units associated with the heat pipes in the condenser region.

$$Fa_{Cd} = \frac{NTU_{Cd}}{2} \tag{95}$$

The dimensionless parameter called "fin analogy" in the condenser region, Fa_{Cd}, is represented through Equation (95).

$$\eta_{TCd} = \frac{tanh(Fa_{Cd})}{Fa_{Cd}} \tag{96}$$

Equation (96) represents the thermal efficiency associated with the condenser[11].

$$\varepsilon_{TCd} = \frac{1}{\frac{1}{\eta_{TCd}NTU_{Cd}} + \frac{1}{2}} \tag{97}$$

Equation (97) represents the thermal effectiveness related to the condenser[11].

$$\dot{Q}_{Cd} = \frac{C_{Cd}\Delta T_{Cdsat}}{\frac{1}{\eta_{TCd}NTU_{Cd}} + \frac{1}{2}} \tag{98}$$

The rate of heat transfer between the air and the heat pipe in the region of the condenser is represented by Equation (98).

$$TCd_{out} = \frac{\dot{Q}_{Cd}}{C_{Cd}} + TCd_{in} \tag{99}$$

The air outlet temperature in the condenser, TCd_{out}, is defined through Equation (99).

2.3. Finned heat pipe crow-flow heat exchanger-FHPHE

The pre-cooling and energy recovery set to form a heat exchanger, with a fresh air inlet with a temperature above 28 °C and a cooled air outlet below 28 °C. The total heat transfer rate in the air conditioning process is equal to the sum of the heat transfer rates in the evaporator and the condenser $\dot{Q}_{Cd}$, according to Equation (100). Equation (101) represents the maximum transfer rate, $\dot{Q}_{Max}$, in the heat exchanger, which C_{min} is the smallest of the thermal capacities of the air involved in the process. Equation (102) represents the heat exchanger's effectiveness in the air conditioning process that passes through the operating room.

$$\dot{Q}_{FHPHE} = \dot{Q}_{Ev} + \dot{Q}_{Cd} \tag{100}$$

$$\dot{Q}_{Max} = C_{\min}(TEv_{in} - TCd_{out}) \tag{101}$$

$$\varepsilon_{FHPHE} = \frac{TEv_{in} - TCd_{out}}{TEv_{in} - TCd_{in}} \tag{102}$$

3. Results and discussion

3.1. The evaporator section of the heat pipe

The evaporator preheats the fresh air that enters the air conditioning system directed to the operating room. The air velocity is measured before it enters the heat exchanger shell, where the heat pipes are arranged. The experimental air inlet velocities in the heat exchanger are 1.5 m/s, 2.0 m/s, and 2.5 m/s. The velocity increases when the air enters the shell because the frontal area suffers a reduction. **Figure 2** presents results for the velocity in the shell as a function of the airflow and the number of fins used in the evaporation tube of the refrigerant fluid. Equations (48)–(51) represent the velocities obtained through the theoretical model and those obtained through the experimental procedure. Velocity increases with the flow rate and decreases with the number of heat pipes as the shell area increases. Therefore, the velocities obtained through the developed model are compatible with experimental results.

Figure 3 shows values for the Nusselt number in the evaporator region as a function of the airflow rate and the number of heat pipes equal to 12, 24, and 36. The Nusselt number grows with the airflow rate decreases with increasing air inlet temperature and the number of heat pipes.

Figure 4 presents results for the number of thermal units associated with the evaporator. The number of thermal units is a critical parameter in theoretical analysis using the thermal efficiency method, the effectiveness method (ε-NTU), or the logarithmic temperature difference method (LMTD). The number of thermal units increases with the number of heat pipes, that is, with the increase in the area available for heat exchange and the increase in the difference between the air inlet temperature and the saturation temperature of the working fluid.

Figure 5 presents results for the global heat transfer coefficient, which decreases with the number of heat pipes and increases with the increase in the air inlet temperature.

The thermal effectiveness in the evaporator region is represented in **Figure 6** as a function of the air inlet temperature, the number of heat pipes, and the airflow rate. The number of fins used in the model is equal to 22. The efficiency increases with the number of heat pipe, decreases with the airflow rate, and suffers a slight variation with the inlet temperature. The experimental values presented through reference[1] are within the range of values obtained through the theoretical model and show a significant growth trend with the number of heat pipes.

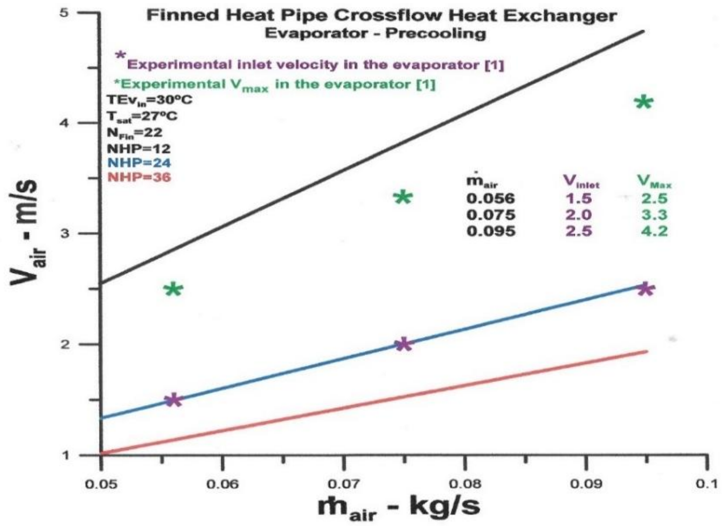

Figure 2. Air velocity versus air mass flow rate.

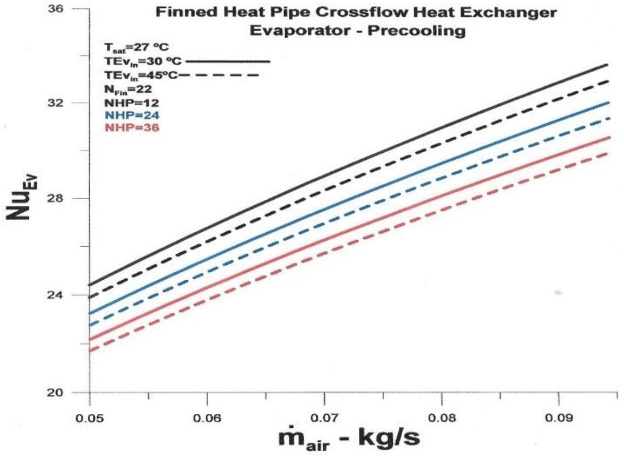

Figure 3. Nusselt number versus air mass flow rate.

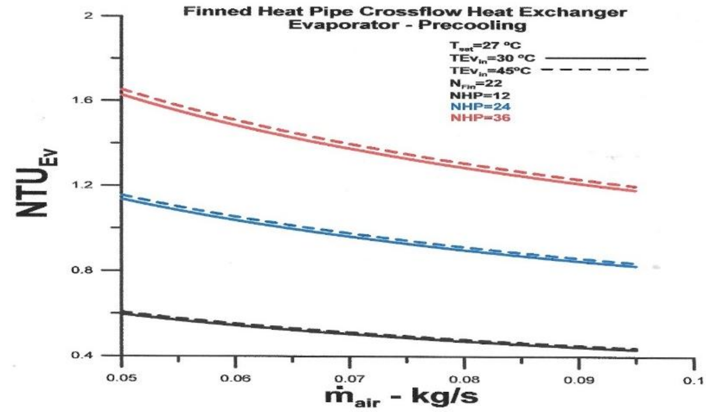

Figure 4. Number of thermal units at the evaporator versus air mass flow rate.

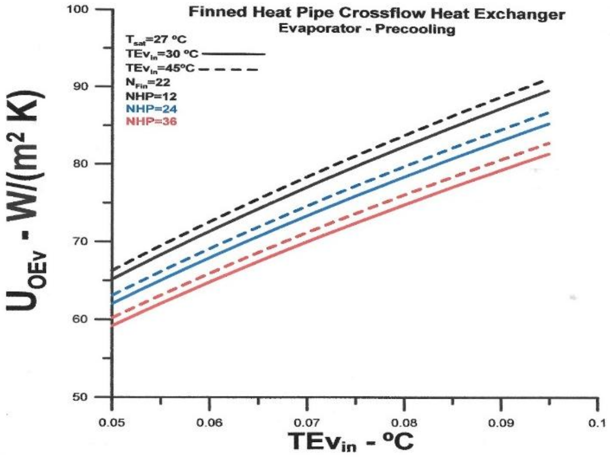

Figure 5. Global heat transfer rate coefficient at the evaporator versus air inlet temperature.

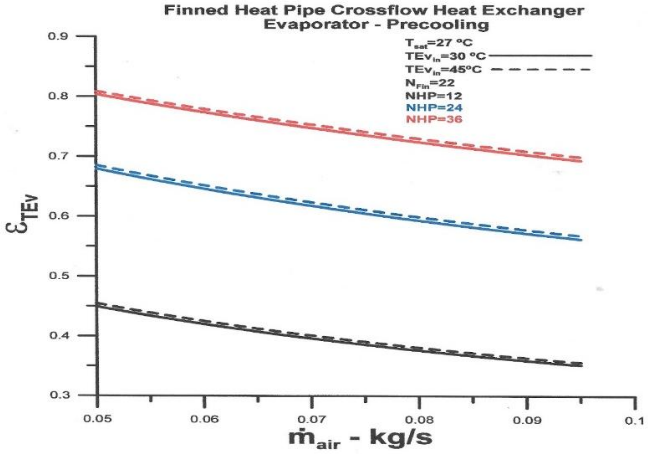

Figure 6. Effectiveness of the evaporator versus number of heat pipes and air inlet temperature.

Figure 7 shows the thermal effectiveness in the evaporator region as a function of heat pipes, airflow rate equal to 0.05 kg/s, and inlet air temperature. Effectiveness increases with the number of heat pipes and air inlet temperature. The theoretical-experimental comparison shows an absolute relative deviation between 2.5% to 22%.

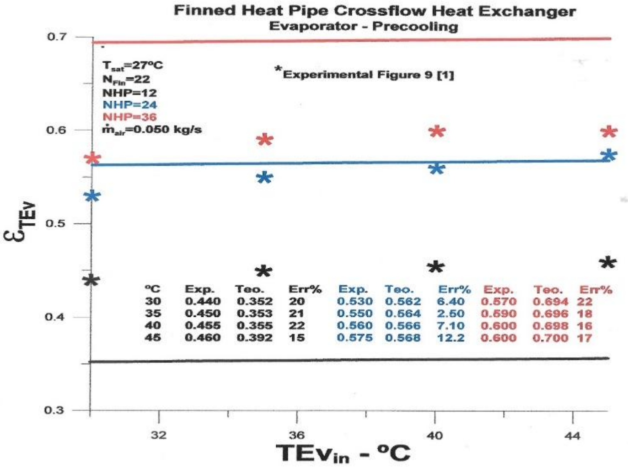

°C	Exp.	Teo.	Err%	Exp.	Teo.	Err%	Exp.	Teo.	Err%
30	0.440	0.352	20	0.530	0.562	6.40	0.570	0.694	22
35	0.450	0.353	21	0.550	0.564	2.50	0.590	0.696	18
40	0.455	0.355	22	0.560	0.566	7.10	0.600	0.698	16
45	0.460	0.392	15	0.575	0.568	12.2	0.600	0.700	17

Figure 7. Effectiveness at the evaporator versus the number of heat pipes and air inlet temperature for mass flowrate equal 0.050 kg/s.

The heat transfer rate in the evaporator is represented in **Figure 8** for heat pipes, mass flow rate, and inlet temperature. The heat transfer rate increases with the number of heat pipes and airflow rate. **Figure 8** demonstrates that the temperature of the air entering the evaporator increases the heat transfer rate since the temperature of the working fluid is constant and equal to 27 °C.

Figure 9 emphasizes the influence of the number of heat pipes, the air inlet temperature, and the air inlet temperature on the heat transfer rate in the evaporator region. The heat transfer rate increases the number of heat pipes and inlet air temperature.

Figures 10 and **11** present results for air outlet temperatures in the evaporator region. **Figure 10** emphasizes the influence of the number of heat pipes and air inlet temperature, and **Figure 11** highlights the impact of the number of heat pipes. The air outlet temperature decreases with an increase in the number of heat pipes. On the other hand, the air inlet temperature increases the outlet temperature since the saturation temperature remains constant. The experimental results presented in reference[1] are within the range of theoretically obtained values with similar qualitative trends. The maximum absolute relative error for the evaporator outlet temperature equals 9.9%, and the minor error equals 0.43%.

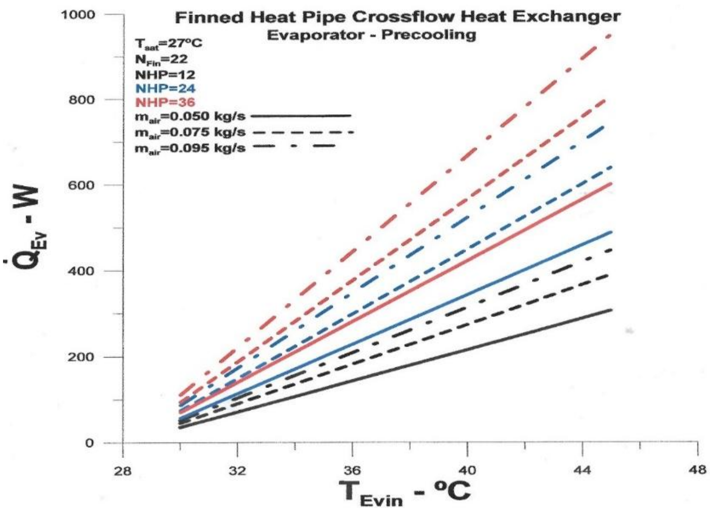

Figure 8. Heat transfer rate at the evaporator versus air mass flow rate and air inlet temperature.

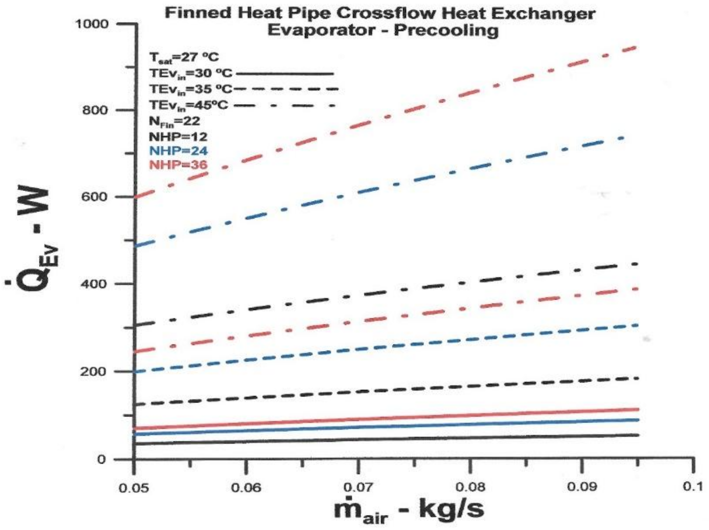

Figure 9. Heat transfer rate at the evaporator versus mass flow rate, number of heat pipes, and air inlet temperature.

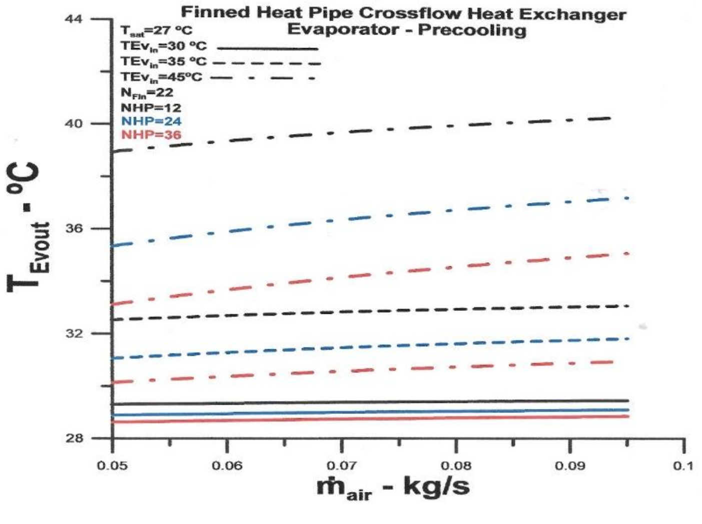

Figure 10. Outlet air temperature at the evaporator versus air mass flow rate, number of heat pipes, and air inlet temperature.

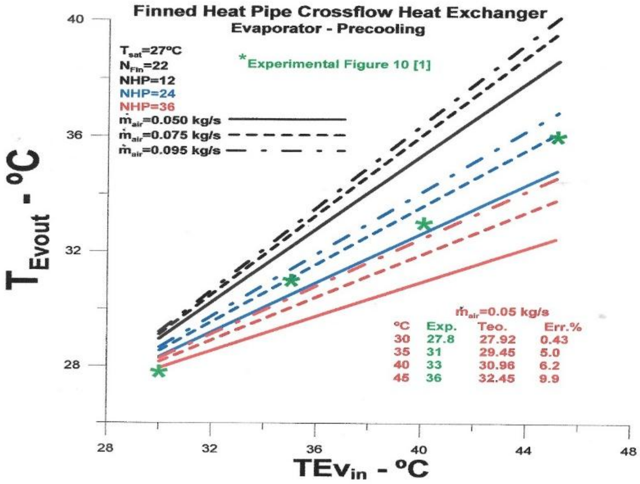

Figure 11. Outlet temperature of the air at the evaporator versus inlet temperature.

The results in **Figures 2–11** demonstrate that the localized theoretical model developed using the concept of thermal efficiency for heat exchangers is consistent in the evaporator region.

The simulations using air inlet temperatures and the number of heat pipes can be used as an instrument for configurations different from those analyzed experimentally. The saturation temperature of 27 °C adopted in the theoretical model proved adequate and consistent with experimental results.

3.2. The condenser section of the heat pipe

Air enters the condenser region at a temperature between 20 °C to 26 °C. As the working fluid condenses, the air is heated and leaves at a higher temperature. The flow rates analyzed are the same for the air in the evaporator, and the fin number equals 25. In this case, the analysis was restricted to the heat transfer rate and outlet temperature, as shown in **Figures 12–15**, because they are the quantities of most significant practical interest.

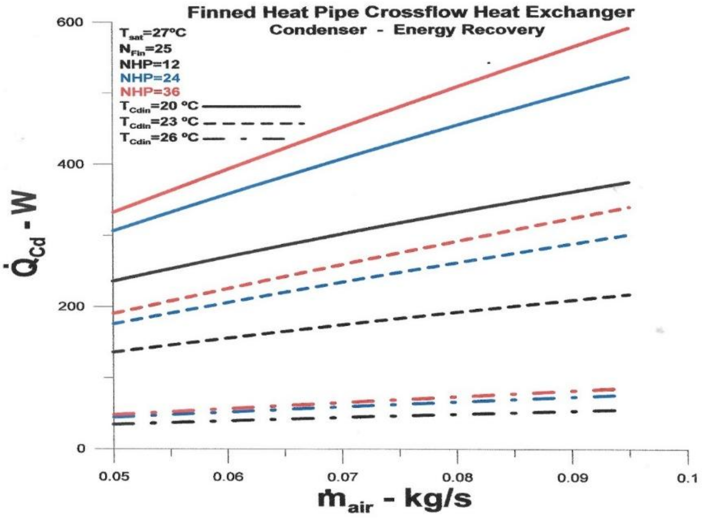

Figure 12. Heat transfer rate at the condenser versus mass flow rate, number of heat pipes, and air inlet temperature.

Figures 12 and **13** present results for the heat transfer rate as a function of the mass flow rate and the air inlet temperature in the condenser, using the number of heat pipes as parameters. It demonstrates that the influence of the air temperature at the condenser air inlet temperature is significant for larger numbers of heat pipes. The heat transfer rate is higher for lower air inlet temperatures due to the more significant temperature difference between the fluids. Higher flow rates for the air present a higher heat transfer rate between the fluids due to the higher thermal capacity.

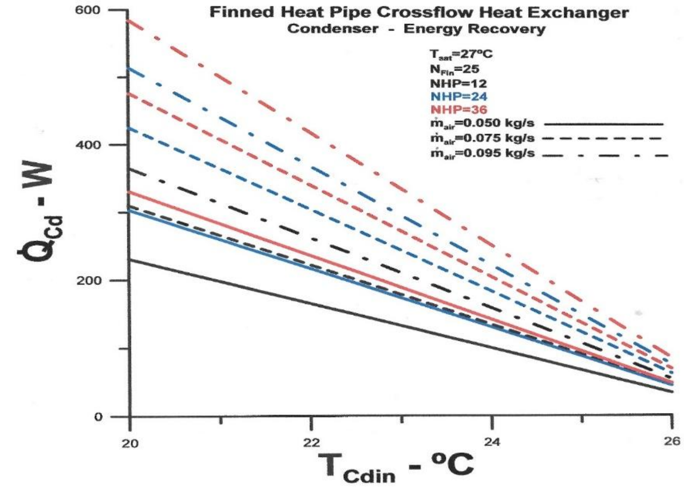

Figure 13. Heat transfer rate at the condenser versus air inlet temperature.

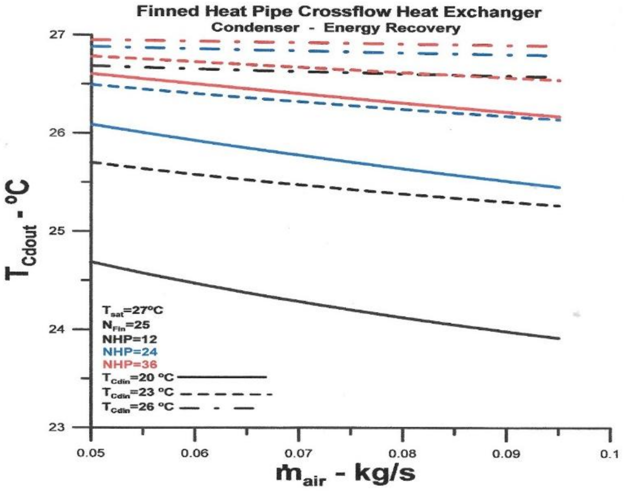

Figure 14. Outlet air temperature at the condenser versus air mass flow rate.

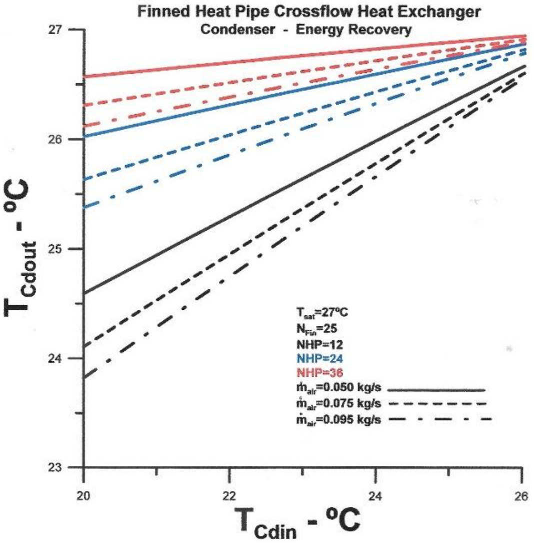

Figure 15. Outlet air temperature at the condenser versus inlet temperature.

The air outlet temperatures in the condenser region, as a function of the inlet temperature, are represented in **Figures 14** and **15**. More significant differences between inlet and outlet temperatures occur for greater numbers of heat pipes. The outlet air temperature is lower for higher air flow rates, as shown in **Figure 15**. The number of heat pipes affects the outlet temperature significantly.

3.3. Finned heat pipe crow-flow heat exchanger-FHPHE

The overall thermal performance of the heat exchanger is shown in **Figures 16** and **17**. The heat transfer rate associated with the heat exchanger equals the sum of the heat transfer rates obtained for the evaporator and condenser, with the temperature difference between evaporator inlet temperature and condenser outlet temperature, as shown in Equations (100) and (101). The global effectiveness is obtained through Equation (102), using the theoretical air outlet temperatures.

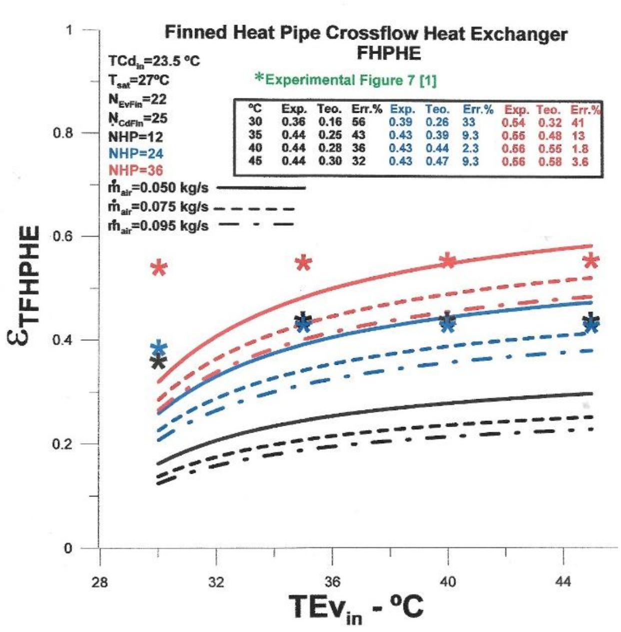

°C	Exp.	Teo.	Err.%	Exp.	Teo.	Err.%	Exp.	Teo.	Err.%
30	0.36	0.16	56	0.39	0.26	33	0.54	0.32	41
35	0.44	0.25	43	0.43	0.39	9.3	0.55	0.48	13
40	0.44	0.28	36	0.43	0.44	2.3	0.56	0.55	1.8
45	0.44	0.30	32	0.43	0.47	9.3	0.56	0.58	3.6

Figure 16. Effectiveness of heat exchanger versus air inlet temperature.

Figure 16 shows the global effectiveness of the heat exchanger as a function of the air inlet temperature in the evaporator. The analysis parameters are the number of heat pipes and air inlet flow rates. Effectiveness increases with increasing air inlet temperature, and the number of heat pipes decreases with increasing flow rate. The experimental results are within the range of theoretically obtained values but show a different qualitative trend. Maximum effectiveness is received for some heat pipes equal to 36 and an inlet temperature equal to 45 °C. The absolute relative error between theoretical and experimental results ranges from 1.8% to 56%.

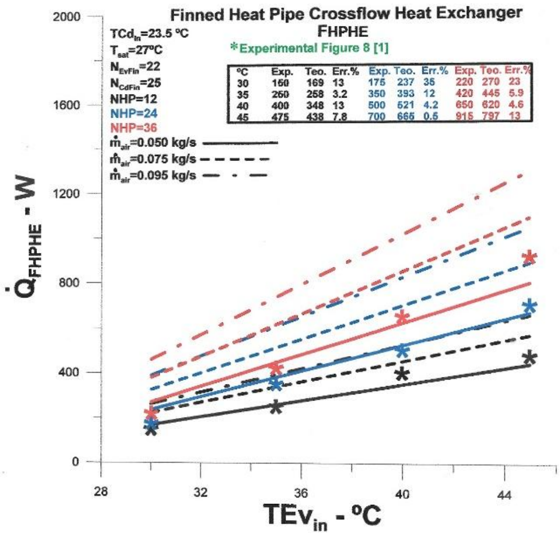

Figure 17. Heat transfer rate of the heat exchanger versus air inlet temperature in the evaporator.

Figure 17 presents results for the overall heat transfer rate for the heat exchanger under analysis, with airflow variation between 0.050 kg/s to 0.095 kg/s and inlet temperature of the air in the condenser equal to 23.5 °C. The heat transfer rate increases with airflow and air inlet temperature. However, the most significant effect on the growth of the heat transfer rate is observed in the variation of the inlet air temperature. Compared with experimental results reported in the study of Sukarno et al.[1], the theoretical results show excellent agreement and demonstrate that the model is consistent and can be used for different temperatures within the temperature range covered by the experiment. The maximum relative absolute error obtained for the heat transfer rate is equal to 35%, and the minimum value is equal to 0.5%. It should be noted that the experimental work used to generate theoretical results does not present error analysis.

In summary, it can be said that, although some basic information is not conveyed in the experimental work that serves as a reference, the theoretical model developed covers a wide range of physical situations with a signed agreement and can be applied in similar or more complex cases, with the necessary local adjustments. Just as the effectiveness method (ε-NTU) is used as an auxiliary tool in the analysis of experimental designs, the thermal efficiency method, with solid foundations based on the "analogy of fins"[11] and the second law of thermodynamics, is a valuable instrument for localized analysis of heat exchangers. One of the advantages of the thermal efficiency method is that tabulated empirical parameters are usually unnecessary, reducing the difficulty in implementation and increasing the reliability of the results.

4. Conclusion

The thermal performance of a heat exchanger with finned heat tubes, used to control the air temperature in the operating room, was analyzed. The heat exchanger under analysis uses the evaporator region as an air pre-cooler and the condenser region as energy recovery. Comparisons were made with experimental results and the global theoretical model (ε-NTU). The local and distributed theoretical model used the concept of thermal efficiency for heat exchangers to determine the thermal quantities of interest.

In summary, the main conclusions reached are:

- Using fins improves thermal performance for the heat exchanger configuration under analysis.

- The theoretical results show excellent consistency and demonstrate that the model can be used for different temperatures within the temperature range covered by the experiment. However, the experimental work does not present an error analysis.
- An excellent experimental and theoretical agreement is observed, which proves that the theoretically developed model with local and distributed parameters is consistent and allows advanced global solutions for the air conditioning system analyzed.

Conflict of interest

The author declares no conflict of interest.

Nomenclature

$Asec$	Cross-section area, $[m^2]$
Atr	Heat transfer area, $[m^2]$
Cp	Specific heat, $[\frac{J}{kgK}]$
C	Thermal capacity, $[\frac{W}{K}]$
C_{min}	Minimum thermal capacity, $[\frac{W}{K}]$
$C^* = \frac{C_{min}}{C_{max}}$	
D_h	Hydraulic diameter, $[m]$
Fa	Fin analogy
h	Coefficient of heat convection, $[\frac{W}{m^2K}]$
k	Thermal conductivity, $[\frac{W}{mK}]$
K	Kelvin
kW	Thermal conductivity of the tube, $[\frac{W}{mK}]$
k_{Fin}	Thermal conductivity of the fin, $[\frac{W}{mK}]$
L	Vertical or horizontal length, $[m]$
$\dot{m}_{air}$	Mass flow rate of the air, $[\frac{kg}{s}]$
N_{Fin}	Number of fins
Nu	Nusselt number
Pr	Prandtl number
$\dot{Q}$	Actual heat transfer rate, $[W]$
$\dot{Q}_{max}$	Maximum heat transfer rate, $[W]$
Re	Reynolds number
T	Temperature, [°C]
Uo	Global heat transfer coefficient, $[\frac{W}{m^2K}]$

Subscripts

boil	Boiling
Cd	Condenser
Cond	Condenser
effect	Effective

Ev	Evaporator
ext	External
HP	Heat pipe
H	Horizontal
in	Inlet
int	Internal
out	Outlet
sat	Saturation
Greek symbols	
α	Thermal diffusivity, $[\frac{m^2}{s}]$
β	The relationship between areas
ρ	Density of the fluid, $[\frac{kg}{m^3}]$
μ	Dynamic viscosity of the fluid, $[\frac{kg}{ms}]$
ν	Kinematic viscosity of the cold fluid, $[\frac{m^2}{s}]$
ε_T	Thermal effectiveness
η_T	Thermal efficiency
ΔT	A difference of temperatures, [°C]
Acronyms	
FHPHE	Finned heat pipe heat exchanger
Ev	Evaporators
Cd	Condenser
NHP	Number of Heat Pipes
N_{Fin}	Number of Fins
Nrows	Number of rows
NTU	Number of thermal units

Reference

1. Sukarno R, Putra N, Hakim II, et al. Multi-stage heat-pipe heat exchanger for improving energy efficiency of the HVAC system in a hospital operating room. *International Journal of Low-Carbon Technologies* 2021; 16(2): 259–267. doi: 10.1093/ijlct/ctaa048
2. Hakim II, Sukarno R, Putra N. Utilization of U-shaped finned heat pipe heat exchanger in energy-efficient HVAC systems. *Thermal Science and Engineering Progress* 2021; 25: 100984. doi: 10.1016/j.tsep.2021.100984
3. Putra NSD, Anggoro T, Winarta A. Experimental study of heat pipe heat exchanger in hospital HVAC system for energy conservation. *International Journal of Advance Science Engineering Information Technology* 2017; 7(3): 871–877. doi: 10.18517/ijaseit.7.3.2135
4. Barrak A. *Heat Pipes Heat Exchanger for HVAC Applications.* IntechOpen; 2021.
5. Stewart SW, Shelton SV, Aspelund KA. Finned tube heat exchanger optimization methodology. In: Proceedings of the 2nd International Conference on Heat Transfer, Fluid Mechanics and Thermodynamics; 23–26 June 2003, Victoria Falls, Zambia.
6. Nogueira E. Thermo-hydraulic optimization of shell and externally finned tubes heat exchanger by the thermal efficiency method and second law of thermodynamics. *International Journal of Chemical and Process Engineering Research* 2022; 9(1): 21–41. doi: 10.18488/65.v9i1.3130
7. Górecki G, Łęcki M, Gutkowski AN, et al. Experimental and numerical study of heat pipe heat exchanger with individually finned heat pipes. *Energies* 2021; 14(17): 5317. doi: 10.3390/en14175317
8. Jouhara H, Chauhan A, Nannou T, et al. Heat pipe based systems—Advances and applications. *Energy* 2017; 128: 729–754. doi: 10.1016/j.energy.2017.04.028

9. Jouhara H, Almahmoud S, Brough D, et al. Experimental and theoretical investigation of the performance of an air to water multi-pass heat pipe-based heat exchanger. *Energy* 2021; 219: 119624. doi: 10.1016/j.energy.2020.119624
10. Rohsenow WM. A method of correlating heat transfer data for surface boiling of liquids. *Transactions of the American Society of Mechanical Engineers* 1952; 74(6): 969–975. doi: 10.1115/1.4015984
11. Fakheri A. Heat exchanger efficiency. *AMSE Journal of Heat and Mass Transfer* 2007; 129(9): 1268–1276. doi: 10.1115/1.2739620
12. Nogueira É. Thermal performance in heat exchangers by the irreversibility, effectiveness, and efficiency concepts using nanofluids. *Journal of Engineering Sciences* 2020; 7(2): F1–F7. doi: 10.21272/jes.2020.7(2).f1

Mechanical Engineering Advances 2023; 1(1): 219.
Original Research Article

Turbine vibration condition monitoring in region 3

Seyed Ali Mousavi[1], **Mohammad Taghipour**[2,*]

[1] *ABA Institute of Higher Education, Qazvin 3441683535, Iran*
[2] *Sohrvardi Institute of Higher Education, Qazvin 4641334147, Iran*
*** Corresponding author:** Mohammad Taghipour, Mohamad.taghipour@srbiau.ac.ir

ARTICLE INFO

Received: 5 September 2023
Accepted: 25 September 2023
Available online: 18 October 2023

doi: 10.59400/mea.v1i1.219

ABSTRACT: The present study aims to investigate the vibration monitoring status in region three of gas transmission operations in Iran. Vibration monitoring is a strong tool for troubleshooting and protecting equipment (turbines). For this purpose, the vibration condition monitoring systems in a gas compression station have been studied. The number and location of vibration sensors, vibration signal transmission to the control room, alarm and stop command, and the ability to perform advanced vibration analysis for troubleshooting and data storage are taken into consideration. The favorable situation of vibration monitoring is provided for the purpose of comparison and conclusions about the status of vibration monitoring and needs have been made.

KEYWORDS: vibration monitoring; gas turbine; maintenance and repair; condition monitoring

1. Introduction

Gas turbines are widely used in various industries, including oil and gas, marine, power generation, aerospace, etc., due to several reasons. High speed, low start-up time, and low power to weight ratio are the main reasons for the use of these machines. Gas turbines have played a significant role in the transmission of natural gas in region three of Iran's gas transmission operations. Today, gas turbines alone have a great role in power generation. Despite all the above-mentioned benefits of using gas turbines, their use at high temperature sometimes leads to the emergence of many problems and costs a lot to repair. Today, long-term use of gas turbines with minimal damage, estimating the remaining life of the various components, especially hot components, as well as their maximum efficiency in different environmental conditions and exploitation of knowledge are problems of these machines.

The status of the implementation of condition monitoring (CM) in gas compression stations is investigated in this study. Gas compression stations include new and old stations. Therefore, the status of the implementation of CM in gas compression stations in the past and present is specified. Cases considered in this study include:

1) Condition monitoring techniques used at the station;
2) Vibrating equipment installed at the station;
3) Vibration analysis used in station;
4) The way of recording vibrations history of turbines;
5) The role of vibration signal in decision-making and planning for repairs.

2. The necessity and importance of research

The use of the maintenance and repair system can play a very important role in reducing the finished price of the final product. But these effects are not only limited to the cost, and the speed of product delivery in the entire supply chain, product quality, reliability, organizational agility and other such factors will also have their own effects, each of which will be a place for reflection. Therefore, it is possible to realize the important role and impact of different maintenance and repair strategies on the business of an economic enterprise. Undoubtedly, in most industrial, production and service units, a large part of the total cost is the repair and maintenance cost. And for this reason, the reforms that take place in this field are short-term. Generally, the main factors that cause abnormal repair and maintenance costs in an industrial unit are: until the improvements are made, the product is not accepted; the downtime related to the timing of repairs and the usual costs of repairs; and maintenance, which are an indication of the organization's need for a repair and maintenance system. If the equipment is not repaired on time, the following factors may occur:

1) Reduce or stop production;
2) Unemployment of human resources directly or indirectly;
3) Delay or stoppage in other production matters in a production line;
4) Creating additional costs;
5) Dissatisfaction and morale destruction of technical and operational staff.

3. Research objectives

In most organizations, preventive maintenance and repair systems need fundamental improvement and optimization. Most maintenance and repair systems are not designed and implemented based on the principles of maintenance and repair management and are formed based on the needs of the time and the needs of the organization little by little, and this issue has caused many of the prominent and key points of the management systems. Preventive maintenance and repairs are neglected. Therefore, for the first step of improvement and optimization, unfortunately, they resort to maintenance and repair software, and a lot of time and energy of the organization is spent on it, and with the passage of time and changes in managers and human resources, the system remains unfulfilled. In this research, the main goal is to improve the status of maintenance and preventive maintenance systems in the area of three gas transmission operations, and this goal is to achieve the following partial goals:

1) Unplanned malfunction of equipment and rework;
2) Prevent parts from being scrapped;
3) Preventing shutdown of production lines and reduction of product;
4) Increasing the quality of repairs and periodic maintenance in the area of three gas transmission operations;
5) Increasing the reliability of the equipment;
6) Reducing the time of repairs and maintenance of equipment in the area of three gas transmission operations.

According to the definitions provided and its wide applications in organizations, the officials of the repair and maintenance unit have not used this concept to improve the performance of the repair and maintenance unit in this area, and in this research, we use the concept of six sigma to improve. We have used the performance of the maintenance and repair unit of the three-gas region so that the officials of this region can compete in the global competitive markets by implementing this method in this region, and it causes cost reduction, high competitiveness, continuous improvement, and increasing the quality and quantity of the product, lack of natural resources and energy, etc.

4. Research background

Taghipour et al.[1] studied "Risk analysis in the management of urban construction projects from the perspective of the employer and the contractor."

Mahboobi et al.[2] discussed "Assessing ergonomic risk factors using combined data envelopment analysis and conventional methods for an auto parts manufacturer", occupational injuries are currently a major contributor to job loss around the world.

Taghipour et al.[3] studied "The impact of ICT on knowledge sharing obstacles in knowledge management process (including case-study)."

Khalilpour et al.[4] studied "The impact of accountant's ethical approaches on the disclosure quality of corporate social responsibility information an Islamic perspective in Iran."

Mirzaie et al.[5] studied "The relationship between social bearing capacities with conflict as a result, in the perception of the visiting historical sites."

Alamdar Khoolaki et al.[6] studied "Effect of integrated marketing communication on brand value with the role of agencys reputation (including case study)."

Taghipouret et al.[7] studied "A survey of BPL technology and feasibility of its application in Iran (Gilan Province)."

Seddigh Marvasti et al.[8] studied "Assessing the effect of the FRP system on compressive and shear bending strength of concrete elements."

Jalili et al.[9] studied "Comparative study of Khaje Rashid al-Din views on Rab-e Rashidi Islamic Utopia and Kevin Lynch ideas."

Taghipour et al.[10] studied "Insurance performance evaluation using BSC-AHP combined technique."

Rezvani et al.[11] discussed "The design of high-rise building with ecological approach in Iran (Alborz Province)."

Taghipour et al.[12] studied "The identification and prioritization of effective indices on optimal implementation of customer relationship management using TOPSIS, AHP methods."

Taghipour and Yazdi[13] studied "Seismic analysis (non-linear static analysis (pushover) and nonlinear dynamic) on Cable-Stayed Bridge."

Taghipour et al.[14] studied "Investigating the relationship between competitive strategies and corporates performance (case study: Parsian Banks of Tehran)."

Taghipour and Moosavi[15] studied "A look at gas turbine vibration condition monitoring in region 3 of gas transmission operation."

Rahmani et al.[16] studied "Providing health, safety and environmental management (HSE) program in metal mining industry (including case study)."

Taghipour and Vaezi.[17] studied "Safe power outlet."

Azarian and Taghipour.[18] studied "The impact of implementing inclusive quality management on organizational trust (case study: educatin)."

Mohammadi et al.[19] studied "Investigating the role and impact of using ICT tools on evaluating the performance of service organizations."

Abdi et al.[20] studied “Predicting entrepreneurial marketing through strategic planning (including case study).”

Khorasani and Taghipour[21] studied “The location of industrial complex using combined model of fuzzy multiple criteria decision making (including case study).”

Taghipour et al.[22] studied “Risk assessment and analysis of the state DAM construction projects using FMEA technique.”

Hoseinpour et al.[23] studied “The problem solving of bi-objective hybrid production with the possibility of production outsourcing through Imperialist Algorithm, NSGA-II, GAPSO Hybid Algorithms.”

Taghipour and Sarchoghaei[24] studied “Evalation of tourist attractions in Bourujerd County with emphasis on development of new markets by using Topsis Model.”

Safdarpour et al.[25] studied “The effect of government support on innovation ability (including a case study).”

Ganjali et al.[26] studied “Strategic analysis of household hazardous waste reduction.”

Taghipour et al.[27] studied “The impact of managerial factors on increasing the productivity of low-level employees (including case study).”

Ganjali et al.[28] studied “Investigating the relationship between environmental awareness and the level of education and occupation of people.”

Baghipour Saramiet et al.[29] studied “Modeling of nurses’ shift work schedules according to ergonomics: a case study in Imam Sajjad (As) Hospital of Ramsar.”

Taghipour et al.[30] studied “The impact of motives from obtaining ISO 9001 certification on organization performance (including case study).”

Molavi and Taghipour[31] studied “A survey on electrical cars advantages.”

Safdarpour et al.[32] studied “The effect of communication on learning ability (including a case study).”

Akbarnezhadbaei et al.[33] studied “Modeling the application of knowledge management system in order to improve the technology governance in the automotive industry of Iran using the data mining environment.”

Molavi and Taghipour[34] studied “An overview of electric vehicle concepts and its features.”

5. Maintenance and repair practices

Maintenance and repair costs in industry are typically 5% to 6% of fixed capital, which reaches 12% in big and heavy industries. Low-quality products should also be added to these costs. Maintenance and repair minimize the total cost by reducing the number of downtimes, stoppages and improving safety.

The industrialists have taken different ways for maintenance and repair. Each of these methods has advantages and disadvantages that can improve or weaken the overall system performance, which is why weak methods are gradually excluded from industrial competition and the old methods of maintenance and repair are employed. Employing advanced methods is essential to achieving sustainable industrial development. The main objective of the changes made to the previous techniques is to reduce maintenance costs, reduce the frequency of stopping the machine (increasing the availability of devices), and identify and fix defects in the machines. Accordingly, the following methods have been used for the maintenance of machines so far:

1) Reactive maintenance;
2) Time base maintenance (TBM);
3) Condition base maintenance (CBM);
4) Proactive maintenance.

6. Condition base maintenance (CBM)

Condition-based maintenance and repair, which is also called predictive maintenance and repair, maintenance and repair based on technical requirements, and contingency maintenance and repair, is the most effective strategy for managing physical assets and is one of the essential elements of RCM besides preventive maintenance (PM), failure finding techniques, redesign, etc. Condition monitoring (CM) tool is used for the establishment and operation of condition based maintenance. In fact, situation or condition monitoring is at the core of this strategy. This strategy is based on the belief that most of the failures of machines and industrial equipment have signs after reaching a certain stage that can be identified in the form of vibration, sound, ultrasonic waves, particle attrition, temperature, and failure can be predicted. Therefore, before reaching a critical stage, the progress of failure can be prevented by planning repair programs and implementing them.

Some of the common techniques in condition monitoring are:

1) The use of the five senses;
2) Vibration analysis;
3) Sound analysis;
4) Ultrasonic analysis;
5) Thermography;
6) Performance analysis;
7) Oil and tribology analysis;
8) The motor circuit analysis and other electrical tests.

The use of predictive maintenance can greatly help reduce maintenance and repair costs. In many productive and administrative activities, maintenance and repair is the most important costly but manageable factor known to increase productivity. According to universally accepted estimates, the cost of maintenance and repair will be reduced to 25% by performing CM programs, while savings resulting from the prevention of reduced production is doubled that is not considered in these estimates.

7. Perspectives in the field of vibration monitoring

What is vibration?

Vibration or mechanical vibrations refer to a kind of dynamical system’s oscillatory movement (reciprocity) that is repeated over a period of time (**Figure 1**).

In its simplest form, this type of movement can be simulated with a mass and a spring. With the induction of a shift in mass attached to a spring and dropping it, oscillation occurs, and its scope can be expressed by a sinusoidal function.

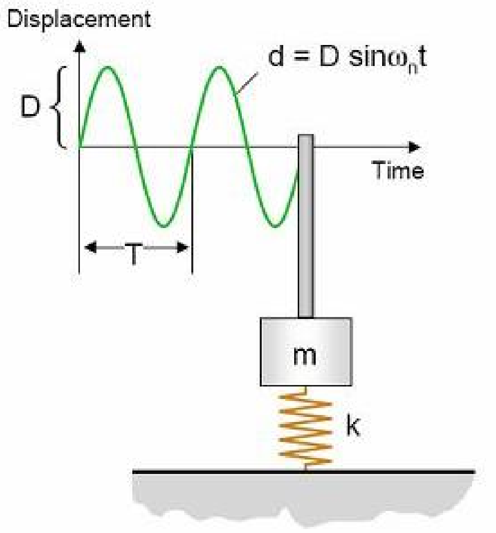

Figure 1. The sinusoidal function of oscillating motion of vibrations.

7.1. Basic concepts of vibration

The important characteristics of vibration include:

- Amplitude, which is a measure of the intensity of vibration.
- Frequency, which is a measure of the rate per unit of time.
- Phase, which is a measure of movement sequence relative to a reference.

Vibration scope can be expressed through three different parameters:

- Displacement;
- Velocity;
- Acceleration.

7.2. What is displacement?

The primary parameter of scope that is about the mass-spring system that gives the position of mass at any moment.

Displacement measurement units:
In the SI system: μm.
In the inch system: mils that is equal to a thousandth of an inch.

7.3. What is velocity?

Velocity is mathematically derived from displacement that shows the rate of change of displacement per unit of time.

Velocity measurement units:
In the metric system: mm/s.
In the inch system: in/s.

7.4. What is acceleration?

Acceleration is mathematically derived from velocity that shows the rate of change of velocity per unit of time.

Acceleration measurement units:

In the metric system: g or m/s2.
In the inch system: g or in/s2.

7.5. The relationship between displacement, velocity and acceleration?

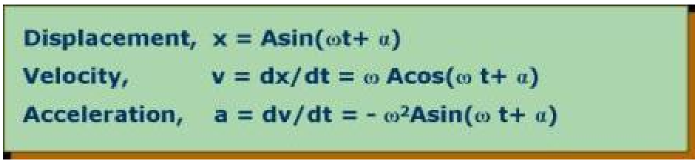

Displacement, $x = A\sin(\omega t + \alpha)$
Velocity, $v = dx/dt = \omega A\cos(\omega t + \alpha)$
Acceleration, $a = dv/dt = -\omega^2 A\sin(\omega t + \alpha)$

In general, the amplitude of each sine wave can be determined in three ways (**Figure 2**):

1) 0–*p* value: zero to peak;
2) *p*–*p* value;
3) Rms value or effective value.

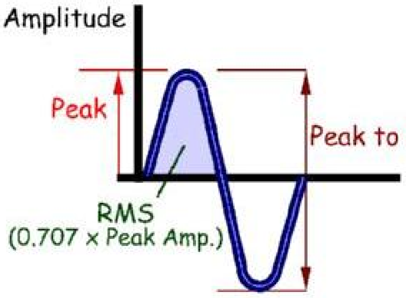

Figure 2. Amplitude of sine wave.

7.6. What is the frequency and phase of the vibrations?

Time period (T) of a movement is a period that repeats its vibrational cycle. The vibration frequency is actually opposite of the period (**Figure 3**).

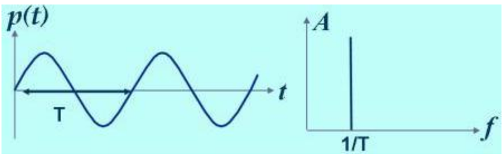

Figure 3. Frequency and phase of vibrations.

Frequency measurement units:
Hertz = 1/s.
cpm = Cycle per minute.
cps = Cycle per second.

Accordingly: 1 Hz = 1 cps = 60 cpm.

Phase is always measured relative to a reference and shows movement sequence relative to that reference.

7.7. Why is it that there is vibration in rotating equipment and machinery?

Generally, there are two types of static and dynamic forces in machines. Vibratory forces are dynamic forces that are created by the existence of shortcomings in the machine. Some of the shortcomings (different from the ideal state) are:

- Design constraints;
- Construction constraints;
- Problems in the initial installation;
- Exploiting problems;
- Failure during repairs;
- And etc.

Since reaching the ideal state is not possible, there is always some vibration on the machines that will be allowed. But with the passage of time and as a result of the subsequent problems, sometimes vibrations increase more than the allowed amount. The situation can be restored to its previous state with analysis and appropriate corrective actions.

The following equation determines the amount of vibration in machine:

$$\text{Vibration} = \text{Vibratory Force}/\text{Impedance}$$

Vibratory forces are usually produced in the car and rotor system (i.e., the rotating section). The impedance is the specification of any mechanical system, including rotating machinery, and describes the vibration transmission path. The vibrations that are normally measured from the static part (stator) of machines, particularly from the bearing housing, are influenced by the two above-mentioned factors. Now these two factors (i.e., the vibratory forces and impedance) are examined separately.

8. Vibratory forces

Some factors causing vibratory forces in the machinery include:

- Misalignment;
- Mass unbalance;
- Abrasion of parts;
- Aerodynamic and hydrodynamic forces;
- Electromagnetic forces;
- Stationary and mobile parts’ contact;
- Friction.

9. Impedance

Mechanical impedance or resistance against the movement is one of the characteristics of mechanical systems that has three components: 1). mass; 2). rigidity; and 3). damping. Some factors intensify vibration without producing any force and only by affecting the impedance. The most important ones are:

- Mechanical looseness;
- Stimulating the natural frequency of components (resonance);
- Weaknesses in the foundation or machine chassis;
- The weakness of the structure.

10. Vibrations as indicator of the status of equipment

Vibrations of rotating equipment (both in terms of amplitude and in terms of other specifications of vibrations) are directly related to its status, and any change, even a minor change, in the status of the equipment (in every respect) will be accompanied by a change in the status of vibrations.

10.1. What is change in the status of equipment?

- Change in terms of equipment utilization.
- Failure (mechanical, electrical, etc.) in equipment.
- Change in the load on the equipment.

Therefore, vibration measurement and analysis are one of the main techniques of condition monitoring of rotating equipment.

10.2. Some of the problems that can be detected through vibration analysis

Some of the problems that can be detected with the help of vibration analysis and analysis of vibration signals in machinery:

1) Mass unbalance;
2) Misalignment;
3) Resonance;
4) Mechanical looseness;
5) Bearing failure;
6) Failure of gear;
7) Eccentricity;
8) The curved shaft;
9) Faulty foundation;
10) Electrical problems;
11) Aerodynamic and hydrodynamic problems;
12) Couplings failure;
13) Belt and pulley problems;
14) Piping problems;
15) Distortion.

The key and important factor for troubleshooting through vibration analysis is that any defect in rotating equipment creates vibrations with their own characteristics (in terms of amplitude, frequency, phase, etc).

11. Processing and information management software

In addition to seismograph devices that are designed for the CM program, specialized software is also offered to connect the system to the computer. The software is used for information management (storage, processing, etc.).

12. Types of vibration meter sensors

Vibration meter sensor is the first device needed for measuring vibrations and is a tool that senses the vibrating movement and converts it to an AC electrical signal proportional to the vibrational motion.

By converting vibrations into an electrical signal, it is possible to store, perform subsequent processes, and also observe signals through electronic devices (data mining equipment).

Some important points about sensors are:

- Sensor type;
- Choosing the correct sensor according to the sensor characteristics (sensitivity, frequency response, dynamic range, measuring range, dimensions, weights, operating temperature, type of

connector, direction of measurement, sensors' feed type);
- Proper installation of the sensor and its cable;
- Positions the sensor and its cable.

The above-mentioned points will be investigated below. First, different types of vibration meter sensors are introduced. In general, according to the working mechanism and main parameters of measurements, vibration meter sensors are classified into three groups:

- Accelerometer;
- Speedometer;
- Displacement meter.

Accelerometers

Accelerometers are made in various types and sizes. There are three types of accelerometers that are:

- Piezoelectric accelerometers;
- Piezoresistive accelerometers;
- Capacitive accelerometers.

Piezoelectric accelerometers are more common and are classified in two compression type and shear type in terms of the impact of vibration on them and production of electrical signal. The main element of this type of accelerometers is made of piezoelectric materials such as quartz or certain types of ceramics. These materials produce electrical signals as a result of stimulation. Schematic of the structure of this kind of sensor can be seen in **Figure 4**:

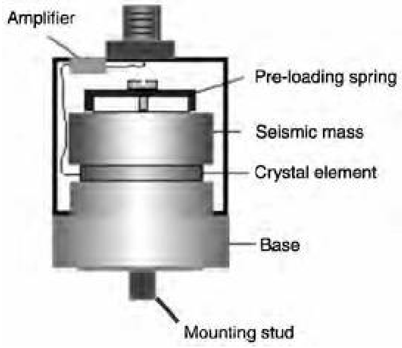

Figure 4. Structure of piezoelectric accelerometer.

As can be seen in the figure, the main components include a mass, crystal material (piezoelectric), a preloading spring, an amplifier, base. This type of configuration is such that the force generated on the piezoelectric material, and thus the electrical signal produced by it is proportional to the acceleration of base. Since the produced signal is usually weak, an internal circuitry is used to amplify the signal. Finally, the sensor output is led toward signal processing devices (data mining devices) through the appropriate cables and can be used for condition monitoring.

Customary vibration analysis methods and techniques for condition monitoring of the machinery. Some of the common techniques of vibration analysis in various applications, especially the issue of condition monitoring and monitoring rotating equipment, include:

- Analysis of the total amount of vibrations;
- Parameters and characteristics of rolling bearings (BCU, BP, Crest factor, *k*-factor, PeakVue, SEE, etc.);
- Analysis of the frequency spectrum (FFT analysis or spectrum);

- Vibration waveform analysis;
- Envelope analysis or vibration signals demodulation;
- Spectrum analysis;
- Analysis of the phase angle;
- Run up and coast down analyses (Bode plot, Nyquist plot, shaft centerline plot, waterfall plot);
- Orbit analysis.

Some of the aforementioned techniques are briefly introduced and then the topic of "detecting common defects in rotating equipment through the frequency analysis of vibration signals and phase angle analysis" is discussed in more detail.

13. Analysis of the total amount of vibrations for condition monitoring

This method is the simplest technique used to assess the condition of rotating machinery. There are different standards for allowable vibration values, including the ISO 10816. It is worth noting that from low to high, normal vibration of the machine occurs in the axial, vertical, and horizontal directions. It is a rule of thumb and may not be true in some cases, but its authenticity has been proven in most cases. However, due to the changes in the pattern, some problems can be easily predicted even without a frequency curve.

13.1. Frequency spectrum analysis (FFT or spectrum analysis) for condition monitoring and troubleshooting

This technique is without doubt one of the most common techniques of vibration signal analysis that is significantly used in condition monitoring and fault diagnosis of rotating machinery (turbines). After some initial processing of vibration signals, the FFT algorithm or fast Fourier transform is used to obtain the frequency spectrum curve. Therefore, the frequency curve is sometimes called FFT curve.

13.2. Vibration waveform analysis and its application for condition monitoring and troubleshooting

Vibration waveform is the vibration signal without almost any processing, which is why it is so important in dynamic analysis of machinery. In fact, some defects such as fractures of gears, defects created by pulses, beat vibrations, and modulation phenomenon are easily detected by analyzing the vibration waveform.

13.3. Analysis of phase angle and its application for detecting the problems of rotating equipment of gas turbine

By comparing the values of the phase angle of vibration at different points and directions of measurement on the machinery or any other structure, a representation of how the various components move relative to each other can be achieved. In some cases, frequency specifications of vibration caused by different faults are quite similar; therefore, the distinction between these defects is not possible only through spectrum curve. In such cases, other vibration signal characteristics such as phase angle are used to separate defects, since despite the similarity of frequency curves (spectrum), phase angle pattern is distinctive for different defects. In general, some of the phase angle applications include:

- Shaft crack detection;
- Dynamic balance;
- Resonance and critical velocity detection;
- Obtaining mode shapes;

- Identifying mass unbalance, misalignment, and curved shaft from each other.

14. Troubleshooting with the help of frequency analysis and spectrum curve in gas turbines

As mentioned in the previous sections, different faults that occur in rotary machinery in gas compressor stations each occur with their own dynamic behavior, or in other words, with a special vibrating feature. One important characteristic of vibration is vibration frequency, and in particular, its relationship with working frequency of the machine (its revolution) in many cases determines the type of fault, or at least, its area.

It should be noted that the measured vibration of the machine is usually a complex signal and a combination of several vibration signals with different frequencies. Frequency analysis, also called spectrum analysis or FFT analysis, is a process of signal processing in which frequency content of vibrational frequency is obtained. In FFT curves, the horizontal axis is frequency, and the vertical axis shows amplitude. As mentioned, in many faults and problems, the frequency of the vibrations is related to the revolution, and in fact, harmonics, or in other words, multiples of machine revolution are seen in FFT curve. These multiples are shown as 1 × RPM, 2 × RPM, 3 × RPM, and so on.

There are many different tables expressing the frequency specifications of common problems. A simplified example can be seen in **Table 1**. As can be seen, the first column shows the kind of problem, the second column shows the related frequencies, and the third column shows the direction with the highest vibration.

Table 1. Frequency specification of common problems of machinery.

Type of the problem	**Frequency and its relationship with revolution**	**The dominant direction and behavior of vibration amplitude**
Mass unbalance	1 × RPM	Radial vibrations with fixed amplitude
Curved shaft	1 × RPM (and 2 × RPM)	High vibration in the axial direction
Rolling element bearing	Quad frequencies of roller bearings	A subtle effect on the overall amplitude of vibration
Journal bearing	1 × RPM	Radial
Misalignment	1~3 × RPM	High radial vibration for offset misalignment and high axial vibrations for angular misalignment
Belt failure	1~3 × Belt RPM	High vibration in the direction of the connection point of the two pulls
Oil whirl	0.42~0.48 × RPM	Unstable vibrations in the radial direction
Gears' problems	Gear mesh frequency (GMF)	Determined according to the prevailing load of the gear (radial or axial).
Structural mechanical looseness	1 × RPM	
Resonance	Specific frequencies of each system	High amplitude vibrations

15. Vibrations' monitoring in the gas compressor station

15.1. The introduction of gas compressor station

Gas compressor station is selected as an example to investigate the status of CM in the country. During the visit to the gas compressor station, six units with a capacity of 25 MW had been exploited. Gas compressor turbines are Siemens, SGT 600.

15.2. Vibration monitoring system

With a glimpse at stations, it can be seen that a lot of attention has been given to the issue of vibrations in the gas compressor station, so that 16 vibration sensors are installed on each unit and vibration signals are brought to control room. Warning and risk values for vibration amplitude are also specified, and in case of high vibration amplitude, alarm or trip command is issued in the control room. Vibration equipment used mainly consists of sensors, cables, connectors, signal processing, acquisition systems, and software processing.

Two acceleration and displacement sensors are used to measure the absolute vibration of bearing shell and the relative shaft vibration in the gas compressor station. Acceleration sensors are Piezoelectric, version CA201, and have been installed on the bearings in the vertical direction. Two acceleration sensors have been installed on each bearing to raise confidence. The installation location of the acceleration sensors on the bearing housing is shown in **Figure 5**.


[redacted]

Figure 5. Location of installing acceleration sensors on the bearing housing.

Displacement sensors used in gas compression stations are of the contact type (Bentley Nevada), 330100-90-05 model. Displacement sensors are mounted on the bearing shell and the tip of the probe is in the vicinity of the shaft. The sensors measure relative displacement of shaft and bearings. The sensor needs an oscillator and demodulator that are installed near it. **Figure 6** shows the location of displacement sensors. In the gas compressor stations, two displacement sensors with ±45 angle to the vertical line are installed on each bearing.

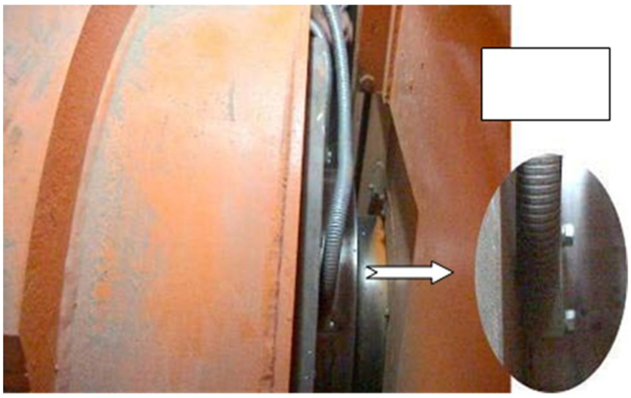

Figure 6. Location of installing displacement sensors on the bearing housing.

15.3. Data acquisition system

To acquire and process the vibration data in gas compressor stations, VM600 system from Vibro-Metr Company is used. VM600 is a complete set used to acquire data, process, protect, and monitor machines. The VM600 system is not fully installed in gas compressor station and only part of it that is related to protection against high vibration is used.

15.4. Software and decision-making system

Vibrating signals and other signals on process are available on the control software in the control room. In the gas compression station, the vibrations are only used for protection. That is, if the vibration signal exceeds a predetermined value, turbine's stop command is issued. Overall amount of vibrations in two-second time intervals is recorded and displayed in the control room. The data is stored in the system for two days and then deleted. Although trend of vibrations is visible within seven days, vibrations are not used for condition monitoring.

Vibratory signals visible in the control room on each gas turbine are as follows:
Two velocity signals (mm/s), which are obtained by integrating the acceleration signal.
A displacement signal (μm peak) equal to the maximum displacement (s).

Vibration protection system of gas compression station is activated with two warnings from the above vibration signals and trip command is issued.

Despite the installation of all required vibration hardware, the vibration spectrum in gas compression station is not available, which is a great problem for this station. In this spectrum, the frequency of the dominant components is seen at frequencies of 50 and 100 Hz. The 50 Hz component corresponds to 1 revolution of shaft (l RPM) and is mainly related to misalignment, and its value (14 μm) is in the allowed limit. The 100 Hz component corresponds to double of the revolution of shaft (2 RPM) and is caused by a lack of alignment, and its value (5 μm) is within the allowed limit. The pattern in the frequency spectrum indicates a healthy condition, and failures will cause a change in it.

16. Summary

A lot of attention has been given to the issue of vibrations in the gas compressor station, so 12 vibration sensors are installed on each turbine. However, vibrations are just seen as protective parameters, and overall, is just taken from among the many pieces of information provided in the vibration spectrum. In the gas compression station, apart from protective system, CM with vibration analysis is not used for high vibrations. Due to the fact that all the vibration sensors are installed in place and the bulk of the hardware required for CM is provided, it seems that the only obstacle to the application of advanced technology for CM in gas compressor station is lack of knowledge rather than the cost of the system. In the gas compressor station, CM systems can be implemented by adding appropriate software and training. The operation is very low cost, and in contrast, it will have a lot of stations. Experience in gas compression station suggests that if they are not aware, benefits of the CM system will not be used despite the high costs and mounting of CM hardware.

Vibration is one of the important parameters to evaluate the status of gas turbine in operation. Manufacturers of gas turbines have monitored this parameter with a view to protecting this system, which is not sufficient for the purposes of maintenance and repairs. For monitoring vibrations in gas turbines, measuring relative and absolute vibration is required. The vibration values of the two measurement models and the relevant locations are provided in ISO standards. Vibrations and vibration status of each machine are often expressed in terms of its overall amplitude that involves all frequencies. The overall amplitude of vibration should be continuously monitored and the status of the machine should be first determined based on it. The maximum amplitude of vibration in turbines and most of the rotary machines happens during the operation revolution. Also, almost all the vibration imperfections have a component in the frequency of operation revolution. In some cases, double function component also contributes to the vibration response. Especially if the measurements are taken in the direction toward generator, these parameters will be observed with a greater amplitude. Amplitude monitoring and the phase of these two components help to determine the exact vibration condition and the type of defects. Gas turbine vibrations are often produced at different frequencies with different amplitudes. Vibration amplitudes bypass the lower blade, and it is necessary to measure them during the process.

One of the most important parameters in determining the status of vibration and type of defects of turbines in journal bearings is measuring air gap from the inner part of the bearing to shaft and also tracing the path of the shaft within the bearing. Due to the installation of two non-contact sensors or motion detectors inside the bearing, movement of the shaft and the air gap can be monitored. Roller bearings are sometimes used in the driver parts. In this case, the software should be capable of processing high signals resulting from the failure of this type of bearing.

Another important issue in monitoring vibrations as well as their processing is a choice of filters. The software should have a variety of different filters to determine the vibration frequency bands. In measuring the vibrations, it should be possible to compare different vibration sensors together. The most important part of the vibration software is Fourier transform. The number of lines in Fourier transform is another important parameter in determining the value of software. With more lines in a fixed band, it is possible to obtain high accuracy in magnification. In measuring the vibrations of gas turbines, different signals are received from different parts with different amplitudes. To realize the importance of the amplitude of the signal, it is required to use signal envelope (envelope spectrum) in some cases, such as signals received from the gearbox or roller bearings. To view the amplitude of all signals with different frequencies and amplitudes, the software must be capable of dividing a Fourier transform diagram into several different frequency bands. This will be done with the use of CPB (constant percentage bandwidth).

17. Conclusion

In this paper, vibration monitoring was studied as a protective and troubleshooting tool and vibration monitoring systems in gas compressor station in region 3 were compared. Vibration monitoring in stations has improved in terms of both the number of sensors and protection. However, the software and decision-making approach based on vibration data have not changed much at stations, and maintenance and repair based on the status of the stations has not found its place yet. Therefore, it seems that there is a need for more education and culture-building in this regard.

In this research, by implementing this method, we were able to reach the following results:

1) By implementing this method, we can reduce various costs, including repair costs.
2) According to the investigations, there are favorable conditions and conditions for the implementation of this system in the region of three gas transmission operations in Iran.
3) There is a significant relationship between the maintenance and repair system and the productivity of the production line employees, and it leads to the productivity and satisfaction of the employees.
4) To improve the system, we should focus and pay more attention on the mechanics group.

Author contributions

All authors contribute to this research.

Funding

This research received no specific grant from any funding agency in the public, commercial or not-

for-profit sectors.

Acknowledgments

We express our gratitude and appreciation for the statements and guidelines of respected professors in the series of industrial engineering, mechanics and industrial management meetings.

Conflict of interest

The authors declare no conflict of interest.

References

1. Taghipour M, Seraj F, Hassani MA, Farahani Kheirabad S. Risk analysis in the management of urban construction projects from the perspective of the employer and the contractor. *International Journal of Organization Leadership* 2015; 4(4): 356–373. doi: 10.33844/ijol.2015.60284
2. Mahboobi M, Taghipour M, Ali Azadeh M. Assessing ergonomic risk factors using combined data envelopment analysis and conventional methods for an auto parts manufacturer. *Work* 2020; 67(1): 113–128. doi: 10.3233/WOR-203257
3. Taghipour M, Mahboobi M, Gharagozlou H. The impact of ICT on knowledge sharing obstacles in knowledge management process (including case-study). *Iranian Journal of Information Processing and Management* 2016; 31(4): 1049–1074. doi: 10.35050/JIPM010.2016.003
4. Khalilpour M, Kamyabi Y, Nabavi Chshmi SA, Taghipour M. The impact of accountant's ethical approaches on the disclosure quality of corporate social responsibility information an Islamic perspective in Iran. *National Academy of Managerial Staff of Culture and Arts Herald* 2018; 1: 1173–1181. doi: 10.32461/2226-3209.1.2018.178689
5. Mirzaie F, Nazari AA, Zargham BH, Taghipour M. The relationship between social bearing capacities with conflict as a result, in the perception of the visiting historical sites. *Journal of Investment and Management* 2015; 4(6): 403–408.
6. Alamdar Khoolaki M, Naami A, Taghipour M. Effect of integrated marketing communication on brand value with the role of agencys reputation (including case study). *Journal of Process Engineering* 2019; 5(11): 30–44.
7. Taghipour M, Safari M, Bagheri H. A survey of BPL technology and feasibility of its application in Iran (Gilan Province). *Science Journal of Circuites, Systems and Signal Processing* 2015; 4(5): 30–40. doi: 10.11648/j.cssp.20150405.11
8. Seddigh Marvasti SMA, Beheshti B, Chegini H, Taghipour M. Assessing the effect of FRP system on compressive and shear bending strength of concrete elements. *International Journal of Innovative Research in Science, Engineering and Technology* 2015; 4(11): 11511–11524. doi: 10.15680/IJIRSET.2015.0411119
9. Jalili L, Ghafourian M, Toopal T, Taghipour M. Comparative study of Khaje Rashid al-Din views on Rab-e Rashidi Islamic Utopia and Kevin Lynch ideas. *International Journal of Archaeology* 2015; 3(5): 39–47. doi: 10.11648/j.ija.20150305.11
10. Taghipour M, Vosough A, Azizi D, Abdi J. Insurance performance evaluation using BSC-AHP combined technique. *National Academy of Managerial Staff of Culture and Arts Herald* 2018; 1: 1158–1166. doi: 10.32461/2226-3209.1.2018.178687
11. Rezvani BA, Ghobadian V, Taghipour D. The design of high-rise building with ecological approach in Iran (Alborz Province). *International Journal of Modern Trends in Engineering and Research* 2015; 2(10): 455–464.
12. Taghipour D, Ganji F, Zolfagharijoo A, et al. The identification and prioritization of effective indices on optimal implementation of customer relationship management using TOPSIS, AHP methods (case study: Pasargad bank). *Management* 2020; 3(4): 43–60. doi: 10.31058/j.mana.2020.34004
13. Taghipour M, Yazdi H. Seismic analysis (non-linear static analysis (pushover) and nonlinear dynamic) on cable-stayed bridge. *American Journal of Civil Engineering* 2015; 3(5): 129–139. doi: 10.11648/j.ajce.20150305.11
14. Taghipour M, Barzegar P, Mahboobi M, Mohammadi S. Investigating the relationship between competitive strategies and corporates performance—Case study: Parsian Banks of Tehran. *Management* 2020; 3(4): 13–28. doi: 10.31058/j.mana.2020.34002
15. Taghipour M, Moosavi SA. A look at gas turbine vibration condition monitoring in region 3 of gas transmission operation. *Journal of Environmental Science, Computer Science and Engineering & Technology* 2020; 9(3): 423–432. doi: 10.24214/jecet.C.9.3.42332

16. Rahamni M, Vaziri Shams S, Abedi V, Taghipour M. Providing health, safety and environmental management (HSE) program in metal mining industry (including case study). *Management* 2021; 4(3): 14–35. doi: 10.31058/j.mana.2021.43002
17. Taghipour M, Vaezi M. Safe power outlet. *Electrical Science & Engineering* 2020; 2(2): 5–10. doi: 10.30564/ese.v2i2.2464
18. Azarian R, Taghipour M. The impact of implementing inclusive quality management on organizational trust (case study: Education). *Journal of Multidisciplinary Engineering Science Studies* 2020; 6(7): 3376–3383.
19. Mohammadi S, Taghipour M, Mahboobi M. Investigating the role and impact of using ICT tools on evaluating the performance of service organizations. *Iranian Journal of Information Processing and Management* 2021; 37(1): 1–26. doi: 10.52547/JIPM.37.1.1
20. Abdi J, Safarian S, Usefi R, Taghipour M. Predicting entrepreneurial marketing through strategic planning (including case study). *Educational Administration Research Quarterly* 2019; 10(39): 127–146.
21. Khorasani Z, Taghipour M. The location of industrial complex using combined model of fuzzy multiple criteria decision making (including case study). *International Journal of Innovation Scientific Research and Review* 2020; 2(7): 268–280.
22. Taghipour M, Sharifzadeh S, Seraj F. Risk assessment and analysis of the state DAM construction projects using FMEA technique. *Trends in Life Sciences an International Peer-Reviewed Journal* 2015; 4(2).
23. Hoseinpour Z, Taghipour M, Beigi JH, Mahboobi M. The problem solving of bi-objective hybrid production with the possibility of production outsourcing through imperialist algorithm, NSGA-II, GAPSO hybrid algorithms. *Turkish Journal of Computer and Mathematics Education* 2021; 12(13): 8090–8111.
24. Taghipour M, Sarchoghaei JA. Evalation of tourist attractions in Bourujerd County with emphasis on development of new markets by using Topsis model. *Science Journal of Business and Management* 2015; 3(5): 175–189. doi: 10.11648/j.sjbm.20150305.16
25. Safdarpour S, Pourkhosravani P, Taghipour M. The effect of government support on innovation ability (including a case study). *Journal of Multidisciplinary Engineering Science and Research* 2023; 2(6): 233–237.
26. Ganjali R, Negaresh Z, Taghipour M. Strategic analysis of household hazardous waste reduction. *International Journal of Educational Foundations and Management* 2023; 11(4): 1–10.
27. Taghipour M, Safdarpour S, Taherian P, et al. The impact of managerial factors on increasing the productivity of low-level employees (including case study). *Management* 2022; 5(2): 16–21. doi: 10.31058/j.mana.2022.52001
28. Ganjali R, Ohadi Digesaraei D, Taghipour M. Investigating the relationship between environmental awareness and the level of education and occupation of people. *International Journal of Educational Foundations and Management* 2023; 11(4): 11–15.
29. Baghipour Sarami F, Bozorgiamiri A, Mououdi MA, Taghipour M. Modeling of nurses' shift work schedules according to ergonomics: A case study in Imam Sajjad (AS) Hospital of Ramsar. *Iranian Journal of Ergonomics* 2016; 4(1): 1–12. doi: 10.20286/joe-04011
30. Taghipour M, Habibi MH, Amin M. The impact of working capital management on the performance of firms listed in Tehran Stock Exchange (TSE). *Journal of Multidisciplinary Engineering Science and Technology* 2018; 7(6): 12146–12154.
31. Molavi A, Taghipour M. A survey on electrical cars advantages. *Progress in Energy & Fuels* 2023; 12(1): 1–14. doi: 10.18282/pef.v12i1.3351
32. Safdarpour S, Pourkhosravani P, Rooholamini V, Taghipour M. The effect of communication on learning ability (including a case study). *Management* 2022; 5(4): 46–54. doi: 10.31058/j.mana.2022.54006
33. Akbarnezhadbaei K, Mohammadi M, Kouloubandi A, Taghipour M. Modeling the application of knowledge management system in order to improve the technology governance in the automotive industry of Iran using the data mining environment. *Journal of Educational Administration Research Quarterly* 2023; 14(55).
34. Molavi A, Taghipour M. An overview of electric vehicle concepts and its features. *International Journal of Educational Foundations and Management* 2022; 11(4).

Mechanical Engineering Advances 2023; 1(1): 258.
Original Research Article

Mechanical properties of polypyrrole/SnO_2 nanocomposites and its LPG sensing application

Md Shakeel Ahmed[1], Ameena Parveen[2,*], Sriram Manjunath[3]

[1] *Department of Physics, Government First Grade College, Hulsoor, Karnataka 585416, India*

[2] *Department of Physics, Government Degree College, Yadgir, Karnataka 585201, India*

[3] *Department of Physics, Government First Grade College, Bellari, Karnataka 583101, India*

*** Corresponding author:** Ameena Parveen, Aparveen981@gmail.com

ARTICLE INFO

Received: 8 October 2023
Accepted: 11 November 2023
Available online: 15 December 2023

doi: 10.59400/mea.v1i1.258

ABSTRACT: Polypyrrole/SnO_2 nanocomposites were created using in-situ polymerization techniques. The nanocomposites were described using scanning electron microscopy (SEM) and transmission electron microscopy (TEM), and their thermal properties were studied using a Differential Scanning Calorimeter (DSC). The DC conductivity of the samples was measured as a function of temperature from 30 ℃ to 1900 ℃, and it was observed that increasing the concentration of tin oxide particles improves conductivity due to polaron hopping and composite chain length extension. The tensile strength of PPy nanocomposites doped in PVA thin film up to 6 wt% indicates 64.2 MPa, which may be related to the homogenous distribution of PPy nanocomposite in PVA. The study reveals that because 50 wt% of the nanocomposites have the highest conductivity and sensitivity, these nanocomposites may be useful in future applications.

KEYWORDS: polypyrrole; scanning electron microscopy; conductivity; sensitivity

1. Introduction

Polypyrrole is a type of conducting polymer that has gained considerable attention and usage in various fields due to its unique properties and applications. This compound has an intriguing structure, exceptional conductivity, and versatility, making it a promising material for use in electronics, energy storage, sensing devices, and even biomedical applications. In this essay, we will discuss the characteristics, synthesis methods, and potential applications of polypyrrole. Polypyrrole is a conjugated polymer consisting of pyrrole monomers linked together through carbon-nitrogen bonds, forming a long chain structure. The presence of alternating single and double bonds along the backbone of the polymer results in the delocalization of electrons, leading to its electrical conductivity. Additionally, the polymer can be doped with various salts or acids to enhance its conductivity further. Polypyrrole also exhibits good mechanical flexibility and stability, making it ideal for various applications[1–4]. Due to their unusual mix of electrical and optical properties and processing advantages, Alan J. Heeger and Hideki Shirakawa conducted extensive research on the new generation of "synthetic metals" in 1976[5]. The electrical conductivity of conjugated polymers is achieved through the delocalization of the electrons, which allows charge mobility along the polymer chain's backbone. Conducting polymers have been synthesized using an oxidizing or reducing method, as well as chemical or electrochemical doping[6–8].

The synthesis of polypyrrole involves two main methods: chemical and electrochemical polymerization. In the chemical method, oxidative polymerization is carried out using an oxidizing agent, such as ferric chloride, in the presence of pyrrole monomers. This process typically occurs in a solvent or in an aqueous solution, resulting in the formation of a black, insoluble powder. On the other hand, electrochemical polymerization involves the electrodeposition of polypyrrole onto an electrode surface. This method offers better control over the polymerization process, as the reaction occurs at a lower temperature and allows for the preparation of thin films[9–12]. Due to its electrical conductivity, polypyrrole has found extensive use in organic electronics. It serves as a highly efficient electrode material in various electronic devices, such as supercapacitors, batteries, and solar cells. The conductive nature of polypyrrole allows for excellent charge transport, ensuring improved performance in energy storage and conversion devices. Additionally, polypyrrole is also being explored for use in gas sensors, as its conductivity changes in the presence of different gases, making it suitable for detecting toxic or hazardous substances[13].

One of the key advantages of tin oxide is its high sensitivity towards reducing gases such as carbon monoxide and methane. When exposed to these gases, tin oxide undergoes a chemical reaction that results in a change in its electrical conductivity. This change can be measured and used to detect the presence and concentration of the target gas[14]. Furthermore, tin oxide sensors are known for their low cost and ease of fabrication. They can be produced using simple techniques such as screen printing or thin film deposition, making them suitable for large-scale production. Additionally, tin oxide sensors exhibit good stability and long-term reliability, making them suitable for continuous monitoring applications[10]. In recent years, researchers have been exploring ways to enhance the performance of tin oxide sensors by modifying their structure and composition. For example, doping tin oxide with other metal oxides or nanoparticles can improve its selectivity for specific gases or chemicals. Additionally, nanostructuring tin oxide films can increase their surface area, leading to improved sensitivity. To begin with, the synthesis of polypyrrole-tin oxide nanocomposites can be achieved through various methods. One common method involves the chemical deposition of polypyrrole onto the surface of tin oxide nanoparticles. This can be done by oxidative polymerization of pyrrole monomers in the presence of tin oxide nanoparticles, resulting in the formation of a conductive polymer layer on the nanoparticles. Another method involves the in-situ polymerization of pyrrole in the presence of tin oxide nanoparticles, where the nanoparticles serve as a template for the growth of polypyrrole. These synthesis methods can be further modified and optimized to control the size, shape, and composition of the nanocomposites, enabling fine-tuning of their properties[15].

Once synthesized, polypyrrole-tin oxide nanocomposites exhibit several enhanced properties compared to their individual components. Firstly, the incorporation of tin oxide nanoparticles into the polypyrrole matrix enhances the electrical conductivity of the nanocomposites. This is attributed to the high electron mobility and good charge transfer ability of tin oxide nanoparticles, which facilitate efficient charge transport within the nanocomposites. Additionally, the presence of polypyrrole in the nanocomposites provides improved mechanical properties, stability, and processability, making them suitable for various applications[16,17].

2. Experimental

2.1. Synthesis of tin oxide nanoparticles

Analytical Reagent grades of $SnCl_4.5H_2O$ and ethanol were successfully used to make tin oxide nanoparticles. To begin, a transparent sol solution was made by dissolving 3.50 gm. of tin chloride pentahydrate in 100 mL ethanol while swirling dynamically. Drop by drop, 4 mL of aqueous ammonia solution was added to the aforementioned solution under steady stirring. For purification, the gel was filtered and washed with ethanol before being dried for 4 h at 60 °C. The resultant powder was calcined for 2 h at 400 °C, yielding ash-colored tin oxide nanoparticles[18–20].

2.2. Synthesis of PPy-SnO_2 nanocomposites

1M aniline solution dissolved in 100 mL of HCl was placed in a 1000 mL beaker and agitated for 5 min before adding 0.5 g (10 wt%) of SnO_2 nanoparticles and stirring with a magnetic stirrer for around 15 min before adding ammonium per sulphate drop by drop. Even after the ammonium per sulphate was completely added, stirring was continued for another 10 min, and the precipitate was allowed to settle for 30 min–40 min. To remove contaminants, the precipitate was filtered and washed numerous times with distilled water. Finally, the precipitate was rinsed with acetone and allowed to dry at room temperature before being ground for 15 min with a mortar and pestle. In the same manner, nanocomposites with 10, 20, 30, 40, and 50 wt% of SnO_2-doped polypyrrole were prepared[21].

3. Preparations of pellet

The powders of polypyrrole and polypyrrole/SnO_2 nanocomposites generated from the synthesis processes outlined earlier were crushed and finely processed in an agate mortar in the presence of an acetone medium. The powder is then squeezed in a hydraulic press to generate pellets with diameters of 10 mm and thicknesses ranging from 1 mm to 2 mm. To improve connections, the pellets of polypyrrole and its metal oxide nanocomposites are covered with silver paste on both sides of the surfaces for temperature-dependent conductivity and sensor experiments[22].

4. Characterizations

The surface morphology of the prepared nanocomposites was examined in powder using a scanning electron microscopy (SEM) Model-EVO-18 (Special Edison, Zeiss, Germany), a transmission electron microscope (TEM), and a differential scanning calorimetry (DSC) instrument: DSC Q20 V24.10 Build 122. Mechanical properties studies were carried out by a Universal Testing Machine (UTM), and through a GPIB interface controlled by a home-made protocol developed in LabView 7.0, stress-strain data is gathered and saved in a data file. The DC conductivity of these nanocomposites was investigated using a Keithley 6514 electrometer, and the sensing capabilities of these nanocomposites were investigated using a laboratory setup.

5. Results and discussion

5.1. Scanning electron microscopy

The scanning electron microscopic image provides valuable insights into the morphology and structure of these nanocomposites. Nanoparticles of tin oxide show in **Figure 1(a)** that the particles are spherical in shape, industrial, and not aggregated with a size of 68 nm. **Figure 1(b)** shows that the SEM morphologies of 30 wt% nanocomposite are highly agglomerated and irregular in shape, and nanoparticles are embedded within the polypyrrole matrix. As observed in the SEM images in **Figure 1(c,d)**, PPy has a typical cauliflower-like or tumour-like form. The presence of SnO_2 in the nanocomposites with a uniform spherical shape provides space factors for PPy orderly growth, resulting in a unique PPy morphology. The particle size of the PPy/SnO_2 nanocomposite is significantly smaller than that of PPy. As a result, the SEM data show that the reactions are astonishingly successful for PPy functionalization[23–25].

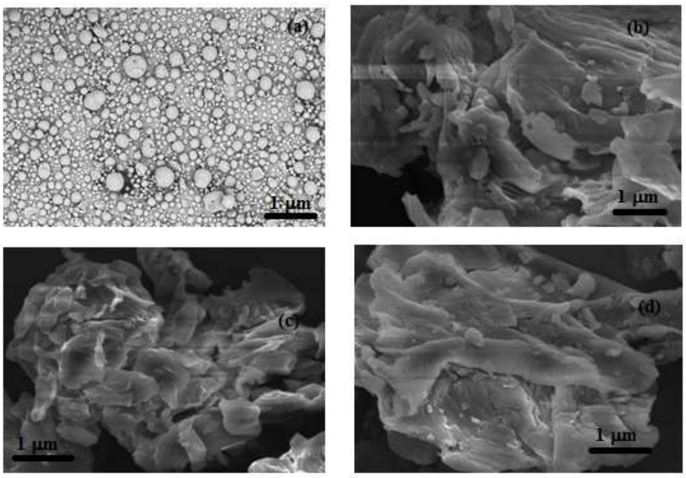

Figure 1. (a) shows a scanning electronic micrograph image of pure polypyrrole and **(b–d)** PPy/tin oxide nanocomposites of 10, 30, and wt%.

5.2. Differential scanning calorimetry

Figure 2 shows the DSC curve of the PPy and PPy/dopant samples with a broad typical endothermic drop, indicating the glass transition temperature of polypyrrole at 99 °C. The shape of the curve suggests that water loss overlaps with the polymer Tg. The incorporation of nanoparticles into polypyrrole matrices has shown significant improvements in their electrical conductivity and mechanical strength. However, understanding the thermal behaviour of these nanocomposites is crucial for their successful integration into practical devices. The absence of any shoulder or melting peak beyond this region shows that the PPy molecules are amorphous and have less sequence. In the case of polypyrrole nanocomposites, DSC can provide valuable insights into their thermal stability and compatibility with other materials. The presence of nanoparticles may affect the polymer's crystallinity or induce changes in its molecular structure. These alterations can be detected through shifts in peak temperatures or changes in enthalpy values observed in DSC curves.

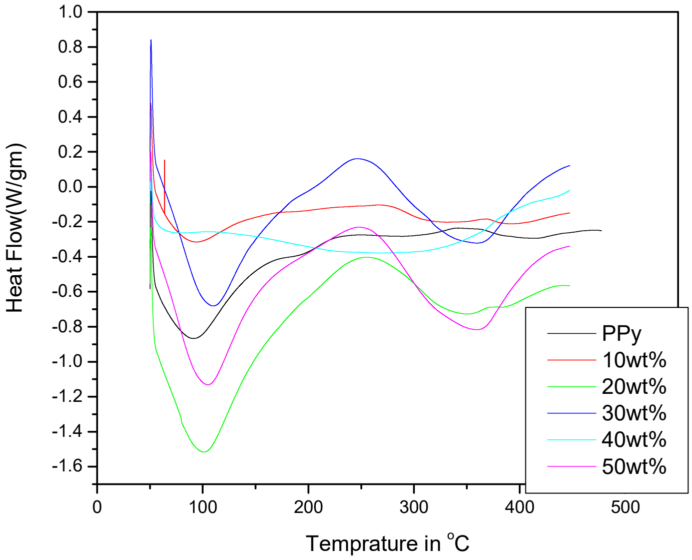

Figure 2. DSC curve against temperature of polypyrrole and PPy/SnO_2 nanocomposites.

Moreover, DSC can also help optimize processing conditions for fabricating polypyrrole nanocomposites by providing information about curing temperatures or reaction kinetics during synthesis. At high temperatures around 100 °C, the DSC curve of the 20 wt% of PPy/SnO_2 nanocomposite trace displays a severe fall. This sharpness means that the crystalline is better. It also features a few more inflection points, one from 330 °C to 360 °C due to the melting of the PPy chain and the other at 360 °C to 400 °C due to phase transition[26–29].

6. DC conductivity

The DC conductivity of polypyrrole tin oxide nanocomposites can be attributed to several factors. Firstly, the presence of tin oxide nanoparticles within the polypyrrole matrix provides additional pathways for electron conduction. These nanoparticles act as conductive bridges, allowing for the efficient transfer of electrons through the material. As a result, the overall conductivity of the nanocomposite increases.

Secondly, the morphology of the nanocomposite plays a crucial role in determining its DC conductivity. The dispersion of tin oxide nanoparticles within the polypyrrole matrix should be uniform to ensure a continuous network of conducting pathways. Achieving this uniform dispersion is a challenging task, as nanoparticles tend to agglomerate, leading to poor conductivity. However, various synthesis techniques, such as in-situ polymerization and electrochemical deposition, have been employed to overcome this challenge and enhance the DC conductivity of the nanocomposite. The temperature-dependent DC conductivity of polypyrrole and polypyrrole/SnO_2 nanocomposites measured at the temperature range of 30 °C to 190 °C, as shown in **Figure 3**. It is observed that the conductivity of the polypyrrole nanocomposites increases with an increase in temperature. The conductivity values of the composites studied are clearly higher than those of pure PPy. The conductivity increases continuously with temperature up to a transition point, indicating semiconductor properties. Temperature increases conductivity due to the migration of charge carriers (polarans) from one localized state to another. The conductivity of 50 wt% of all nanocomposites is higher, indicating that conductivity is determined not only by ion mobility (SnO_2) but also by charge carrier hopping. The conductivity is proportional to it and follows an expression of the type[30,31]:

$$\sigma\,(T) = \sigma_0 \exp\,[-T_0/T)^{1/4}]$$

where σ is the conductivity, T is the applied temperature, and σ_0 is the conductivity at the characteristic initial temperature T_0.

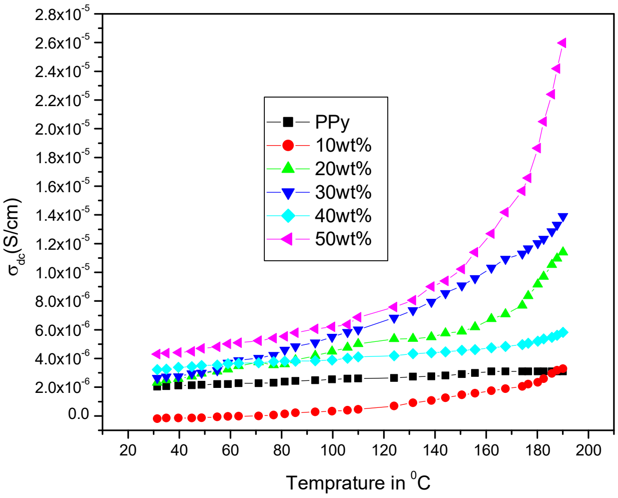

Figure 3. DC conductivity against temperature of PPy/SnO_2 nanocomposites.

Figure 4 shows the tensile strength of PPy nanocomposites doped in PVA in different weight percentages to fabricate the electrically conducting sensor encapsulation thin films. It is found that the tensile strength decreases with an increase in PPy nanocomposites doped in PVA thin film up to 6 wt%, which shows 64.2 MPa. This may be due to the homogeneous distribution of PPy nanocomposite in PVA and well-ordered network formation. Further, it is also noted that the elongation of the PVA is significantly affected by the agglomeration of PPy nanocomposite in the PVA thin film when doped above 6 wt%. The maximum elongation of Ppy nanocomposite in PVA by 6 wt% may be due to the limit of critical concentration[32–34].

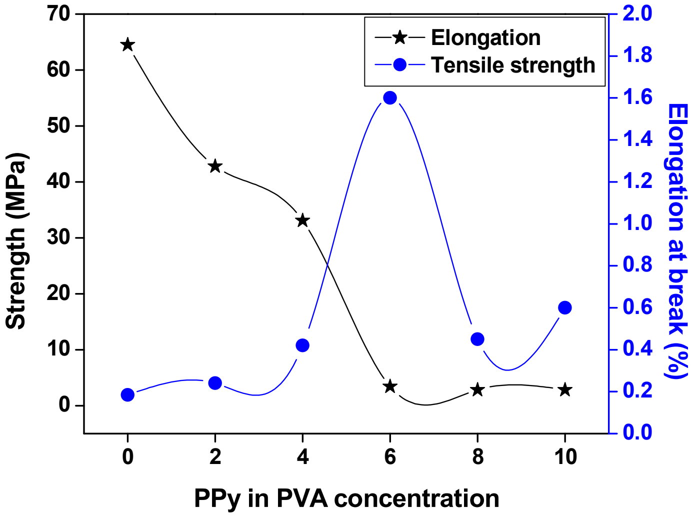

Figure 4. shows the mechanical properties of PPy nanocomposites in PVA thin films.

7. Sensing study

Figure 5 depicts the sensitivity of a Polypyrrole/SnO_2 nanocomposite for LPG sensing. The LPG sensing performance of the Ppy-SnO_2 nanocomposites is primarily attributed to the synergistic effect between the two materials. When exposed to LPG, the surface of the Ppy-SnO_2 nanocomposites undergoes chemical reactions and structural changes, resulting in a change in their electrical properties. These changes can be conveniently measured through electrical resistance variations, making Ppy-SnO_2 nanocomposites an ideal material for LPG sensing applications[35,36]. The polymer recovers to its original size after the gas is removed, restoring the conducting channels. Surface reactions are a possible mechanism for detecting LPG gas by LPG. The surface modification of Ppy-SnO_2 nanocomposites has been reported to enhance the gas-sensing capability of the material. The tin oxides act as a surface coating, increasing the surface area and providing additional active sites for gas adsorption. This leads to a higher sensitivity and faster response time of the Ppy-SnO_2 nanocomposites towards LPG. When compared to other nanocomposites, 30 wt% exhibits a high sensitivity of 86.5%. Surface reactions, consequent charge transfer processes with the underlying SnO_2, and the transport method through the sensing material and shape of the sensing layer all influence overall conduction in a sensor element[37–39].

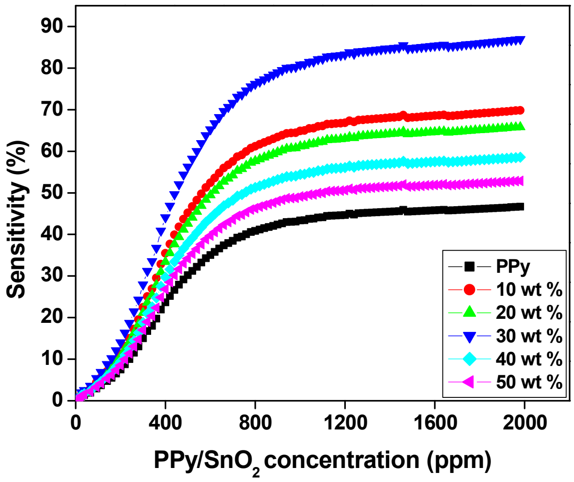

Figure 5. shows the sensitivity of PPy/SnO_2 nanocomposites.

8. Conclusion

The fabrication of conducting PPy/SnO_2 nanocomposites utilizing an in-situ chemical polymerization technique is described in this paper. These composites' conductivity and sensing characteristics were investigated. The influence of SnO_2 concentration on conductivity qualities has been studied. At room temperature, the composites' LPG sensing characteristics were examined, and the better responsiveness of the PPy-SnO_2 nanocomposite was explained in terms of the synergetic interaction of both PPy and SnO_2 particles. It is confirmed that the tensile strength decreases with an increase in PPy nanocomposites doped in PVA thin film up to 6 wt%, which shows 64.2 MPa, which may be due to the homogeneous distribution of PPy nanocomposite in PVA. The development of Ppy-SnO_2 nanocomposites for LPG sensing has emerged as a promising research area. The combination of polypyrrole's excellent electrical conductivity and tin oxide's high sensitivity towards gases has resulted in a material with enhanced gas-sensing properties. Further studies focusing on optimizing the synthesis methods and exploring different dopants or additives are necessary to fully exploit the potential of Ppy-SnO_2 nanocomposites for LPG sensing applications. This research holds great promise for the development of efficient and accurate gas sensors, contributing to the advancement of technology in various industries.

Author contributions

Conceptualization, methodology, writing—original draft preparation, and validation, MSA and AP; formal analysis, SM and AP; investigation, MSA; resources, data curation, and writing—review and editing, SM; visualization, and supervision, AP. All authors have read and agreed to the published version of the manuscript.

Conflict of interest

The authors declare no conflict of interest.

References

1. Kotresh S, Ravikiran YT, Vijayakumari SC, Thomas S. Interfacial p-n heterojunction of polyaniline-nickel ferrite nanocomposite as room temperature liquefied petroleum gas sensor. *Composite Interfaces* 2017; 24(6): 549–561. doi: 10.1080/09276440.2017.1241523

2. Mu B, Zhang W, Wang A. Template synthesis of graphene/polyaniline hybrid hollow microspheres as electrode materials for high-performance supercapacitor. *Journal of Nanoparticle Research* 2014; 16: 2432. doi: 10.1007/s11051-014-2432-0
3. Jafari Y, Ghoreishi SM, Shabani-Nooshabadi M. Electrochemical deposition and characterization of polyaniline-graphene nanocomposite films and its corrosion protection properties. *Journal of Polymer Research* 2016; 23: 91. doi: 10.1007/s10965-016-0983-8
4. Lee RH, Chi CH, Hsu YC. Platinum nanoparticle/self-doping polyaniline composite based counter electrodes for dye-sensitized solar cells. *Journal of Nanoparticle Research* 2013; 15: 1733. doi: 10.1007/s11051-013-1733-z
5. Shin S, Kim J, Kim YH, Kim SI. Enhanced performance of organic light-emitting diodes by using hybrid anodes composed of graphene and conducting polymer. *Current Applied Physics* 2013; 13: S144–S147. doi: 10.1016/j.cap.2013.01.016
6. Patil SV, Bulakhe RN, Deshmukh PR, et al. LPG sensing by p-polyaniline/n-PbS heterojunction capacitance structure. *Sensors and Actuators A: Physical* 2013; 201: 387–394. doi: 10.1016/j.sna.2013.07.019
7. Joshi SS, Gujar TP, Shinde VR, Lokhande CD. Fabrication of n-CdTe/p-polyaniline heterojunction-based room temperature LPG sensor. *Sensors and Actuators B: Chemical* 2008; 132(1): 349–355. doi: 10.1016/j.snb.2008.01.059
8. Patil SJ, Lokhande AC, Yadav AA, Lokhande CD. Polyaniline/Cu_2ZnSnS_4 heterojunction based room temperature LPG sensor. *Journal of Materials Science: Materials in Electronics* 2016; 27: 7505–7508. doi: 10.1007/s10854-016-4729-5
9. Singh S, Singh A, Yadav BC, Tandon P. Synthesis, characterization, magnetic measurements and liquefied petroleum gas sensing properties of nanostructured cobalt ferrite and ferric oxide. *Materials Science in Semiconductor Processing* 2014; 23: 122–135. doi: 10.1016/j.mssp.2014.02.048
10. Kumar ER, Jayaprakash R, Devi GS, Reddy PSP. Magnetic, dielectric and sensing properties of manganese substituted copper ferrite nanoparticles. *Journal of Magnetism and Magnetic Materials* 2014; 355: 87–92. doi: 10.1016/j.jmmm.2013.11.051
11. Sulthana S, Rafiuddin, Khan MZ, Umar K. Synthesis and characterization of copper ferrite nanoparticles doped polyaniline. *Journal of Alloys and Compounds* 2012; 535: 44–49. doi: 10.1016/j.jallcom.2012.04.081
12. Sun ZX, Su FW, Forsling W, Samskog PO. Surface Characteristics of magnetite in aqueous suspension. *Journal of Colloid and Interface Science* 1998; 197(1): 151–159. doi: 10.1006/jcis.1997.5239
13. Jiang J, Li L, Xu F. Polyaniline-LiNi ferrite core-shell composite: Preparation, characterization and properties. *Materials Science and Engineering: A* 2007; 456(1–2): 300–304. doi: 10.1016/j.msea.2006.11.143
14. Zhuravlev VA, Minin RV, Itin VI, Lilenko IY. Structural parameters and magnetic properties of copper ferrite nanopowders obtained by the sol-gel combustion. *Journal of Alloys and Compounds* 2017; 692: 705–712. doi: 10.1016/j.jallcom.2016.09.069
15. Kotresh S, Ravikiran YT, Tiwari SK, Vijaya Kumari SC. Polyaniline-cadmium ferrite nanostructured composite for room-temperature liquefied petroleum gas sensing. *Journal of Electronic Materials* 2017; 46: 5240–5247. doi: 10.1007/s11664-017-5535-4
16. Quillard S, Louarn G, Lefrant S, MacDiarmid AG. Vibrational analysis of polyaniline: A comparative study of leucoemeraldine, emeraldine, and pernigraniline bases. *Physical Review B* 1994; 50: 12496–12508. doi: 10.1103/PhysRevB.50.12496
17. Geethalakshmi D, Muthukumarasamy N, Balasundaraprabhu R. Effect of dopant concentration on the properties of HCl-doped PANI thin films prepared at different temperatures. *Optik* 2014; 125(3): 1307–1310. doi: 10.1016/j.ijleo.2013.08.014
18. Wang PC, Dan Y, Liu LH. Effect of thermal treatment on conductometric response of hydrogen gas sensors integrated with HCl-doped polyaniline nanofibers. *Materials Chemistry and Physics* 2014; 144(1–2): 155–161. doi: 10.1016/j.matchemphys.2013.12.035
19. Li X, Wang G, Li X. Surface modification of nano-SiO_2 particles using polyaniline. *Surface and Coatings Technology* 2005; 197(1): 56–60. doi: 10.1016/j.surfcoat.2004.11.021
20. Waldron RD. Infrared spectra of ferrites. *Physical Review Journals Archive* 1955; 99(6): 1727–1735. doi: 10.1103/PhysRev.99.1727
21. Zhang X, Feng M, Qu R, et al. Catalytic degradation of diethyl phthalate in aqueous solution by persulfate activated with nano-scaled magnetic $CuFe_2O_4$/MWCNTs. *Chemical Engineering Journal* 2016; 301: 1–11. doi: 10.1016/j.cej.2016.04.096
22. Khairy M. Synthesis, characterization, magnetic and electrical properties of polyaniline/$NiFe_2O_4$ nanocomposite. *Synthetic Metals* 2014; 189: 34–41. doi: 10.1016/j.synthmet.2013.12.022
23. Khafagy RM. Synthesis, characterization, magnetic and electrical properties of the novel conductive and magnetic polyaniline/$MgFe_2O_4$ nanocomposite having the core-shell structure. *Journal of Alloys and Compounds* 2011; 509(41): 9849–9857. doi: 10.1016/j.jallcom.2011.07.008

24. Briceño S, Castillo HD, Sagredo V, et al. Structural, catalytic and magnetic properties of $Cu_{1-x}Co_xFe_2O_4$. *Applied Surface Science* 2012; 263: 100–103. doi: 10.1016/j.apsusc.2012.09.007
25. Li X, Wang G, Li X. Surface modification of nano-SiO_2 particles using polyaniline. *Surface and Coatings Technology* 2005; 197(1): 56–60. doi: 10.1016/j.surfcoat.2004.11.021
26. Min S, Wang F, Han Y. An investigation on synthesis and photocatalytic activity of polyaniline sensitized nanocrystalline TiO_2 composites. *Journal of Materials Science* 2007; 42: 9966–9972. doi: 10.1007/s10853-007-2074-z
27. Mane AT, Navale ST, Sen S, et al. Nitrogen dioxide (NO_2) sensing performance of p-polypyrrole/n-tungsten oxide hybrid nanocomposites at room temperature. *Organic Electronics* 2015; 16: 195–204. doi: 10.1016/j.orgel.2014.10.045
28. Patterson AL. The scherrer formula for X-Ray particle size determination. *Physical Review Journals Archive* 1939; 56(10): 978–982. doi: 10.1103/PhysRev.56.978
29. Faisal M, Khasim S. Ku-band EMI shielding effectiveness and dielectric properties of polyaniline-Y_2O_3 composites. *Polymer Science Series A* 2014; 56: 366–372. doi: 10.1134/S0965545X14030055
30. Hou H, Xu G, Tan S, Zhu Y. A facile sol-gel strategy for the scalable synthesis of $CuFe_2O_4$ nanoparticles with enhanced infrared radiation property: Influence of the synthesis conditions. *Infrared Physics & Technology* 2017; 85: 261–265. doi: 10.1016/j.infrared.2017.07.008
31. Sonker RK, Yadav BC. Development of Fe_2O_3-PANI nanocomposite thin film based sensor for NO_2 detection. *Journal of the Taiwan Institute of Chemical Engineers* 2017; 77: 276–281. doi: 10.1016/j.jtice.2017.04.042
32. Ali MN, Chakradhar Goud S, Roy AS. A facile and large-area fabrication method of super hydrophobic self-cleaning polysiloxane/TiO_2 nanocomposite films and its dielectric properties. *Journal of Materials Science: Materials in Electronics* 2020; 31: 12570–12578. doi: 10.1007/s10854-020-03807-8
33. Senthilkumar B, Vijaya Sankar K, Sanjeeviraja C, Kalai Selvan R. Synthesis and physico-chemical property evaluation of PANI-$NiFe_2O_4$ nanocomposite as electrodes for supercapacitors. *Journal of Alloys and Compounds* 2013; 553: 350–357. doi: 10.1016/j.jallcom.2012.11.122
34. Sen T, Shimpi NG, Mishra S, Sharma R. Polyaniline/γ-Fe_2O_3 nanocomposite for room temperature LPG sensing. *Sensors and Actuators B: Chemical* 2014; 190: 120–126. doi: 10.1016/j.snb.2013.07.091
35. Barde RV. Preparation, characterization and CO_2 gas sensitivity of polyaniline doped with sodium superoxide (NaO_2). *Materials Research Bulletin* 2016; 73: 70–76. doi: 10.1016/j.materresbull.2015.08.026
36. Navale ST, Khuspe GD, Chougale MA, Patil VB. Camphor sulfonic acid doped PPy/α-Fe_2O_3 hybrid nanocomposites as NO_2 sensors. *Royal Society of Chemistry* 2014; 4: 27998–28004. doi: 10.1039/C4RA02924K
37. Yang X, Li L, Yan F. Polypyrrole/silver composite nanotubes for gas sensors. *Sensors and Actuators B: Chemical* 2010; 145(1): 495–500. doi: 10.1016/j.snb.2009.12.065
38. Kotresh S, Ravikiran YT, Vijaya Kumari SC, et al. Solution-based spin cast processed polypyrrole/niobium pentoxide nanocomposite as room temperature liquefied petroleum gas sensor. *Materials and Manufacturing Processes* 2016; 31(15): 1976–1982. doi: 10.1080/10426914.2016.1151047
39. Barkade SS, Pinjari DV, Nakate UT. Ultrasound assisted synthesis of polythiophene/SnO_2 hybrid nanolatex particles for LPG sensing. *Chemical Engineering and Processing: Process Intensification* 2013; 74: 115–123. doi: 10.1016/j.cep.2013.09.005

Mechanical Engineering Advances 2023; 1(1): 92.
Review Article

A theoretical approach to be applied in heat exchangers by using the thermal efficiency concept and the second law of thermodynamic

Élcio Nogueira

Universidade do Estado do Rio de Janeiro–DME/FAT/UERJ, Resende 27537-000, Brazil; elcionogueira@hotmail.com

ARTICLE INFO

Received: 20 June 2023
Accepted: 14 July 2023
Available online: 21 August 2023

doi: 10.59400/mea.v1i1.92

ABSTRACT: A review of the concepts of thermal efficiency and thermal and hydraulic irreversibilities is presented, applying the second law of thermodynamics and thermodynamic Bejan number. An example problem, typical of thermal heat exchange between two fluids, is given, with a dimensionless solution for parallel and counterflow flows. The quantities of interest presented through the example are thermal efficiency, thermal effectiveness, thermal irreversibility, the relationship between outlet and inlet temperatures versus the number of thermal units, and outlet temperature for hot fluid. The theory presented in this review has been applied to numerous problems related to heat exchangers over the last three years, as per references.

KEYWORDS: thermal efficiency concept; second law of thermodynamics; Bejan number; heat exchangers

1. Introduction

A review of the second law of thermodynamics on heat and mass transfer was published during the 1980s, where the fundamental mechanisms responsible for entropy generation were analyzed[1]. In addition, it was demonstrated how to balance the irreversibility of heat transfer versus viscous dissipation and how reducing irreversibility at the component level affects the entire system[1,2].

Herwig[3] discusses and presents research suggestions related to the second law of thermodynamics and suggests applying a procedure for the analysis of thermal systems. He called this procedure the Second Law Analysis–SLA.

Heat exchanger efficiency, defined based on the second law, provides a new way to design and analyze heat exchangers.

Efficiency is defined for heat exchangers based on the second law of thermodynamics: thermal efficiency represents the true potential concerning a heat exchanger that enables the maximum heat exchange potential for the configuration under analysis. Potential does not mean the heat transfer rate between fluids, represented by thermal effectiveness, the relationship between the actual heat transfer rate, and the maximum theoretically possible heat transfer rate. When efficiency is high, the temperature difference between the fluids is high. When efficiency is minimal, the temperature difference between the fluids reaches a minimum level for the heat exchanger configuration under analysis. In this last condition, the effectiveness got its maximum possible value.

The definition discussed here was established by Fakheri[1]. It is shown that there is an ideal balanced counterflow heat exchanger that has the same product UoA, the same arithmetic mean temperature difference, and the same temperature ratio between cold and hot fluid that corresponds to the current heat exchanger. Also, the heat capacities of the ideal heat exchanger are equal to the minimum heat capacity of the actual heat exchanger. Therefore, the ideal heat exchanger generates the least entropy, is the most efficient, the least irreversible, and allows maximum heat transfer between fluids.

As with the definition of efficiency for fins, efficiency for heat exchangers has significant practical consequences since the heat exchange potential between fluids can be measured and obtained. When the thermal efficiency has reached its minimum value for a given configuration, the heat exchange potential is exhausted and has maximum thermal irreversibility. Therefore, it allows savings in heat exchanger design since it makes no sense to work beyond the minimum thermal efficiency.

Another important concept used in this chapter is the ratio between the thermal entropy generation rates and the total entropy generation rate of the heat exchanger, called the thermodynamic Bejan number[2]. When the viscous entropy generation rate is very high concerning the thermal entropy generation rate, the cost-benefit caused by viscous dissipation in the flow is very high.

From this point on, it will cover, in mathematical terms, a consolidated part of the long trajectory covered by some of the researchers who established the concepts mentioned above. They indeed overcame the obstacles and paved the way. The credits due are explicit in the references cited.

The concepts presented and discussed in this work were applied to heat exchanger problems[3–14] to understand how they can help classify, sizing, and optimize heat exchangers. Each application has its peculiarities in construction details, physical dimensions, the use of special devices, and the area of application in the industry. The initial difficulty in applying the model lies in obtaining the peculiarities. The literature available makes it possible to get such information if it is not received from the sector interested in the analysis.

2. Methodology

Bejan[2] uses the first and second laws of thermodynamics to determine the expression that makes it possible to calculate the rate of entropy generation in a system:

$$\dot{S}_{gen} = \frac{\dot{Q}\Delta T}{T^2(1+\frac{\Delta T}{T})} + \frac{\dot{m}}{\rho D_h T}(-\frac{dp}{dx}) = \dot{S}_{genT} + \dot{S}_{genf} \tag{1}$$

$\dot{S}_{genT}$ and $\dot{S}_{genf}$ correspond to the entropy generation rate associated with the temperature field and the entropy generation rate related to viscous dissipation.

Equation (1) can be better interpreted in the context of our work if we associate common concepts in heat transfer and fluid mechanics, that is:

$$f = \frac{\rho D_h}{2G^2}(-\frac{dp}{dx}) \tag{2}$$

f is the friction factor. D_h is the hydraulic diameter related to the heat exchanger $\frac{dp}{dx}$ corresponds to the pressure drop.

$$G = \frac{\dot{m}}{A} \tag{3}$$

$\dot{m}$ is the mass flow rate and A the cross-sectional area through which the fluid flows.

$$Re = \frac{GD_h}{\mu} \tag{4}$$

Re is the Reynolds number associated with the flow.

$$D_h = \frac{4A}{p} \tag{5}$$

p is the perimeter associated with the cross-sectional area.

$$St = \frac{\frac{\dot{Q}}{(p^2 \Delta T)}}{C_p G} \tag{6}$$

St is the Stanton number and $\frac{\dot{Q}}{(p^2 \Delta T)}$ corresponds to the average heat transfer coefficient.

Finally, we can rewrite the equation for the rate of entropy generation:

$$\dot{S}_{gen} = \frac{\dot{Q}^2}{4T^2 \dot{m} C_p St} + \frac{2\dot{m}^3 f}{\rho^2 T A^2} \tag{7}$$

The Stanton number is the prevalent factor for thermal irreversibility, and the friction factor is dominant for viscous irreversibility. It is a fact that the Stanton number and friction factor grow simultaneously, and what reduces thermal irreversibility increases viscous irreversibility.

Returning to the crucial parameter for our analyses, the definition of thermal efficiency for heat exchanger, we have:

$$\eta_T = \frac{\dot{Q}}{\dot{Q}^{\eta}_{max}} \tag{8}$$

where,

$$\dot{Q}^{\eta}_{max} = U_O A(\bar{T}_h - \bar{T}_c) \tag{9}$$

$\dot{Q}^{\eta}_{max}$ is the maximum heat transfer rate and $(\bar{T}_h - \bar{T}_c)$ is the arithmetic mean temperature difference between the fluids.

Fakheri[1] clarifies that Equations (8) and (9) establish that any actual heat exchanger with the same product $U_O A$ and the same arithmetic mean temperature difference has a thermal efficiency lower than 1. The maximum heat transfer rate occurs in a balanced counterflow heat exchanger.

Through Equations (8) and (9), it is evident that if the thermal efficiency is determined, the heat transfer rate can be obtained through the maximum heat transfer rate.

Thermal efficiency can be determined for usual heat exchangers through the following expression:

$$\eta_T = \frac{tanh(Fa)}{Fa} \tag{10}$$

where, Fa is the fin analogy number.

Equation (10) means that usual heat exchangers have the same functional expression for the thermal efficiency as the expression used to determine the efficiency of an insulated constant-area fin. If the expression is applicable, there is now an opening for thermal efficiency calculation for heat exchangers that makes it possible to determine the heat transfer rate, which is closely linked to thermal irreversibility. Fakheri[1] presents expressions for calculating the thermal efficiency for usual heat exchangers, which depend on two parameters, NUT and C*, similarly to what happens with the thermal effectiveness in the ε-NTU procedure.

One of the significant obstacles to developing theoretical models in the area is that the NTU parameter is strongly dependent on the Nusselt number and the latter on the Reynolds and Prandtl numbers. The Nusselt number, or the correlated quantities, suffers variations with the heat exchanger type, physical and geometric constitution, and special devices that improve performance. The expression for the Nusselt number for a particular configuration is usually obtained from experimental data, which generates empirical correlations. Fortunately, there is a vast literature on the various types of heat exchangers, and the difficulty can be overcome through a thorough search.

The usual expressions for determining are[2]:

$$Fa = \frac{NTU(1 - C^*)}{2} \; counter\ flow \tag{11}$$

$$Fa = \frac{NTU(1 + C^*)}{2} \; parallel\ flow \tag{12}$$

$$Fa = \frac{NTU}{2} \; single\ stream \tag{13}$$

$$Fa = \frac{NTU\sqrt{1 + C^{*2}}}{2} \; single\ shell \tag{14}$$

The relevant fact in our analysis is that the concepts of thermal effectiveness and thermal efficiency can be related through Equations (13) and (14) with Equations (8) and (9), which integrates two distinct procedures in favour of a better understanding of the phenomena related to heat exchangers. So, we have:

$$\eta_T = \frac{\varepsilon \dot{Q}_{max}^{\varepsilon}}{\dot{Q}_{max}^{\eta}} \tag{15}$$

soon,

$$\eta_T = \frac{\varepsilon_T C_{min}(Th_i - Tc_i)}{U_o A(\bar{T}_h - \bar{T}_c)} \tag{16}$$

It is possible to obtain an expression for the effectiveness as a function of thermal efficiency. There is an expression for the arithmetic mean temperature difference as a function of the difference in outlet temperatures.

The arithmetic mean temperature difference between the fluids can be obtained by the following expression.

$$(\bar{T}_h - \bar{T}_c) = \frac{Th_i + Th_o}{2} + \frac{Tc_i + Tc_o}{2} \tag{17}$$

From Equation (17) and Equations (19) and (20), an expression is determined for the arithmetic mean temperature difference as a function of the inlet temperature difference between the fluids and the thermal effectiveness, that is:

$$(\bar{T}_h - \bar{T}_c) = \frac{(Th_i - Tc_i)[2 - \varepsilon_T(1 + C^*)]}{2} \tag{18}$$

It can be shown, therefore, that the thermal effectiveness can be obtained from the thermal efficiency:

$$\varepsilon_T = \frac{1}{\frac{1}{\eta_T NTU} + \frac{(1 + C^*)}{2}} \tag{19}$$

soon,

$$\dot{Q} = \frac{C_{min}(Th_i - Tc_i)}{\frac{1}{\eta_T NTU} + \frac{(1 + C^*)}{2}} \tag{20}$$

One of the advantages of using the concept of thermal efficiency for heat exchangers is that the use of complex diagrams and equations can be avoided. It is an approach to the analysis of heat exchangers that allows a more comprehensive, systemic view when thermal and viscous irreversibilities are included.

Assuming that there is no heat exchange with the medium that the specific heat of both fluids is constant, the entropy generation rate can be obtained as a function of thermal irreversibilities by the following equation:

$$\dot{S}_{gen} = C_{\min}\sigma_T + C_{\min}\sigma_f = \dot{S}_{genT} + \dot{S}_{genf} \tag{21}$$

where,

$$\sigma_T = \frac{C_h}{C_{min}} \ln\left(\frac{Th_o}{Th_i}\right) + \frac{C_c}{C_{min}} \ln\left(\frac{Tc_o}{Tc_i}\right) \tag{22}$$

$$\sigma_f = -\frac{C_h}{C_{min}} \mathrm{R}\ln\left(\frac{P_{ho}}{P_{hi}}\right) - \frac{C_c}{C_{min}} R \ln\left(\frac{P_{co}}{P_{ci}}\right) \tag{23}$$

σ_T and σ_f are the thermal and viscous irreversibilities, respectively. P_{ho} and P_{hi} are the outlet and inlet pressures of the hot fluid.

$$R = \frac{(Th_i - Th_o)}{(Tc_0 - Tc_i)} \tag{24}$$

Finally, we have:

$$Be = \frac{\dot{S}_{genT}}{\dot{S}_{genT} + \dot{S}_{genf}} \tag{25}$$

Be is the thermodynamic Bejan number, which compares the thermal entropy generation with the total entropy generation of the system.

Before ending the chapter, let's learn a little more with Bejan[2] applying the concepts of entropy generation using usual dimensionless parameters that represent the momentum diffusivity and the thermal diffusivity, the Reynolds Re, and Nusselt number Nu . The development below applies to turbulent flow in ducts with a circular cross-section, and in this case, we have:

$$D_h = D, \quad A = \pi\frac{D^2}{4}, \quad P = \pi D \tag{26}$$

$$Re = \frac{4\dot{m}}{\pi D\mu} \quad and \quad Nu = StRePr \tag{27}$$

Pr is the Prandtl number.

For the configuration under analysis, Equation (7) becomes:

$$\dot{S}_{gen} = \frac{\dot{Q}^2}{\pi T^2 DkNu} + \frac{32\dot{m}^3 f}{\pi^2\rho^2 TD^5} \tag{28}$$

For a fully developed turbulent regime, we have the following usual expressions for Nusselt number and friction factor:

$$Nu = 0.023\, Re^{0.8}\, Pr^{0.4} \quad and \quad f = 0.046\, Re^{-0.2} \tag{29}$$

When Equation (29) is introduced in Equation (28), we have an expression for entropy generation that depends only on the Reynolds number for a fixed Prandtl number. We can then obtain the Reynolds number that minimizes the entropy generation, that is:

$$Re_{opt} = 2.023\, Pr^{-0.071}\, {B_o}^{0.356} \tag{30}$$

where,

$$B_o = \dot{m}\dot{Q} - \frac{\rho}{\mu^{5/2}(kT)^{1/2}} \tag{31}$$

The minimum value for entropy generation rate can be obtained in a completely turbulent flow regime in a duct with a circular cross-section.

$$\dot{s}_{gen,min} = \dot{s}_{gen}(Re_{opt}) \tag{32}$$

It can be shown that the effect of the Reynolds number on entropy generation is obtained through the following relationship:

$$\frac{\dot{s}_{gen}}{\dot{s}_{gen,min}} = 0.056(\frac{Re}{Re_{opt}})^{-0.8} + 0.144(\frac{Re}{Re_{opt}})^{4.8} \tag{33}$$

3. Basic example of an application for thermal analysis of counterflow and parallel flow heat exchangers

3.1. Formulation

$$C_{max}\ defined\ hot\ fluid \tag{34}$$

C_{max} is the thermal capacity of the hot fluid.

$$Th_i = 2.0 \quad defined \tag{35}$$

Th_i represents the inlet temperature of the hot fluid numerically.

$$Tc_i = 1.0 \quad defined \tag{36}$$

Tc_i represents the inlet temperature of cold fluid.

$$C_{min} = C^* C_{max} \tag{37}$$

C_{min} is the thermal capacity of cold fluid, and C^* is the ratio of thermal capabilities.

$$Fa = \frac{NTU(1 - C^*)}{2}\ counter\ flow \tag{38}$$

$$Fa = \frac{NTU(1 + C^*)}{2}\ parallel\ flow \tag{39}$$

Fa is the fin analogy number.

$$\eta_T = \frac{tanh(Fa)}{Fa} \tag{40}$$

η_T is the thermal efficiency.

$$\varepsilon_T = \frac{1}{\frac{1}{\eta_T NTU} + \frac{(1 + C^*)}{2}} \tag{41}$$

ε_T is the thermal effectiveness.

$$\dot{Q} = \varepsilon C_{min}(Th_i - Tc_i) \tag{42}$$

$\dot{Q}$ is the heat transfer rate.

$$Th_O = Th_i - \frac{\dot{Q}}{C_{max}} \tag{43}$$

Th_O is the outlet temperature of the hot fluid.

$$Tc_O = Tc_i + \frac{\dot{Q}}{C_{min}} \tag{44}$$

Tc_O is the outlet temperature of the cold fluid.

$$\sigma_T = \frac{C_h}{C_{min}} \ln\left(\frac{Th_o}{Th_i}\right) + \frac{C_c}{C_{min}} \ln\left(\frac{Tc_o}{Tc_i}\right) \tag{45}$$

σ_T is thermal irreversibility.

3.2. Results and discussions

The presented results deal with a dimensionless simulation with reference data defined a priori. The main parameters for data analysis are the Number of Thermal Units (NTU) and the ratio between the fluids' minimum and maximum thermal capacities (C^*). The thermal efficiency of the heat exchanger, the central magnitude of the recommended analytical method, depends only on these two parameters. All other quantities are defined and determined based on thermal efficiency.

Figure 1 shows the efficiency of the heat exchanger for configuration against the flow as a function of the number of thermal units and having as parameters the relationship between the thermal capacities. Thermal efficiency tends to its maximum value when the number of thermal units approaches zero, regardless of the thermal capacity ratio. That is, thermal efficiency is high for low NTU values. When the heat capacity of the heat exchanger tends to its maximum value, that is, equal to 1, the thermal efficiency tends to its minimum value, regardless of the number of thermal units. Thermal efficiency decreases with the decrease in the ratio between the thermal capacities and the increase in the number of thermal units. As already mentioned, thermal efficiency measures the potential for heat exchange between fluids because the greater the thermal efficiency, the greater the temperature difference between them. However, it does not provide information about the order of magnitude, for example, the rate of heat transfer.

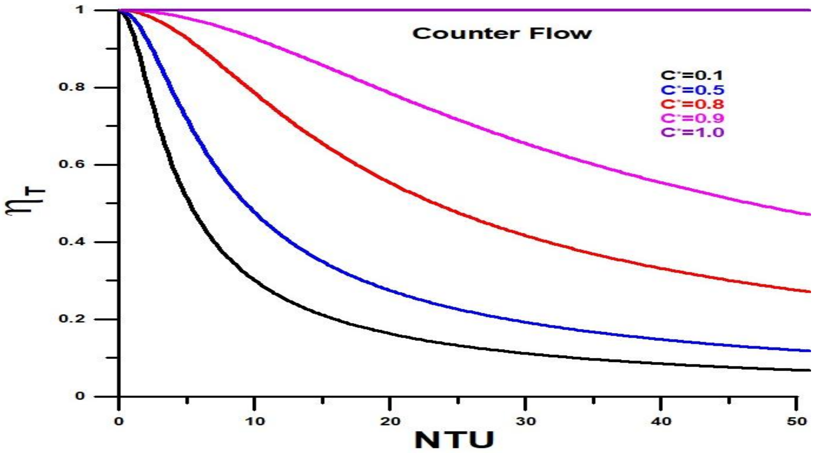

Figure 1. Thermal efficiency versus the number of thermal units for counter-flow configuration.

Figure 2 shows the thermal efficiency of the heat exchanger for parallel flow configuration. There is a great difference between the two configurations under analysis in this case. For configuration parallel flow, the efficiency is only high for a low number of thermal units, regardless of the relationship between the thermal capacities. The result shows that the potential for heat exchange between fluids is only high for low NTU.

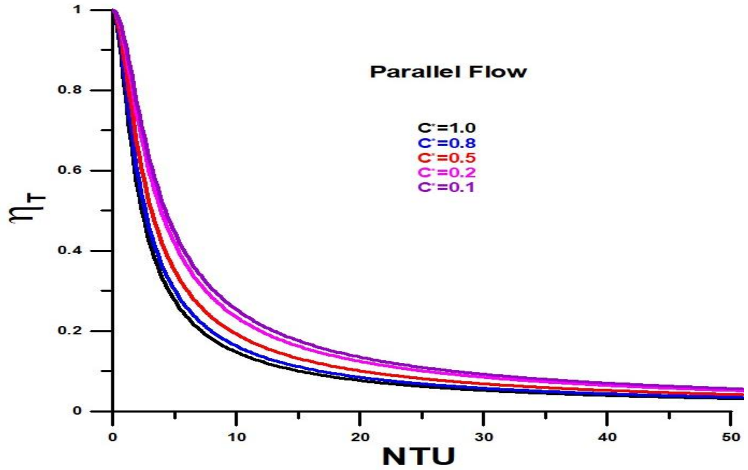

Figure 2. Thermal efficiency versus the number of thermal units for parallel flow configuration.

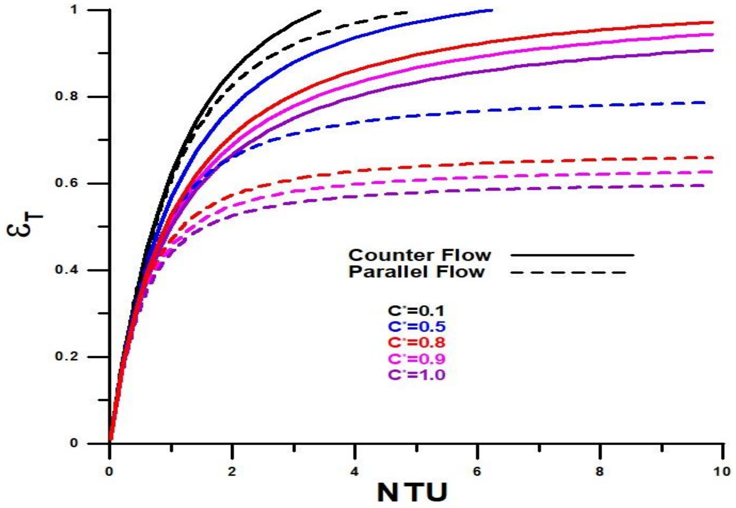

Figure 3. Thermal effectiveness versus the number of thermal units.

Figure 3 shows thermal effectiveness for both the settings under analysis. There are great differences between both. Effectiveness grows with the increase in thermal units in all situations under study. The value of thermal effectiveness is generally high for counterflow configuration compared to parallel flow configuration. When the relationship between thermal capabilities is low, the thermal effectiveness achieves values close to the maximum theoretically possible for low thermal units for both settings. With the increase in the relationship between thermal capabilities, the maximum value reached for effectiveness decreases but remains relatively high for counterflow configuration. The relevant fact is that in a parallel flow configuration, the potential for heat exchange remains stagnant for a higher number of thermal units, and increasing the number of thermal units is unproductive. Concerning the configuration in parallel flow, the results demonstrate that it is advantageous to invest in diminishing the number of thermal units, if necessary.

Thermal irreversibility, **Figure 4** shows a qualitative trend similar to thermal effectiveness. In parallel flow configuration, irreversibility remains stagnant for a high number of thermal units, demonstrating that the heat exchange potential has been exhausted. For configuration in counterflow, however, irreversibility grows for low values of thermal units. It decreases slightly after undergoing a maximum value, meaning that there is heat exchange potential for high thermal units number.

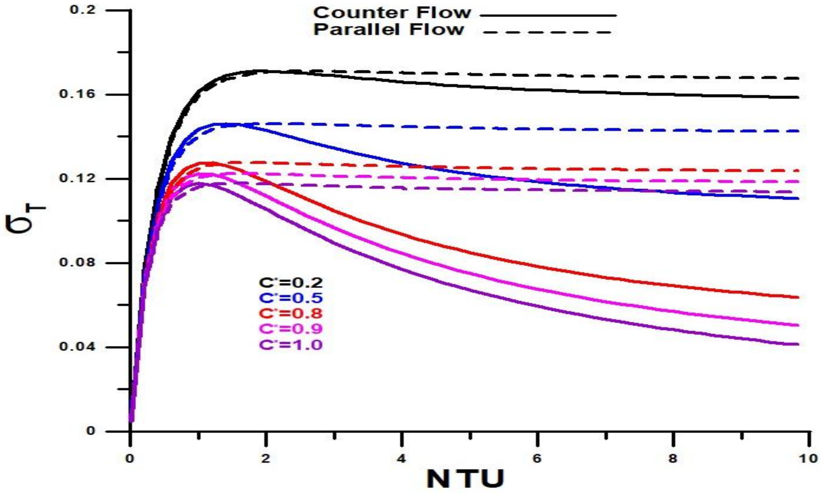

Figure 4. Thermal irreversibility versus the number of thermal units.

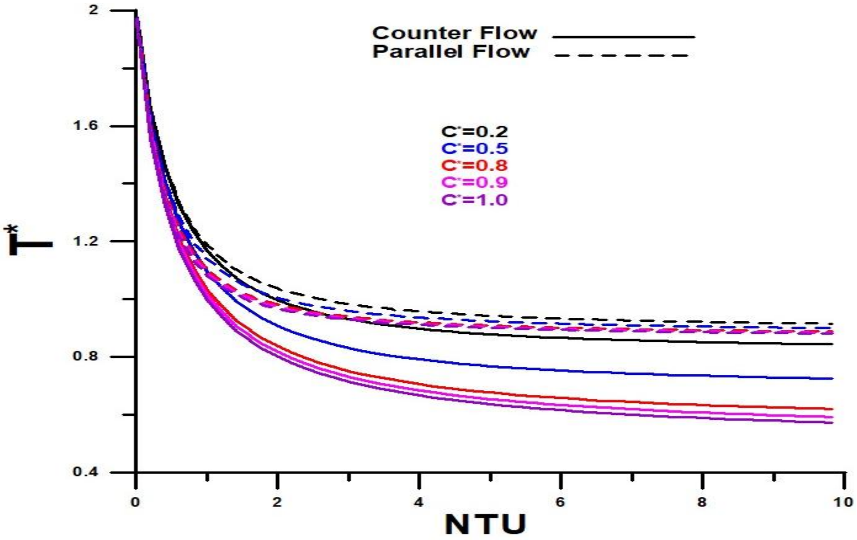

Figure 5. Relationship between outlet and inlet temperatures versus the number of thermal units.

The situation already analyzed reflected in the relationship between the fluid outlet temperatures, **Figure 5**. The temperature difference is maximum for the number of thermal units tending to zero. Still, it decreases rapidly for low values, demonstrating the great potential for heat exchange in this region. This decrease is more significant for counterflow configuration. The smallest differences between temperatures occur for high values for the relationship between thermal capacities.

Furthermore, the temperature difference between the fluids in the counter-flow configuration is significant and almost irrelevant for the configuration in a parallel flow configuration. The relationship between the thermal capacities has the greatest influence on the counterflow configuration. Again, it is observed that there is no justification for increasing the number of thermal units for the parallel flow configuration since the temperature differences between the fluids do not change.

To consolidate the results and complete the analysis, present results for the absolute hot fluid's output temperature in the temperature unit, **Figure 6**.

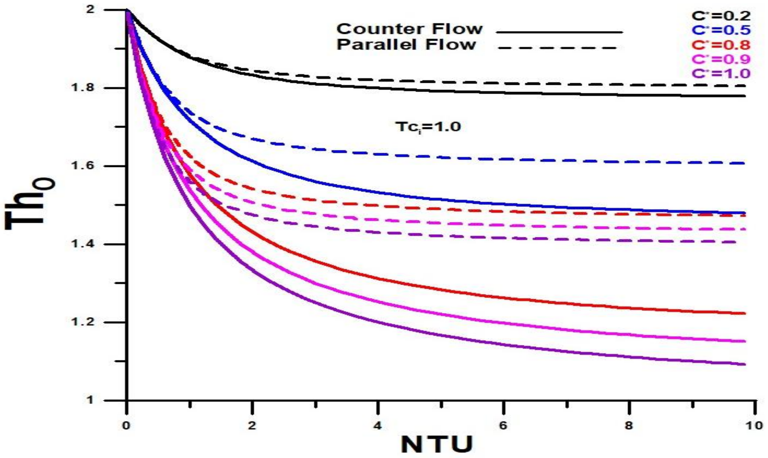

Figure 6. Outlet temperature for hot fluid.

The relevant drop in the hot fluid temperature occurs for smaller values of the number of thermal units for all the relationships between the thermal capacities. For high values of the heat capacity ratio, the hot fluid outlet temperatures tend towards the cold fluid inlet when the number of heat units is high. There is a significant difference in the hot fluid outlet temperature concerning the configurations under analysis. The important fact, in final terms, is that, regardless of the configuration, the best result obtained for the outlet temperature occurs for high values of the relationship between the thermal capacities, that is, when both values of thermal capacity approach.

4. Conclusion

A standard procedure for solving problems associated with heat exchangers was presented using classical and dimensionless analyses. When available, these procedures depend on physical and geometric characteristics and input variables, such as fluid flows, inlet temperatures, and outlet temperatures, but this last is not essential.

The example presented makes evident the importance of dimensionless analysis. Furthermore, the use of the concept of thermal efficiency of heat exchangers is a valuable instrument for a better understanding of the quantities involved in the study of heat exchangers.

It is established that there is a solid, simple, and functional dimensionless procedure for the rating, sizing, and optimization of heat exchangers.

For those initiated in the procedure described, it is suggested to revise the steps presented in this work. In addition, it can be a valuable auxiliary tool for troubleshooting.

Conflict of interest

The author declares no conflict of interest.

References

1. Fakheri A. Heat exchanger efficiency. *Journal of Heat and Mass Transfer* 2007; 129(9): 1268–1276. doi: 10.1115/1.2739620
2. Bejan A. The thermodynamic design of heat and mass transfer processes and devices. *International Journal of Heat and Fluid Flow* 1987; 8(4): 258–276. doi: 10.1016/0142-727X(87)90062-2
3. Herwig H. Second law analysis of momentum and heat transfer problems: Guidelines for future research directions. *International Review of Mechanical Engineering* 2010; 4(5): 488–490.

4. Nogueira É. Thermal performance in heat exchangers by the irreversibility, effectiveness, and efficiency concepts using nanofluids. *Journal of Engineering Sciences* 2020; 7: F1–F7. doi: 10.21272/jes.2020.7(2).f1
5. Nogueira É. Efficiency and effectiveness thermal analysis of the shell and helical coil tube heat exchanger used in an Aqueous Solution of Ammonium Nitrate Solubility (ANSOL) with 20% H_2O and 80% AN. *Journal of Materials Science and Chemical Engineering* 2021; 9(6): 24–45. doi: 10.4236/msce.2021.96003
6. Nogueira É. Thermodynamic performance of boehmite alumina nanoparticle shapes in the counterflow double pipe heat exchanger. *Journal of Engineering Sciences* 2022; 9(1): F1–F10. doi: 10.21272/jes.2022.9(1).f1
7. Nogueira É. Efficacy of the number of plates, fluid flow rate and volume fractions of aluminum oxide nanoparticles on thermal performance of gasket plate heat exchanger. *International Journal of Engineering Research Updates* 2022; 2(1): 25–38. doi: 10.53430/ijeru.2022.2.1.0027
8. Nogueira É. Efficiency and effectiveness method versus ε-NTU method with application in finned flat tube compact heat exchanger with water-ethylene Glycol as nanofluid base of iron oxide nanoparticles. *Journal of Materials Science and Chemical Engineering* 2022; 10: 1–17. doi: 10.4236/msce.2022.102001
9. Nogueira É. Entropy generation analysis in a gasket plate heat exchanger using non-spherical shape of alumina boehmite nanoparticles. *Ovidius University Annals of Chemistry* 2022; 33(1): 41–49. doi: 10.2478/auoc-2022-0006
10. Nogueira É. Efficiency and effectiveness concepts applied in shell and tube heat exchanger using ethylene Glycol-water based fluid in the shell with nanoparticles of Copper Oxide (CuO). *Journal of Materials Science and Chemical Engineering* 2020; 8: 1–12. doi: 10.4236/msce.2020.88001
11. Nogueira É. Effects of R134a saturation temperature on a shell and tube condenser with the nanofluid flow in the tube using the thermal efficiency and effectiveness concepts. *World Journal of Nano Science and Engineering* 2021; 11: 1–24. doi: 10.4236/wjnse.2021.111001
12. Nogueira É. Thermohydraulic performance in the flow of Copper Oxide (CuO) or Aluminum Oxide (Al_2O_3) water-borne nanofluids in a finned flat tube heat exchanger (automotive radiator). *IOSR Journal of Mechanical and Civil Engineering* 2019; 16(5): 1–12. doi: 10.9790/1684-160540112
13. Nogueira É. The effectiveness method (ε-NTU) to analyze the thermal performance of the flat tube multi-louvered finned radiator with silver nanoparticles suspension in ethylene Glycol. *International Journal of Advanced Technology and Engineering Exploration* 2020; 7(66). doi: 10.19101/IJATEE.2020.762040
14. Nogueira E. Thermal-hydraulic performance of Graphene Nanoribbon and Silicon Carbide nanoparticles in the multi-louvered radiator for cooling diesel engine. *Journal of Engineering Sciences* 2020; 7(1): F22–F29. doi: 10.21272/jes.2020.7(1).f2

Mechanical Engineering Advances 2023; 1(1): 94.
Original Research Article

Multigrid method for the solution of thermal elastohydrodynamic lubrication point contact problem with surface asperities

Vishwanath B. Awati*, **Parashuram M. Obannavar**, **Mahesh Kumar Nanjaiah**

Department of Mathematics, Rani Channamma University, Belagavi 591156, India

* **Corresponding author:** Vishwanath B. Awati, awati.vb@rcub.ac.in

ARTICLE INFO

Received: 26 September 2023
Accepted: 30 September 2023
Available online: 15 October 2023

doi: 10.59400/mea.v1i1.94

ABSTRACT: The paper presents, the numerical investigation of point contact thermal elasto-hydrodynamic lubrication (EHL) with surface asperities are analyzed. The effect of temperature and surface roughness on fluid film thickness is studied in detail. The governing equations comprises Reynolds, film thickness, load balance and energy equations with appropriate boundary conditions. The second order finite difference approximation is used to discretize the governing equations and the resultant nonlinear system of algebraic equations is solved using Multigrid V-cycle with full approximation scheme (FAS) technique. Multi level multi integration (MLMI) technique is employed to solve the film thickness equation. The obtained results are illustrated in the form of graphs and tables which are comparable with earlier findings. The film thickness profiles shows dimple near to the outlet region due to temperature-viscosity wedge mechanism. Isothermal minimum film thickness is higher than the thermal minimum film thickness. Minimum film thickness is much smaller due to slide to roll ratio is positive ascompared to negative, whereas the behavior of central film thickness is contrast as that of minimum film thickness.

KEYWORDS: thermal; EHL; multigrid method; FAS; slide to roll ratio; MLMI

1. Introduction

The thermal effect plays a vital role in tribo components such as gears, cams, tappets and rolling bearings etc. For these components, the load is applied over a small contact region which results high pressure generated within the contact region, it leads to deform the contacting surfaces. This phenomenon of lubrication is widely known as elasto-hydrodynamic lubrication (EHL). The simulation of EHL point contactis able to understand the failure of these components and temperature is a key factor in galling or scuffing of these components. The effects of pressure, temperature and film thickness are influenced by surface roughness of the contacting surfaces that are viewed on microscopic level.

In 1961, Crook[1] theoretically studied the hydrodynamic line contact problem by the mechanism of heat generation and removal in oil film. Sternlicht et al.[2] examined the fluid behavior in the contact area and understand the impact of lubricant on rolling contact fatigue life. The numerical solution of coupled Reynolds, elasticity, energy equations were analyzed through mean viscosity across fluid film was discussed by Cheng and Sternlicht[3]. Dowson and Whitker[4] used numerical methodology for the solution of EHL problem, due to the impact of sliding on the performance of EHL contact, further, relation between temperature and pressure distribution were analyzed. Murch and Wilson[5] deliberated the viscous heat instead of conventional Reynolds equation in the inlet region of EHL problem and noticed that constriction in the film thickness is due to viscous heating. Thermal EHL of an elliptical contact problem were numerically elucidatedusing finite difference method with viscosity and density depends on pressure was analyzed by Bruggemann and Kollmann[6].

The detailed analysis of thermal EHL point contact problem was discussed by Kim and Sadeghi[7,8] by considering pure rolling and low slip conditions in order to get the solution. Further, work reveals the importance of shear heating under pure rolling/sliding conditions and predicts that shear heating is in the Hertzian zone. Salehizadeh and Saka[9], Wolff and Kubo[10] and Kazama et al.[11] scrutinized the thermal EHL line contact problem by adopting a parabolic cross-film temperature profile to reduce three-dimensional problem into two-dimensional problem as well as the discretization cost of energy equation. Thermal EHL circular contact problem were analyzed using Multigrid method to determine the solution of Reynolds and film thickness equations under pure rolling/sliding conditions was discussed by Lee et al.[12]. Ehret et al.[13] debated the thermal EHL elliptical contact problem and adopted Lee et al.[12] numerical procedure to understand the effects of spin on elliptical contacts and also noticed that, high temperature across the fluid film. Qu et al.[14] determined the occurrence of steady-state dimple phenomenon is due to temperature-viscosity wedge mechanism on thermal EHL circular contacts and Yang et al.[15] confirms the occurrence of steady state dimple. Guo et al.[16] numerically studied the thermal EHL circular contact problem by considering slide to roll ratio which is more than 2 as calculated, also predict the formation of dimples, behavior of traction and variations of dimples which are compared with experimental findings. Kim et al.[17] debatedthe thermal EHL circular contact problem with a Newtonian fluid by using moving heat source equation given by Carslaw and Jaeger numerically by multigrid technique. The non-Newtonian thermal EHL circular contact problem was analyzed numerically by Kim et al.[18] and attained the results which are compared with experimental findings of Cann and Spikes[19]. The Erying model was implemented to thermal EHL point contact problem by Liu et al.[20] and they introduced a novel technique to calculate the effective viscosity of Erying fluid.

Generally there are no completely smooth surfaces in machine components. Many researchers are investigated the impact of surface topography on EHL contacts, and these surface topography was laconically known as micro-EHL. The surface uncouth includes longitudinal, transverse and isotropic. The isotropic uncouth describes no apparent directions and it is randomly distributed. The surface roughness influences on hydrodynamic fluid flow entraining action which in turn the impact of lubricating performance. The surface roughness collision can be analyzed by using statistical models viz. stochastic and deterministic models.

The stochastic model considers only few numbers of statistical parameters to reveal the impact of surface roughness on contacts and fluids. Greenwood and Williamson[21] showed that the deformation is mainly depends on the topography of the surface and introduced the criterion for differentiate the surface which touch elastically from those of which touch plastically, Greenwood and Tripp[22] introduced the general theory of contact between two rough plane surfaces. Patir and Chang[23] used stochastic model is to explore the effect of surface roughness on hydrodynamic lubrication. And defined the average Reynolds equation for rough surfaces and defined it in terms of pressure and shear flow factors. The deterministic model was used to understand the surface roughness on EHL line contact problem was discussed by Sadeghi and Sui[24]. Chang[25] numerically evaluated the thermal EHL problem with rolling/sliding contacts rough surfaces by using Newton-Raphson method and energy equation were solved using control volume finite element method. Hu and Zhu[26] determined the numerical solution of mixed EHL point contact problem, further computed 3-D surface roughness under different rolling/sliding conditions. Wang et al.[27] analyzed mixed EHL problem by considering Patir and

Chang[23] average flow and obtained results are compared with Hu and Zhu[26]. The improvements in EHL together with surface roughness interaction give rise to a new methodology for predicting stribeck curve. Lu et al.[28] reported the results of series of experiments conducted on journal bearings together with a theoretical prediction of the stribeck-type behavior. And these were compared with the results of mixed EHL model for line contact which are in good agreement with experiment findings.

The deterministic model is used to solve thermal EHL circular and elliptical contact problems numerically to compute pressure and temperature of mixed lubrication discussed by Deolalikar et al.[29]. Yang et al.[30] studied thermal EHL elliptical contact problem for rolling/sliding conditions with non-Newtonian fluid model by considering both transverse and longitudinal surface roughness. And conclude that thermal and non-Newtonian effects can be enlarged significantly by the surface waviness. The impact of surface roughness on friction coefficients were discussed by Akbarzadeh and Khonsari[31]. Sojoudi and Khonsari[32] analyzed EHL point contact problem by considering rough surface, estimated the friction coefficient behavior under different operating parameters. Zhu and Wang[33] studied the deterministic model for mixed lubrication of EHL line, circular and elliptical contact problems to verify the performance of lubricating films. Masjedi and Khonsari[34] deliberated the inclusion of surface roughness in EHL point contact, a statistical based elasto-plastic model was used to investigate the influence of surface roughness. The isothermal EHL point contact problem with bio-based oil as lubricant on smooth and rough surface asperity was numerically studied by Awati et al.[35] further concludes that the bio-based product bring out an alternative source of lubricant to reduce the energy crises. Zhang et al.[36] presented the point contact thermal EHL problem with zero entrainment velocity (ZEV) by considering both Newtonian and Erying model. The impact of transverse oriented ridges was analyzed through thermal EHL and mentioned the impact of ridges on pressure, film thickness, friction coefficients and temperatures were studied by Cui et al.[37]. Awati et al.[38] studied the thermal EHL line contact problem numerically by using multigrid method through full approximation scheme (FAS) technique with bio-based oil as lubricant. And noticed that the reduction in the minimum film thickness for high speed and shown pressure spike as function of relevant operating parameters. The size effect on EHL of roller pairs considering the both Newtonian and Erying fluid thermal EHL problems under steady state was discussed by Liu et al.[39] further, concluded that the size effect is more pronounced in thermal elastohydrodynamic lubrication (TEHL) as compared to isothermal EHL. Hulqvist et al.[40] studied the effect of surface roughness on EHL contact problem in order to improve the durability and friction performance of machine elements. The concept of how the slip effects temperature rise and its coupling effect with heat are still unknown. But the researcher like Zhao et al.[41] discussed the effect of boundary slip on thermal EHL point contact problem. And studied the coupled effects on boundary slip and heat on EHL contacts under large slide to roll ratios. The influence of the dimension change of bush-pin on the pressure, oil film thickness temperature rise and traction coefficient in contact zone using the thermal EHL model of finite line contact was analyzed by Zhang et al.[42]. Zhang et al.[43] discussed the variations of oil film pressure, thickness and temperature rise in the contact zone of plate pin pair in silent chains numerically. In order to understand the interplay of boundary slip and heat Zhao and Wong[44] used the complete thermal EHL of a non-wetting/wetting contact under a high slide to roll ratios.

1.1. Multigrid method

Most of the computational modelling in engineering problems often involves the solution of system of linear/nonlinear algebraic equations and are represented in the form of matrix. The computation of the problem becomes difficult whenever large number of unknowns or increase in the size of coefficient matrix, the solution of these equations by direct method via. Gaussian elimination method is computationally intensive and it involves round off errors. Iterative methods offer alternative tools, because they provide the solution with minimum round off errors and to be more amenable to parallel processing. Iterative methods such as Gauss-Seidel have few drawbacks viz. slow convergence due to accumulation of round off errors or low frequency error components are not removed efficiently after certain iterations. These methods also requires to start with good or near initial approximations so that the convergence become faster or achieved with less number of iterations which is not possible in the case of nonlinear problems.

Multigrid method is a powerful iterative method that circumvents the convergence of the problems of other iterative methods. This method uses iteration on a variety of grid sizes or matrix sizes to speed up the convergence of the solution. Further, the method has many applications in a wide range of problems including solution of differential and integral equations. The Gauss-Seidel iteration method slow down the convergence as the grid size increases. Multigrid method prevents slow convergence on grids of different sizes; thus, it substantially reduces all frequency error components.

Brandt[45] introduced multigrid method to solve large system of linear as well as non-linear algebraic equations. Lubrecht et al.[46] adopted multigrid method for the solution of EHL point contact problem. Later, Venner[47] introduced dipole Jacobi relaxation technique to enhance the performance of multigrid method. The relaxation scheme is the main feature of this method that decides efficiency of the method and it decreases the error components. The main advantages of this method are that, the convergence speed is independent of discretization points. Two types of relaxation schemes are employed in this technique; one of the schemes is Jacobi distributive line relaxation which is applied to domain where pressure is more pronounced in the contact region. Another one is Gauss-Seidel relaxation is applied where the pressure is less severe i.e., to inlet and outlet regions.

Full Approximation Scheme (FAS) algorithm

Multigrid is a powerful iterative method which converges much faster as compared to other iterative methods. This method eliminates high frequency error components on the finer grid with only few number of relaxation sweeps, whereas low frequency error components are unaltered with further or number of relaxation sweeps. By restriction operator is used to determine the solution to coarser grid, the low frequency error components acts as high frequency error components and are easily eliminated with few number of relaxation sweeps. Thus, the solution is obtained at finer grid by using prolongation, added to the solution to get more approximate solution. The procedure is repeated until the convergence is achieved. The algorithm of multigrid method comprising two grids is as follows.

- The system of non-linear algebraic equations are represented as

$$L^{\hat{\hbar}}(\breve{u})^{\hat{\hbar}} = f^{\hat{\hbar}},$$

where, L denotes the nonlinear operator, $\breve{u}$ is the exact solution and f is the right hand side function, $\hat{\hbar}$ represents the fine grid mesh.

- Residual at the fine grid can be computed as

$$\nabla^{\hat{\hbar}} = f^{\hat{\hbar}} - L^{\hat{\hbar}}\left(\breve{v}^{\hat{\hbar}}\right), e^{\hat{\hbar}} = \breve{u}^{\hat{\hbar}} - \breve{v}^{\hat{\hbar}},$$

where, $\breve{v}$ is the approximate solution to the exact solution$\breve{u}$.

- Thus, residual and current approximate solution can be restricted to coarse grid as

$$\nabla^{2\hat{\hbar}} = I_{\hat{\hbar}}^{2\hat{\hbar}}\nabla^{\hat{\hbar}} = I_{\hat{\hbar}}^{2\hat{\hbar}}\left(f^{\hat{\hbar}} - L^{\hat{\hbar}}\left(\breve{v}^{\hat{\hbar}}\right)\right) \text{ and } \breve{v}^{2\hat{\hbar}} = I_{\hat{\hbar}}^{2\hat{\hbar}}\breve{v}^{\hat{\hbar}},$$

where $I_{\hat{\hbar}}^{2\hat{\hbar}}$ is restrict operator.

- Then compute the coarse grid as

$$L^{2\hat{\hbar}}\left(\breve{u}^{2\hat{\hbar}}\right) = L^{2\hat{\hbar}}\left(\breve{v}^{2\hat{\hbar}}\right) + \nabla^{2\hat{\hbar}}$$

- Now, solve the coarser grid approximation to error as $e^{2\hat{\hbar}} = \breve{u}^{2\hat{\hbar}} - \breve{v}^{2\hat{\hbar}}$. In the next step interpolate the error approximation to fine grid and correct the current fine grid approximation as

$$\breve{v}^{\hat{\hbar}} \leftarrow \breve{v}^{\hat{\hbar}} + I_{2\hat{\hbar}}^{\hat{\hbar}} e^{2\hat{\hbar}}$$

where, $I_{2\hat{\hbar}}^{\hat{\hbar}}$ is prolongation operator.

- Apply two to three Gauss-Seidel relaxation sweeps in order to get more approximate solution.

The present work is mainly focuses on thermal behavior of EHL point contact problem, and also analyzes the surface roughness effect under thermal conditions. The study encompass Reynolds, film thickness and energy equations, these equations were solved simultaneously by using multigrid technique with Gauss-Seidel relaxation process with low relaxation factor is employed, and film thickness equation were solved by using multi level multi integration (MLMI) method and Gauss-Seidel iteration process is used solve energy equation.

2. Governing equations

The physical configuration of governing equations characterizeslubrication conditions materialize between a ball and plane. The circumferential velocity $u_2$of the ball and plane is moving with velocity u_1 is parallel tou_2 and axes of the system are placed at centre of the contact. The x-axis is same orientation as the entering velocity, although z-axis is aimed perpendicular from surface 1 to the surface 2.

2.1. Reynolds equation

The Reynolds equation for EHL point contact regime is same as Lee et al.[12] and across fluid film thickness of the lubricant properties are assumed to be constant, also the lubricant act as Newtonian fluid. The viscosity and density are dependent on both pressure and mean temperature of the film. As a consequence, the thermal Reynolds equation reads as,

$$\frac{\partial}{\partial x}\left(\frac{\rho \hbar^3}{\eta}\frac{\partial p}{\partial x}\right) + \frac{\partial}{\partial y}\left(\frac{\rho \hbar^3}{\eta}\frac{\partial p}{\partial y}\right) - 12\bar{u}\frac{\partial(\rho\hbar)}{\partial x} = 0, \text{ where } \bar{u} = \frac{u_1+u_2}{2} \tag{1}$$

The dimensionless parameters used in this study are

$$X = \frac{x}{a};\ Y = \frac{y}{a};\ P = \frac{p}{p_{\hbar}};\ H = \frac{\hbar R}{a^2};\ \rho^* = \frac{\rho}{\rho_0};\ \eta^* = \frac{\eta}{\eta_0};\ U = \frac{\eta_0\bar{u}}{ER};\ W = \frac{w}{E'R^2};\ \hat{W} = \frac{\widehat{w}}{a};\ T^* = \frac{T}{T_0};\ M = W(2U)^{-3/4};\ L = G(2U)^{1/4};\ G = \alpha E;\ SR = \frac{2(u_1-u_2)}{u_1+u_2} \tag{2}$$

By using Equation (2) in Equation (1), the dimensionless Reynolds equation becomes

$$\frac{\partial}{\partial X}\left(\varepsilon\frac{\partial P}{\partial X}\right) + \frac{\partial}{\partial X}\left(\varepsilon\frac{\partial P}{\partial Y}\right) - \lambda\frac{\partial(\bar{\rho}H)}{\partial X} = 0 \tag{3}$$

where $\lambda = \frac{12\eta_0\bar{u}R^2}{a^3p_{\hbar}}$, $\varepsilon = \frac{\bar{\rho}H^3}{\eta^*}$, and boundary conditions for Equation (3) is given as;

At the inlet region $P(X_{in}, Y) = 0$; At the outlet region $P(X_{out}, Y) = 0$, $\frac{\partial P(X_{out},Y)}{\partial X} = 0$; and at the two sides $P|_{Y=\pm 2} = 0$.

The viscosity-pressure-temperature relation proposed by Roelands et al.[48] used to incorporate the change in viscosity along with pressure and temperature expressed as

$$\eta = \eta_0\, exp\{[ln(\eta_0 - 9.67)][-1 + (1 + 5.1\times 10^{-9}p)^z] - \gamma(T - T_0)\} \tag{4}$$

where, γ denotesthe temperature-viscosity coefficient, η_0 is the inlet viscosity of lubricant, T is the temperature and T_0 denotes the initial temperature. The dimensionless form of Equation (4) becomes

$$\eta^* = exp\{[ln(\eta_0 - 9.67)][-1 + (1 + 5.1 \times 10^{-9} p_{\hbar} P)^z] - \gamma(T^* - 1)\} \tag{5}$$

Dowson and Higginson[49] proposed density-pressure relation is adopted with modifications to the effect of temperature is given as,

$$\rho = \rho_0 \left(1 + \frac{0.6 \times 10^{-9} p}{1 + 1.7 \times 10^{-9} p}\right) [1 - \beta(T - T_0)] \tag{6}$$

where, β is the thermal expansivity. The dimensionless form of Equation (6) can be expressed as

$$\bar{\rho} = \left(1 + \frac{0.6 \times 10^{-9} p_{\hbar} P}{1 + 1.7 \times 10^{-9} p_{\hbar} P}\right) [1 - \beta(T^* - 1)] \tag{7}$$

2.2. Film thickness equation

Consider two bodies are elastic and semi-infinite; also the deformation of bounding surface is taken into consideration. The radii of curvature of ball are greater than the contact length, for undeformed surface of the parabolic approximation is adopted. The point contact EHL film thickness equation is given by

$$\hbar(x,y) = \hbar_{00} + \frac{x^2}{2R} + \frac{y^2}{2R} + \frac{2}{\pi E'} \int_{-\infty}^{\infty} \int_{-\infty}^{\infty} \frac{p(x', y')dx' dy'}{\sqrt{(x - x')^2 + (y - y')^2}} + \mathfrak{R}(x,y) \tag{8}$$

The dimensionless form of Equation (8) can be written as

$$H(X,Y) = H_{00} + \frac{X^2 + Y^2}{2} + \frac{2}{\pi^2} \int_{-\infty}^{\infty} \int_{-\infty}^{\infty} \frac{P(X', Y')dX' dY'}{\sqrt{(X - X')^2 + (Y - Y')^2}} + \mathfrak{R}(X,Y) \tag{9}$$

where $\mathfrak{R}(X,Y) = \bar{A} \, cos\left(\frac{2\pi\hat{X}}{\hat{W}}\right)$, $\hat{X} = X\,cos(\varphi) - Y\,sin(\varphi)$, $\hat{W} = \bar{w}/b$ denotes the dimensionless wavelength, $\bar{A} = amp/\hbar_{\hbar}$ denotes the non-dimensional amplitude, $\hbar_{\hbar} = b^2/R$ denotes maximum Hertzian deformation, φ denotes the orientation angle.

2.3. Force balance equation

The force balance equation with respect to point contact problem becomes

$$\int_{-\infty}^{\infty} \int_{-\infty}^{\infty} p(x,y)dxdy - w = 0 \tag{10}$$

The dimensionless form of Equation (10) becomes

$$\int_{-\infty}^{\infty} \int_{-\infty}^{\infty} P(X,Y)dXdY = \frac{2\pi}{3} \tag{11}$$

2.4. Energy equation

The detailed study of energy equation for a Newtonian fluid is given by Pai[50] and Liu[51]. The temperature distribution within the fluid film shall be computed from the solution of energy equation by considering convective term in the present study.

$$c_p \rho \left(u\frac{\partial T}{\partial x} + v\frac{\partial T}{\partial y} - w\frac{\partial T}{\partial z}\right) = ku\frac{\partial^2 T}{\partial z^2} - \frac{T}{\rho}\frac{\partial \rho}{\partial T}\left(u\frac{\partial p}{\partial x} + vu\frac{\partial p}{\partial y}\right) + \eta\left[\left(\frac{\partial u}{\partial z}\right)^2 + \left(\frac{\partial v}{\partial z}\right)^2\right] \tag{12}$$

The dimensionless form of Equation (12) can be expressed as

$$\frac{c_p\rho_0E'\ a^3}{\eta_0kR}\left(\bar{\rho}U^*\frac{\partial T^*}{\partial X}+\bar{\rho}V^*\frac{\partial T^*}{\partial Y}\right)-\frac{c_p\rho_0E'\ a^2}{\eta_0k}\bar{\rho}W^*\frac{\partial T^*}{\partial Z}=\frac{\partial^2T^*}{\partial Z^2}-\frac{E'\ p_{\hbar}a^3}{\eta_0kT_0R}\frac{\partial\bar{\rho}}{\partial T^*}\frac{1}{\bar{\rho}} \left(U^*\frac{\partial P}{\partial X}+V^*\frac{\partial P}{\partial Y}\right)T^*+\frac{E'^2R^2}{k\eta_0T_0}\left[\left(\frac{\partial U^*}{\partial Z}\right)^2+\left(\frac{\partial V^*}{\partial Z}\right)^2\right]\eta^* \tag{13}$$

where

$$U^*=U_1^*+\frac{p_{\hbar}a^3}{R^3E'}\frac{\partial P}{\partial X}\left(\int_0^Z\frac{Z}{\eta^*}dZ-\frac{\int_0^H(Z/\eta^*)dZ^2}{\int_0^H(1/\eta^*)dZ}\int_0^Z\frac{1}{\eta^*}dZ\right)+\frac{U_2^*-U_1^*}{\int_0^H(1/\eta^*)dZ}\int_0^Z\frac{1}{\eta^*}dZ \tag{13a}$$

$$V^*=\frac{p_{\hbar}a^3}{R^3E'}\frac{\partial P}{\partial Y}\left(\int_0^Z\frac{Z}{\eta^*}dZ-\frac{\int_0^H(Z/\eta^*)dZ}{\int_0^H(1/\eta^*)dZ}\int_0^Z\frac{1}{\eta^*}dZ\right) \tag{13b}$$

The dimensionless temperature boundary condition for upper surface may be expressed as

$$T_{up}^*=\frac{k\sqrt{\eta_0R}}{\sqrt{\pi\rho_1c_1k_1u_1E'a^3}}\int_{-\infty}^X\left(\frac{\partial T^*}{\partial Z}\right)_{Z=0}\frac{dS}{\sqrt{X-S}}+1 \tag{14}$$

The temperature boundary condition for the lower surface may be expressed in dimensionless form as

$$T_{dw}^*=\frac{k\sqrt{\eta_0R}}{\sqrt{\pi\rho_2c_2k_2u_2E'a^3}}\int_{-\infty}^X\left(\frac{\partial T^*}{\partial Z}\right)_{Z=H}\frac{dS}{\sqrt{X-S}}+1 \tag{15}$$

3. Method of solution

3.1. Discretization of governing equations

The governing mathematical modelling of physical equations viz. Reynolds, film thickness, load balance and energy equations are discretized by using second order finite difference approximations. The domain of computation is $[X_{in},X_{out}]=[-4,1.5]$, $[Y_{in},\ Y_{out}]=[-2,2]$ and Equation (3) can be discretized as

$$\left(\frac{\xi_{i-1/2,j}P_{i-1,j}-\left(\xi_{i-1/2,j}+\xi_{i+1/2,j}\right)P_{i,j}+\xi_{i+1/2,j}P_{i+1,j}}{\Delta X^2}\right)+\left(\frac{\xi_{i,j-1/2}P_{i,j-1}-\left(\xi_{i,j-1/2}+\xi_{i,j+1/2}\right)P_{i,j}+\xi_{i,j+1/2}P_{i,j+1}}{\Delta Y^2}\right)-\left(\frac{\bar{\rho}_iH_i-\bar{\rho}_{i-1}H_{i-1}}{\Delta X}\right)=0, \tag{16}$$

where $\xi=\frac{\varepsilon}{\lambda}$. The film thickness Equation (9) can be discretized as

$$H_{i,j}=H_{00}+\frac{X_i^2}{2}+\frac{Y_j^2}{2}+\frac{2}{\pi^2}\sum_{k=1}^N\sum_{l=1}^N K_{i,j,k,l}P_{k,l}-\bar{A}\cos\left(\frac{2\pi X'_j}{\hat{W}}\right) \tag{17}$$

where $K_{i,j,k,l}$ denotes the kernel and is given by Venner and Lubrecht[52].

$$K_{i,j,k,l}=-|X_p|\,arcsin\,\hbar\left(\frac{Y_p}{X_p}\right)+|Y_p|\,arcsin\,\hbar\left(\frac{X_p}{Y_p}\right)-|X_m|\,arcsin\,\hbar\left(\frac{Y_p}{X_m}\right)-|Y_p|\,arcsin\,\hbar\left(\frac{X_m}{Y_p}\right)-|X_p|\,arcsin\,\hbar\left(\frac{Y_m}{X_p}\right)-|Y_m|\,arcsin\,\hbar\left(\frac{X_p}{Y_m}\right)+|X_m|\,arcsin\,\hbar\left(\frac{Y_m}{X_m}\right)+|Y_m|\,arcsin\,\hbar\left(\frac{X_m}{Y_m}\right) \tag{18}$$

and $X_p = X_k - X_i + \frac{\Delta X}{2}$; $X_m = X_k - X_i - \frac{\Delta X}{2}$; $Y_p = Y_l - Y_j + \frac{\Delta Y}{2}$; $Y_m = Y_l - Y_j - \frac{\Delta Y}{2}$.

The energy equation represented in Equation (13) can be written as

$$\frac{\partial^2 T^*}{\partial Z^2} + A_2\left(\bar{\rho}U^*\frac{\partial T^*}{\partial X} + \bar{\rho}V^*\frac{\partial T^*}{\partial Y}\right) - 2A_5\bar{\rho}W^*\frac{\partial T^*}{\partial Z} + A_3\frac{1}{\bar{\rho}}\left(U^*\frac{\partial P}{\partial X} + V^*\frac{\partial P}{\partial Y}\right)T^* = A_4\left[\left(\frac{\partial U^*}{\partial Z}\right)^2 + \left(\frac{\partial V^*}{\partial Z}\right)^2\right]\eta^* \tag{19}$$

The discretized form of Equation (19) as

$$\frac{1}{\Delta Z^2}\left(T^*_{k-1} - 2T^*_k + T^*_{k+1}\right) - A_5\bar{\rho}W^*_k\frac{1}{\Delta Z}\left(T^*_{k+1} - T^*_{k-1}\right) + A_3\left(U^*_k\frac{\partial P}{\partial X} + V^*_k\frac{\partial P}{\partial Y}\right)\frac{T^*_k}{\bar{\rho}_k} + A_2\left(\bar{\rho}_k U^*_k\frac{T^*_{i,j,k} - T^*_{i-1,j,k}}{\Delta X} + \bar{\rho}_k V^*_k\frac{T^*_{i,j,k} - T^*_{i,j-1,k}}{\Delta Y}\right) = A_4\left[\left(\frac{\partial U^*}{\partial Z}\right)^2 + \left(\frac{\partial V^*}{\partial Z}\right)^2\right]\eta^*_k \tag{20}$$

where $A_2 = \left(\frac{-c\rho E'a^3}{\eta_0 kR}\right)$, $A_3 = \left(\frac{-E'p_{\hbar}a^3D}{\eta_0 kR}\right)$, $A_4 = \left(\frac{E'^2R^2}{\eta_0 kT_0}\right)$, $A_5 = \left(\frac{-c\rho_0E'a^2}{2\eta_0 k}\right)$.

By omitting the subscripts *i, j.* in Equation (20) and it can be written as

$$A_{1,k}T^*_{k-1} + A_{2,k}T^*_k + A_{3,k}T^*_{k+1} = A_{4,k} \tag{21}$$

where $= 2, 3, 4, \ldots N_Z - 1$. $A_{1,k} = \frac{1}{\Delta Z^2} + A_5\bar{\rho}_kW^*_k\frac{1}{\Delta Z}$,

$$A_{2,k} = -2\frac{1}{\Delta Z^2} + A_2\bar{\rho}_k\frac{1}{\Delta X}\left(U^*_k + V^*_k\right) + A_3\frac{1}{\bar{\rho}_k}\left(U^*_k\frac{\partial P}{\partial X} + V^*_k\frac{\partial P}{\partial Y}\right),\ A_{3,k} = \frac{1}{\Delta Z^2} - A_5\bar{\rho}_kW^*_k\frac{1}{\Delta Z},$$

$$A_{4,k} = A_4\left[\left(\frac{\partial U^*}{\partial Z}\right)^2 + \left(\frac{\partial V^*}{\partial Z}\right)^2\right]\eta^*_k + A_2\bar{\rho}_k\frac{1}{\Delta X}\left(U^*_kT^*_{i-1,j,k} + V^*_kT^*_{i,j-1,k}\right).$$

The temperature boundary conditions are discretized as

$$A_{1,N_Z}T^*_{N_Z-1} + A_{2,N_Z}T^*_{N_Z} = A_{4,N_Z} \tag{22}$$

where $A_{1,N_Z} = 1 + \frac{4}{3}A_6\sqrt{\Delta X}\frac{N_Z-1}{H}$, $A_{2,N_Z} = -\frac{4}{3}A_6\sqrt{\Delta X}\frac{N_Z-1}{H}$, $A_{4,N_Z} = 1 - A_6\sqrt{\Delta X}\frac{N_Z-1}{H}C_{C1}$.

The discretized form of Equation (11) becomes

$$\Delta X\Delta Y\sum_{i=1}^{N}\sum_{j=1}^{N}P_{i,j} = \frac{2\pi}{3} \tag{23}$$

The inlet boundary condition is $P(X_{in}, Y) = 0$ and the outlet negative pressure is set to zero. The discretized boundary conditions are

$$P(X_{in}, Y) = 0 \text{ and } \frac{P(X_{out}, Y) - P(X_{out-1}, Y)}{\Delta X} = 0 \tag{24}$$

and the side boundary conditions becomes $P(X, Y = \pm 2) = 0$.

3.2. Solution procedure

For this problem, at each grid level pressure is relaxed by applying Gauss-Seidel relaxation scheme. Let us denote $(LP)_{i,j}$by $L_{i,j}\ P$ represents algebraic equation for pressure on each grid level and it can be written as

$$L_{i,j}(P) = F_{i,j}\left(i = 1, 2, 3, \ldots n_x, j = 1,2,3, \ldots n_{y-1}\right).$$

Let $c_1$be an under relaxation factor, the process for pressure iteration can be expressed as

$$\hat{P}_{i,j} = \bar{P}_{i,j} + c_1\delta_{i,j},$$

where $\delta_{i,j} = \left(\frac{\partial L_{i,j}}{\partial P_{i,j}}\right)^{-1} r_{i,j}$,

$$r_{i,j} = F_{i,j} - \left[\xi_{i-1/2,j}\hat{P}_{i,j} - \left(\xi_{i-1/2,j} + \xi_{i+1/2,j}\right)\bar{P}_{i,j} + \xi_{i+1/2,j}P_{i,j}\right]\frac{1}{\Delta X^2}$$
$$-\begin{bmatrix}\xi_{i,j-1/2}\hat{P}_{i,j-1} - \left(\xi_{i,j-1/2} + \xi_{i,j+1/2}\right)\hat{P}_{i,j} \\ +\xi_{i,j+1/2}\hat{P}_{i,j+1}\end{bmatrix}\frac{1}{\Delta Y^2} + \left(\bar{\rho}_{i,j}\bar{H}_{i,j} - \bar{\rho}_{i-1}\hat{H}_{i-1,j}\right)\frac{1}{\Delta X},$$
$$\left(\frac{\partial L_{i,j}}{\partial P_{i,j}}\right) = -\left(\xi_{i-1/2,j} + \xi_{i+1/2,j}\right)\frac{1}{\Delta X^2} - \left(\xi_{i,j-1/2} + \xi_{i,j+1/2}\right)\frac{1}{\Delta Y^2} - \frac{2}{\pi^2}\left(\bar{\rho}_{i,j}K_{ij,ij}^{\Delta\Delta\Delta} - \bar{\rho}_{i-1,j}K_{i-1j,ij}^{\Delta\Delta\Delta}\right),$$

where $\hat{P}_{i,j}, \hat{P}_{i-1,j}$ and $\hat{H}_{i,j}, \hat{H}_{i-1,j}$ are the previous iteration values and are replaced by $\bar{P}_{i,j}$ and $\bar{H}_{i,j}$ are the new values of pressure and film thickness respectively. After computing pressure from FAS scheme, MLMI method is employed to obtain deformation with initial pressure and temperature. The obtained pressure is used to solve energy equation by using finite difference with Gauss-Seidel iteration method. The obtained temperature from energy equation is used to solve Reynolds equation for pressure and compute temperature using the updated pressure. The procedure is continued until the convergence criteria is satisfied i.e.,

$$\frac{\sum\left|\bar{P}_{i,j} - \hat{P}_{i,j}\right|}{\sum \bar{P}_{i,j}} \leq 1 \times 10^{-04}, \frac{\sum\left|\bar{T}^*_{i,j} - \hat{T}^*_{i,j}\right|}{\sum \bar{T}^*_{i,j}} \leq 1 \times 10^{-05}.$$

where $\bar{T}^*$ is the updated temperature value and $\hat{T}^*$ is previous temperature value.

4. Results and discussion

The EHL point contact problem lubricated with Newtonian fluid and surface roughness is examined numerically by using multigrid method with FAS technique. The governing Reynolds and load balance equations are solved using FAS scheme and film thickness equation is solved by using MLMI technique and energy equation is solved by using Gauss-Seidel iteration scheme. These equations are simultaneously solved to get pressure, film thickness and temperature profiles. For the present numerical computation, 5-V cycles are used in order to get the solution with 64 × 64 grid points.

Table 1 shows the physical parameters used in the present study which includes both solid and lubricant properties. The comparison of isothermal results of central and minimum film thickness withthermal film thickness are illustrated in **Table 2**, and obtained results are compared with Hamrock and Dowson[53] empirical formula and results agree very well.

Table 1. Solid and lubricants properties.

Parameters	**Values**
Ambient viscosity	0.04
Equivalent radius	0.16
Elastic modulus(GPa)	206
Inlet temperature of the lubricant (K)	303
Thermal conductivity of surfaces(W/mK)	46
Thermal conductivity of lubricant (W/mK)	0.14
Density (Kg/m^3)	7850
Specific heat of contact solids	470
Specific heat of lubricant (J/KgK)	2000
Ambient density (Kg/m^3)	890
Density of surfaces (Kg/m^3)	2000
Temperature-viscosity coefficient	−1.1
Temperature-density coefficient of lubricant (K^{-1})	−0.00065

Table 2. Minimum and central film thickness values are compared with Hamrock and Dowson empirical values for different loads.

Load M	**Isothermal film thickness**		**Thermal film thickness**		**Hamrock and Dowson**[53]	
	H_{min}	H_{cen}	H_{min}	H_{cen}	H_{min}	H_{cen}
40	0.6199	0.2450	0.1688	0.2585	0.0989	0.1634
60	0.1190	0.1807	0.1178	0.1944	0.0733	0.1213
100	0.0730	0.1258	0.0729	0.1335	0.0502	0.0834

Figures 1 and **2** illustrates the isothermal and thermal film thickness distributions for load varying from $M = 20$ to $100$with constant speed $L = 12.04$, it is observed that, the occurrence of dimple in the thermal film thickness is due to temperature-viscosity wedge mechanism. The contour plots of isothermal and thermal film thickness distributions show a horse shoe constriction, minimum film thickness present in the side lobes is noticed and it is shown in **Figures 3** and **4** respectively for varying load $M = 20$ to 100 with constant speed $L = 12.04$. The comparison between isothermal and thermal film thickness contours is also depicted, with slide to roll ratio 0.25. **Figures 5** and **6** predicts the isothermal and thermal pressure distribution profiles for different load ranging from $M = 20$ to $100$for constant speed $L = 12.04$ with SR = 0.25. It is perceived that pressures spike decreases with increase in load parameter also both isothermal and thermal pressure and film thickness profiles are demonstrated in **Figure 7** for various load $M = 20, 40, 80, 100$ at a constant speed $L = 12.04$.

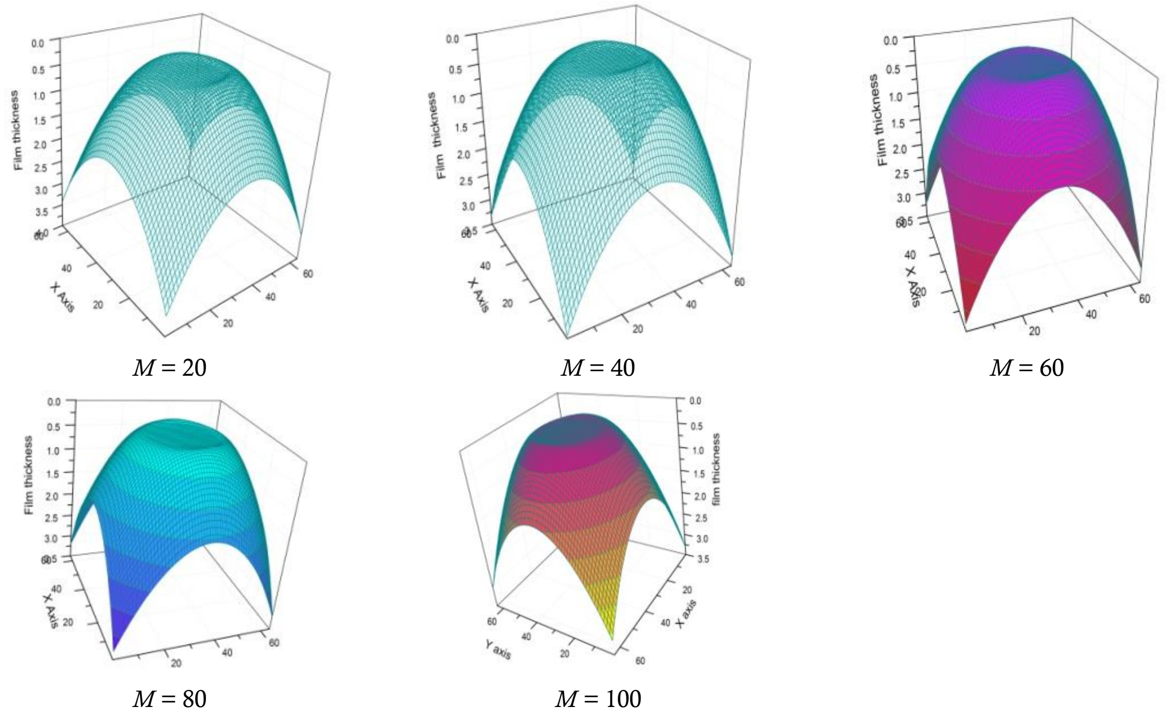

M = 20 *M* = 40 *M* = 60

M = 80 *M* = 100

Figure 1. Isothermal film thickness profiles for varying load from M = 20 to 100 with constant speed $L = 12.04$.

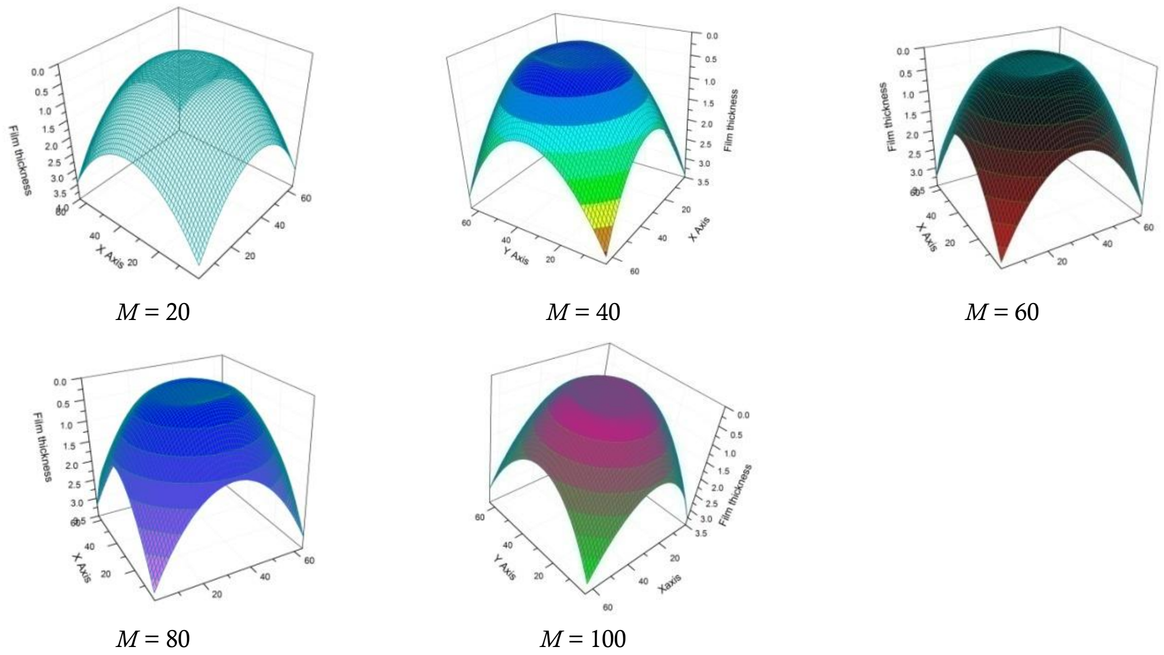

M = 20 *M* = 40 *M* = 60

M = 80 *M* = 100

Figure 2. Thermal film thickness profiles for varying load from *M* = 20 to 100 with the constant speed *L* = 12.04.

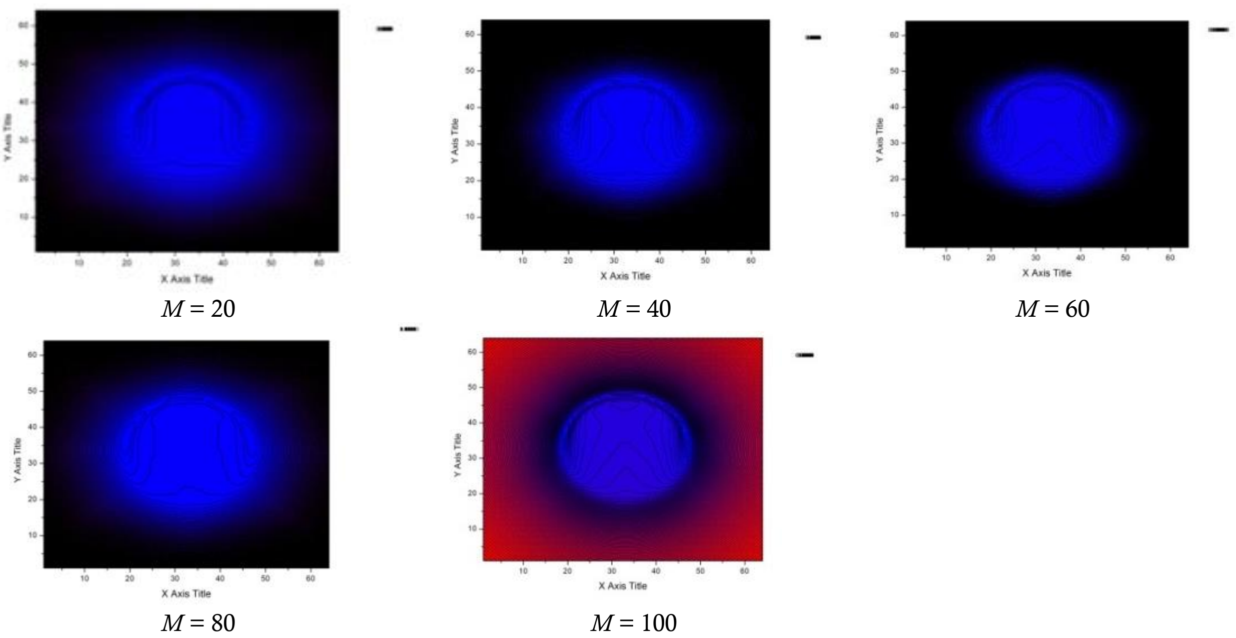

M = 20 *M* = 40 *M* = 60

M = 80 *M* = 100

Figure 3. Contour plot of isothermal film thickness profiles for varying load from *M* = 20 to 100 with the constant speed *L* = 12.04.

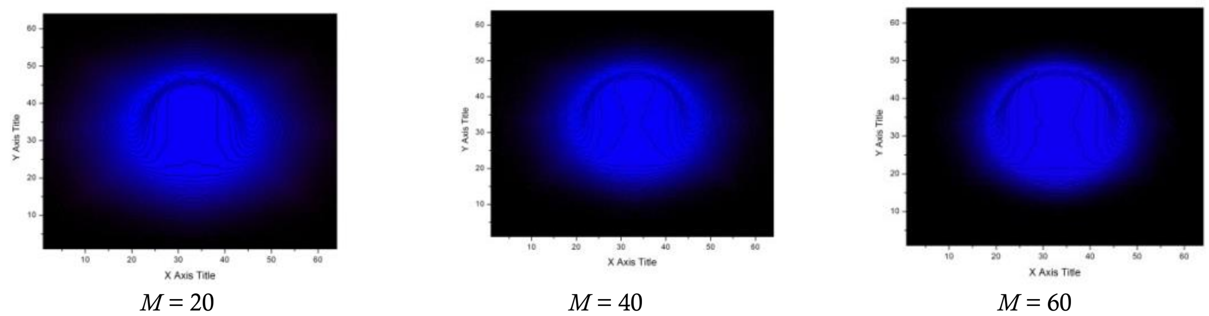

M = 20 *M* = 40 *M* = 60

Figure 4. (*Continued*).

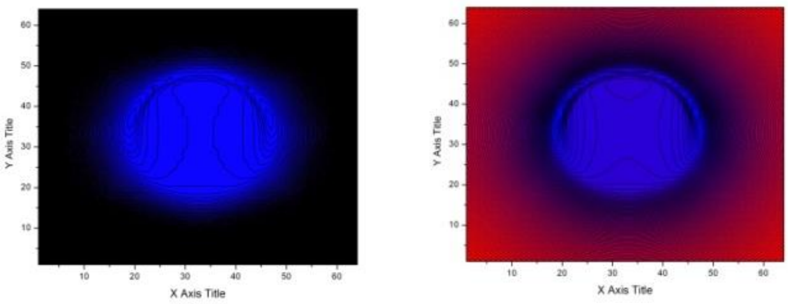

M = 80 *M* = 100

Figure 4. Contour plot of thermal film thickness profiles for varying load from *M* = 20 to 100 with the constant speed *L* = 12.04.

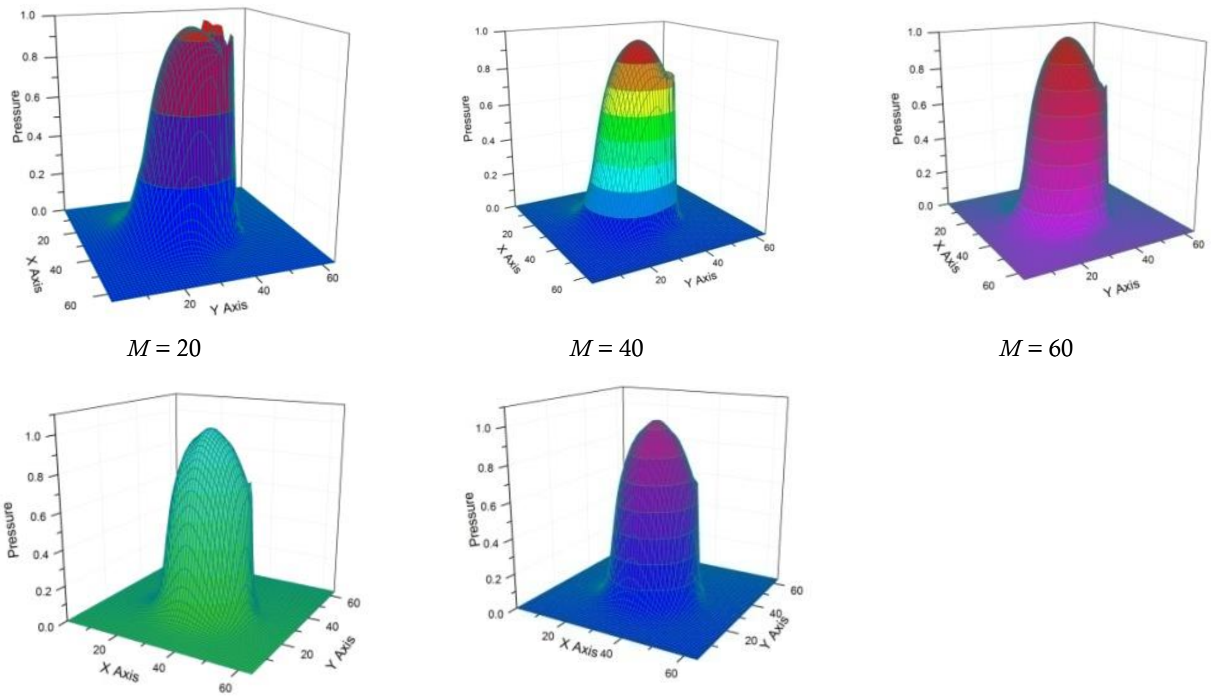

M = 20 *M* = 40 *M* = 60

M = 80 *M* = 100

Figure 5. Isothermal pressure distributions for varying load from *M* = 20 to 100 with the constant speed *L* = 12.04.

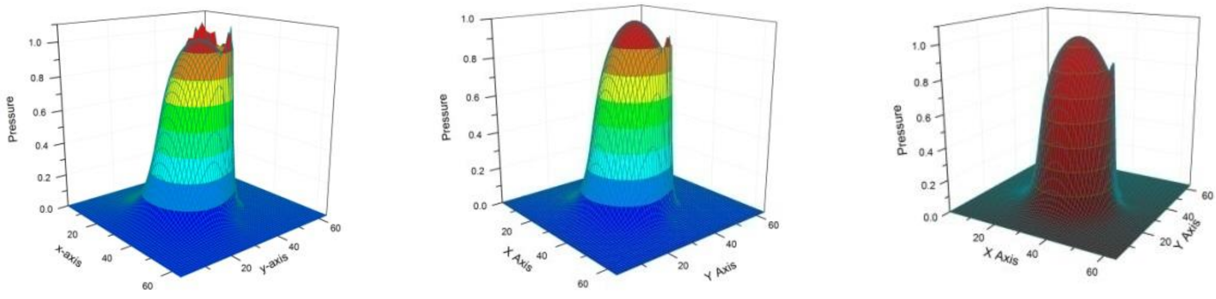

M = 20 *M* = 40 *M* = 60

Figure 6. (*Continued*).

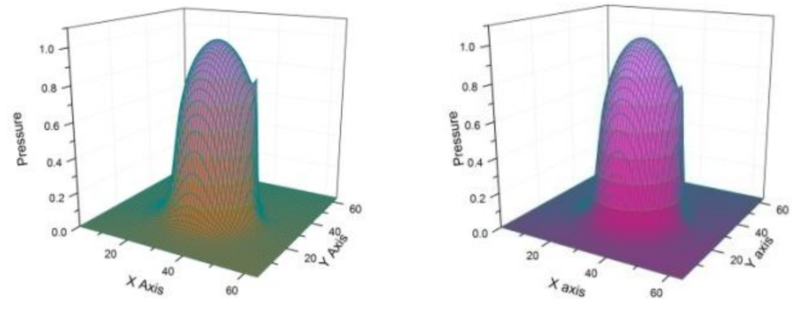

M = 80 M = 100

Figure 6. Thermal pressure distributions for varying load from M = 20 to 100 with the constant speed L = 12.04.

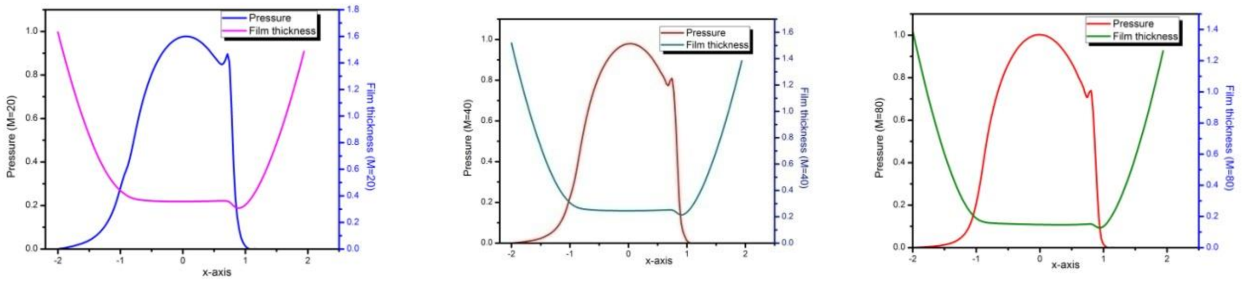

(a) M = 20 **(b)** M = 40 **(c)** M = 80

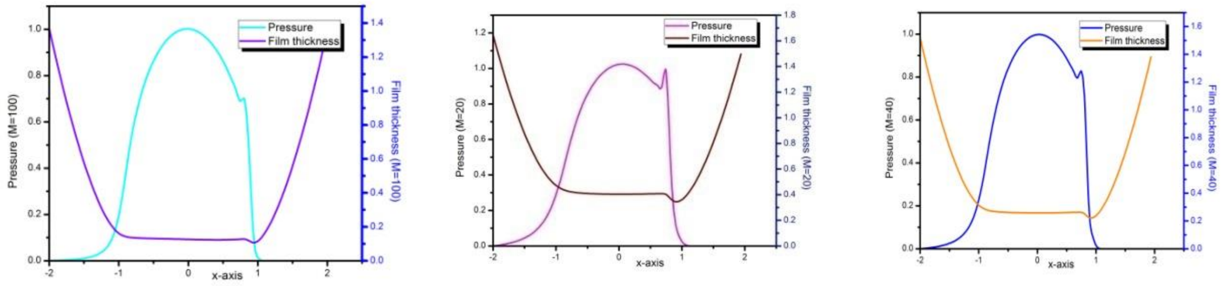

(d) M = 100 **(e)** M = 20 **(f)** M = 40

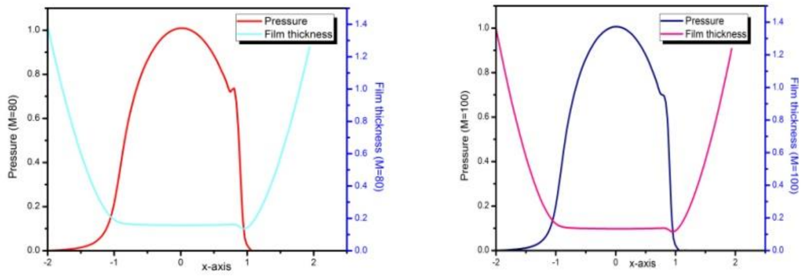

(g) M = 80 **(h)** M = 100

Figure 7. (a)–(d) represent the isothermal pressure and film thickness profiles; and **(e)–(h)** represent thermal pressure and film thickness profiles for varying load from M = 20 to 100 with the constant speed L = 12.04.

Figures 8 and **9** show the mid-film temperature distributions and are exemplified in layer wise temperature profiles, it envisages that, mid-film temperature is much higher than that of surface temperatures, also the mid-film temperature is portrayed in layer 3 and surface temperatures are shown in layer 1 and 2 is describedin **Figure 9**, with varying load $M = 20 - 100$ with $L = 12.04$ and slide to roll ratio 0.25. For varying speed from $L = 13.05, 13.63, 14.27, 14.83$ with constant load $M = 20$ and slide to roll ratio is 0.25, the **Figure 10a–h** demonstrates the pressure distributions with constant load $M = 20$.

The pressure spike increases with increase in speed and comparison between isothermal and thermal pressure distributions are presented in **Figure 10a–d** and **Figure 10e–h**.

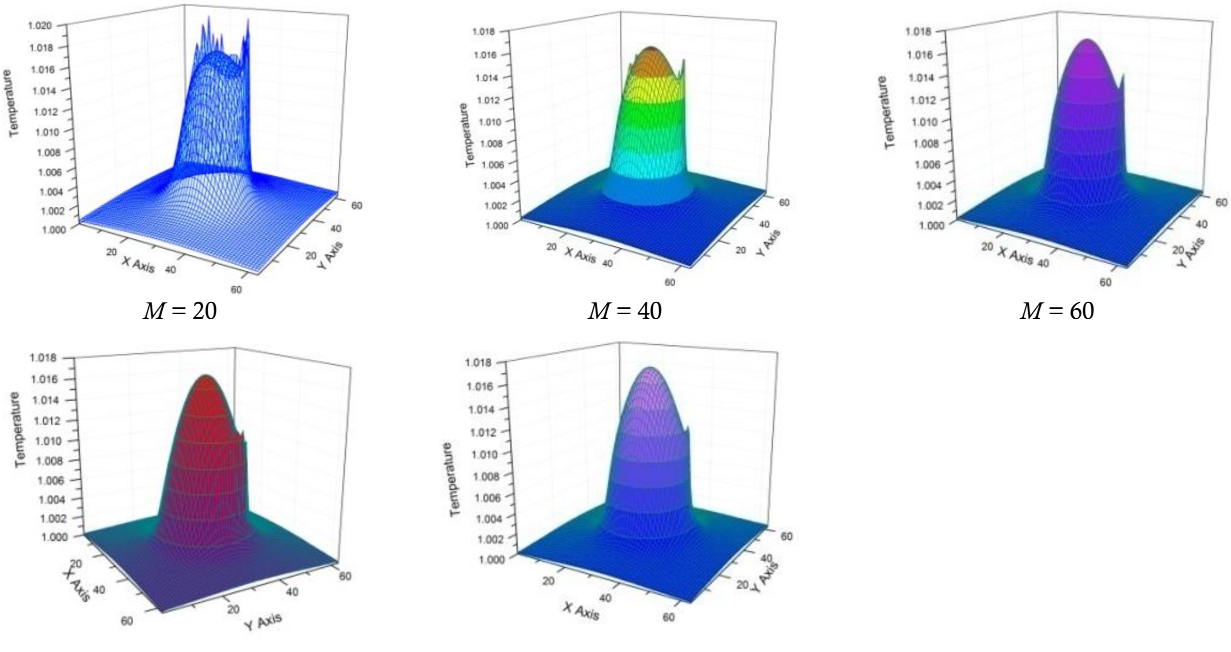

M = 20 *M* = 40 *M* = 60

M = 80 *M* = 100

Figure 8. Mid-film temperature distributions for varying load from *M* = 20 to 100 with the constant speed *L* = 12.04.

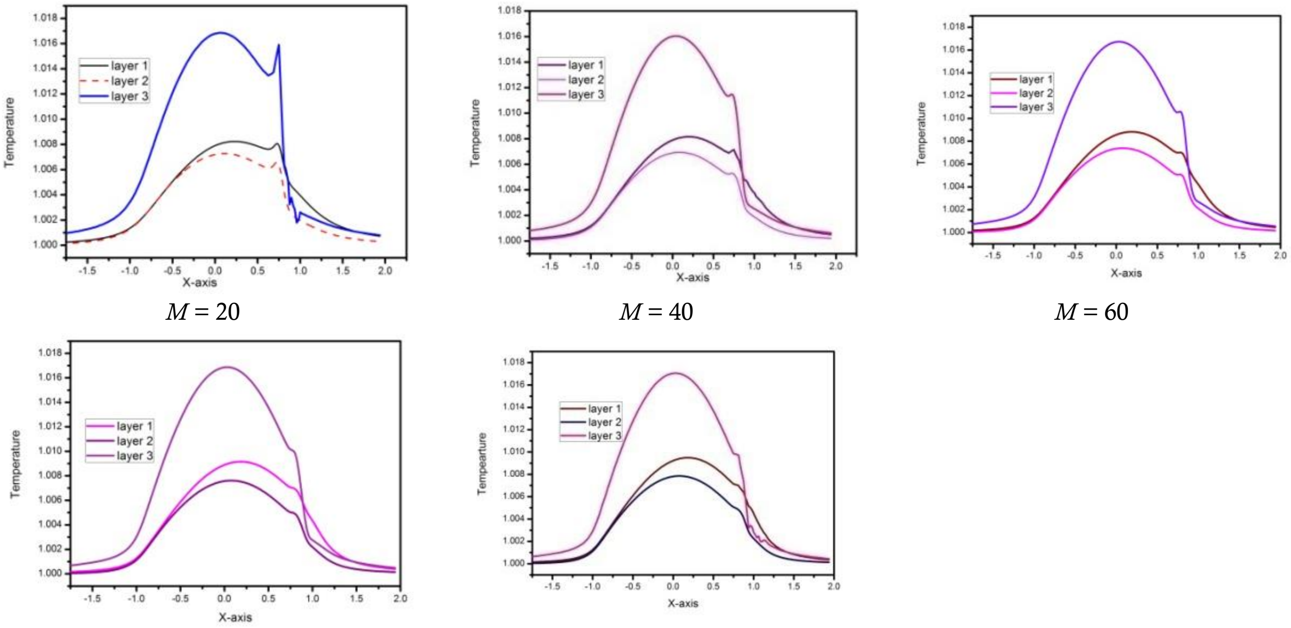

M = 20 *M* = 40 *M* = 60

M = 80 *M* = 100

Figure 9. Layer-wise temperature profiles for varying load from *M* = 20 to 100 with the constant speed *L* = 12.04.

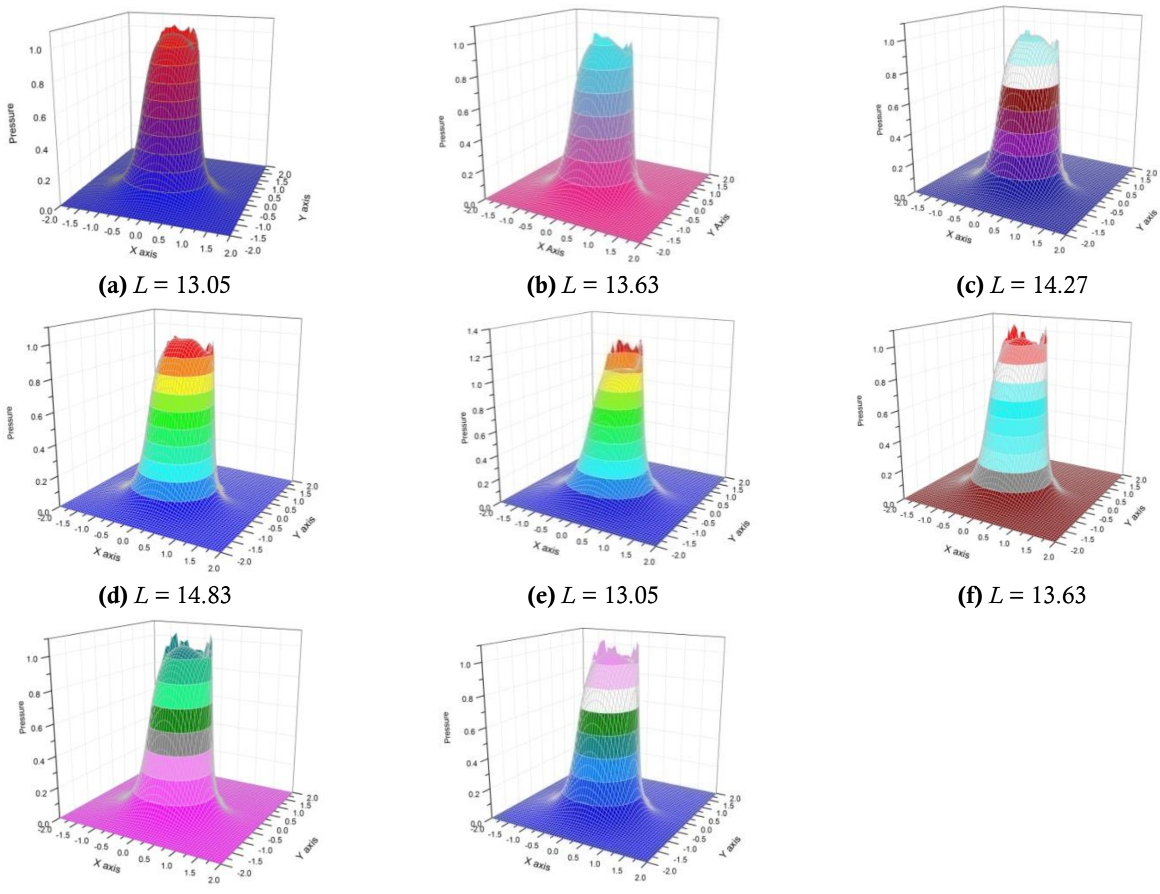

(a) $L = 13.05$ **(b)** $L = 13.63$ **(c)** $L = 14.27$

(d) $L = 14.83$ **(e)** $L = 13.05$ **(f)** $L = 13.63$

(g) $L = 14.27$ **(h)** $L = 14.83$

Figure 10. (a)–(d) represents the isothermal pressure profiles; and **(e)–(h)** represents thermal pressure profiles for varying speed from $L = 13.05$, 13.63, 14.27 and 14.83 with constant load $M = 20$.

The isothermal as wellas thermal film thickness distributions are depicted in **Figure 11**, for varying speed with constant load and slide to roll ratio $L = 13.05, 13.63, 14.27, 14.83. M = 20$, SR = 0.25 respectively, also shows that the occurrence of dimple. The minimum and central film thickness decreases as the speed increases. The contour plots of isothermal and thermal film thickness are exemplified in **Figure 12**, it displays the horse shoe constriction is noticed, also isothermal, thermal pressure and film thickness profiles for varying speed is represented in **Figure 13**. It is observed that, the pressure spike increases with increase in speed. Mid-film temperature profiles are described in **Figure 14** and layer wise surface, mid film temperatures are also demonstrated.

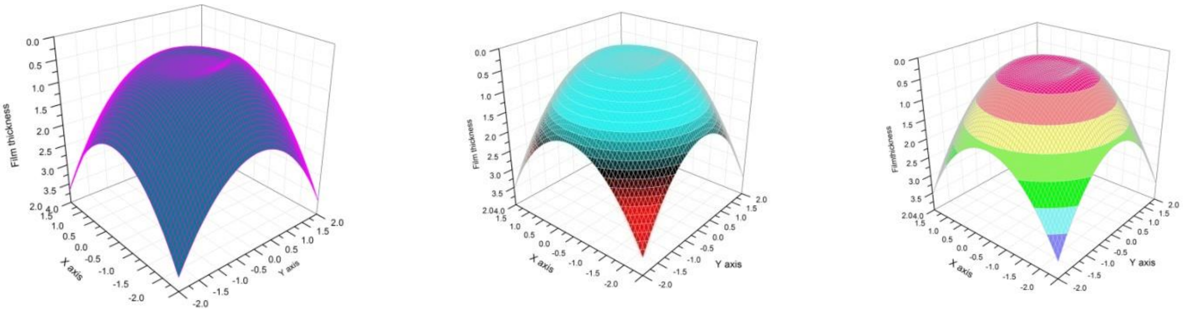

(a) $L = 13.05$ **(b)** $L = 13.63$ **(c)** $L = 14.27$

Figure 11. (*Continued*).

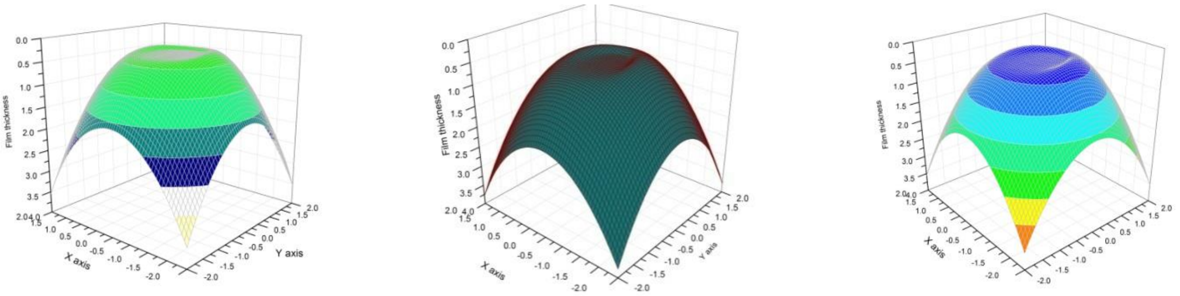

(d) L = 14.83 **(e)** L = 13.05 **(f)** L = 13.63

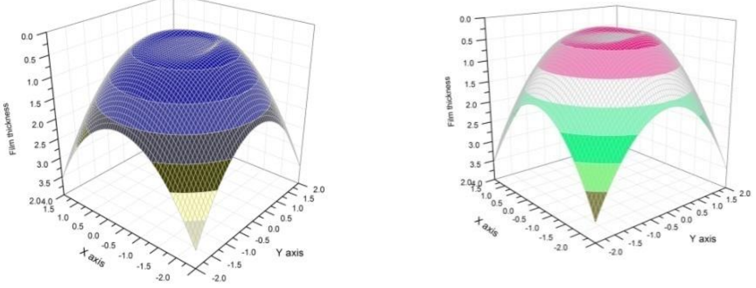

(g) L = 14.27 **(h)** L = 14.83

Figure 11. (a)–(d) represents the isothermal film thickness profiles; and **(e)–(h)** represents thermal film thickness profiles for varying speed from L = 13.05, 13.63, 14.27 and 14.83, with constant load M = 20.

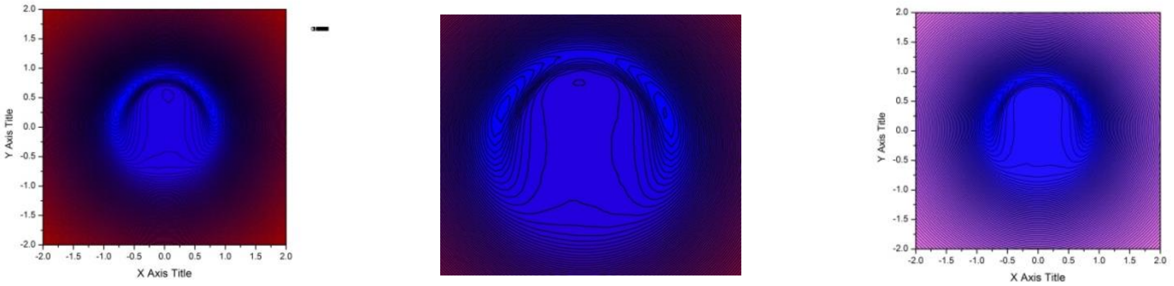

(a) L = 13.05 **(b)** L = 13.63 **(c)** L = 14.27

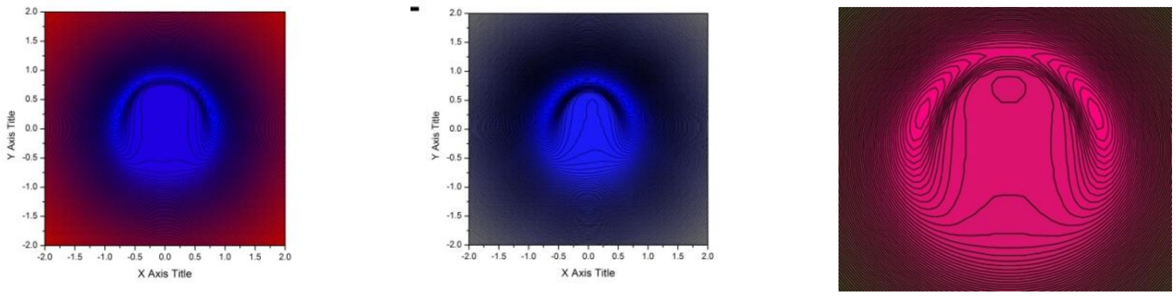

(d) L = 14.83 **(e)** L = 13.05 **(f)** L = 13.63

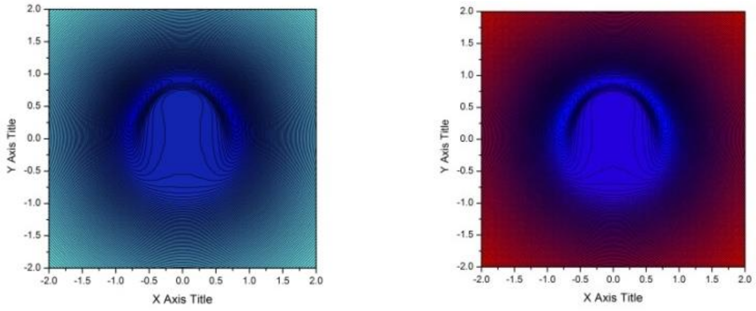

(g) L = 14.27 **(h)** L = 14.83

Figure 12. (a)–(d) represents the contour plots of isothermal film thickness profiles; and **(e)–(h)** represents contour plots of thermal film thickness profiles for varying speed from L = 13.05, 13.63, 14.27 and 14.83, with constant load M = 20.

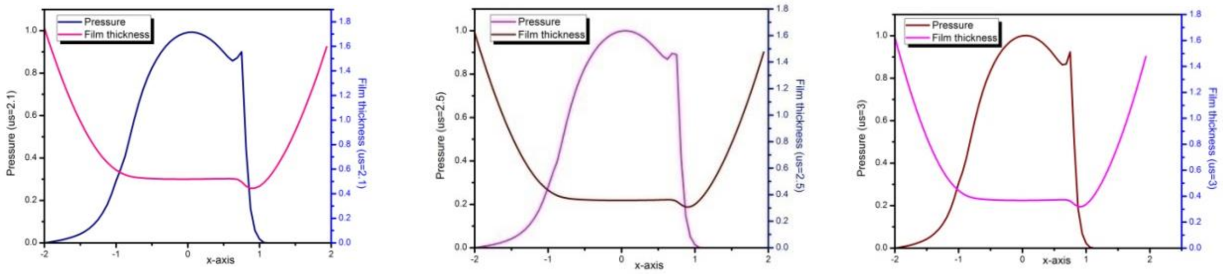

(a) $L = 13.05$ **(b)** $L = 13.63$ **(c)** $L = 14.27$

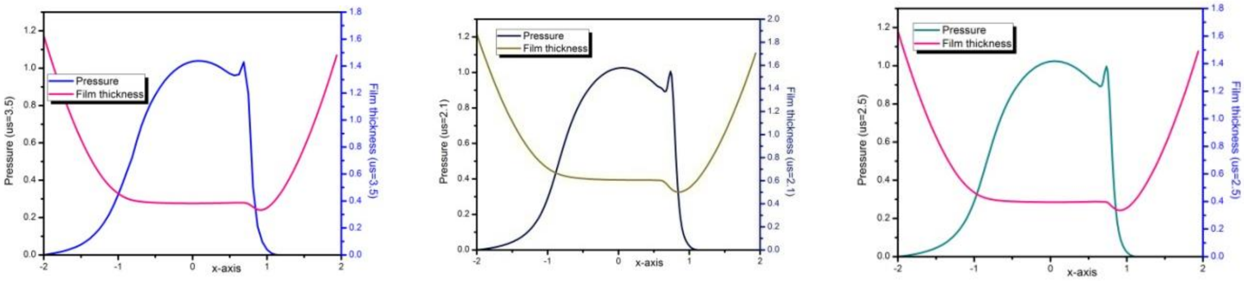

(d) $L = 14.83$ **(e)** $L = 13.05$ **(f)** $L = 13.63$

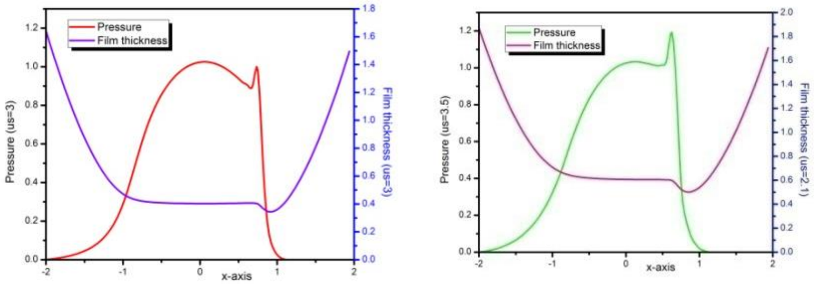

(g) $L = 14.27$ **(h)** $L = 14.83$

Figure 13. **(a)–(d)** represents the isothermal pressure and film thickness profiles; and **(e)–(h)** represents thermal pressure and film thickness profiles for varying speed from $L = 13.05$, 13.63, 14.27 and 14.83, with constant load $M = 20$.

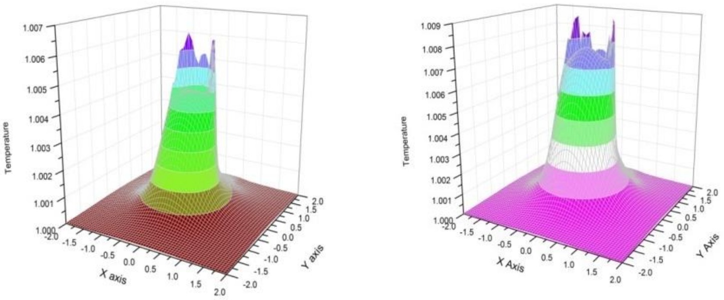

$L = 13.05$ $L = 13.63$

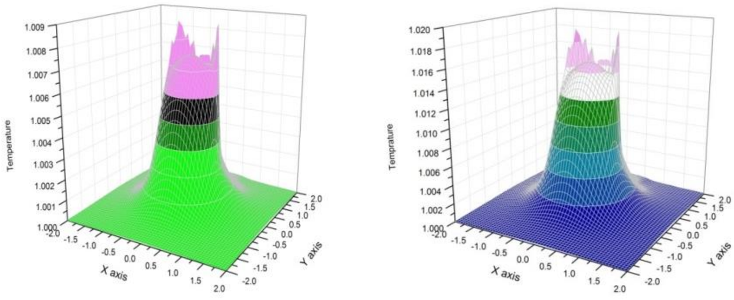

$L = 14.27$ $L = 14.83$

Figure 14. Mid-film temperature profiles for varying speed from $L = 13.05$, 13.63, 14.27 and 14.83, with constant load $M = 20$.

The surface roughness is included in the present computation i.e., $\bar{A}\, cos\left(\frac{2\pi X'}{\hat{W}}\right)$, where $\bar{A} = 0.495 \times 10^{-06}$ the amplitude is $\hat{W} = 0.25 \times 10^{-03}$ is the dimensionless wavelength. The waviness oriented at 45° to the direction of entrainment under thermal conditions with SR = 0.25. Ehret et al.[54] considered only isothermal case and studied the effect of waviness on film thickness under high load with pure sliding conditions. It is examined that, the effect of waviness under thermal conditions and SR. The isothermal and thermal pressure profiles for various load $M = 126, 150, 200, 350, 500$ with SR = 0.25 is inspected and described in **Figures 15** and **16**. It shows that, the ridges and pressure spike appear at the outlet region. The contour plots of isothermal and thermal film thickness distributions are illustrated in **Figures 17** and **18** respectively. Actually wavinessdescribes flow at the entrance of the contact and lubricant leakage flow which accumulates at the entrance. The layer wise temperature profiles are depicted in **Figure 19** and it depicts that, finger like projections in the temperature profiles.

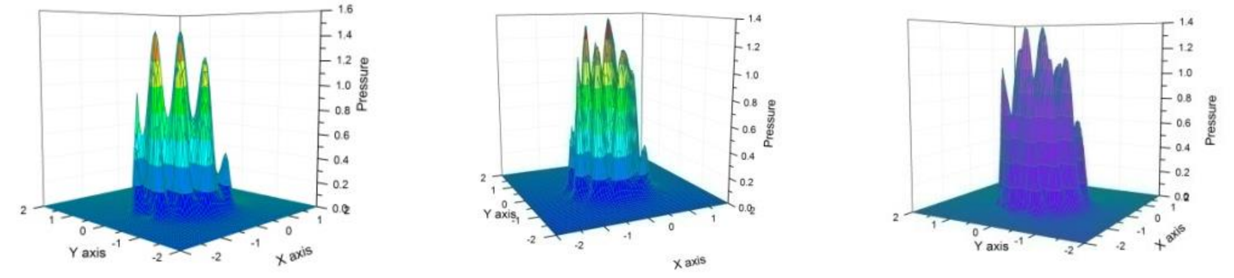

M = 126 M = 150 M = 200

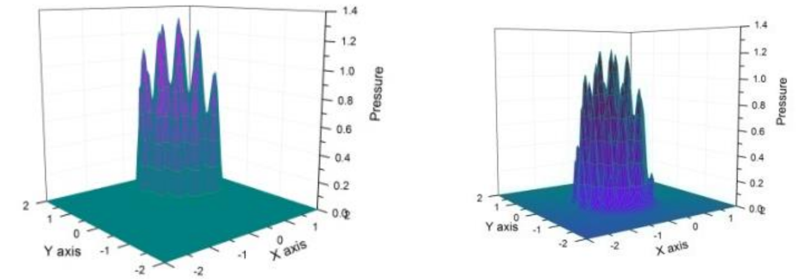

M = 350 M = 500

Figure 15. Isothermal pressure distributions for various load M = 126, 150, 200, 350, 500 with the constant speed L = 12.34 and surface roughness.

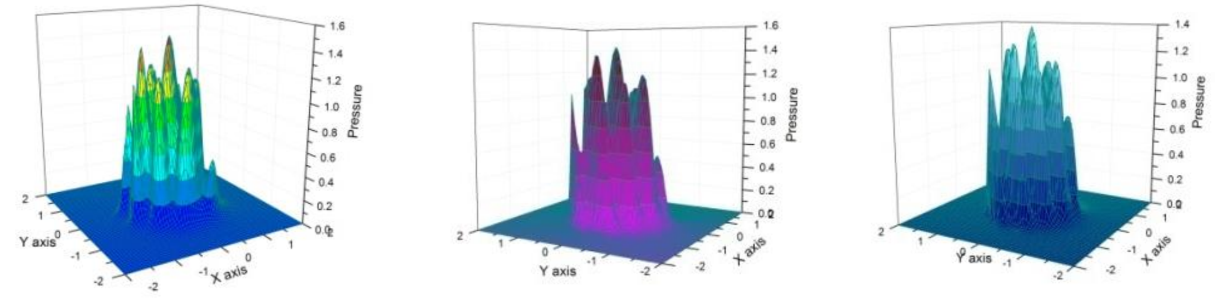

M = 126 M = 150 M = 200

Figure 16. (*Continued*).

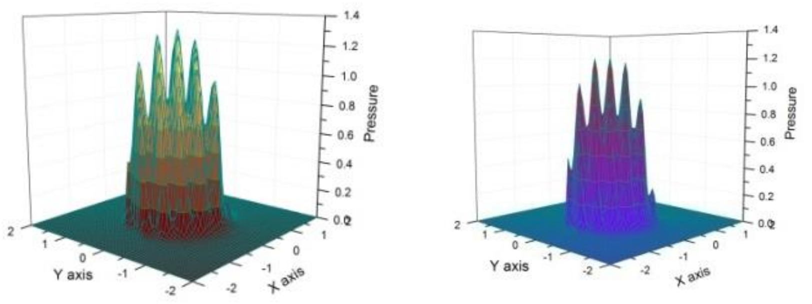

$M = 350$ $M = 500$

Figure 16. Thermal pressure distributions for various load $M = 126, 150, 200, 350, 500$ with the constant speed $L = 12.34$ and surface roughness.

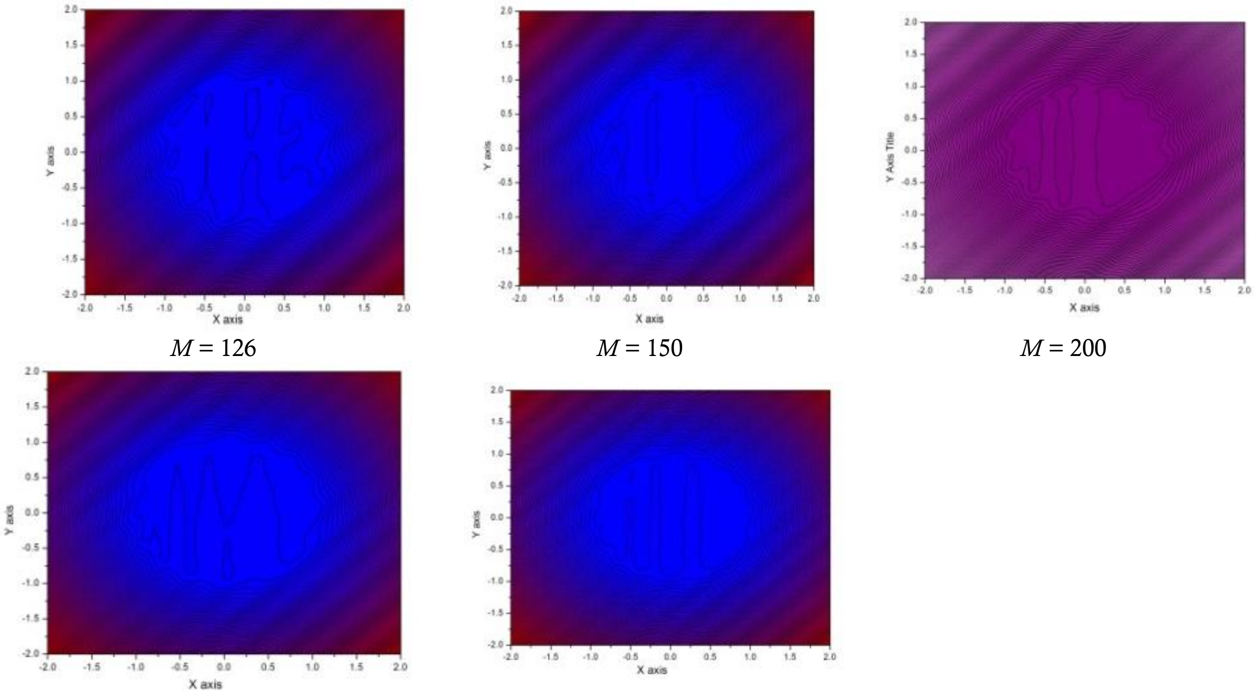

$M = 126$ $M = 150$ $M = 200$

$M = 350$ $M = 500$

Figure 17. Contour plot of isothermal film thickness for various load $M = 126, 150, 200, 350, 500$ with the constant speed $L = 12.34$ and surface roughness.

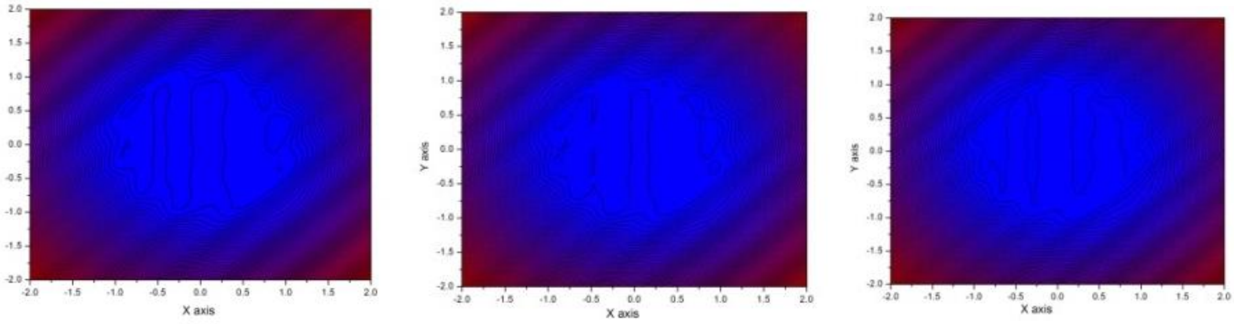

$M = 126$ $M = 150$ $M = 200$

Figure 18. (*Continued*).

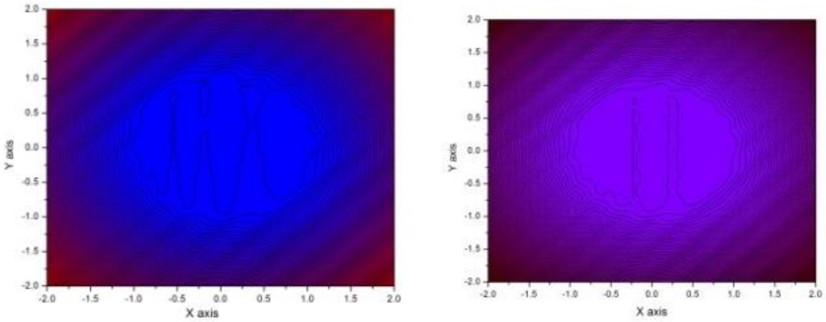

M = 350 *M* = 500

Figure 18. Contour plot of thermal film thickness for various load *M* = 126, 150, 200, 350, 500 with the constant speed *L* = 12.34 and surface roughness.

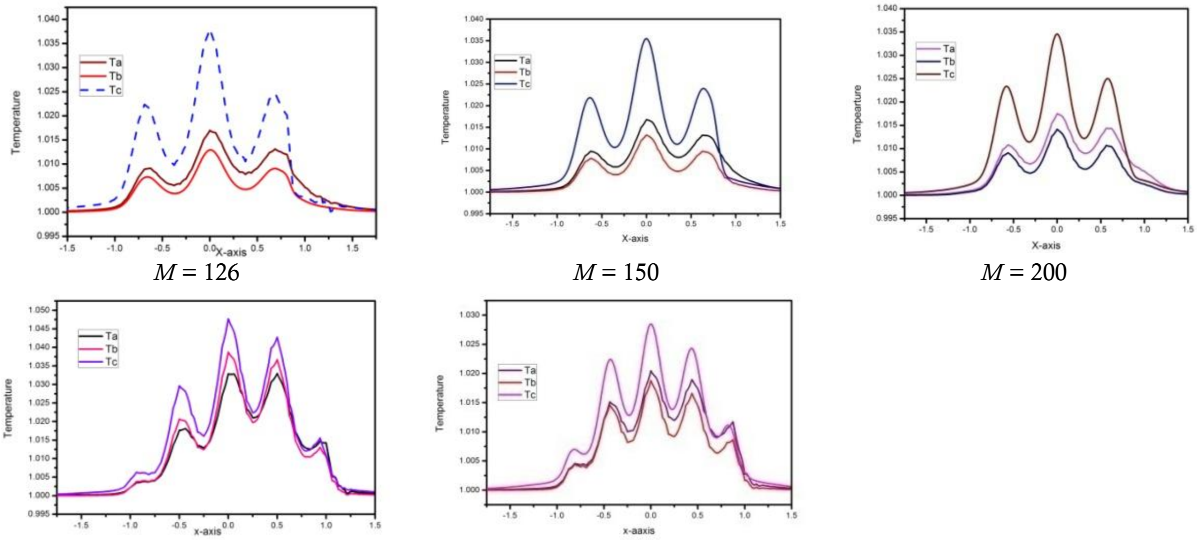

M = 126 *M* = 150 *M* = 200

M = 350 *M* = 500

Figure 19. Layer-wise temperature profiles for various load *M* = 126, 150, 200, 350, 500 with the constant speed *L* = 12.34 and surface roughness.

The effect of slide to roll ratio on fluid film thickness is discussed for SR = −1, −0.5, 0, 0.5,1. The contour plots of isothermal and thermal film thickness profiles are illustrated in **Figures 20** and **21** respectively. It predicts that, the minimum film thickness is much smaller when slide to roll ratio is positive as compared to negative. Whereas central film thickness contrasts to that of minimum film thickness, is described in **Table 3**. It is perceived that, the position of minimum film thickness in the contour plots, when slide to roll ratio is negative, minimum film thickness located at the side lobes of horse shoe shaped constriction. As slide to roll ratio becomes positive the location of minimum film thickness shift towards back of the horse shoe constriction. The isothermal and thermal pressure profiles are exemplified respectively in **Figures 22** and **23**, and mid-film temperature distributions are depicted in **Figure 24**. The load $M = 57.21$ with speed $L = 10.52$, when the slide to roll ratio increases from 0.5 to1, the pressure spike and central pressure increases due to the action of temperature-viscosity wedge term and there is occurrence of another peak. Also, central pressure and pressure spike values are smaller when slide to roll ratio is negative. The occurrence and action of temperature-viscosity wedge action is purely governed by EHL pressure spike.

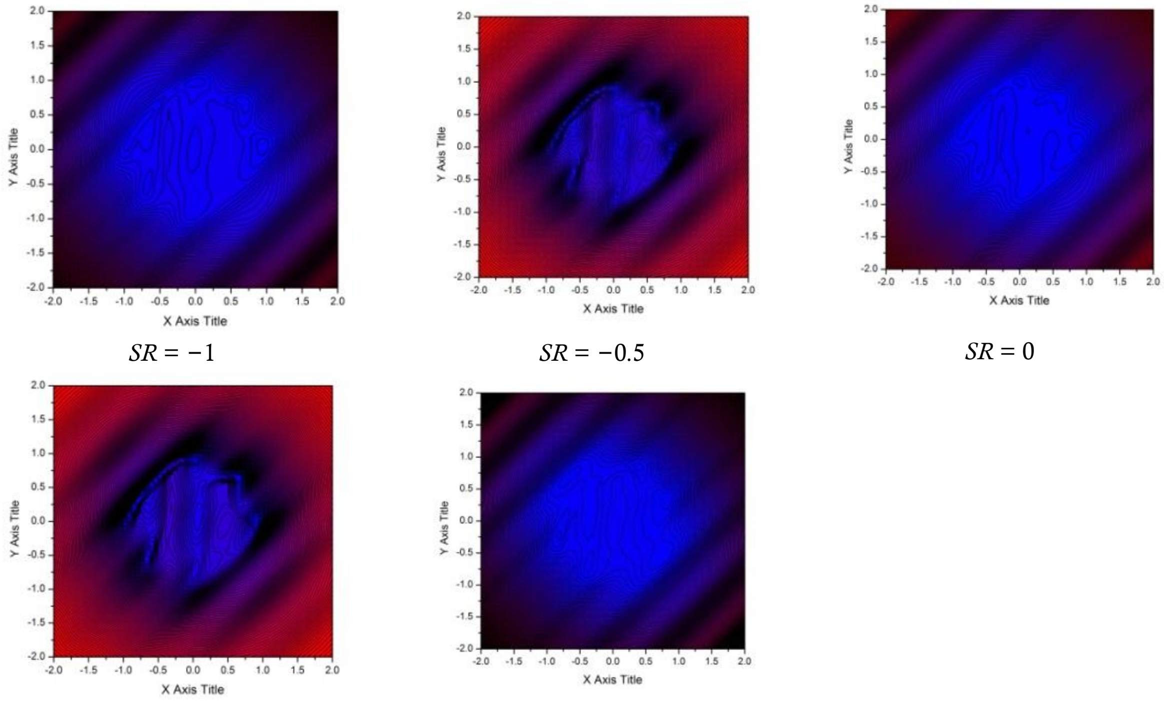

$SR = -1$ $SR = -0.5$ $SR = 0$

$SR = 0.5$ $SR = 1$

Figure 20. Contour plot of isothermal film thickness for various slide to roll ratio at constant load and speed with surface roughness.

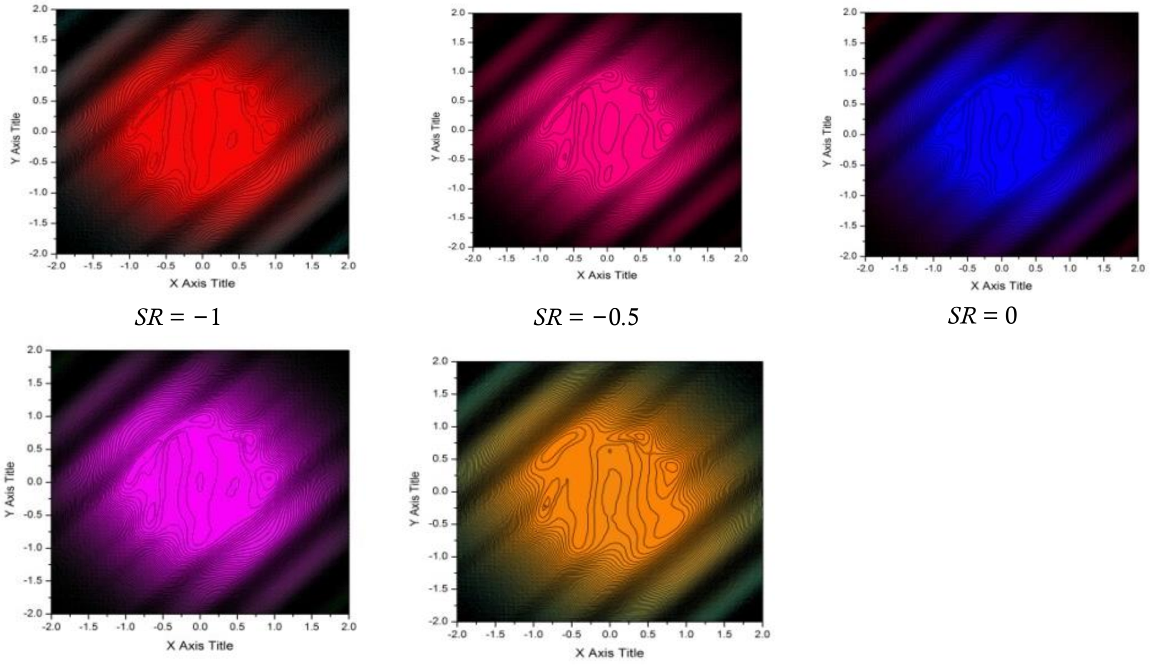

$SR = -1$ $SR = -0.5$ $SR = 0$

$SR = 0.5$ $SR = 1$

Figure 21. Contour plot of thermal film thickness for various slide to roll ratio at constant load and speed with surface roughness.

Table 3. Comparison of isothermal and thermal film thickness for various slide to roll ratios.

Slide to roll ratio (SR)	Isothermal film thickness		Thermal film thickness	
	H_{min}	H_{cen}	H_{min}	H_{cen}
−1	0.1683	0.2433	0.0818	0.1783
−0.5	0.1669	0.2405	0.1498	0.2428
0	0.1687	0.2437	0.1684	0.2597
0.5	0.1650	0.2372	0.1530	0.2449
1	0.1669	0.2405	0.1117	0.2058

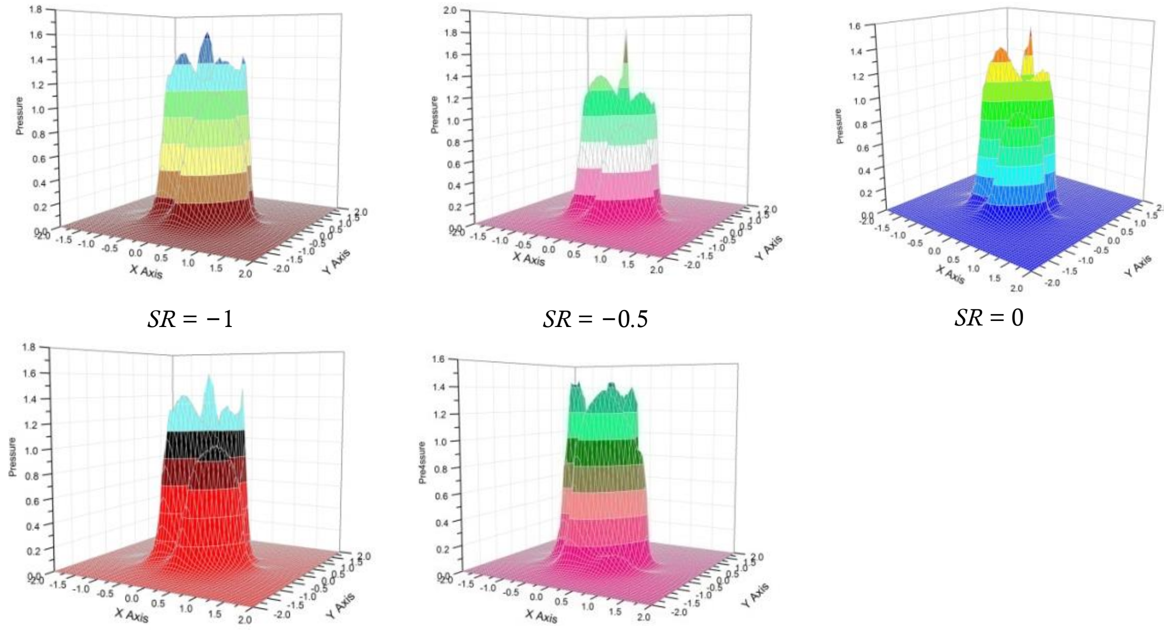

$SR = -1$ $SR = -0.5$ $SR = 0$

$SR = 0.5$ $SR = 1$

Figure 22. Isothermal pressure distributions for various slide to roll ratio at constant load and speed with surface roughness.

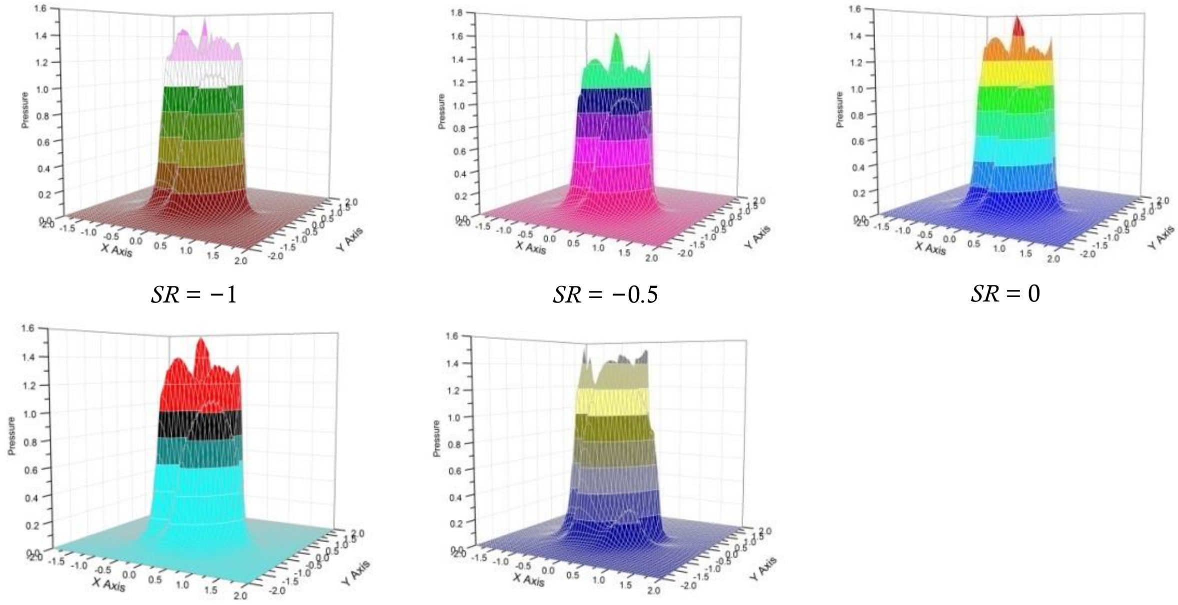

$SR = -1$ $SR = -0.5$ $SR = 0$

$SR = 0.5$ $SR = 1$

Figure 23. Thermal pressure profiles for various slide to roll ratio at constant load and speed with surface roughness.

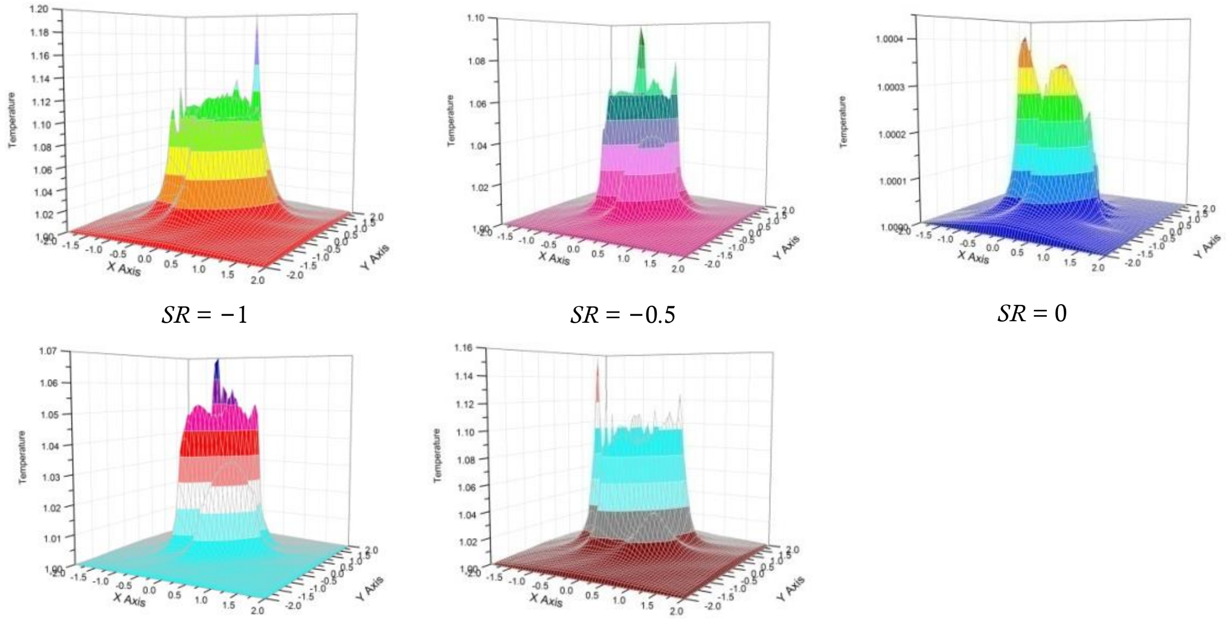

$SR = -1$ $SR = -0.5$ $SR = 0$

$SR = 0.5$ $SR = 1$

Figure 24. Mid-film temperature distributions for various slide to roll ratio at constant load and speed with surface roughness.

5. Conclusions

From theabove study the following conclusions are drawn

1) The pressure spike and film thickness decreases with increase in load, whereas pressurespike and film thickness increases with increase in speed.
2) Isothermal minimum film thickness is larger than the thermal minimum film thickness due to rise in the temperature at the contact region.
3) Surface temperature distribution is smaller as compared to contact temperature distribution.
4) When slide to roll ratio is positive the pressure spike and central pressure profiles increases due to the action of temperature-viscosity wedge term and there is occurrence of another peak. Also, the central pressure and pressure spike values are smaller when slide to roll ratio is negative.
5) Minimum film thickness is much smaller when slide to roll ratio is positive as compared to negative, whereas central film thickness behavior is contrast to that of minimum film thickness.

Author contributions

Conceptualization, VBA; methodology, VBA, PMO and MKN; validation, VBA, PMO and MKN; formal analysis, PMO and MKN; investigation, VBA, PMO and MKN; writing—original draft preparation, VBA, PMO and MKN; writing—review and editing, VBA, PMO and MKN; supervision, VBA. All authors have read and agreed to the published version of the manuscript.

Conflict of interest

The authors declare no conflict of interest.

References

1. Crook AW. The lubrication of rollers III. A theoretical discussion of friction and the temperatures in the oil film. Philosophical Transactions of the Royal Society of London. Series A, Mathematical and Physical Sciences 1961; 254(1040): 237–258.doi: 10.1098/rsta.1961.0016

2. Sternlicht B, Lewis P, Flynn P. Theory of lubrication and failure of rolling contacts. Journal of Basic Engineering 1961; 83(2): 213–222. doi: 10.1115/1.3658927
3. Cheng HS, Sternlicht B. A numerical solution for the pressure, temperature, and film thickness between two infinitely long, lubricated rolling and sliding cylinders, under heavy loads. Journal of Basic Engineering 1965; 87(3): 695–704.doi: 10.1115/1.3650647
4. DowsonD, Whitaker AV. Paper 4: A numerical procedure for the solution of the elastohydrodynamic problem of rolling and sliding contacts lubricated by a Newtonian fluid. Proceedings of the Institution of Mechanical Engineers 1965; 180(2): 57–71.doi: 10.1243/PIME_CONF_1965_180_064_0
5. Murch LE, Wilson WRD. A thermal elastohydrodynamic inlet zone analysis. Journal of Lubrication Technology 1975; 97(2): 212–216. doi: 10.1115/1.3452559
6. BruggemannH, Kollmann FG. A numerical solution of the thermal elastohydrodynamic lubrication in an elliptical contact. Journal of Lubrication Technology 1982; 104(3): 392–400. doi: 10.1115/1.3253231
7. Kim KH, Sadeghi F. Three-dimensional temperature distribution in EHD lubrication: Part I—Circular contact. Journal of Tribology 1992; 114(1): 32–41. doi: 10.1115/1.2920864
8. Kim KH, Sadeghi F. Three-dimensional temperature distribution in EHD lubrication: Part II—Point contact and numerical formulation. Journal of Tribology 1993; 115(1): 36–45. doi: 10.1115/1.2920984
9. Salehizadeh H, Saka N. Thermal non-Newtonian elastohydrodynamic lubrication of rolling line contacts. Journal of Tribology 1991; 113(3): 481–491.doi: 10.1115/1.2920649
10. Wolff R, Kubo A. The application of Newton-Raphsonmethod to thermal elastohydrodynamic lubrication of line contacts. Journal of Tribology 1994; 116(4): 733–740.doi: 10.1115/1.2927327
11. Kazama T, Ehret P, Taylor CM. On the effects of the temperature profile approximation in thermal Newtonian solutions of elastohydrodynamic lubrication line contacts. Proceedings of the Institution of Mechanical Engineers, Part J: Journal of Engineering Tribology 2001; 215(1): 109–120.doi: 10.1243/1350650011541666
12. Lee RT, Hsu CH, KuoWF. Multilevel solution for thermal elastohydrodynamic lubrication of rolling/sliding circular contacts. Tribology International 1995; 28(8): 541–552. doi: 10.1016/0301-679X(96)85542-3
13. Ehret P, DowsonD, Taylor CM. Thermal effects in elliptical contacts with spin conditions. Tribology Series 1999; 36: 685–703. doi: 10.1016/S0167-8922(99)80088-1
14. Qu S, Yang P, Guo F. Theoretical investigation on the dimple occurrence in the thermal EHL of simple sliding steel-glass circular contacts. Tribology International 2000; 33(1): 59–65.doi: 10.1016/S0301-679X(00)00031-1
15. Yang P, Qu S,Kaneta M, Nishikawa H. Formation of steady dimples in point TEHL contacts. Journal of Tribology 2001; 123(1): 42–49.doi: 10.1115/1.1332399
16. Guo F, Yang P, Qu S. On the theory of thermal elastohydrodynamic lubrication at high slide-roll ratios—Circular glass-steel contact solution at opposite sliding. Journal of Tribology 2001; 123(4): 816–821. doi: 10.1115/1.1330739
17. Kim HJ, Ehret P, Dowson D, Taylor CM. Thermal elastohydrodynamic analysis of circular contacts part 1: Newtonian model. Proceedings of the Institution of Mechanical Engineers, Part J: Journal of Engineering Tribology 2001; 215(4): 339–352.doi: 10.1243/1350650011543583
18. Kim HJ, Ehret P, Dowson D, Taylor CM. Thermal elastohydrodynamic analysis of circular contacts part 2: Non-Newtonian model. Proceedings of the Institution of Mechanical Engineers, Part J: Journal of Engineering Tribology 2001; 215(4): 353–362. doi: 10.1243/1350650011543592
19. CannPM,Spikes HA. Determination of the shear stress of lubricants in elastohydrodynamic contacts. Tribology Transactions 1989; 32(3): 414–422. doi: 10.1080/10402008908981908
20. Liu X, Jiang M, Yang P, Kaneta M. Non-Newtonian thermal analyses of point EHL contacts using the Eyring model. Journal of Tribology 2005; 127(1): 70–81. doi: 10.1115/1.1843161
21. Greenwood JA, Williamson JBP. Contact of nominally flat surfaces. Proceedings of the Royal Society of London (A). Mathematical and Physical Sciences 1966; 295(1442): 300–319. doi: 10.1098/rspa.1966.0242
22. Greenwood JA, Tripp JH. The contact of two nominally flat rough surfaces. Proceedings of the Institution of Mechanical Engineers 1970; 185(1): 625–633.doi: 10.1243/PIME_PROC_1970_185_069_02
23. Patir N, Cheng HS. An average flow model for determining effects of three-dimensional roughness on partial hydrodynamic lubrication. Journal of Lubrication Technology 1978; 100(1): 12–17. doi: 10.1115/1.3453103
24. Sadeghi, F, SuiPC. Thermal elastohydrodynamic lubrication of rough surfaces. Journal of Tribology 1990; 112(2): 341–346. doi: 10.1115/1.2920262
25. Chang L. A deterministic model for line-contact partial elastohydrodynamic lubrication. Tribology International 1995; 28(2): 75–84.doi: 10.1016/0301-679X(95)92697-4
26. Hu YZ,Zhu D. A full numerical solution to the mixed lubrication in point contacts. Journal of Tribology 2000; 122(1): 1–9. doi: 10.1115/1.555322

27. Wang QJ, Zhu D, Cheng HS, et al. Mixed lubrication analyses by a macro-micro approach and a full-scale mixed EHL model. Journal of Tribology 2004; 126(1): 81–91. doi: 10.1115/1.1631017
28. Lu X, Khonsari MM, Gelinck ERM. The stribeck curve: Experimental results and theoretical prediction. Journal of Tribology 2006; 128(4): 789–794. doi: 10.1115/1.2345406
29. Deolalikar N, Sadeghi F, Marble S. Numerical modeling of mixed lubrication and flash temperature in EHL elliptical contacts. Journal of Tribology 2008; 130(1): 011004. doi: 10.1115/1.2805429
30. Yang P, Cui J, Jin ZM, DowsonD. Influence of two-sided surface waviness on the EHL behavior of rolling/sliding point contacts under thermal and non-Newtonian conditions. Journal of Tribology 2008; 130(4): 041502. doi: 10.1115/1.2958078
31. Akbarzadeh S, Khonsari MM. Performance of spur gears considering surface roughness and shear thinning lubricant. Journal of Tribology 2008; 130(2): 021503. doi: 10.1115/1.2805431
32. Sojoudi H, Khonsari MM. On the behavior of friction in lubricated point contact with provision for surface roughness. Journal of Tribology 2010; 132(1): 012102. doi: 10.1115/1.4000306
33. Zhu D, Wang QJ. Effect of roughness orientation on the elastohydrodynamic lubrication film thickness. Journal of Tribology 2013; 135(3): 031501.doi: 10.1115/1.4023250
34. Masjedi M, Khonsari MM. On the effect of surface roughness in point-contact EHL: Formulas for film thickness and asperity load. Tribology International 2015; 82(A): 228–244. doi: 10.1016/j.triboint.2014.09.010
35. Awati VB, Naik S, Kumar M.Multigrid method for the solution of EHL point contact with bio-based oil as lubricants for smooth and rough asperity. Industrial Lubrication and Tribology 2018; 70(4): 599–611.doi: 10.1108/ILT-12-2016-0314
36. Zhang B, Wang J, Omasta M, Kaneta M. Variation of surface dimple in point contact thermal EHL under ZEV condition. Tribology International 2016; 94: 383–394.doi: 10.1016/j.triboint.2015.09.036
37. Cui J, Yang P, Kaneta M, Krupka I. Numerical study on the interaction of transversely oriented ridges in thermal elastohydrodynamic lubrication point contacts using the Eyring shear-thinning model. Proceedings of the Institution of Mechanical Engineers, Part J: Journal of Engineering Tribology 2017; 231(1): 93–106.doi: 10.1177/1350650116646943
38. Awati VB, Kumar NM, Bujurke NM. Numerical solution of thermal EHL line contact with bio-based oil as lubricant. Australian Journal of Mechanical Engineering 2022; 20(1): 231–244.doi: 10.1080/14484846.2019.1699720
39. Liu X, Cui J, Yang P. Size effect on the behavior of thermal elastohydrodynamic lubrication of roller pairs. Journal of Tribology 2012; 134(1): 011502. doi: 10.1115/1.4005515
40. Hultqvist T, Vrcek A, Marklund P, et al. Transient analysis of surface roughness features in thermal elastohydrodynamic contacts. Tribology International 2019; 141: 10595.doi: 10.1016/j.triboint.2019.105915
41. Zhao Y, Wong PL, Mao JH. Solving coupled boundary slip and heat transfer EHL problem under large slide-roll ratio conditions. Tribology International 2019; 133: 73–87.doi: 10.1016/j.triboint.2019.01.013
42. Zhang M, Wang J, Yang P, et al. A thermal EHL investigation for size effect of finite line contact on bush-pin hinge pairs in industrial chains. Industrial Lubrication and Tribology 2019; 72(5): 695–701.doi: 10.1108/ILT-10-2019-0448
43. Zhang M, Wang J, Cui J, Yang P. A thermal investigation on plate-pin hinge pairs in silent chains using a narrow finite line contact. Industrial Lubrication and Tribology 2020; 72(10): 1139–1145. doi: 10.1108/ILT-11-2019-0498
44. Zhao Y, Wong PL. Thermal-EHL analysis of slip/no-slip contact at high slide-to-roll ratio. Tribology International 2021; 153: 106617. doi: 10.1016/j.triboint.2020.106617
45. Brandt A. Multi-level adaptive solutions to boundary-value problems. Mathematics of Computation 1977; 31(138): 333–390.
46. Lubrecht AA, ten Napel WE, Bosma R.Multigrid, an alternative method of solution for two-dimensional elastohydrodynamically lubricated point contact calculations. Journal of Tribology 1987; 109(3): 437–443.doi: 10.1115/1.3261467
47. Venner C. Multilevel Solution of the EHL Line and Point Contact Problems [PhD thesis]. University of Twente; 1991.
48. Roelands CJA, Winer WO, Wright WA. Correlational aspects of the viscosity-temperature-pressure relationship of lubricating oils.(Dr In dissertation at Technical University of Delft, 1966). Journal of Lubrication Technology 1971; 93(1): 209–210.doi: 10.1115/1.3451519
49. Dowson D, Higginson GR. Elasto-Hydrodynamic Lubrication: The Fundamentals of Roller Gear Lubrication. Pergamon Press; 1966.
50. Pai SI. Viscous Flow Theory, Vol. 1 (One): Laminar Flow. D. Van Nostrand Company; 1956.
51. Liu J. Thermal Non-Newtonian Elastohydrodynamic Lubrication of Point Contacts [PhD thesis]. The University of Leeds; 1994.

52. Venner CH, Lubrecht AA. Multi-Level Methods in Lubrication. Elsevier; 2000.
53. Hamrock BJ, Dowson D. Isothermal elastohydrodynamic lubrication of point contacts: Part 3—Fullyflooded results. Journal of Lubrication Technology 1977; 99(2): 264–275. doi: 10.1115/1.3453074
54. Ehret P, Dowson D, Taylor CM, Wang D. Analysis of isothermal elastohydrodynamic point contacts lubricated by Newtonian fluids using m-ultigrid methods. Proceedings of the Institution of Mechanical Engineers, Part C: Journal of Mechanical Engineering Science 1997; 211(7): 493–508.doi: 10.1243/0954406971521881

Mechanical Engineering Advances 2023; 1(1): 132.
Original Research Article

Thermal and viscous irreversibilities in the heat exchanger of individually finned heat pipes using freon R404A as the working fluid

Élcio Nogueira

Department of Mechanic and Energy, State University of Rio de Janeiro, Resende 27537-000, Rio de Janeiro, Brazil; elcionogueira@hotmail.com

ARTICLE INFO

Received: 16 September 2023
Accepted: 20 September 2023
Available online: 18 October 2023

doi: 10.59400/mea.v1i1.132

ABSTRACT: This work aims to apply a theoretical procedure to determine the performance of the heat exchanger of individually finned heat pipes used in an air conditioning system. The relevant physical quantities are defined and specified locally in the evaporator and condenser sections. The results obtained in the sections are associated with the theoretical determination of the global performance of the heat exchanger. Global theoretical results are compared with global experimental results. Thermal effectiveness, heat transfer rate, pressure drop, thermal and viscous irreversibilities, and thermodynamic Bejan number are determined at the evaporator, condenser, and heat exchanger. The relevant variables used to determine the results are the number of fins per heat pipe and rows of heat pipes. The theoretical-experimental comparison demonstrates that the localized model applied in the analysis is consistent and can be used as a design and comprehensive analysis tool for finned heat exchangers. The performance of the heat exchanger demonstrated exceptional when comparing irreversibilities through the Bejan number, indicating a favorable cost-benefit ratio for the fins less than 30 and the number of heat pipes equal to 49. Bejan's thermodynamic number, which uses results related to thermal and viscous irreversibilities, demonstrated that one should look for the relationship between thermal irreversibility versus total irreversibility and that fin numbers between 10 and 20 for heat pipes equal to 49 provide a better cost-benefit ratio. The absolute percentage errors obtained between theoretical and experimental values, for an experimental number of fins equal to 30, for the overall heat transfer rate and overall thermal effectiveness range from 2.0% to 42.1%.

KEYWORDS: heat exchanger; individually finned heat pipe; air conditioning; freon R404A; thermal irreversibility; viscous irreversibility

1. Introduction

This work aims to apply the theory of thermal efficiency, based on the fin analogy and the second law of thermodynamics, to determine quantities of practical interest related to finned heat tube heat exchangers. The pioneering method advocated was initially applied locally in the evaporator and Condenser. The results obtained locally were used for theoretical-experimental comparison using global experimental results obtained for the heat exchanger under analysis[1].

The heat exchanger under analysis consisted of individually finned heat pipes and was taken from theoretical-experimental work, presented through reference[1]. The apparatus was designed so that the configuration of the heat pipes is in a staggered formation. The number of heat pipes ranges from 7 to 49, and the number of rows from 3 to 21. The number of fins per heat pipe ranges from 0 to 40 in the theoretical model.

Górecki et al.[1] perform modeling and present an experimental study on a heat exchanger used as energy recovery in small air conditioning systems composed of individually finned heat pipes and R404A refrigerant as the working fluid. Parametric calculations were performed, and it was concluded that 20 rows of finned heat pipes in the staggered arrangement guarantee efficiency close to 60%. The experimental results showed a good level of agreement with the developed model. The heat pipes used in the experiments are 1 mm thick copper tubes with an external diameter of 20 mm, with aluminum fins. They used a computational model to obtain heat transfer rates, effectiveness, and pressure drop. The 20-row heat pipes exhibited stable efficiency and acceptable pressure drop. They used 70 heat pipes in staggered arrangements of four and three tubes.

Nogueira[2] uses a theoretical model to calculate the thermal performance of heat exchangers with individually finned heat pipes. The model is localized and applied individually to the evaporator, condenser, and heat exchanger regions. The quantities used for performance analysis were the number of fins per heat pipe, the number of heat pipes, the inlet temperatures, and the flow rates of hot and cold fluids. Freon 404A refrigerant was used as a working fluid for cooling the evaporator and energy recovery in the condenser. A comparison was made with global experimental data on the heat exchanger under analysis. It obtained air velocity, Nusselt number, heat transfer rate, thermal effectiveness, and air outlet temperature results. It demonstrated that the localized theoretical approach is consistent and can be used as a comprehensive analysis tool for heat exchangers using heat pipes.

Fakheri[3] introduced the concept of thermal efficiency for heat exchangers, which is determined using a factor called "the fin analogy number". A dimensionless number makes it possible to characterize different configurations of heat exchangers in a single functional formula based on the efficiency of an insulated fin at the end and constant area. The physical parameters that characterize the dimensionless number in question, the global heat transfer coefficient, and the relationship between the thermal capacities of the means that exchange heat with each other makes it possible to determine the thermal efficiency automatically and elegantly. The developed method brought a theoretical alternative to the traditional Logarithmic Mean Temperature Difference (LMTD) and Number of Thermal Units (NTU) methods, with the advantage of not requiring additional empirical parameters. Based on the second law of thermodynamics, the analytical process has undoubtedly solved many practical problems.

Nogueira[4] uses the concept of thermal efficiency to determine the thermal performance of shell and tube heat exchangers with external fins. The problem involves cooling machine oil using non-spherical cylindrical nanoparticles of Boehmite Alumina. The main quantities used in the analysis are the thermal effectiveness, the thermal and viscous irreversibilities, and the thermodynamic Bejan number. It was determined that increasing the number of finned tubes from two to six tubes is cost-effective at the expense of the high viscous dissipation caused by the oil in the annular region. The introduction of nanoparticles shows a slight decrease in the Bejan number despite significantly improving thermal performance.

Nogueira[5] applies the second law of thermodynamics to obtain outlet temperatures of the fluids in a shell and tube heat exchanger. It uses the concepts of thermal efficiency, thermal effectiveness, and thermal irreversibility to get relevant results. Water flows in the shell, and a mixture of water and ethylene glycol associated with nanoparticles flows in the tubes. Results for Reynolds number and heat transfer rate are used to justify the output data, demonstrating that the flow regime significantly affects the thermal performance of the heat exchanger.

Putra et al.[6] conducted an experimental procedure to analyze the thermal performance of heat pipes in heat recovery to reduce electricity consumption. The heat exchanger consists of several tubular heat pipes staggered in up to six rows. The fins were attached individually to each heat pipe. The experiments showed a strong influence of the air inlet temperature in the evaporator and the air inlet velocity.

Höhne[7] simulates through computational fluid dynamics (CFD) the heat and mass transfer processes in a heat pipe to analyze thermal performance and save energy. It uses a homogeneous multiphase model to simulate the heat pipe's evaporation, condensation, and phase change processes. He claims that there is reasonable agreement between the computational implementation and experimental results from the literature. He is confident that using advanced computational models will become analysis tools for heat exchangers using heat pipes.

Jouhara et al.[8] conducted a theoretical-experimental investigation of heat exchangers with multipass heat pipes. The system consists of copper heat pipes in a staggered configuration to transfer energy from a hot gas to water in the condenser. The experiment was carried out by changing the number of passages in the evaporator through several deflectors for a single section of the condenser. They report that changing the number of passes from one to 5 allows for a 25% improvement in the efficiency of the heat exchanger. Two theoretical models were implemented, LMTD and ε-NTU, to determine the heat exchanger outlet temperatures. Theoretical-experimental validation demonstrated that the LMTD model predicted the performance of the heat exchanger with a +15.5% error, while the maximum error obtained through the ε-NTU model was 19%.

Barrak[9] states that energy consumption has increased mainly in developing countries, and energy waste will also increase. He argues that air conditioning units are the primary energy consumers and that energy recovery could be feasible if energy recovery units are attached to air conditioning units. In this sense, he says, it is vital that researchers focus on energy recovery devices and that heat pipes are promising devices for accomplishing this task.

Jouhara et al.[10] recognize heat pipes as passive devices with no moving parts, more efficient for heat exchange between two fluids because of their high thermal conductivity. Due to their thermal superconductivity, they realize that adding heat pipes makes them ideal for industrial applications requiring a high heat transfer rate. They state that the applications of heat pipes range from low-temperature cryogenic applications to systems that work at very high temperatures. They point out that implementing heat pipes as waste heat recovery can reduce the cost of the process, with lower energy consumption, in several industrial sectors.

Abd El-Baky and Mohamed[11] claim that heat pipes are used for energy recovery in air conditioning systems. In these cases, heat pipes, such as in hospital operating rooms, are intended to recover sensible heat when the inlet and return air must not be mixed. They report using a fresh and return air current system connected to a heat pipe heat exchanger in an energy recovery system. Estimate the optimal effectiveness of the heat pipe heat exchanger and compare it with experimental data. They claim that the results show a 48% increase in efficiency and heat transfer to the evaporator when the fresh air temperature is raised to a convenient level. Furthermore, they claim that the enthalpy ratio increases to about 85% with the fresh air inlet temperature increase. They clarify that using heat pipes allows for transporting much heat over a considerable distance without additional energy input to the system.

Sukarno et al.[12] report that specific requirements related to thermal comfort in hospital operating rooms require the development of efficient systems for air conditioning and that energy recovery in the form of heat and that one method capable of accomplishing this task is the use of heat pipe heat exchangers. They describe experiments with heat pipe heat exchangers having three, six, and nine rows arranged in a staggered configuration, with four heat pipes in each row. They conduct theoretical analysis based on the ε-NTU model to predict the system's thermal performance under study. They determine a maximum efficiency of 62.6% in a system with nine rows of heat pipes. They conclude that the ε-NTU method can analyze energy recovery systems that apply heat pipes.

Abedalh et al.[13] test a heat pipe heat exchanger in an air conditioning system to reduce energy consumption. The tested heat exchanger consists of 40 copper heat pipes arranged in four rows. They performed several experiments and determined the effectiveness and rate of heat recovery at different air inlet velocities. The maximum level obtained for effectiveness was 64.6%, and the highest value of heat recovered was 923.4 watts.

Amini et al.[14] investigate the industrial heat storage process to reduce energy consumption. They use phase change material (PCM) for latent heat storage. For the use of PCMs, which have low conductivity, they used finned heat pipes loaded with water as working fluid incorporated in the PCM volume. The evaporation section of the heat pipe is heated through the condensation of a steam flow, which heats the tubes and the PCM tank, which has a melting temperature of 89 °C and a crystallization point of 77 °C. The heat absorbed in the evaporator is discharged through the heat pipes to the PCMs in the condenser. They conclude that the experiments carried out do not correspond to optimized conditions, requiring further investigations to determine how the heat pipes should be incorporated into the idealized heat exchanger to improve the phase change rate of the PCM.

Hakim et al.[15] experimented with a finned U-shaped heat pipe heat exchanger (HPHE) in a vertical configuration to reduce building energy consumption. They present results for the effectiveness and dehumidification capacity of the U-shaped HPHE coupled to the heating, ventilation, and air conditioning (HVAC) system. Demonstrate that two-row U-shaped HPHE increases the 39.9% coefficient of performance over HVAC without HPHE and can reduce 21.6% relative humidity, which results in energy savings for pre-cooling and heating. They conclude that the U-shaped finned heat pipe is a solution for upgrading an HVAC system.

2. Methodology

The system under analysis was experimentally evaluated and published by Górecki et al.[1]. The schematic diagram of the equipment can be found in **Figure 1** of the work mentioned above. It consists of heat pipes with individual fins (IFHPHE).

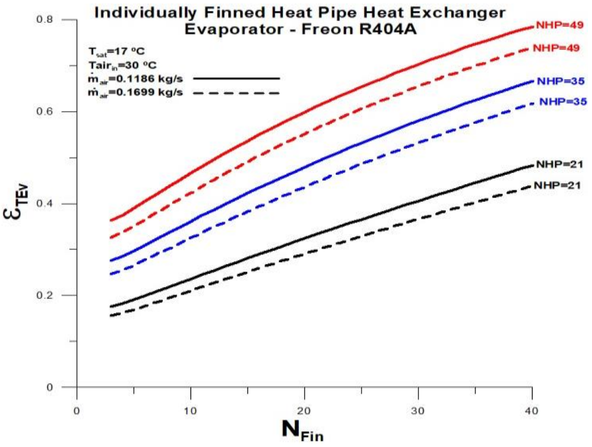

Figure 1. Thermal effectiveness versus fin number in the evaporator section.

The saturation temperature of the working fluid (R404A) in the heat pipe is represented by Equation (1).

$$T_{sat} = 17.0\ ℃\ fixed\ by\ definition \tag{1}$$

The saturation pressure of the working fluid (R404A) can be obtained through Equation (2):

$$P_{sat} = 614.1316315 + 17.18802462T_{sat} + 0.3276728108T_{sat}^2 \tag{2}$$

Equations (3)–(21) represent the properties of the working fluid (R404A) as a function of the saturation temperature. All properties were taken from literature tables valid for the element under analysis, and the numerical determination through polynomials was obtained through graphic software.

$$\rho_l = 1148.516119 - 2.934024895T_{sat} - 0.0425519003T_{sat}^2 \tag{3}$$

$$\begin{gathered}\rho_v = 29.62609253 + 1.088373933T_{sat} + 0.002241182059T_{sat}^2 \\ +0.0003618637607T_{sat}^3\end{gathered} \tag{4}$$

$$h_l = 200.2774524 + 1.356658428T_{sat} + 0.00586628846T_{sat}^2 \tag{5}$$

$$\begin{gathered}h_v = 368.3562439 + 0.5331782112T_{sat} - 0.0005307756065T_{sat}^2 \\ -6.0092036610^{-5}T_{sat}^3\end{gathered} \tag{6}$$

$$h_{lv} = h_v - h_l \tag{7}$$

Table 1 presents the properties of the working fluid (R404A).

Table 1. Properties of the working fluid (R404A) at saturation temperature.

T_{sat} ℃	$\rho_l \frac{kg}{m^3}$	$\rho_v \frac{kg}{m^3}$	$h_l\ -J/kg$	$h_v\ -J/kg$	$h_{lv}\ -J/kg$
17.0	1086.34	50.55	225.04	376.97	151.94

$$P_{sat} = 1001.02\ \text{Pa} \tag{8}$$

$$k_{R404l} = 0.0863\ \frac{W}{mK} \tag{9}$$

$$k_{R404v} = 0.01346 \tag{10}$$

$$Cp_{R404l} = 1530 \tag{11}$$

$$Cp_{R404v} = 870 \tag{12}$$

$$\mu_{R404l} = 1.2810^{-4} \tag{13}$$

$$\mu_{R404v} = 1.2210^{-5} \tag{14}$$

$$\nu_{R404l} = \frac{\mu_{R404l}}{\rho_{R404l}} \tag{15}$$

$$\nu_{R404v} = \frac{\mu_{R404v}}{\rho_{R404v}} \tag{16}$$

$$\rho_{R404l} = 1086.34 \tag{17}$$

$$\alpha_{R404l} = \frac{k_{R404l}}{\rho_{404l} Cp_{404l}} \tag{18}$$

$$\alpha_{R404v} = \frac{k_{R404v}}{\rho_{404v} Cp_{404v}} \tag{19}$$

$$Pr_{R404l} = \frac{\nu_{R404l}}{\alpha_{R404l}} \tag{20}$$

$$Pr_{R404v} = \frac{\nu_{R404v}}{\alpha_{R404v}} \tag{21}$$

The number of rows of Heat Pipes (HP) is defined by Equation (22).

$$N_{rows} = 3\ default;\ 3 \le N_{rows} \le 21 \tag{22}$$

Equation (23) represents the total number of heat pipes in the heat exchanger, and the number of fins N_{Fin} considered in the evaporator or condenser is defined by Equation (24). Equation (25) represents the volume flow rate of the air.

$$NHP = \frac{N_{rows}}{3}(3+4);\ 7 \le NHP \le 49 \tag{23}$$

$$N_{Fin} = 30 default;\ 0 \le N_{Fin} \le 70 \tag{24}$$

$$\dot{V}_{air} = \frac{370.0}{3600}\frac{m^3}{s} default;\ \frac{370.0}{3600} \le \dot{V}_{air} \le \frac{550.0}{3600} \tag{25}$$

The properties of the air, dependent on the inlet temperature $Tair_{in}$, can be obtained by the following Equations (26)–(29). All properties were taken from literature tables valid for the element under analysis, and the numerical determination through polynomials was obtained through graphic software.

Equation (26) is represented by thermal conductivity, and the dynamic, absolute viscosity of air characterizes Equation (27). The specific heat of air represents Equation (28). The density of the air is represented by Equation (29).

$$k_{air} = 6.91744186\ 10^{-5} Tair_{in} + 0.02462173663 \tag{26}$$

$$\mu_{air} = 1.95483621\ 10^{-5} + 2.735058039\ 10^{-9} Tair_{in} + 2.309587479\ 10^{-10}\ Tair_{in}^2 - 4.505882353\ 10^{-13} Tair_{in}^3 \tag{27}$$

$$Cp_{air} = 1003.728948 + 0.06727399886 * Tair_{in} + 3.565918367\ 10^{-6}\ Tair_{in}^2 + 8.222222222\ 10^{-7} Tair_{in}^3 \tag{28}$$

$$\rho_{air} = 1.219135515 - 0.002152770329 Tair_{in} - 3.64047479\ 10^{-7} Tair_{in}^2 + 1.705882353\ 10^{-9} Tair_{in}^3 \tag{29}$$

Table 2 presents air properties at the reference temperature.

Table 2. Air properties at the reference temperature.

$\boldsymbol{Tair_{in}}$ ℃	$\boldsymbol{k_{air}} - \boldsymbol{\frac{W}{mK}}$	$\boldsymbol{\mu_{air}} - \boldsymbol{\frac{kg}{ms}}$	$\boldsymbol{\rho_{air}} - \boldsymbol{\frac{kg}{m^3}}$	$\boldsymbol{Cp_{air}} - \boldsymbol{\frac{J}{kgK}}$
30.0 ℃	2.67×10^{-2}	1.98×10^{-5}	1.15	1005.77

$$\nu_{air} = \frac{\mu_{air}}{\rho_{air}} \tag{30}$$

$$\alpha_{air} = \frac{k_{air}}{\rho_{air} Cp_{air}} \tag{31}$$

Equation (32) represents the Prandtl number associated with the air.

$$Pr_{air} = \frac{\nu_{air}}{\alpha_{air}} \tag{32}$$

The surface tension for water, represented by $\boldsymbol{\sigma_{Water}}$, is given by Equation (33)[10].

$$\sigma_{Water} = 0.07275\left(1 - 0.002(K - 291)\right) \tag{33}$$

where $\boldsymbol{K}$ is saturation temperature in Kelvin.

The assumed constant for the surface-fluid combination represents Equation (34)[16].

$$C_{sf} = 0.006 \tag{34}$$

The mass flow rate of air at the inlet of the heat exchanger $\dot{m}_{air}$ is defined by Equation (35).

$$\dot{m}_{air} = \rho_{air}\dot{V}_{air} \tag{35}$$

The localized analytical approach is subdivided into the evaporator, the condenser, and the global Finned Heat Pipe Heat Exchanger (FHPHE).

2.1. Equations for the evaporator section of the heat exchanger

In the evaporator region, the cooling of the heated fresh air, the inlet temperature of heated fresh air varies between 20 °C and 50 °C. The inlet volume flow rate of fresh heated air in the evaporator region varies between 0.1078 m^3/s and 0.1528 m^3/s.

The formulation to simulate the heat exchange process in the evaporator is established through Equations (36)–(87).

The fresh air inlet temperature in the evaporator region, defined by Equation (36), is represented by $\boldsymbol{TEv_{in}}$.

$$TEv_{in} = 30.0\ ℃\ default; \quad 20.0\ ℃ \le TE_{in} \le 50.0\ ℃ \tag{36}$$

The estimated heat transfer coefficient for the boiling process, initially presented by Rohsenow[16] and related by Jouhara et al.[10], is given by $\boldsymbol{h_{boil}}$.

$$h_{boil} = \mu_l h_{lv} \left(\frac{g(\rho_l - \rho_v)}{\sigma_{water}}\right)^{1/2} \left(\frac{Cp_l}{C_{sf} h_{lv} Pr_l}\right)^3 \Delta T_{sat}^2 \tag{37}$$

$$\Delta T_{Evsat} = TEv_{in} - T_{sat} \tag{38}$$

The outside and inside diameters of the heat pipe are represented by $\boldsymbol{D_{ext}}$ and $\boldsymbol{D_{int}}$ are given by Equation (39), Equation (40)[1].

$$D_{ext} = 22.0\ 10^{-3}\ m \tag{39}$$

$$D_{\text{int}} = 20.0 10^{-3}\ m \tag{40}$$

The thermal conductivity of the heat pipe material (Copper), represented by Equation (41), is given by $\boldsymbol{k_W}$.

$$k_W = 235.0 \tag{41}$$

$\boldsymbol{LEv}$, illustrated by Equation (42), is the length of the heat pipe evaporation section and $\boldsymbol{WHE}$, represented by Equation (43), is the shell's width.

$$LEv = 250.010^{-3} \tag{42}$$

$$WHE = 200.0\ 10^{-3} \tag{43}$$

$$t_{Fin} = 0.810^{-3} \tag{44}$$

The thermal conductivity of the fin material (Aluminum) is given by $\boldsymbol{k_{Fin}}$.

$$k_{Fin} = 401.0 \tag{45}$$

The effective heat exchange length associated with the heat pipes in the evaporator is obtained by $\boldsymbol{LEv_{effec}}$. The thickness of a fin represented is given by $\boldsymbol{t_{Fin}}$. The space between fins, defined through Equation (46), is provided by $\boldsymbol{Sp_{Fin}}$.

$$Sp_{Fin} = 2.5\ 10^{-3}\ by\ definition \tag{46}$$

$$LEv_{effec} = LEv - NFin(t_{Fin} + Sp_{Fin}) \tag{47}$$

The hydraulic diameter of the heat exchanger in the evaporator region is given by $\boldsymbol{Dh_{Ev}}$. The Reynolds number associated with air, represented by Equation (49), is provided by $\boldsymbol{Re_{air}}$.

$$Dh_{EV} = \frac{4WHELEv_{effec}}{2(WHE + LEv_{effec})} \tag{48}$$

$$Re_{air} = \frac{4\dot{m}_{air}}{\pi Dh_{Ev}\mu_{air}} \tag{49}$$

Equation (50) represents the effective area occupied by the air in the evaporator.

$$A\,sec_{air} = \frac{\dot{m}_{air}Dh_{Ev}}{Re_{air}\ \mu_{air}} \tag{50}$$

The air velocity in the evaporator is represented by $\boldsymbol{V_{air}}$.

$$V_{air} = \frac{\dot{m}_{air}}{A\,sec_{air}\ \rho_{air}} \tag{51}$$

$$Dext_{Fin} = 50.010^{-3} \tag{52}$$

$$D\,int_{Fin} = D_{ext} \tag{53}$$

The effective heat transfer area in the evaporator Atr_{HP}, associated with heat pipes, is established by Equation (55). The effective heat transfer area associated with the fin system, Atr_{Fin}, and the total heat transfer area, A_{Total}, are represented by Equations (54), Equations (56).

$$Atr_{Fin} = NFinNHP\frac{\pi}{4}(Dext_{Fin}^2 - D\,int_{Fin}^2) \tag{54}$$

$$Atr_{HP} = NHP\pi D_{ext}(LEv - NFinSp_{Fin}) \tag{55}$$

$$A_{Total} = Atr_{Fin} + Atr_{HP} \tag{56}$$

$$Vair_{\max} = \frac{\dot{V}_{air}}{A\sec_{air}} \tag{57}$$

$$dr = 24.010^{-3}\ assumed \tag{58}$$

$$Re_{dr} = \frac{Vair_{max}}{\nu_{air}} \tag{59}$$

The Nusselt number for the air, as reported by Górecki et al.[1] is represented by $\boldsymbol{Nu_{air}}$. The convection heat transfer coefficient associated with air in the Evaporator is given by $\boldsymbol{h_{air}}$.

$$Nu_{air} = 0.1387\,\mathrm{Re}_{dr}^{0.718}\,\mathrm{Pr}_{air}^{(1/3)}\left(\frac{Sp_{Fin}}{Dext_{Fin} - D\mathrm{int}_{Fin}}\right)^{0.296} \tag{60}$$

$$h_{air} = \frac{Nu_{air} k_{air}}{dr} \tag{61}$$

$$mL_{Fin} = \sqrt{\frac{2h_{sair}}{k_{Fin} t_{Fin}}}\, t_{Fin} \tag{62}$$

The fin efficiency for the evaporator section is defined by $\boldsymbol{\eta_{Fin}}$[11].

$$\eta_{Fin} = \frac{\mathrm{Tanh}(mL_{Fin})}{mL_{Fin}} \tag{63}$$

$$\beta = \frac{Atr_{Fin}}{A_{Total}} \tag{64}$$

The efficiency associated with the set of fins in the evaporator, weighted by the area of heat exchange of the fins, is represented through $\boldsymbol{\eta'_{Fin}}$.

$$\eta'_{Fin} = \beta\eta_{Fin} + (1 - \beta) \tag{65}$$

The global heat transfer coefficient associated with air in the evaporator, Uo_{Ev}, is given by Equation (66).

$$Uo_{Ev} = \frac{1}{\frac{1}{h_{boil}} + \frac{D_{ext} - D_{int}}{kW} + \frac{1}{\eta'_{Fin} h_{air}}} \tag{66}$$

The heat capacity of the air in the evaporator is given by C_{Air}.

$$C_{Air} = \dot{m}_{air} Cp_{air} \tag{67}$$

$$C_{Ev} = C_{air} \tag{68}$$

The number of thermal units associated with air in the evaporator, NTU_{Ev}, is given by Equation (69).

$$NTU_{Ev} = \frac{Uo_{Ev} A_{Total}}{CEv} \tag{69}$$

The dimensionless number, called "fin analogy", is represented $\boldsymbol{Fa}$as defined by Fakheri[3] and reported by Nogueira[5].

$$Fa = \frac{NTU\sqrt{1 + C^{*2}}}{2} \quad for\ cross - flow \tag{70}$$

The thermal efficiency associated with the heat exchanger is $\boldsymbol{\eta_T}$[11].

$$\eta_T = \frac{tanh(Fa)}{Fa} \tag{71}$$

The thermal effectiveness related to the heat exchanger is $\boldsymbol{\varepsilon_T}$[11].

$$\varepsilon_T = \frac{1}{\frac{1}{\eta NTU} + \frac{1 + C^*}{2}} \tag{72}$$

The heat exchanger's thermal efficiency depends on two fundamental parameters: $\boldsymbol{NTU}$ e $\boldsymbol{C^*} = \frac{\boldsymbol{C_{min}}}{\boldsymbol{C_{max}}}$. For the physical conditions under analysis $\boldsymbol{C^*} = \mathbf{0.0}$. Then,

$$Fa_{Ev} = \frac{NTU_{Ev}}{2} \tag{73}$$

$$\eta_{TEv} = \frac{tanh(Fa_{Ev})}{Fa_{Ev}} \tag{74}$$

$$\varepsilon_{TEv} = \frac{1}{\dfrac{1}{\eta_{TEv} NTU_{Ev}} + \dfrac{1}{2}} \tag{75}$$

The heat transfer rate between the air and the heat pipe in the evaporating region is given by $\dot{\boldsymbol{Q}}_{\boldsymbol{Ev}}$.

$$\dot{Q}_{Ev} = \frac{C_{Ev} \Delta T_{Evsat}}{\dfrac{1}{\eta_{TEv} NTU_{Ev}} + \dfrac{1}{2}} \tag{76}$$

After passing through the evaporator, the outlet air temperature is represented through Equation (77).

$$TEv_{out} = TEv_{in} - \frac{\dot{Q}_{Ev}}{C_{Ev}} \tag{77}$$

$$X_t = Dext_{Fin} \tag{78}$$

$\boldsymbol{f}_{\boldsymbol{Ev}}$, represented by Equation (79), is the friction factor associated with the flow rate in the evaporator. In this work, for the configuration under analysis and some fins equal to 30, the coefficient value was conveniently adjusted to 0.7465.

$$f_{Ev} = 0.7465 \, \mathrm{Re}_{dr}^{(-0.316)} (\frac{X_t}{dr})^{(-0.927)} \tag{79}$$

Δp_{Ev} , represented by Equation (80), is the pressure drop in the evaporator.

$$\Delta p_{Ev} = 2 f_{Ev} N_{rows} \rho_{air} Vair_{max} \tag{80}$$

The thermal irreversibility in the evaporator is represented by Equation (81).

$$\sigma_{TEv} = ln(\frac{TEv_{in}}{TEv_{out}}) \tag{81}$$

The entropy generation associated with the thermal field in the evaporator is represented by Equation (82).

$$\dot{S}_{genTEv} = \sigma_{TEv} C_{Ev} \tag{82}$$

$\boldsymbol{P}_{\boldsymbol{2Ev}}$ is the outlet pressure in the evaporator.

$$P_{2Ev} = P_{atm} + \Delta p_{Ev} \tag{83}$$

$$Rh_{Ev} = \frac{TEv_{in} - TEv_{out}}{TEv_{in} - T_{sat}} \tag{84}$$

$\boldsymbol{\sigma}_{\boldsymbol{fEv}}$ is the viscous irreversibility in the evaporator.

$$\sigma_{fEv} = Rh_{Ev} \ln(\frac{P_{atm}}{P_{2Ev}}) \tag{85}$$

The entropy generation associated with the flow field in the evaporator is represented by Equation (86).

$$\dot{S}_{genfEv} = \sigma_{fEv} C_{Ev} \tag{86}$$

The thermodynamic Bejan number in the evaporator is represented by Equation (87).

$$Be_{Ev} = \frac{\dot{S}_{genTEv}}{\dot{S}_{genTEv} + \dot{S}_{genfEv}} \tag{87}$$

2.2. Equations for the condenser section of the heat exchanger

The air conditioning is sucked through the exhaust pipes and passes through the heat pipe condenser region. The saturation temperature of the working fluid is higher than the temperature of the air conditioning, which varies between 0 °C and 15 °C. The inlet volume flow rate of the air conditioning in the condenser region varies between 0.1028 m^3/s and 0.1472 m^3/s[1].

The formulation used to simulate the heat exchange process in the condenser is established through Equations (88)–(113).

The air temperature at the condenser inlet, $\boldsymbol{TCd_{in}}$, is represented by Equation (88).

$$TCd_{in} = 0.0\ °C\ ;\ \ 0.0\ °C \leq TCd_{in} \leq 15.0\ °C \tag{88}$$

Equation (89) represents the temperature difference between the condenser's air and the working fluid.

$$\Delta T_{Cdsat} = T_{sat} - TCd_{in} \tag{89}$$

The condenser section's length is represented through Equation (90).

$$LCd = LEv \tag{90}$$

Equation (91) represents the effective length of the condenser for the heat exchange.

$$LCd_{effec} = LCd - N_{Fin}(t_{Fin} + Sp_{Fin}) \tag{91}$$

The hydraulic diameter in the region of the capacitor, $\boldsymbol{Dh_{Cd}}$, is represented by Equation (92).

$$Dh_{Cd} = \frac{4WHELCd_{effec}}{2(WHE + LCd_{effec})} \tag{92}$$

The Reynolds number of air in the condenser region, $\boldsymbol{Re_{air}}$, is represented through Equation (93).

$$Re_{air} = \frac{4\dot{m}_{air}}{\pi Dh_{Cd}\mu_{air}} \tag{93}$$

The airflow area in the condenser, $A\text{sec}_{air}$, is given by Equation (94).

$$A\,sec_{air} = \frac{\dot{m}_{air}Dh_{Cd}}{Re_{air}\,\mu_{air}} \tag{94}$$

The condensation transfer coefficient in the heat pipe is provided by h_{Cond}, as reported by Nogueira[5].

$$h_{Cond} = 0.943[\frac{[\rho_l(\rho_l - \rho_v)h_{lv}gk_W^3]}{(\mu_W LCd\Delta T_{sat})}]^{1/4} \tag{95}$$

$$Uo_{Cd} = \frac{1}{\frac{1}{h_{Cond}} + \frac{D_{ext} - D_{int}}{kW} + \frac{1}{\eta'_{Fin}h_{air}}} \tag{96}$$

Equation (96) represents the global heat transfer coefficient.

$$C_{Air} = \dot{m}_{air}Cp_{air} \tag{97}$$

The air's heat capacity in the condenser's region is characterized by C_{Cd}.

$$C_{Cd} = C_{air} \tag{98}$$

Equation (99) represents the number of thermal units associated with the heat pipes in the condenser region.

$$NTU_{Cd} = \frac{Uo_{Cd}A_{Total}}{C_{Cd}} \tag{99}$$

The dimensionless parameter called "fin analogy" in the condenser region is represented $\boldsymbol{Fa_{Cd}}$.

$$Fa_{Cd} = \frac{NTU_{Cd}}{2} \tag{100}$$

Equation (101) represents the thermal efficiency associated with the condenser.

$$\eta_{TCd} = \frac{tanh(Fa_{Cd})}{Fa_{Cd}} \tag{101}$$

Equation (102) represents the thermal effectiveness related to the condenser.

$$\varepsilon_{TCd} = \frac{1}{\frac{1}{\eta_{TCd}NTU_{Cd}} + \frac{1}{2}} \tag{102}$$

The heat transfer rate between the air and the heat pipe in the condenser region is characterized by Equation (103).

$$\dot{Q}_{Cd} = \frac{C_{Cd}\Delta T_{Cdsat}}{\frac{1}{\eta_{TCd}NTU_{Cd}} + \frac{1}{2}} \tag{103}$$

The air outlet temperature in the condenser is represented through $\boldsymbol{TCd_{out}}$.

$$TCd_{out} = \frac{\dot{Q}_{Cd}}{C_{Cd}} + TCd_{in} \tag{104}$$

$\boldsymbol{f_{Cd}}$, illustrated by Equation (105), is the friction factor associated with the flow in the condenser.

$$f_{Cd} = 0.7465\,\mathrm{Re}_{dr}{}^{(-0.316)}(\frac{X_t}{dr})^{(-0.927)} \tag{105}$$

Δp_{Cd}, represented by Equation (106), is the pressure drop in the condenser.

$$\Delta p_{Cd} = 2f_{Cd}N_{rows}\rho_{air}Vair_{max} \tag{106}$$

The thermal irreversibility in the condenser is represented by Equation (107).

$$\sigma_{TCd} = ln(\frac{TCd_{in}}{TCd_{out}}) \tag{107}$$

The entropy generation associated with the thermal field in the condenser is represented by Equation (108).

$$\dot{S}_{genTCd} = \sigma_{TCd}C_{Cd} \tag{108}$$

$\boldsymbol{P_{2Cd}}$ is the outlet pressure in the condenser.

$$P_{2Cd} = P_{atm} + \Delta p_{Cd} \tag{109}$$

$$Rh_{Cd} = \frac{TCd_{in} - TCd_{out}}{TCd_{in} - T_{sat}} \tag{110}$$

$\boldsymbol{\sigma_{fCd}}$ is the viscous irreversibility in the condenser.

$$\sigma_{fCd} = Rh_{Cd}\ln(\frac{P_{atm}}{P_{2Cd}}) \tag{111}$$

The entropy generation associated with the flow field in the condenser is represented by Equation (112).

$$\dot{S}_{genfCd} = \sigma_{fCd}C_{Cd} \tag{112}$$

The thermodynamic Bejan number in the condenser is represented by Equation (113).

$$Be_{Cd} = \frac{\dot{S}_{genTCd}}{\dot{S}_{genTCd} + \dot{S}_{genfCd}} \tag{113}$$

2.3. Equations for individually finned heat pipe crow-flow heat exchanger (IFHPHE)

The cooling and energy recovery set to form a heat exchanger, with a fresh air inlet with a temperature above 17 °C and a cooled air outlet below 17 °C. The total heat transfer rate in the air conditioning process is equal to the sum of the heat transfer rates in the evaporator and the condenser $\dot{\boldsymbol{Q}}_{\boldsymbol{Cd}}$, according to Equation (114). Equation (115) represents the maximum transfer rate, $\dot{\boldsymbol{Q}}_{\boldsymbol{Max}}$, in the heat exchanger, which $\boldsymbol{C}_{\boldsymbol{min}}$ is the smallest of the thermal capacities of the air involved in the process. Equation (116) represents the heat exchanger's effectiveness in air conditioning.

$$\dot{Q}_{IFHPHE} = \dot{Q}_{Ev} + \dot{Q}_{Cd} \tag{114}$$

$$\dot{Q}_{Max} = C_{\min}(TEv_{in} - TCd_{out}) \tag{115}$$

$$\varepsilon_{IFHPHE} = \frac{\dot{Q}_{IFHPHE}}{\dot{Q}_{Max}} \tag{116}$$

$$\Delta p_{IFHPHE} = \Delta p_{Ev} + \Delta p_{Cd} \tag{117}$$

$$\sigma_{THPHE} = \sigma_{TEv} + \sigma_{TCd} \tag{118}$$

$$\sigma_{fHPHE} = \sigma_{fEv} + \sigma_{fCd} \tag{119}$$

$\boldsymbol{Be}_{\boldsymbol{HPHE}}$ is the thermodynamic Bejan number associated with the heat exchanger.

$$Be_{HPHE} = \frac{\sigma_{THPHE}}{\sigma_{THPHE} + \sigma_{fHPHE}} \tag{120}$$

3. Results and discussion

The thermal effectiveness in the evaporator section is analyzed for two air mass flow rates, within a borderline range for the air conditioning system $\dot{\boldsymbol{m}}_{\boldsymbol{air}} = \boldsymbol{0.1699\ kg/s}$, in **Figure 1** The variables used in the analysis are the number of fins per heat pipe and the number of heat pipes. Effectiveness decreases with increasing airflow and increases with the number of fins and heat pipes. For example, for multiple fins equal to 40 and heat pipes equal to 49, the thermal efficiency reaches a value close to 80%. When the number of heat pipes equals 21, the thermal effectiveness reaches 40% for the smallest flow rate. The thermal effectiveness is relatively high in all analyzed situations, and it is what is expected for a well-dimensioned heat exchanger.

The heat transfer rate in the evaporator, **Figure 2**, has the same trend as the effectiveness in qualitative terms. However, the maximum value for the heat transfer rate occurs for the highest mass flow rate of air due to the highest heat capacity. The highest observed heat transfer rate is for $\boldsymbol{NHP = 49}$ and $\boldsymbol{N}_{\boldsymbol{Fin}} = \boldsymbol{40}$, as expected.

The thermal irreversibility of the Evaporator is represented in **Figure 3** and shows a growth trend similar to that of thermal effectiveness in qualitative terms. The most significant thermal irreversibility is observed for $\boldsymbol{NHP = 49}$ and $\boldsymbol{N}_{\boldsymbol{Fin}} = \boldsymbol{40}$, with a value close to 0.45 for lower airflow. A high value for thermal effectiveness is expected for heat exchangers.

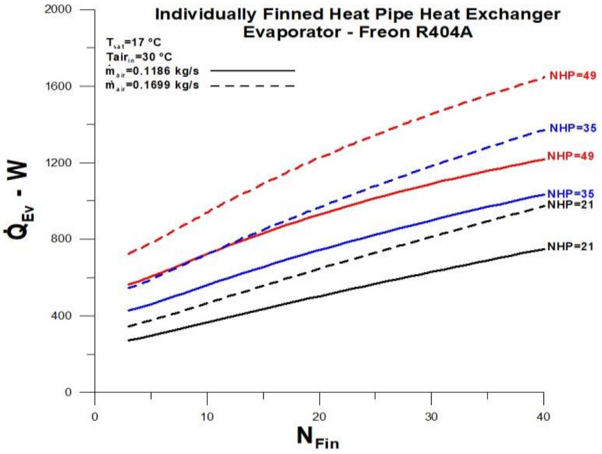

Figure 2. Heat transfer rate versus fin number in the evaporator section.

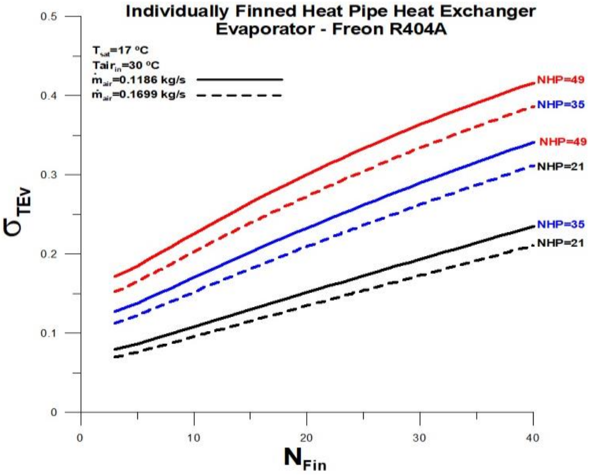

Figure 3. Thermal irreversibility versus fin number in the evaporator section.

The air outlet temperature in the evaporator region is represented in **Figure 4** for an air inlet temperature equal to 30 °C and a Freon saturation temperature equal to 17 °C. The temperature decreases with an increasing number of heat pipes and the number of fins. The lowest air outlet temperature is obtained for the most downward airflow over-analysis. The lowest value corresponds to approximately 19 °C, for $NHP = 49$, $N_{Fin} = 40$ e $\dot{m}_{air} = 0.1186\ kg/s$.

Figure 5 shows the pressure drop in the evaporator region as a function of the number of fins per heat pipe, the number of heat pipes, and the airflow. As expected, the increase in air flow significantly increases the pressure drop in the Evaporator. The highest value obtained for the pressure drop in the Evaporator corresponds to approximately 120 Pa, for $NHP = 49$, $N_{Fin} = 40$ e $\dot{m}_{air} = 0.1699\ kg/s$.

The viscous irreversibility in the Evaporator shows a growth trend similar to the pressure drop, as seen in **Figure 6**. The highest value obtained for the thermal irreversibility in the Evaporator corresponds to approximately 60%, for $NHP = 49$,$N_{Fin} = 40$ e $\dot{m}_{air} = 0.1699\ kg/s$. High viscous irreversibility is detrimental in terms of cost for a heat exchanger.

The number of fins per heat pipe and the number of heat pipes in the evaporator region significantly affect the value of the Bejan number, **Figure 7**. The smallest value for the Bejan number is observed for $NHP = 49$, $N_{Fin} = 40$ e $\dot{m}_{air} = 0.1699\ kg/s$**,** numerically, approximately equal to 0.4. The highest value observed for the Bejan number corresponds roughly to 0.9 for heat pipes without fins and lower airflow due to lower viscous irreversibility. The lower number of heat pipes, $NHP = 21$, and higher number of fins enable a high cost-benefit ratio above 0.7.

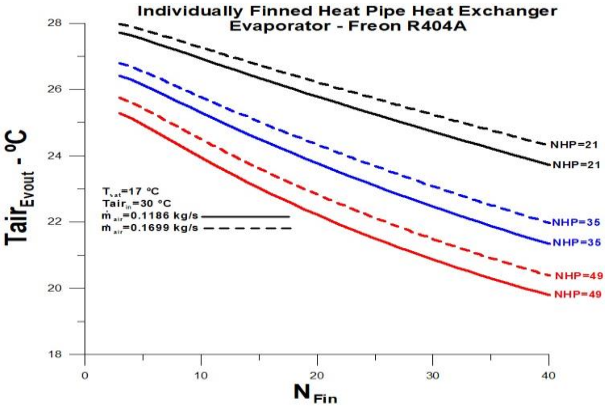

Figure 4. Air outlet temperature versus fin number in the evaporation section.

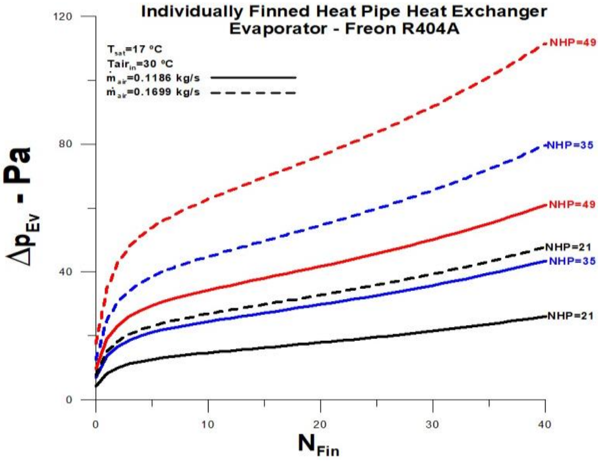

Figure 5. Pressure drops versus fin number in the evaporation section.

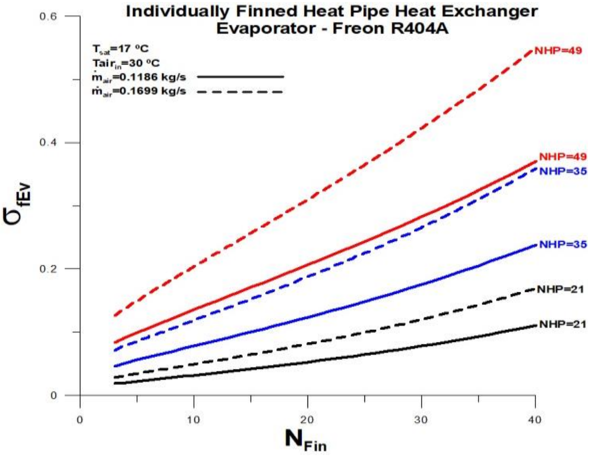

Figure 6. Viscous irreversibility versus fin number in the evaporation section.

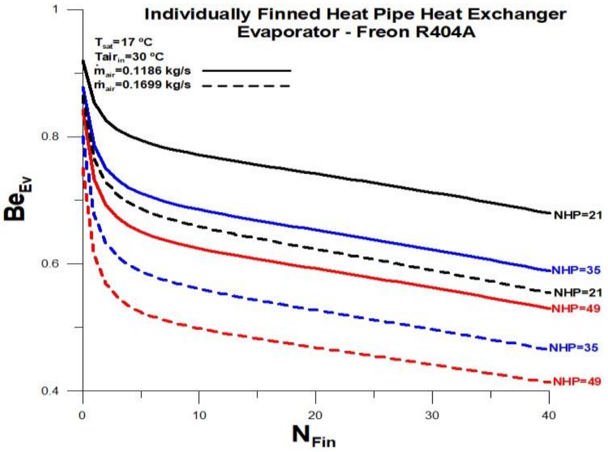

Figure 7. Bejan number versus fin number in the evaporation section.

The thermal effectiveness in the condenser section is analyzed for two air mass flow rates, within a borderline range for the air conditioning system, that is, $\dot{m}_{air} = 0.1186\ kg/s$ e $\dot{m}_{air} = 0.1699\ kg/s$, in **Figure 8**. The variables used in the analysis are the number of fins per heat pipe and the number of heat pipes. Effectiveness decreases with increasing airflow and increases with the number of fins and heat pipes. For example, for some fins equal to 40 and heat pipes equal to 49, the effectiveness reaches a value close to 70%.

The heat transfer rate in the condenser, **Figure 9**, has the same trend as the effectiveness in qualitative terms. However, the maximum value for the heat transfer rate occurs for the highest mass flow rate of air due to the highest heat capacity—the highest observed heat transfer rate for $NHP = 49$ e $N_{Fin} = 40$.

The air outlet temperature in the condenser region is represented in **Figure 10** for an air inlet temperature equal to 0.0 °C and a Freon saturation temperature equal to 17 °C. The outlet temperature increases with an increasing number of heat pipes and the number of fins. The highest air outlet temperature is obtained for the lowest airflow over-analysis. The highest value corresponds to approximately 13 °C, for $NHP = 49$, $N_{Fin} = 40$ e $\dot{m}_{air} = 0.1253\ kg/s$.

Figure 11 shows the pressure drop in the condenser region as a function of the number of fins per heat pipe, the number of heat pipes, and the airflow. As expected, the increase in air flow significantly increases the pressure drop in the Evaporator. The highest value obtained for the head loss in the Evaporator corresponds to approximately 120 Pa, for $NHP = 49$,$N_{Fin} = 40$ e $\dot{m}_{air} = 0.1795\ kg/s$.

The number of fins per heat pipe and the number of heat pipes in the condenser region significantly affect the value of the Bejan number, **Figure 12**. The lowest value for the Bejan number is observed for $NHP = 49$ e $N_{Fin} = 40$ and $\dot{m}_{air} = 0.1795\ kg/s$, numerically, approximately equal to 0.4. The highest value observed for the Bejan number corresponds roughly to 0.95 for heat pipes without fins and lower airflow due to lower viscous irreversibility. There is less heat exchange without fins, but the relative weight between thermal irreversibility and total irreversibility is high.

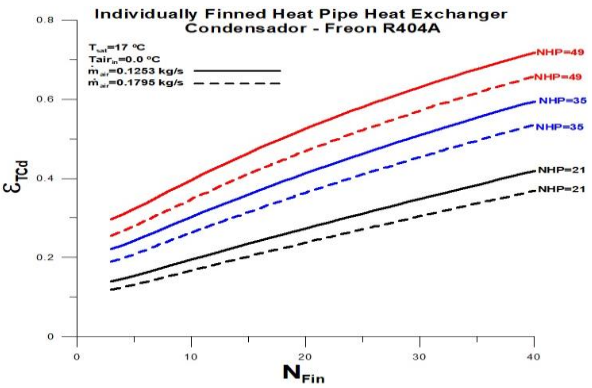

Figure 8. Thermal effectiveness versus fin number in the condenser section.

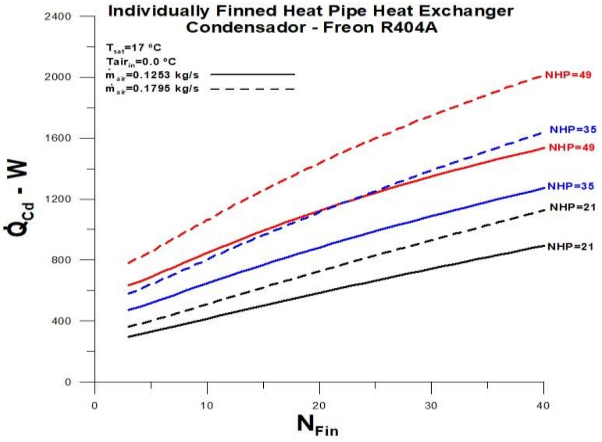

Figure 9. Heat transfer rate versus fin number in the condenser section.

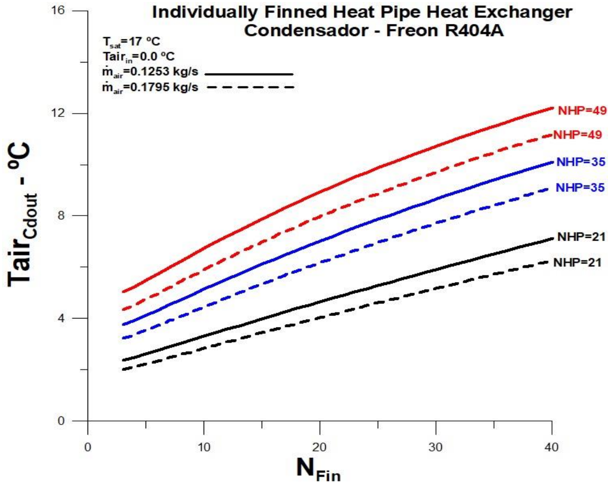

Figure 10. Air outlet temperature versus fin number in the condenser section.

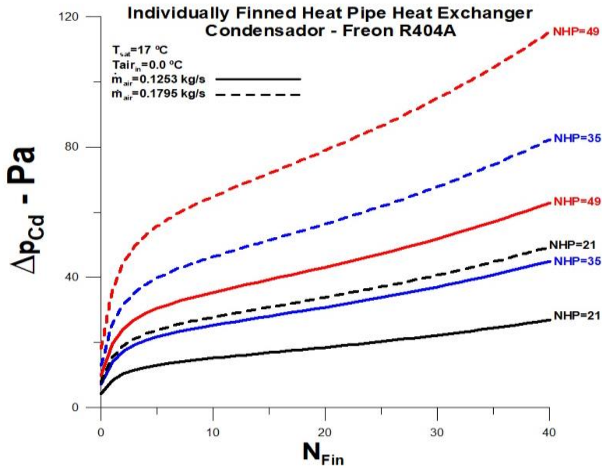

Figure 11. Pressure drops versus fin number in the condenser section.

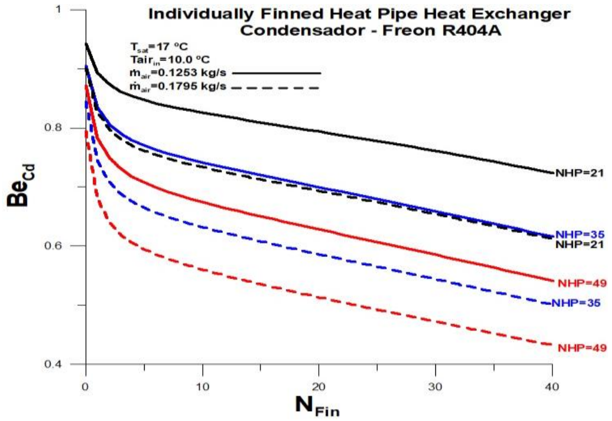

Figure 12. Bejan number versus fin number in the condenser section.

Figure 13 presents theoretical and experimental results for the heat transfer rate for the heat exchanger under analysis. The experimental data have shown when compared with the theoretical results, demonstrate that the number of fins in the heat exchanger is between 10 and 40 fins and that the observed theoretical trend is compatible with the experiment since the total transfer rate of heat tends to grow with the number of rows, and with the number of fins. The thermal effectiveness tends to be the maximum possible when the number of fins is equal to 40, and the number of heat pipes is equal to 49 since, in this case, the heat transfer rate coincides with the maximum value (**Figure 14**).

When comparing the total theoretical pressure drop with experimental results, it is evident that the number of fins in the original heat exchanger is equal to 30 fins, as shown in **Figure 15**. However, the theoretical value results from the stipulated coefficient in the friction factor Equation (79), Equation (105), and once again, the theoretical results obtained are consistent with what is expected with the total pressure drop when increasing the number of fins from 10 to 40.

Figure 16 presents results for the thermodynamic Bejan number related to the heat exchanger. The highest cost-benefit ratio is associated with the lowest number of fins per heat pipe, equal to 10. However, fins equal to 10 correspond to the lowest heat transfer rate, as shown in **Figure 13**. There must be a compromise between the number of fins and the outlet temperature of the air. **Figure 10** shows a more significant number of fins and a greater number of heat pipes, allowing for a higher outlet temperature.

It is evident that there must be a compromise with all the analyzed factors, and a satisfactory cost-benefit ratio, thermal irreversibility versus total irreversibility, must be sought. In this sense, it is concluded that fins between 10 and 20 for heat pipes equal to 49 provide a better cost-benefit ratio.

The results obtained individually and globally are adequate and consistent concerning the expected values for all the quantities analyzed. The global results for the heat exchanger, obtained through the results presented individually for the evaporator and condenser, demonstrate that the theoretical model's implementation strategy can contribute to improving the heat exchanger acting locally. For example, the number of fins used on the evaporator need not be the same for the evaporator. **Figures 13** and **14** show theoretical-experimental comparisons for fundamental quantities related to the heat exchanger. The values of the absolute percentage deviations obtained are between 2.0% and 42.1%, with an average deviation equal to 22.5% for effectiveness and 15.9% for the heat transfer rate.

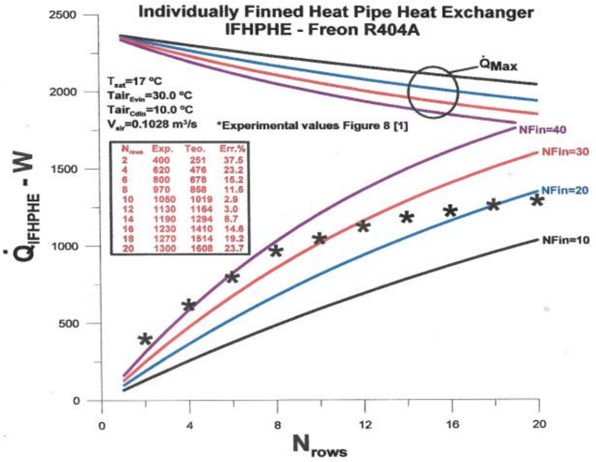

N_{rows}	Exp.	Teo.	Err.%
2	400	251	37.5
4	620	476	23.2
6	800	678	15.2
8	970	858	11.5
10	1050	1019	2.9
12	1130	1164	3.0
14	1190	1294	8.7
16	1230	1410	14.6
18	1270	1514	19.2
20	1300	1608	23.7

Figure 13. Heat transfer rate for the heat exchanger versus the number of rows.

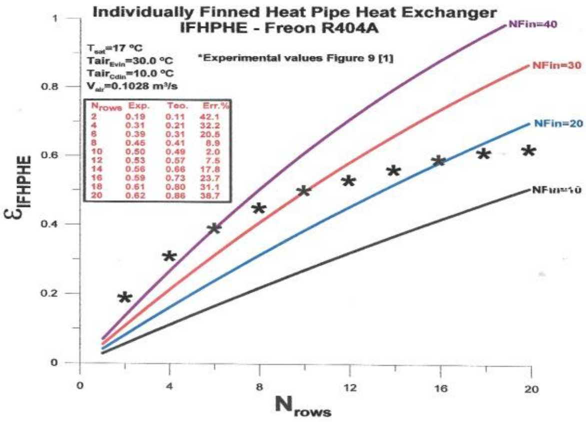

N_{rows}	Exp.	Teo.	Err.%
2	0.19	0.11	42.1
4	0.31	0.21	32.2
6	0.39	0.31	20.5
8	0.45	0.41	8.9
10	0.50	0.49	2.0
12	0.53	0.57	7.5
14	0.56	0.66	17.8
16	0.59	0.73	23.7
18	0.61	0.80	31.1
20	0.62	0.86	38.7

Figure 14. Effectiveness of the heat exchanger versus the number of rows.

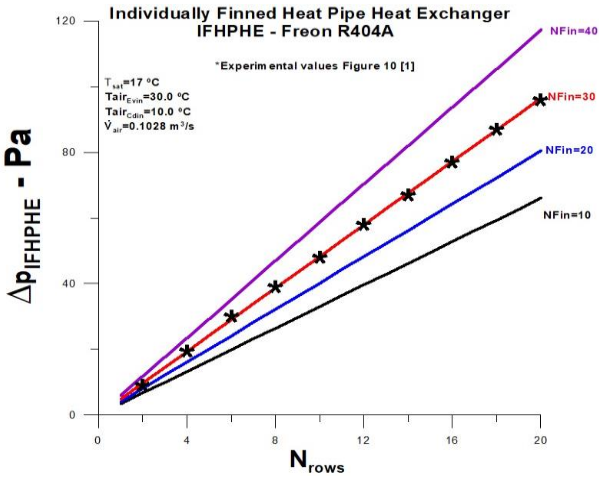

Figure 15. Total pressure drops versus the number of rows.

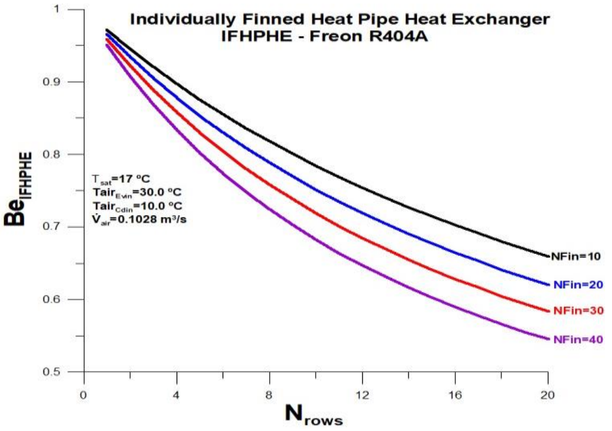

Figure 16. Bejan thermodynamic number for heat exchanger versus the number of rows.

4. Conclusion

The thermal and viscous irreversibility in the heat exchanger, composed of individually finned heat pipes, is analyzed for two air mass flow rates within a borderline range for the air conditioning system, that is, $\dot{m}_{air} = 0.1186\ kg/s$ e $\dot{m}_{air} = 0.1699\ kg/s$. The variables used in the analysis are the number of fins per heat pipe and the number of heat pipes.

The main results obtained through the theoretical analysis were:

- The number of fins per heat pipe and the number of heat pipes significantly affect the value of the Bejan number, and a satisfactory cost-benefit ratio, thermal irreversibility versus total irreversibility, must be sought.
- A compromise between the number of fins and the number of heat pipes with the outlet temperature of the air.
- The highest cost-benefit ratio is associated with the lowest number of fins per heat pipe, equal to 10.
- Considering the air outlet temperature, the number of fins between 10 and 20 for heat pipes equal to 49 for the Evaporator and Condenser provides a better cost-benefit ratio.
- The values of the absolute percentage deviations obtained are between 2.0% and 42.1%, with an average deviation equal to 22.5% for effectiveness and 15.9% for the heat transfer rate.

The recommended individualized procedure proved consistent and can be used to improve the thermal-hydraulic performance of a finned heat tube heat exchanger. Refining the model and determining the exact number of fins that allow the best cost-benefit ratio is possible in the study under analysis.

Conflict of interest

The author declares no conflict of interest.

Nomenclature

$Asec$	cross-section area, $[m^2]$
Atr	heat transfer area, $[m^2]$
Cp	specific heat, $[\frac{J}{kgK}]$
C	thermal capacity, $[\frac{W}{K}]$
C_{min}	minimum thermal capacity, $[\frac{W}{K}]$
$C^* = \dfrac{C_{min}}{C_{max}}$	
D_h	hydraulic diameter, $[m]$
Fa	fin analogy
h	coefficient of heat convection, $[\frac{W}{m^2K}]$
k	thermal conductivity, $[\frac{W}{mK}]$
K	kelvin
k_W	thermal conductivity of the tube, $[\frac{W}{mK}]$
k_{Fin}	thermal conductivity of the fin, $[\frac{W}{mK}]$
L	vertical or horizontal length, $[m]$
$\dot{m}_{air}$	mass flow rate of the air, $[\frac{kg}{s}]$
N_{Fin}	number of fins
Nu	nusselt number
Pr	prandtl number
$\dot{Q}$	actual heat transfer rate, $[W]$
$\dot{Q}_{max}$	maximum heat transfer rate, $[W]$
Re	reynolds number
T	temperatures, [°C]
Uo	global heat transfer coefficient, $[\frac{W}{m^2K}]$

Subscripts

boil	ebulição
Cd	condenser
Cond	condenser
effect	effective
Ev	evaporator
ext	external

HP	heat pipe
H	horizontal
in	inlet
int	internal
out	outlet
sat	saturation

Greek symbols

α	thermal diffusivity, $[\frac{m^2}{s}]$
β	the relationship between areas
ρ	density of the fluid, $[\frac{kg}{m^3}]$
μ	dynamic viscosity of the fluid, $[\frac{kg}{ms}]$
ν	kinematic viscosity of the cold fluid, $[\frac{m^2}{s}]$
ε_T	thermal effectiveness
η_T	thermal efficiency
ΔT	a difference of temperatures, [°C]

Acronyms

FHPHE	finned heat pipe heat exchanger
Ev	evaporators
Cd	condenser
NHP	number of heat pipes
NFin	number of fins
Nrows	number of rows
NTU	number of thermal units

References

1. Górecki G, Łęcki M, Gutkowski AN, et al. Experimental and numerical study of heat pipe heat exchanger with individually finned heat pipes. Energies 2021; 14(17): 5317. doi: 10.3390/en14175317
2. Nogueira E. Localized theoretical analysis of thermal performance of individually finned heat pipe heat exchanger for air conditioning with freon r404a as working fluid. Materials Science and Chemical Engineering 2023; 11(8): 61–85. doi: 10.4236/msce.2023.118005
3. Fakheri A. Heat Exchanger Efficiency. Heat Transfer 2007; 129(9): 1268–1276. doi: 10.1115/1.2739620
4. Nogueira E. Thermo-hydraulic optimization of shell and externally finned tubes heat exchanger by the thermal efficiency method and second law of thermodynamics. International Journal of Chemical and Process Engineering Research 2022; 9(1): 21–41. doi: 10.18488/65.v9i1.3130
5. Nogueira É. Thermal performance in heat exchangers by the irreversibility, effectiveness, and efficiency concepts using nanofluids. Journal of Engineering Sciences 2020; 7(2): F1–F7. doi: 10.21272/jes.2020.7(2).f1
6. Putra NSD, Anggoro T, Winarta A. Experimental study of heat pipe heat exchanger in hospital hvac system for energy conservation. International Journal of Advance Science Engineering Information Technology 2017; 7(3): 871–877. doi: 10.18517/ijaseit.7.3.2135
7. Höhne T. CFD simulation of a heat pipe using the homogeneous model. International Journal of Thermofluids 2022; 15: 100163. doi: 10.1016/j.ijft.2022.100163
8. Jouhara H, Almahmoud S, Brough D, et al. Experimental and theoretical investigation of the performance of an air to water multi-pass heat pipe-based heat exchanger. Energy 2021; 219: 119624. doi: 10.1016/j.energy.2020.119624

9. Barrak A. Heat pipes heat exchanger for HVAC applications. In: Vega MA (editor). Heat Transfer—Design, Experimentation, and Applications. IntechOpen; 2021.
10. Jouhara H, Chauhan A, Nannou T, et al. Heat pipe-based systems—Advances and applications. Energy 2017; 128: 729–754. doi: 10.1016/j.energy.2017.04.028
11. Abd El-Baky MA, Mohamed MM. Heat pipes heat exchanger for heat recovery in air conditioning. Applied Thermal Engineering 2007; 27(4): 795–801. doi: 10.1016/j.applthermaleng.2006.10.020
12. Sukarno R, Putra N, Hakim II, et al. Multi-stage heat-pipe heat exchanger for improving energy efficiency of the HVAC system in a hospital operating room. International Journal of Low-Carbon Technologies 2021; 16(2): 259–267. doi: 10.1093/ijlct/ctaa048
13. Abedalh AS, Yasin NJ, Ameen HA. Thermal performance of HAVC system using heat pipe heat exchanger. Journal of Mechanical Engineering Research and Developments 2021; 44(2): 336–344.
14. Amini A, Miller J, Jouhara H. An investigation into the use of the heat pipe technology in thermal energy storage heat exchangers. Energy 2017; 136: 163–172. doi: 10.1016/j.energy.2016.02.089
15. Hakim II, Sukarno R, Putra N. Utilization of u-shaped finned heat pipe heat exchanger in energy-efficient HVAC systems. Thermal Science and Engineering Progress 2021; 25: 100984. doi: 10.1016/j.tsep.2021.100984
16. Rohsenow WM. A method of correlating heat transfer data for surface boiling of liquids. Transactions of the American Society of Mechanical Engineers 1952; 74(6): 969–975. doi: 10.1115/1.4015984

ACADEMIC
ACADEMIC PUBLISHING PTE LTD

Academic Publishing Pte. Ltd.

Add: 73 Upper Paya Lebar Road, #07-02B-01, Centro Bianco, Singapore 534818
Tel: +65 83184869
E-mail: editorial_office@acad-pub.com
Web: http://ojs.acad-pub.com/